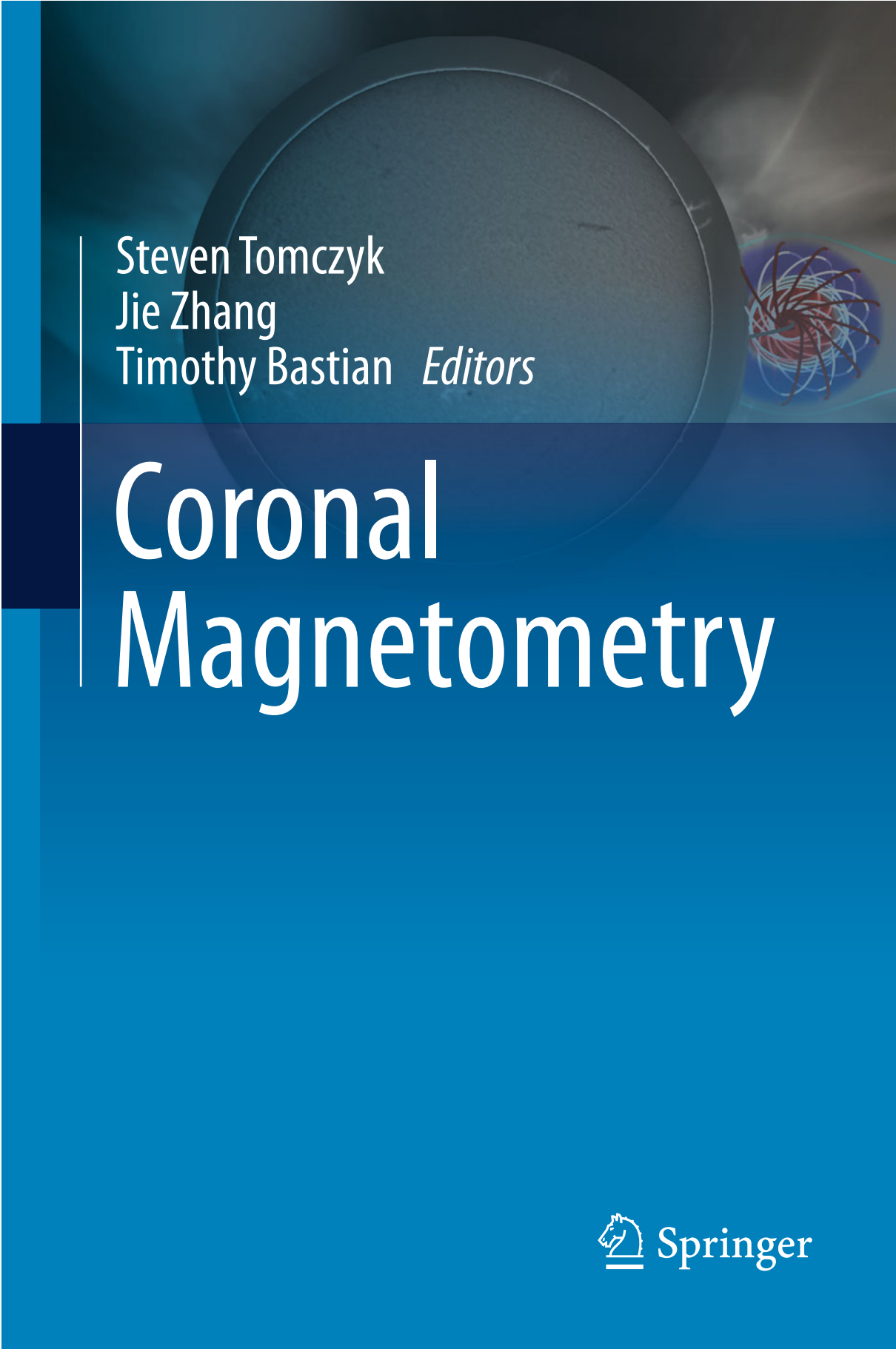
Steven Tomczyk
Jie Zhang
Timothy Bastian Editors
Coronal
Magnetometry
Springer

Coronal Magnetometry

Steven Tomczyk · Jie Zhang · Timothy Bastian
Editors

Coronal Magnetometry

Previously published in *Solar Physics* Volume 288, Issue 2, 2013
and Volume 289, Issue 8, 2014

Springer

Editors
Steven Tomczyk
National Center for Atmospheric Research
Boulder, CO, USA

Timothy Bastian
National Radio Astronomy Observatory
Charlottesville, VA, USA

Jie Zhang
George Mason University
Fairfax, VA, USA

ISBN 978-1-4939-2037-2 ISBN 978-1-4939-2038-9 (eBook)
DOI 10.1007/978-1-4939-2038-9
Springer New York Heidelberg Dordrecht London

Library of Congress Control Number: 2014948457

Cover Image: A twisted magnetic structure (model) superposed on observations of the solar atmosphere. Background: the solar eclipse of 11 July 1991 (image credit: High Altitude Observatory (HAO) and Rhodes College); Solar disk image: HAO Mauna Loa Solar Observatory Polarimeter for Inner-Coronal Studies (PICS) observations in H α; Model image: Gibson and Low (*Astrophysical Journal* **493**, 460, 1998) model of twisted magnetic field lines, visualized as by Rachmeler *et al.* (*Solar Physics* **288**, 617, 2013, page 155 of this book).

Printed on acid-free paper

Springer is part of Springer Science+Business Media (www.springer.com)

Contents

CORONAL MAGNETOMETRY

DOI 10.1007/978-1-4939-2038-9_1
Reprinted from *Solar Physics* Journal, DOI 10.1007/s11207-013-0432-3

Preface

Steven Tomczyk · Jie Zhang · Timothy Bastian · John W. Leibacher

Published online: 5 November 2013

Magnetic fields are the dominant energy source for heating the Sun's corona and for producing energetic solar activity such as flares and coronal mass ejections. Solar magnetic fields are also the dominant factor in structuring the coronal plasma and in shaping the heliosphere that encompasses the Earth and the other planets. Over the past three decades, remote-sensing observations of the vector magnetic field in the solar photosphere have become routine. Direct diagnostics of coronal magnetic fields, however, are still in their infancy and remain technically challenging. Nevertheless, driven by advances in instrumentation and by society's need to understand and predict coronal processes, it is anticipated that rapid growth in coronal magnetic-field diagnostics will be made in the next decade.

This *Topical Issue* of *Solar Physics* is devoted to the nascent field of coronal magnetometry. Most contributed articles were first presented at the "Workshop on Coronal Magnetism –

Coronal Magnetometry
Guest Editors: S. Tomczyk, J. Zhang, and T.S. Bastian

S. Tomczyk
High Altitude Observatory/National Center for Atmospheric Research, Boulder, CO, USA
e-mail: tomczyk@ucar.edu

J. Zhang
George Mason University, Fairfax, VA, USA
e-mail: jzhang7@gmu.edu

T. Bastian
National Radio Optical Astronomy Observatory, Charlottesville, VA, USA
e-mail: tbastian@nrao.edu

J.W. Leibacher (✉)
National Solar Observatory, Tucson, AZ, USA
e-mail: john.leibacher@gmail.com

J.W. Leibacher
Institut d'Astrophysique Spatial, Orsay, France

Connecting Models to Data and the Corona to the Earth", which was held 21 – 23 May 2012 in Boulder, Colorado, USA (www.hao.ucar.edu/CoronalMagnetismWorkshop/). The purpose of the workshop was to foster the development of tools to interpret current and future measurements of coronal magnetic fields. The *Coronal Multi-channel Polarimeter* (Tomczyk *et al.*, 2001) instrument is now obtaining routine observations of coronal polarization, and improved measurements are on the horizon in the visible to IR spectral regions with the construction of the *Advanced Technology Solar Telescope* (Keil *et al.*, 2003). At radio wavelengths the upgrade of the *Owens Valley Solar Array* (Gary and Hurford, 1994) and the construction of the *Chinese Spectral Radioheliograph* (Yan *et al.*, 2009) will open access to a variety of powerful diagnostics that are complementary to those at IR wavelengths. In addition, the *Frequency Agile Solar Radiotelescope* (Bastian, 2003) and the *Coronal Solar Magnetism Observatory* (www.cosmo.ucar.edu/) were recently recommended by the US National Research Council Solar and Space Physics Decadal Survey (Baker and Zurbuchen, 2013) which promise comprehensive and routine measurements of coronal magnetic fields and plasma.

Following the scientific organization of the workshop, this *Topical Issue* covers the following subjects:

i) Techniques for measuring coronal magnetism from UV to radio wavelengths.
ii) Instruments and facilities to observe coronal magnetism.
iii) Forward and inverse modeling of the observed signatures of coronal magnetism.
iv) Extrapolations of photospheric magnetic fields into the corona.
v) The role of coronal magnetism in solar activity, space weather, and space climate.

Acknowledgements The organizers gratefully acknowledge support for this meeting from the US National Science Foundation through base funding of NCAR/HAO and thank HAO Director Michael Thompson for his support. The members of the Scientific Organizing Committee of the workshop were Tim Bastian, Marc DeRosa, Haosheng Lin, Vic Pizzo, Steven Tomczyk, Brian Welsch, and Jie Zhang.

Articles

Tomczyk, S., Zhang, J., Bastian, T., Leibacher, J.W.: 2013, Coronal Magnetic Fields: Preface. *Solar Phys.* **288**, 463. doi:10.1007/s11207-013-0432-3.

Judge, P.J., Habbal, S., Landi, E.: 2013, From Forbidden Coronal Lines to Meaningful Coronal Magnetic Fields. *Solar Phys.* **288**, 467. doi:10.1007/s11207-013-0309-5.

Régnier, S.: 2013, Magnetic Field Extrapolations into the Corona: Success and Future Improvements. *Solar Phys.* **288**, 481. doi:10.1007/s11207-013-0367-8.

Wang, R., Yan, Y, Tan, B.: 2013, Three-Dimensional Nonlinear Force-Free Field Reconstruction of Solar Active Region 11158 by Direct Boundary Integral Equation. *Solar Phys.* **288**, 507. doi:10.1007/s11207-013-0422-5.

Peter, H.: 2013, Magnetic Field Diagnostics and Spatio-Temporal Variability of the Solar Transition Region. *Solar Phys.* **288**, 531. doi:10.1007/s11207-013-0270-3.

Gary, D.E., Fleishman, G D., Nita, G.M.: 2013, Magnetography of Solar Flaring Loops with Microwave Imaging Spectropolarimetry. *Solar Phys.* **288**, 549. doi:10.1007/s11207-013-0299-3.

Long, D.M., Williams, D.R., Régnier, S., Harra, L.K.: 2013, Measuring the Magnetic-Field Strength of the Quiet Solar Corona Using "EIT Waves". *Solar Phys.* **288**, 567. doi:10.1007/s11207-013-0331-7.

Shen, Y.D.: 2013, Observations of a Quasi-periodic, Fast-Propagating Magnetosonic Wave in Multiple Wavelengths and Its Interaction with Other Magnetic Structures. *Solar Phys.* **288**, 585. doi:10.1007/s11207-013-0395-4.

Forland, B.C., Gibson, S.E., Dove, J.B., Rachmeler, L.A., Fan Y.: 2013, Coronal Cavity Survey: Morphological Clues to Eruptive Magnetic Topologies. *Solar Phys.* **288**, 603. doi:10.1007/s11207-013-0361-1.

Rachmeler, L.A., Gibson, S.E., Dove, J.B., DeVore, C.R., Fan, Y.: 2013, Polarimetric Properties of Flux Ropes and Sheared Arcades in Coronal Prominence Cavities. *Solar Phys.* **288**, 617. doi:10.1007/s11207-013-0325-5.

Tian, H., Tomczyk, S., McIntosh, S.W., Bethge, C., de Toma, G., Gibson, S.: 2013, Observations of Coronal Mass Ejections with the Coronal Multichannel Polarimeter. *Solar Phys.* **288**, 637. doi:10.1007/s11207-013-0317-5.

Kim, I., Alexeeva, I.V., Bugaenko, O.I., Popov, V.V., Suyunova E.Z.: 2013, Comments on Near-Limb Zeeman and Hanle Diagnostics. *Solar Phys.* **288**, 651. doi:10.1007/s11207-013-0419-0.

References

Baker, D.N., Zurbuchen, T.H.: 2013, *Solar and Space Physics: A Science for a Technological Society*, US National Academies Press, Washington.

Bastian, T.S.: 2003, The frequency agile solar radiotelescope. *Adv. Space Res.* **32**, 2705. doi:10.1016/S0273-1177(03)90454-6.

Gary, D.E., Hurford, G.J.: 1994, Coronal temperature, density, and magnetic field maps of a solar active region using the Owens Valley Solar Array. *Astrophys. J.* **420**, 903.

Keil, S.L., Rimmele, T., Keller, C.U., Hill, F., Radick, R.R., Oschmann, J.M., Warner, M., Dalrymple, N.E., Briggs, J., Hegwer, S.L., Ren, D.: 2003, Design and development of the Advanced Technology Solar Telescope (ATST). *Proc. SPIE* **4853**, 240.

Tomczyk, S., Card, G.L., Darnell, T., Elmore, D.F., Lull, R., Nelson, P.G., Streander, K.V., Burkepile, J., Casini, R., Judge, P.G.: 2001, An instrument to measure coronal emission line polarization. *Solar Phys.* **247**, 411. ADS:2008SoPh..247..411T, doi:10.1007/s11207-007-9103-6.

Yan, Y., Zhang, J., Wang, W., Liu, F., Chen, Z., Ji, G.: 2009, The Chinese Spectral Radioheliograph – CSRH. *Earth Moon Planets* **104**, 97.

DOI 10.1007/978-1-4939-2038-9_2
Reprinted from *Solar Physics* Journal, DOI 10.1007/s11207-013-0309-5

From Forbidden Coronal Lines to Meaningful Coronal Magnetic Fields

P.G. Judge · S. Habbal · E. Landi

Received: 26 December 2012 / Accepted: 16 April 2013 / Published online: 5 June 2013

Abstract We review methods to measure magnetic fields within the corona using the polarized light in magnetic-dipole (M1) lines. We are particularly interested in both the global magnetic-field evolution over a solar cycle, and the local storage of magnetic free energy within coronal plasmas. We address commonly held skepticisms concerning angular ambiguities and line-of-sight confusion. We argue that ambiguities are, in principle, no worse than more familiar remotely sensed photospheric vector fields, and that the diagnosis of M1 line data would benefit from simultaneous observations of EUV lines. Based on calculations and data from eclipses, we discuss the most promising lines and different approaches that might be used. We point to the S-like [Fe XI] line ($J = 2$ to $J = 1$) at 789.2 nm as a prime target line (for the *Advanced Technology Solar Telescope* (ATST) for example) to augment the hotter 1074.7 and 1079.8 nm Si-like lines of [Fe XIII] currently observed by the *Coronal Multi-channel Polarimeter* (CoMP). Significant breakthroughs will be made possible with the new generation of coronagraphs, in three distinct ways: i) through single-point inversions (which encompasses also the analysis of MHD wave modes), ii) using direct comparisons of synthetic MHD or force-free models with polarization data, and iii) using tomographic techniques.

Coronal Magnetometry
Guest Editors: S. Tomczyk, J. Zhang, and T.S. Bastian

The National Center for Atmospheric Research is sponsored by the National Science Foundation.

P.G. Judge (✉)
High Altitude Observatory, National Center for Atmospheric Research, P.O. Box 3000, Boulder, CO 80307-3000, USA
e-mail: judge@ucar.edu

S. Habbal
Institute for Astronomy, 2680 Woodlawn Drive, Honolulu, HI 96822, USA
e-mail: shadia@ifa.hawaii.edu

E. Landi
Department of Atmospheric, Oceanic and Space Sciences, University of Michigan, Ann Arbor, MI 48109, USA
e-mail: elandi@umich.edu

Keywords Solar corona · Solar magnetism

1. Introduction

Measurement of solar magnetic fields has been a goal of solar physics since the discovery of the Zeeman effect in sunspots by Hale (1908). Our purpose here is to review how magnetic-dipole (M1) lines, formed in coronal plasma, might be used to address particular questions in coronal and heliospheric physics: How does the coronal magnetic-field vector evolve over the solar sunspot cycle? Can we measure some of the free magnetic energy on observable scales in the corona, and its changes, say, before and after a flare?

Theoretical work by Charvin (1965) spurred experimental studies of the polarization of magnetic-dipole lines, such as [Fe XIII] $3p^2\,{}^3P_1 \rightarrow 3p^2\,{}^3P_0$ at 1074.7 nm, as a way to constrain coronal magnetic fields. The lines are optically thin in the corona; their intensities are $\lesssim 10^{-5}$ of the disk continuum intensities. Thus they can be observed only during eclipses or using coronagraphs that occult the solar disk.

Here, we review M1 emission-line polarization towards the specific goal of measuring the vector magnetic field $[\mathbf{B}(\mathbf{r};t)]$ throughout a sub-volume of the corona. To date, this has not been achieved. We have little idea of the true origin of CMEs, flares, and coronal heating. even though coronal plasma has been regularly observed since the 1930s. The latest of several decades of high-cadence images of coronal plasma from space reveal more details but are limited to studying effects, not causes, of coronal dynamics, since such instruments measure thermal, not magnetic, properties. To discover the cause of coronal dynamics we must measure $\mathbf{B}(\mathbf{r};t)$ above the photosphere – the region of the atmosphere where free energy is stored and quickly released – since it is the free energy associated with electrical current systems within coronal plasmas that drives these phenomena. Measurements of $\mathbf{B}(\mathbf{r};t)$ in the photosphere have been done for decades, but photospheric dynamics occurs under mixed β conditions (β = gas/magnetic pressure ≈ 1). In contrast, the low-β coronal plasma should exist in simpler magnetic configurations, perhaps more amenable to straightforward interpretation. In MHD the electrical currents are simply $\mathbf{j} = \nabla \times \mathbf{B}(\mathbf{r};t)$. Given sufficiently accurate measurements of $\mathbf{B}(\mathbf{r};t)$ in the low-β corona, both $\mathbf{j}$ and the free energy itself can in principle be derived.

Like all observational studies, this is bandwidth-limited exercise. We can investigate structures only from the smallest resolvable scales $[\ell]$ to the largest $\approx \mathrm{R}_\odot \approx 700$ Mm, and on time scales longer than the smallest time $[\tau]$ needed to acquire the data. The spatial range will be limited by foreseeable observational capabilities to $\ell \gtrsim 1$ Mm. Successful tomographic-inversions using solar rotation to slice through the 3D corona require $\tau \gtrsim 1$ day, during which the corona is viewed from angles differing by $\approx 1/4$ radian. Given our goal, it is clear that we will not be able to investigate either the dissipation scales of magnetic fields, nor changes in magnetic fields on rapid dynamical time scales $\lesssim \mathrm{R}_\odot / C_\mathrm{A} \approx 350$ seconds of the inner corona (here $C_\mathrm{A} \approx 2$ Mm s^{-1} is the Alfvén speed). However, these limitations are not new. In any case, coronal dynamics and flares involve a slow build-up and sudden release of magnetic free energy (Gold and Hoyle, 1960). This energy build-up can indeed, and should be, explored through new measurements of $\mathbf{B}(\mathbf{r};t)$.

2. The Inverse Problem

2.1. General Considerations

Consider a heliocentric coordinate system with Sun center at $\mathbf{r} \equiv (x, y, z) = \mathbf{0}$, with the line of sight along z, and x, y being in the plane of the sky. Given a set of observations

$[\{I_{i\ldots4,\nu}(x,y,t)\}]$ of the four Stokes parameters $[IQUV]$ at n frequencies $[\nu]$ across a M1 line at time t, we seek solutions for $\mathbf{B}(x,y,z;t)$ over an observable sub-volume of the corona $\approx \Delta x \Delta y \Delta z$. We can write

$$I_{i,\nu}(x,y;t) = \int_{\Delta z} \varepsilon_i\big(\mathbf{S}(\mathbf{r};t)\big)\,\mathrm{d}z = \Phi_i\big(\mathbf{S}(\mathbf{r};t)\big). \tag{1}$$

The M1 lines – having small oscillator strengths – are optically thin through the corona. Under these conditions ε_i is a non-linear, but *local* function of a "source vector" S_j, $j = 1,\ldots,n$. The price for "optical thinness" is that Δz encompasses the entire line of sight through the corona to the solar disk or into space. Tomography specifically takes advantage of this. There is, however, skepticism in the community concerning the magnetic-field measurements under optically thin conditions that we address in Section 2.4. The non-linearity arises because the Stokes parameters $\mathbf{I}$ depend on the "atomic alignment" $[\sigma_0^2(\alpha_0 J)]$, a scalar quantity that is a linear combination of magnetic-substate populations. The alignment can be positive, negative, or zero, as discussed below. Ignoring the alignment would make the problem linear in the source term (like the standard emission-measure problem for line intensities only).

The source $[\mathbf{S}]$ must be written as a function of $\mathbf{r}$ and time $[t]$ in terms of necessary thermodynamic and magnetic parameters. At a minimum this means specifying

$$\mathbf{S}(\mathbf{r};t) = \big\{\rho(\mathbf{r};t), \mathbf{v}(\mathbf{r};t), T(\mathbf{r};t), \mathbf{B}(\mathbf{r};t)\big\},$$

for plasma with density ρ moving with velocity $\mathbf{v}$ at temperature T. These quantities must be supplemented by calculations that give the local distributions of ionization states and electron density. Any formal "inverse" solution is of the form

$$\mathbf{S}(\mathbf{r};t) = \Phi^{-1}\mathbf{I}(x,y;t), \tag{2}$$

where $\mathbf{I}$ is the $4n$-long "vector" of observed Stokes parameters. Clearly, a 3D array of scalar and vector fields such as $\mathbf{S}(\mathbf{r};t)$ cannot be recovered from one set of measurements $[\mathbf{I}(x,y;t)]$ that are integrated over Δz. Additional information is needed.

A "good diagnostic" maps components of $\mathbf{I}$ into $\mathbf{S}$. If Equation (1) were linear (or were linearized) we could write (*e.g.* Craig and Brown, 1986)

$$\mathbf{S} = \big(\mathbf{\Phi}^{\mathrm{T}}\mathbf{\Phi}\big)^{-1}\mathbf{\Phi}^{\mathrm{T}}\mathbf{I}. \tag{3}$$

The eigen-spectrum of matrix $(\mathbf{\Phi}^{\mathrm{T}}\mathbf{\Phi})^{-1}$ measures the degree to which measurements of $\mathbf{I}$ can be used to determine $\mathbf{S}$. As usual, the formal operation given by Equation (3) should not be taken as an inverse solution: it is ill-posed (Craig and Brown, 1986).

2.2. Origin of Polarization of Magnetic-Dipole Coronal Lines

Polarization of spectral lines is generated in two ways (*e.g.* Casini and Landi Degl'Innocenti, 2008). Any process that produces unequal sub-level populations, such as anisotropy of illuminating radiation, also produces polarization of light in the emitted radiative transitions to/from a given atomic level. When magnetic-substate populations are equal, the state is "naturally populated" and light is unpolarized. The second way is to separate the substates in energy, so that spectroscopy can discriminate states of polarized light associated with the specific changes in energy of states with different sub-level quantum numbers $[M]$, no matter how the sub-levels are populated. Magnetic- and electric-fields thus are imprinted on spectral-line polarization through the Zeeman and Stark effects. Since charge neutrality is a good approximation in coronal plasma (*e.g.* Parker, 2007), electric fields and the associated

stresses are far smaller than those for the magnetic field, and in quasi-static situations can be ignored. We focus on the magnetic fields.

Adopting the notation of Casini and Judge (1999), for M1 emission-lines between upper- and lower-levels with quantum numbers αJ ($J =$ total angular momentum) and $\alpha_0 J_0$, the ε_i terms in Equation (1) are proportional to a term of the form

$$\epsilon_{JJ_0} = \frac{h\nu}{4\pi} N_{\alpha_0 J} A_{\alpha_0 J \rightarrow \alpha_0 J_0}. \tag{4}$$

This term is simply the emission coefficient (ignoring stimulated emission) for the *unpolarized* transfer problem, in units of erg cm^{-3} sr^{-1} s^{-1}. The population density of the upper-level can be factored as usual as

$$N_{\alpha_0 J} = \frac{N_{\alpha_0 J}}{N_{\rm ion}} \frac{N_{\rm ion}}{N_{\rm el}} \frac{N_{\rm el}}{N_{\rm H}} \frac{N_{\rm H}}{n_{\rm e}} n_{\rm e}. \tag{5}$$

We label the first factor on the RHS of the above equation f: it is the ratio of the upper-level population of the level emitting the photons to the total ion population. The remaining factors are, in order, the ionization fraction, element abundance, ratio of hydrogen nuclei number density to the electron number density $n_{\rm e}$, and lastly $n_{\rm e}$ itself. For strong lines (electric dipole or "E1" lines in the EUV/soft X rays) $f \propto n_{\rm e}$ and $\exp(-h\nu/kT)$, so that $N_{\alpha_0 J} \propto n_{\rm e}^2 G(T)$ as usual. For M1 lines $f \propto n_{\rm e}^{\beta}$ with $0 < \beta < 1$, but generally $h\nu/kT \ll 1$, so the temperature dependence of $N_{\alpha_0 J}$ enters mostly the ionization fraction. Under coronal ionization-equilibrium conditions this factor is a function only of temperature T.

The polarized terms $[\varepsilon_i]$ also depend on the anisotropy of the incident photospheric radiation, particle collisions, the strength and direction of the coronal magnetic field, and the direction of the line of sight. M1 lines have large radiative lifetimes ($\tau_{\rm R} \approx A^{-1}_{\alpha_0 J \rightarrow \alpha_0 J_0} \approx 10^{-1}$ s). The Larmor frequency $[\nu_{\rm L} \approx \mu_{\rm B} B/h]$ is much larger than the inverse lifetime of the level: $\nu_{\rm L}\tau_{\rm R} \gg 1$. This is the "strong field" (or "saturation") limit of the Hanle effect. If the photospheric irradiation is rotationally symmetric and spectrally flat, the atomic polarization is in the special form of alignment $[\sigma^2_0(\alpha_0 J)]$, which in terms of substate populations is written

$$\sigma^2_0(\alpha J) = \frac{\sqrt{5}}{\sqrt{J(J+1)(2J-1)(2J+3)}} \sum_M \left[3M^2 - J(J+1)\right] \frac{N(\alpha_0 J M)}{N(\alpha_0 J)}. \tag{6}$$

Circularly polarized light is generated only by the "σ"-components ($\Delta M = \pm 1$) of the Zeeman effect. The M1 emission coefficients $\varepsilon_i^{(j)}$ for Stokes parameter i are (Section 4 of Casini and Judge, 1999):

$$\varepsilon_0^{(0)}(\nu, \hat{\mathbf{k}}) = \epsilon_{JJ_0} \phi(\nu_0 - \nu) \left[1 + D_{JJ_0} \sigma^2_0(\alpha_0 J) \mathcal{T}^2_0(0, \hat{\mathbf{k}})\right], \tag{7}$$

$$\varepsilon_i^{(0)}(\nu, \hat{\mathbf{k}}) = \epsilon_{JJ_0} \phi(\nu_0 - \nu) D_{JJ_0} \sigma^2_0(\alpha_0 J) \mathcal{T}^2_0(i, \hat{\mathbf{k}}) \quad (i = 1, 2), \tag{8}$$

$$\varepsilon_3^{(1)}(\nu, \hat{\mathbf{k}}) = -\sqrt{\frac{2}{3}} \nu_{\rm L} \epsilon_{JJ_0} \phi'(\nu_0 - \nu) \left[\bar{g}_{\alpha_0 J, \alpha_0 J_0} + E_{JJ_0} \sigma^2_0(\alpha_0 J)\right] \mathcal{T}^1_0(3, \hat{\mathbf{k}}), \tag{9}$$

where j in $\varepsilon_i^{(j)}$ is the leading order in the Taylor-series expansion of the emission coefficient with frequency.[1] $\phi(\nu_0 - \nu)$ is the line profile [Hz^{-1}], $\phi'(\nu_0 - \nu)$ its first derivative with respect to ν, remaining terms (except $\nu_{\rm L}$) are dimensionless. The factor D_{JJ_0} depends only on angular momenta, and E_{JJ_0} also depends on the Landé g-factor of the transition: $\bar{g}_{\alpha_0 J, \alpha_0 J_0}$.

[1] For M1 coronal lines the $\Delta M = 0$ "π"-components are proportional to $\phi''(\nu_0 - \nu)$. These are orders of magnitude weaker than the zeroth-order alignment-generated component, which is $\propto \phi(\nu_0 - \nu)$.

The tensor $\mathcal{T}_0^{1,2}(i,\hat{\mathbf{k}})$ relates the angular distribution and polarization of emitted radiation to the direction of the observer. In terms of angles γ_B and Θ_B, defining the magnetic azimuth in the plane-of-the-sky and inclination along the line-of-sight, these are

$$\mathcal{T}_0^2(0,\hat{\mathbf{k}})_{M1} = \frac{1}{2\sqrt{2}}\left(3\cos^2\Theta_B - 1\right),$$
$$\mathcal{T}_0^2(1,\hat{\mathbf{k}})_{M1} = \frac{3}{2\sqrt{2}}\cos 2\gamma_B \sin^2\Theta_B,$$
$$\mathcal{T}_0^2(2,\hat{\mathbf{k}})_{M1} = -\frac{3}{2\sqrt{2}}\sin 2\gamma_B \sin^2\Theta_B,$$
$$\mathcal{T}_0^1(3,\hat{\mathbf{k}})_{M1} = \sqrt{\frac{3}{2}}\cos\Theta_B.$$

2.3. M1 Lines from One Point in the Corona

Sometimes coronal images are dominated by emission from one small region, such as from a small section of an active region loop at $\mathbf{r}_0 = (x_0, y_0, z_0)$. In this case the source $\mathbf{S}(\mathbf{r};t) = \mathbf{S}(t)\delta(x-x_0)\delta(y-y_0)\delta(z-z_0)$ and the measured $\mathbf{I}$ is simply $\propto \varepsilon_i^{(j)}$ evaluated at $\mathbf{r} = (x_0, y_0, z_0)$. By inspection of expressions for ε_i we see that

i) The magnetic-field *strength* is encoded only in circular polarization through $\varepsilon_3^{(1)}(\nu,\hat{\mathbf{k}})$, via ν_L, and only as the *product* $B\cos\Theta_B$.
ii) The usual weak-field "magnetograph formula" – taking the ratio of Equation (9) and the derivative of Equation (7) – does not only depend on the Landé g-factor $\bar{g}_{\alpha_0 J,\alpha_0 J_0}$. In the presence of a non-zero alignment, the ratio includes smaller terms including $\sigma_0^2(\alpha_0 J)$ in both numerator and denominator.
iii) The magnetic-field *azimuth* γ_B is encoded in the linear polarization as $\gamma_B = -\frac{1}{2}\arctan(\varepsilon_2^0/\varepsilon_1^0)$.

Of course, in reality, measured quantities $[\mathbf{I}]$ are integrals of these elementary $\varepsilon_i^{(j)}$ coefficients along the line of sight.

2.4. "Long" Line of Sight Integrations

A concern sometimes expressed among solar physicists is that M1 coronal emission-lines form over such large distances that they have limited use in diagnosing magnetic fields. The perceived problem is that the magnetic field changes too much along the long lines of sight $L_c \approx R_\odot$. Mathematically we might say

$$\left|\frac{\partial B_i}{\partial s}\right| L_c \gtrsim \left|\langle B_i\rangle\right|, \tag{10}$$

for magnetic vector component B_i.

Let us apply the same arguments to a familiar situation in which there is far less such preconceived skepticism: the solar photosphere. It is indeed a "thin" layer (500 km) compared with the solar radius, but this does not mean that it is "thin" (small L_c) in the sense implied by Equation (10). Photospheric magnetic fields are highly intermittent in space and time. Consider formation of polarized light from a simple cylindrical "flux tube" of diameter 160 km in the solar photosphere (*e.g.* Steiner, 1994, left panel of Figure 1). The photon mean free path [mfp] in the photosphere $L_p \approx H_p$ is $\approx$120 km, as indicated by "mfp". Clearly there is structure in the thermal and magnetic conditions *well below the photon mfp*.

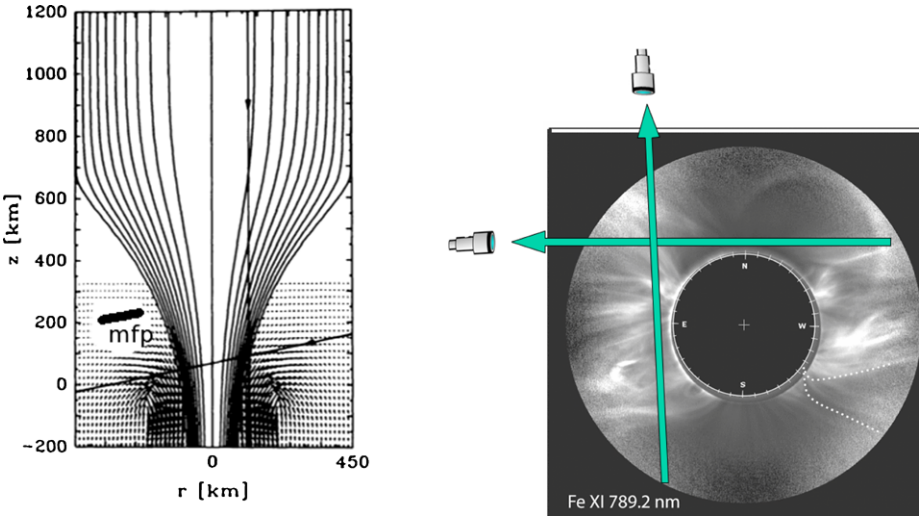

Figure 1 Left: magnetic-field lines and velocity vectors for a flux tube extending from beneath the photosphere into the chromosphere, from Steiner (1994) but annotated with the photon mean free path. Two rays intercepting the boundary between magnetised plasma are shown, along which spectral lines are formed. Right: an image of the corona during the July 2011 eclipse in the Fe XI 789.2 nm line is shown, obtained by one of us (SH). Two integration rays are shown. Note that this image already has been integrated in one dimension, thus in 3D such rays intercept much less structure than this image might seem to suggest.

As discussed by Steiner and others, this leads to "peculiar" Stokes profiles – the "Stokes-V area asymmetry" being one parameter of particular interest. The point here is not that peculiar Stokes profiles can be explained, but that in photospheric problems of interest, one must diagnose magnetic fields in situations where the inequality in Equation (10) holds!

Consider next the second panel of Figure 1, showing rays through an image of the corona during eclipse. The rays intercept many different structures, and again the condition in Equation (10) applies. But this image misrepresents the LOS confusion because the structures shown are already integrated along the orthogonal LOS (in and out of the page). In 3D, the actual rays will intercept far fewer of these structures than is suggested by this image. It is by no means clear that the LOS integration is worse in the corona than in the photosphere, when it comes to trying to diagnose magnetic fields of interest.[2]

2.5. Atomic Alignment

A proper interpretation of M1 emission-lines requires knowledge of $\sigma_0^2(\alpha_0 J)$, in an inversion it must be solved for as part of the solution for $\mathbf{S}(\mathbf{r};t)$ (Judge, 2007). The alignment comes from solutions to atomic sub-level population calculations. Even in statistical-equilibrium, the equations are non-linear coupled multi-level systems requiring numerical solution. This presents a problem for inversions since this expands the solution space to include the alignment itself, which becomes non-linear in the source parameters $\mathbf{S}(\mathbf{r};t) = \{\rho(\mathbf{r};t), \mathbf{v}(\mathbf{r};t), T(\mathbf{r};t), \mathbf{B}(\mathbf{r};t)\}$.

[2]When observing the photosphere on larger scales, with a lower resolution (say $1''$; 725 km), the magnetic-flux tube structure shown is washed out. The magnetic field on the larger scales is still of interest, indeed most observations are made in this limit. However, the physical processes associated with flux tubes are not directly accessible to $1''$-resolution observations.

To understand the non-linearities we can consider atomic models of increasing complexity. First consider a two-level atomic model for a $J = 1 \rightarrow J_0 = 0$ transition excited only by photospheric radiation, for which analytic solutions are available from, *e.g.*, Casini and Landi Degl'Innocenti (2008). Their Equation (12.23) gives

$$\sigma_0^2(1) = \frac{w}{2\sqrt{2}}\left(3\cos^2\vartheta_{\rm B} - 1\right) \quad \text{(two-level atom, } J = 1 \rightarrow J_0 = 0\text{)}, \tag{11}$$

where w measures the radiation anisotropy. Here, $\vartheta_{\rm B}$ (different from $\Theta_{\rm B}$) measures the local angle between the magnetic-field vector and solar gravity vector (central axis of the radiation cone). When the center-to-limb variation of the intensity is zero, $w = \frac{1}{2}(1 + \cos\vartheta_{\rm M})\cos\vartheta_{\rm M}$ (ϑ_M is the angle subtended by the solar radius at a point [**r**] in the corona). In this case the alignment is generated by anisotropic but rotationally symmetric radiation in the transition itself.

The magnitude of alignment is reduced by processes tending to populate sub-levels naturally, making $\frac{N(\alpha_0 JM)}{N(\alpha_0 J)} \rightarrow 1/(2J+1)$ and so $|\sigma_0^2(\alpha J)| \rightarrow 0$ in Equation (6). Collisions with particles having isotropic distribution functions thus reduce the magnitude of any existing alignment. Such collisions tend to leave the angular dependence of existing alignment essentially unchanged. This result is demonstrated through the multi-level calculations for Fe XIII by Judge (2007), where the alignment of the upper-levels ($3p^2\,{}^3P_{J=2,1}$) of the 1074.7 and 1079.8 nm lines of Fe XIII were found to factorize as

$$\sigma_0^2(\alpha_0 J) \approx k_J(T_{\rm e}, n_{\rm e}, \vartheta_{\rm M})\frac{1}{2}\left(3\cos^2\vartheta_{\rm B} - 1\right), \tag{12}$$

to within 0.7 % and 3.2 %, respectively. The level-dependent term $k_J(T_{\rm e}, n_{\rm e}, \vartheta_{\rm M})$, an approximate generalization of the factor $\frac{w}{\sqrt{2}}$ in Equation (11), is a positive definite factor depending only on local thermal conditions and the nature of the disk irradiation through $\vartheta_{\rm M}$. It is not linear in any of these variables. The factor $k_J(T_{\rm e}, n_{\rm e}, \vartheta_{\rm M})$ thus determines the magnitude of the alignment for any orientation of the coronal magnetic field given by the other factor in variable $\vartheta_{\rm B}$. In Equations (7) and (9) it enters expressions for Stokes-I and -V only as small first order corrections that leave the signs of these terms unchanged.

As a general rule the magnitude of $k_J(T_{\rm e}, n_{\rm e}, \vartheta_{\rm M})$ is smaller for larger values of J, since the number of sub states $[2J + 1]$ is larger. Thus the 1079.8 nm transition of Fe XIII ($J = 2 \rightarrow J = 1$) has a smaller linear polarization than the 1074.7 nm ($J = 1 \rightarrow 0$) transition. Transitions such as 1079.8 nm with small $k_J(T_{\rm e}, n_{\rm e}, \vartheta_{\rm M})$ will therefore be useful since then the non-linear terms are commensurately smaller in the Stokes-I and V parameters.

For the $J = 1$ level, Equation (11) represents an upper limit to Equation (12), a limit which applies when collisions are negligible (*e.g.*, $n_{\rm e} \rightarrow 0$). The alignment generated by anisotropic irradiation is reduced by sum of all the collisions coupling the $J = 1$ sub-levels to others in the 26-level atom. This behavior is expected in many other M1 lines of interest.

If the alignment can be shown to be zero, there is no linear polarization and only the Stokes-I, V profiles can be used to get a "standard" line-of-sight magnetogram for $B\cos\Theta$. If it is finite, it can take either sign because of the factor $(3\cos^2\vartheta_{\rm B} - 1)$, and it leads directly to linear polarization. Observed minima in linear polarization, obtained for example with the *Coronal Multi-channel Polarimeter* (CoMP: Tomczyk *et al.*, 2008), often reflect the Van Vleck condition $(3\cos^2\vartheta_{\rm B} = 1)$, giving a direct indication of part of the magnetic-field's geometry. Passing across such minima one finds a 90° change in direction of the linear-polarization vector as $(3\cos^2\vartheta_{\rm B} - 1)$ and the alignment changes sign, according to Equation (8). This is a tell-tale sign of the Van Vleck effect even under the presence of significant integrations along the line-of-sight (LOS).

With these arguments we can summarize the role of the alignment as follows (*e.g.* Judge, 2007):

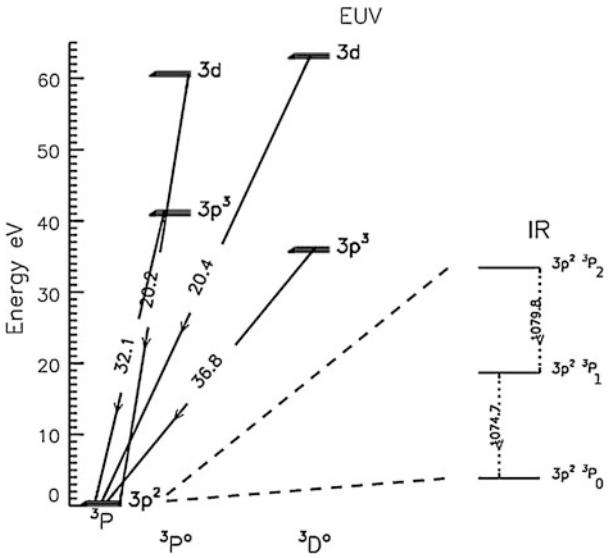

Figure 2 Term diagram for Fe XIII showing the strongest E1 transitions of each multiplet, and the M1 lines among the levels of the ground term. The 1074.7 nm line has upper-level $J = 1$, lower $J = 0$. Each configuration shown has EUV line ratios sensitive to density and photospheric radiation field as a result of the competition for sub-level populations in the ground term.

i) The magnetic-field *azimuth* has the well-known 90° ambiguity, *unless* the sign of $\sigma_0^2(\alpha_0 J)$ can be determined, in which case there remains a 180° ambiguity.
ii) The magnitude and sign of the alignment $\sigma_0^2(\alpha_0 J)$ affects all four Stokes parameters.
iii) Measurements of electron-density-sensitive lines at IR and EUV wavelengths will help determine $|\sigma_0^2(\alpha_0 J)|$ and should be included as part of the vector of observables [**I**].
iv) Measurements of M1 lines from $J > 1$ levels (*e.g.* Fe XI 782.9 nm, Fe XIII 1079.8 nm) with their smaller alignment $|\sigma_0^2(\alpha_0 J)|$ will make inversions more linear. In comparison with strongly aligned transitions (Fe XIII 1074.7 nm for example), such transitions have smaller $|\sigma_0^2(\alpha_0 J)|$ non-linear factors for I and V in Equations (7) and (9).

2.6. Selection of Lines for Inversion

Judge (2007) has examined how the alignment might be constrained – even determined – from observations, in the simplest case where a single point dominates all emission from an M1 coronal line. For a given set of such measurements [**I**], he has shown that there are generally multiple roots to the governing equations for the atomic alignment. The solutions correspond to different scattering geometries that are compatible with data (see his Table 2). Even in principle there is no unique solution.

However, Judge considered a data set consisting of just one M1 line. From Section 2.5, it is clear that the inversion problem will benefit from more data that can restrict the range of thermal conditions that, at each point in the corona, are compatible with data. In effect this will limit the level-dependent factor $[k_J(T_\mathrm{e}, n_\mathrm{e}, \vartheta_\mathrm{M})]$ in $\sigma_0^2(\alpha_0 J)$.

Both M1 and E1 EUV spectral lines contain temperature- and density-sensitive lines, which can be used to help determine $k_J(T_\mathrm{e}, n_\mathrm{e}, \vartheta_\mathrm{M})$, thereby helping resolve ambiguities inherent in using single M1 lines. Thus the data to be inverted should be expanded to include a variety of lines. Let us focus on Fe XIII as a concrete example. A term diagram is shown in Figure 2. Fe XIII (Si-like) has a density-sensitive pair of M1 lines (1074.7 and 1079.8 nm) as well as various pairs in the EUV. These arise mainly because of the competing roles of radiative excitation, de-excitation, and collisions in determining the (sub) level populations among the ground $^3P_{J=0,1,2}$ term. Figure 3 shows ratios of EUV lines for

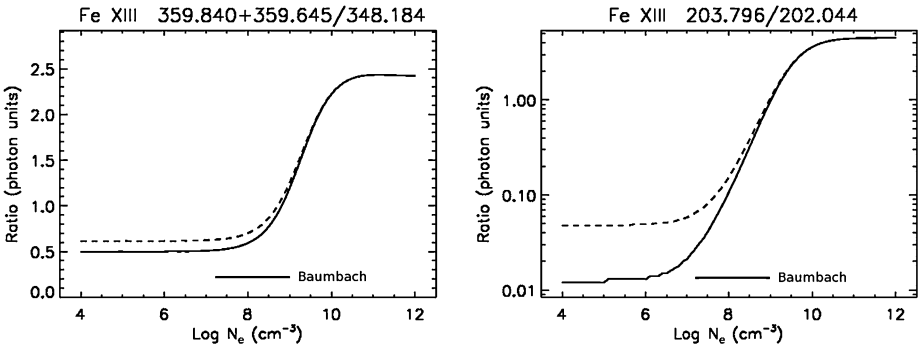

Figure 3 Typical density-sensitive line intensity ratios computed for Fe XIII. Left panel: intensity ratios from a blend of two lines near 35.97 nm to another line, all within the $3s3p^3\,{}^3D^o$–$3s^23p^2\,{}^3P$ multiplet. Right panel: a ratio of two lines within the $3s^23p3d\,{}^3D^o$–$3s^23p^2\,{}^3P$ multiplets. Dashed lines include radiative excitation, solid lines do not. Note that the ratios are sensitive in a density regime of interest [$n_e \approx 10^8$ cm^{-3}]. Note that the wavelengths are in Å units not nm in the figure, and that atomic alignment is ignored in these calculations. The line marked "Baumbach" shows typical variations in electron density 1.005 to about 1.4 $R_\odot$ as given by Baumbach in Allen (1973).

Table 1 An example of a set of lines in Fe XIII for magnetic inversions.

λ [nm]	Type	Data needed	Transition and Comments
1074.7	M1	*IQUV*	$3p^2\,{}^3P_1$–$3p^2\,{}^3P_0$, large $\lvert\sigma_0^2(\alpha_0 J)\rvert$
1079.8	M1	*IQUV*	$3p^2\,{}^3P_2$–$3p^2\,{}^3P_1$, small $\lvert\sigma_0^2(\alpha_0 J)\rvert$
35.97	E1	*I*	$3s3p^3\,{}^3D^0_{1,2}$–$3p^2\,{}^3P_1$, blend of two lines
34.82	E1	*I*	$3s3p^3\,{}^3D^0_1$–$3p^2\,{}^3P_0$
20.38	E1	*I*	$3p3d\,{}^3D^0_3$–$3p^2\,{}^3P_2$
20.20	E1	*I*	$3p3d\,{}^3P^0_1$–$3p^2\,{}^3P_0$

Fe XIII that are sensitive to the radiation field and electron density, together with the range of densities expected in the low corona from Section 84 of Allen (1973). Table 1 lists various transitions that might be observed and put into the "vector of observations" [**I**] for inversion. Joint CoMP and EUV measurements with the EIS instrument on the *Hinode* spacecraft have already been made in August and November 2012, including the Fe XIII lines of 1074.7, 10 798, 20.38 and 20.20 nm. Since CoMP observes almost daily, there will be other observations where yet more Fe XIII lines are available for analysis.

Other suitable ions (from the bright lines computed by Judge, 1998) include S-like Fe XI with an M1 line near 789.2 nm, B-like Mg VIII (3028 nm), C-like Si IX (3934 nm), and of course the red and green coronal lines (Cl-like Fe X and Al-like Fe XIV, respectively). There are various pros/cons with the selection of lines. For example Fe XI 789.2 nm shows remarkable structure in eclipse images (Habbal *et al.*, 2011), it lies in the near infrared so has low stray light and reasonable sensitivity to the Zeeman effect. It is formed at lower temperatures than Fe XIII and hence may be useful in cooler regions of the corona, say over coronal holes. As noted, this line is expected to have a small atomic alignment so that although the linear polarization will be small in 789.2 nm, so will the alignment corrections to the emission coefficients for Stokes-I and -V. It should therefore be considered as a prime target for future observations. A term diagram for Fe XI is shown in Figure 4. Cases can also be made for the other strong lines of various ions discussed by Judge (1998).

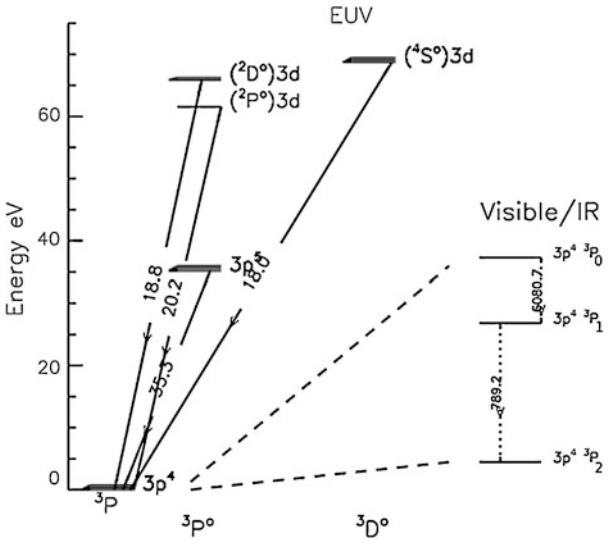

Figure 4 Term diagram for S-like Fe XI. Unlike Si-like Fe XIII, the ground level has $J = 2$, the 789.2 nm transition occurs between the upper $J = 1$ level and the ground level. The $J = 0 \rightarrow J = 1$ is at the anomalously large wavelength near 6082 nm because the Fe XI ion's levels are close together as jj coupling competes with LS coupling (see Judge, 1998).

3. Tomographic Inversions

Slicing through the volume containing magnetic fields by observing lines of sight at different angles opens up the possibility of full 3D vector-field recovery. Some studies of vector tomography have been made by[3] Kramar, Inhester, and Solanki (2006), Kramar and Inhester (2007). These are preliminary in that they explore either I, V or I, Q, U, not the full Stokes vector. Further, just one theoretical emission-line was "inverted" so that the observed data contain limited information on the alignment $\sigma_0^2(\alpha_0 J)$. They conclude, however, that

> We are confident that this data set is also sufficient to yield a realistic coronal magnetic-field model. This, however, has to be verified in future [numerical] experiments.

Their method attempts to handle the existence of null spaces in the inversion by standard techniques of adding a "regularization" parameter. Thus far they have investigated the minimization of the functional

$$L(\mathbf{B}) = \mu(\mathbf{I}_{\rm OBS} - \mathbf{I}_{\rm SIM}) \cdot (\mathbf{I}_{\rm OBS} - \mathbf{I}_{\rm SIM}) + \int (\nabla \cdot \mathbf{B})^2 \, {\rm d}^3 V, \tag{13}$$

where the integral is over the coronal volume. Minimization of $L(\mathbf{B})$ simply forces the selection of a 3D magnetic field to minimize the differences between observed $\mathbf{I}_{\rm OBS}$ and computed $\mathbf{I}_{\rm SIM}$ intensities and polarized Stokes parameters, subject to the additional constraint depending on μ. μ is a parameter that determines how much of the solution is determined by the data (μ large) and by the physically imposed divergence constraint (μ small). (Note that μ should include the estimates of the observed uncertainties for each component of the vector of observables too.)

The divergence constraint alone means that the space of curl-free vector fields is a null space: potential-field components along the LOS are invisible to Stokes-I and V. They

[3]Note that their studies are naturally in the strong-field limit of the Hanle effect, although they refer (inaccurately) to "the Hanle effect".

speculate that by adding the force-free constraint into the regularization (as $\int |\mathbf{J} \times \mathbf{B}|^2 \, \mathrm{d}^3 V$), this null space might be eliminated.

It should be remembered that such inversions rely on stereoscopic observations of coronal M1 lines (not currently possible) or on the assumption that the corona is a solidly rotating body, observed from the Earth over periods of at least a day.

If we combine our understanding from Section 2 with tomography, we see that with a general forward modeling code such as that written by Judge and Casini (2001), we can in principle invert a vector of observations including M1 lines with large and small alignment factors and selected E1 lines, to obtain the desired solutions for $\mathbf{B}(\mathbf{r}; t)$. Key to this effort will be the regular detection of the Stokes-V parameters of M1 lines, something that has not yet been achieved owing to the small apertures of coronagraphs currently used. Unpublished work by Judge using the prototype CoMP instrument ($d = 20$ cm) acquired in February 2012 gives an upper limit of 0.15 % for the maximum ratio of V/I in 1079.8 nm. In 70-minute integrations and a low ($20''$) spatial resolution, Lin, Kuhn, and Coulter (2004) achieved a sensitivity below 0.01 %, leading to a Stokes-V amplitude over an active region of about $0.0001I$, with a 0.46-m diameter coronagraph.

Clearly, bigger telescopes are needed at excellent sites for this kind of work to succeed. The *COronal Solar Magnetism Observatory* [COSMO] offers one possible solution.

4. Discussion

The tomographic-inversion scheme outlined above is the only way to invert formally data vectors to recover the coronal $\mathbf{B}(\mathbf{r}; t)$. The scheme relies on solar rotation and assuming the coronal structures are stationary over periods of a day or longer, or on the future availability of stereoscopic measurements both from Earth and from a spacecraft (like the *Solar TErrestrial RElations Observatory* [STEREO]) at a significant elongation from the Earth. The latter possibility has yet to be discussed at all and so is decades away. The former is naturally limited, but should be pursued once regular observations of the weak Stokes-V signal are available. The CoMP instrument is a prototype for larger instruments which should achieve this goal (*e.g.* the *Advanced Technology Solar Telescope* [ATST], COSMO).

4.1. Local Analyses of Coronal Loops

It seems prudent also to relax our goal of reconstructing $\mathbf{B}(\mathbf{r}; t)$ via tomography and look to other ways that we might make progress in this area. One possibility is to assume that we can identify a single plasma loop in an M1 transition, as routinely done for EUV or X-ray data. In such a case the source vector [**S**] only has contributions predominantly from lines of sight that intersect the loop. Also let us assume that observations from another viewpoint (EUV data from STEREO for example) are available that fix the heliocentric coordinates of the plasma loop. This additional information enables us to diagnose magnetic fields beyond what is possible from an isolated measurement of the Stokes profiles of a single point (Judge, 2007). However, as for EUV lines, no useful information outside the plasma-loop volume is available. Nevertheless this should be pursued.

4.2. Direct Synthesis *vs.* Observations

Another avenue to explore adding information to the data is to assume that we know more about the current-carrying structures that we are looking for. Thus, by building synthetic

maps of M1 lines from models of the magnetic field and coronal plasma, and comparing them directly with observations, one can hope to extract meaningful information. It may be possible to argue that the data are inconsistent with a class of model ("i"), whereas another class ("ni") is not inconsistent. Science advances often by identifying models of class (i), those of class (ni) being acceptable subject to further investigation. This will be a fruitful approach; already some initial comparisons reveal models of type (ni) (Rachmer *et al.*, 2013) but as of yet we are not aware interesting cases in class (i). There are obvious cases where potential fields, extrapolated from the lower atmosphere fall into class (i), but this finding serves merely to show that some free magnetic energy appears necessary to describe coronal structures. This is something we have known for decades through other arguments (*e.g.* Gold and Hoyle, 1960).

These are early days though. The main issue with this approach is that

> There are more things in heaven and earth, Horatio, than are dreamt of in your philosophy. – Hamlet

4.3. Closing Thoughts on the "Line-of-Sight Problem"

Consider the idea that in highly conducting plasma, one can trace magnetic fields by looking at morphology of plasma loops. This was a motivation for the *Transition Region and Coronal Explorer* [TRACE] mission (hence its name) and it has yielded many such morphological analysis of "coronal magnetism", including seismology (one nice example is that of Aschwanden *et al.*, 1999). Apparently the LOS issues do not present special challenges in these analyses of coronal-intensity measurements. One might argue that these are seen against the dark solar disk (any EUV continuum emission from the low temperature photosphere/low chromosphere is very dark), whereas the M1 coronal lines must be observed above the limb against a dark background. But even in this case, isolated bright plasma loops organized into an active region offer no greater path lengths for integration than observations on the disk. Indeed, the discovery of MHD wave modes in the M1 Fe XIII 1074.7 nm line Tomczyk *et al.* (2007) indicates that, just as for EUV work, line of sight confusion is not an overwhelming problem.

We conclude that, *as in all remotely sensed magnetic data*, line-of-sight issues are important but not intractable. Often, using M1 lines we will be interested in the coronal magnetic fields above active regions. These present themselves as bright isolated plasma loops in M1 coronal lines just as the EUV and X ray lines do (Bray *et al.*, 1991), dominating the contributions to the Stokes vectors along the line of sight.

5. Conclusions

Scientific skepticism is healthy, and we certainly need to be skeptical of interpretations of all remotely sensed data of an object such as the Sun. We have shown that the optically thin forbidden coronal lines suffer from the same kinds of interpretational problems as do other diagnostics of solar magnetism. We have suggested several ways to augment the data of isolated points in the corona – for which we have vast null spaces of unexplorable parameters – using tomography and traditional ideas concerning the smoothness and continuity of magnetic fields in coronal structures, applied universally to EUV and X-ray intensity data.

It will be interesting to see how a full vector inversion including lines sensitive to thermodynamic parameters – both visible/IR M1 lines and EUV lines – will serve to further

constrain tomographic-inversions. Certain schemes (especially "direct [matrix] inversions") can be very fast, but these require linear equations which is manifestly not the case (see the equations above). It is, however, possible that the non-linearities introduced by the alignment into these equations can be treated to some degree by a formal (Newton–Raphson style) linearization scheme. This seems promising given that we have lines with quite different alignment factors (1074.7 *vs.* 1079.8 or 798.2 nm) and thus different non-linear amplitudes, but this is an area that remains to be explored.

Several ways forward are reviewed while we await the arrival of high-sensitivity ($\lesssim 10^{-4}$) polarization data from telescopes (ATST, COSMO) needed for tomographic inversions that can recover the vector field throughout volumes of the corona.

Acknowledgements PGJ gratefully acknowledges the Physics Department at Montana State University where this work was largely carried out, in support of a sabbatical funded by MSU, and by the Advanced Study Program and High Altitude Observatory of the National Center for Atmospheric Research.

References

Allen, C.W.: 1973, *Astrophysical Quantities*, Athlone, London.

Aschwanden, M.J., Fletcher, L., Schrijver, C.J., Alexander, D.: 1999, Coronal loop oscillations observed with the transition region and coronal explorer. *Astrophys. J.* **520**, 880.

Bray, R.J., Cram, L.E., Durrant, C.J., Loughhead, R.E.: 1991, *Plasma Loops in the Solar Corona*, Cambridge University Press, Cambridge.

Casini, R., Landi Degl'Innocenti, E.: 2008, In: Fujimoto, T., Iwamae, A. (eds.) *Plasma Polarization Spectroscopy* **247**, Springer, Berlin.

Casini, R., Judge, P.G.: 1999, Spectral lines for polarization measurements of the coronal magnetic field. II. Consistent theory of the Stokes vector for magnetic dipole transitions. *Astrophys. J.* **522**, 524.

Charvin, P.: 1965, Étude de la polarisation des raies interdites de la couronne solaire. Application au cas de la raie verte λ5303. *Ann. Astrophys.* **28**, 877.

Craig, I.J.D., Brown, J.C.: 1986, *Inverse Problems in Astronomy*, Hilger, Bristol.

Gold, T., Hoyle, F.: 1960, On the origin of solar flares. *Mon. Not. Roy. Astron. Soc.* **120**, 89.

Habbal, S.R., Druckmüller, M., Morgan, H., Ding, A., Johnson, J., Druckmüllerová, H., Daw, A., Arndt, M.B., Dietzel, M., Saken, J.: 2011, Thermodynamics of the solar corona and evolution of the solar magnetic field as inferred from the total solar eclipse observations of 2010 July 11. *Astrophys. J.* **734**, 120.

Hale, G.E.: 1908, On the probable existence of a magnetic field in Sun-spots. *Astrophys. J.* **28**, 315.

Judge, P.G.: 1998, Spectral lines for polarization measurements of the coronal magnetic field. I. Theoretical intensities. *Astrophys. J.* **500**, 1009.

Judge, P.G.: 2007, Spectral lines for polarization measurements of the coronal magnetic field. V. Information content of magnetic dipole lines. *Astrophys. J.* **662**, 677.

Judge, P.G., Casini, R.: 2001, A synthesis code for forbidden coronal lines. In: Sigwarth, M. (ed.) *Advanced Solar Polarimetry – Theory, Observation, and Instrumentation* **CS-236**, Astron. Soc. Pac., San Francisco, 503.

Kramar, M., Inhester, B.: 2007, Inversion of coronal Zeeman and Hanle observations to reconstruct the coronal magnetic field. *Mem. Soc. Astron. Ital.* **78**, 120.

Kramar, M., Inhester, B., Solanki, S.K.: 2006, Vector tomography for the coronal magnetic field. I. Longitudinal Zeeman effect measurements. *Astron. Astrophys.* **456**, 665.

Lin, H., Kuhn, J.R., Coulter, R.: 2004, Coronal magnetic field measurements. *Astrophys. J. Lett.* **613**, L177.

Parker, E.N.: 2007, *Conversations on Electric and Magnetic Fields in the Cosmos*, Princeton University Press, Princeton.

Rachmer, L., Gibson, S.E., Dove, J.B., DeVore, C.R., Fan, Y.: 2013, Polarimetric properties of flux ropes and sheared arcades in coronal prominence cavities. *Solar Phys.* doi:10.1007/s11207-013-0325-5.

Steiner, O.: 1994, Theoretical models of magnetic flux tubes: structure and dynamics. In: Jefferies, J.T., Deeming, D., Rabin, D.R. (eds.) *Infrared Solar Physics*, *Proceedings IAU Symposium* **154**, *Tucson*, Kluwer, Dordrecht, 407.

Tomczyk, S., McIntosh, S.W., Keil, S.L., Judge, P.G., Schad, T., Seeley, D.H., Edmondson, J.: 2007, Alfvén waves in the solar corona. *Science* **317**, 1192.

Tomczyk, S., Card, G.L., Darnell, T., Elmore, D.F., Lull, R., Nelson, P.G., Streander, K.V., Burkepile, J., Casini, R., Judge, P.G.: 2008, An instrument to measure coronal emission line polarization. *Solar Phys.* **247**, 411. ADS:2008SoPh..247..411T, doi:10.1007/s11207-007-9103-6.

DOI 10.1007/978-1-4939-2038-9_3
Reprinted from *Solar Physics* Journal, DOI 10.1007/s11207-013-0367-8

Magnetic Field Extrapolations into the Corona: Success and Future Improvements

S. Régnier

Received: 21 December 2012 / Accepted: 16 July 2013 / Published online: 27 August 2013

Abstract The solar atmosphere being magnetic in nature, the understanding of the structure and evolution of the magnetic field in different regions of the solar atmosphere has been an important task over the past decades. This task has been made complicated by the difficulties to measure the magnetic field in the corona, while it is currently known with a good accuracy in the photosphere and/or chromosphere. Thus, to determine the coronal magnetic field, a mathematical method has been developed based on the observed magnetic field. This is the so-called magnetic field extrapolation technique. This technique relies on two crucial points: i) the physical assumption leading to the system of differential equations to be solved, ii) the choice and quality of the associated boundary conditions. In this review, I summarise the physical assumptions currently in use and the findings at different scales in the solar atmosphere. I concentrate the discussion on the extrapolation techniques applied to solar magnetic data and the comparison with observations in a broad range of wavelengths (from hard X-rays to radio emission).

Keywords Active regions · Corona, models · Corona, structures · Magnetic fields, models

1. Introduction

With the advent of photospheric magnetographs/magnetometers in the 1960s, it has soon been realised that the coronal magnetic field can be derived by assuming an equilibrium state. The main forces exerted on the coronal plasma are the plasma pressure, the gravitational force, and the magnetic or Lorentz forces. This gives the magnetohydrostatic equilibrium:

$$-\nabla p + \rho \mathbf{g} + \mathbf{j} \times \mathbf{B} = \mathbf{0} \tag{1}$$

Invited Review

Coronal Magnetometry
Guest Editors: S. Tomczyk, J. Zhang, and T.S. Bastian

S. Régnier (✉)
Jeremiah Horrocks Institute, University of Central Lancashire, Preston, Lancashire PR1 2HE, UK
e-mail: SRegnier@uclan.ac.uk

where p and ρ are the plasma pressure and density, $\mathbf{g}$ is the gravity, $\mathbf{j}$ is the electric current density, and $\mathbf{B}$ is the magnetic field. This equation is a partial different equation, which can be solved by imposing a set of boundary conditions in a finite or semi-finite domain of computation. In addition, Maxwell's equation given the divergence-freeness of the magnetic field has also to be considered. The technique is the so-called magnetic field extrapolation/reconstruction (nowadays both words are used without distinction). Two problems have to be distinguished:

i) to numerically solve the system of equations,
ii) to incorporate solar data into the numerical codes.

Both problems need a careful treatment as the convergence of a well-established numerical code does not imply the convergence of the same code with a specific dataset. In this review, I will address the magnetic field extrapolations performed using photospheric/chromospheric magnetograms as boundary conditions. This indeed assumes that the algorithms to extrapolate the magnetic field are behaving well with data.

The magnetograms used as boundary conditions are recorded by ground-based or space-born instruments. For this review, the pros and cons of different instruments are not taken into account and only the physics problems and results addressed in the cited papers are considered. The aim of this review is to show that the magnetic field extrapolation techniques have been used to tackle successfully a broad range of solar physics issues.

Recently, two reviews have been published with a different focus to this paper: i) Wiegelmann and Sakurai (2012) focused their discussion on the non-linear force-free field methods with a short section on the comparison with the structures of the solar corona, ii) Mackay and Yeates (2012) describe the progress in the modelling of global photospheric and coronal magnetic fields which includes extrapolation techniques as well as flux transport models which are not discussed here.

The review is organised as follows. I first give a brief review of the different models used to reconstruct the solar atmospheric magnetic field (see Section 2). In Section 3, the important quantities that can be derived from a magnetic field configuration are listed. Thus, the results obtained from magnetic field extrapolations are discussed for the quiet Sun (see Section 4), and for active regions (see Section 5). To conclude (see Section 6), I discuss the issues which are still to be resolved, and the further developments that I envision for the magnetic field extrapolation techniques.

2. A Brief Review of Numerical Models

Magnetic field extrapolation techniques aim at solving a system of differential equations with the appropriate set of boundary conditions. An extrapolation scheme is judged on the well-posedness of the problem, that is to say, to find the right combination of boundary conditions to solve a particular physical problem. I will thus distinguish between

i) the goodness of the numerical scheme which is usually tested with analytical and/or semi-analytical solutions, and
ii) the goodness of the extrapolation which includes the effects of the boundary conditions as provided by observations.

Most of the schemes described below are good numerical schemes; however, their behaviour when extrapolating solar data can be significantly different, or has not yet been tested.

2.1. Potential Fields

The potential field is the solution of Laplace's equation:

$$\nabla^2 \mathbf{B} = 0. \tag{2}$$

The solutions of this equation are well-known as harmonic functions in different geometries. The potential field is relatively easy to compute as it only requires the knowledge of the normal component of the magnetic field on the boundaries of the domain. For instance, to compute the potential field in a Cartesian box only the normal/vertical component is needed on the bottom boundary as often provided by line-of-sight magnetic field measurements, whilst a closed/open boundary can be imposed on the side and top boundaries. The first potential field extrapolation techniques have been in the early 1960s with the development of photospheric magnetographs (Schmidt, 1964; Altschuler and Newkirk, 1969; Levine and Altschuler, 1974; Schatten, Wilcox, and Ness, 1969; Adams and Pneuman, 1976; Levine, Schulz, and Frazier, 1982; Hakamada, 1995; Rudenko, 2001). Several methods have been compared by Seehafer (1982) showing that the connectivity and geometry of field lines can be different from one model to the other.

2.2. Force-Free Fields

We usually distinguish between potential field and force-free field extrapolations even if the potential field is a particular case of force-free field, and thus has similar properties of existence and stability (Molodensky, 1974). The force-free fields assume implicitly that the solar atmospheric plasma is a low β plasma.

2.2.1. Linear Force-Free Field

The linear force-free (LFF) field is described by the following equation:

$$\nabla \times \mathbf{B} = \alpha \mathbf{B} \tag{3}$$

where α is a scalar called the force-free parameter. The boundary conditions are given by the normal component of the magnetic field on the boundaries of the computational box, to which a guess for the α-value is added. The numerical methods to solve this linear problem include vertical integration, Green's functions, Fourier transforms, spherical harmonics, and boundary integrals in either Cartesian or spherical coordinates (Nakagawa and Raadu, 1972; Levine and Altschuler, 1974; Seehafer, 1975; Chiu and Hilton, 1977; Nakagawa, Wu, and Tandberg-Hanssen, 1978; Alissandrakis, 1981; Wu and Wang, 1984, 1985; Semel, 1988; Durrant, 1989; Gary, 1989; Yan, 1995; Abramenko and Yurchishin, 1996; Kusano and Nishikawa, 1996; Amari, Boulmezaoud, and Maday, 1998; Clegg, Bromage, and Browning, 1999; Clegg *et al.*, 2000). Very few studies of the behaviour of LFF field algorithms have been performed (Li, Song, and Li, 2009).

As it is obvious from photospheric vector magnetic field observations that a single value of α cannot describe the coronal magnetic field (Leka and Skumanich, 1999; Leka, 1999), several methods have been attempted to derive the geometry of a single coronal loop using the α-value that will best fit the observed loop (Wiegelmann and Neukirch, 2002; Carcedo *et al.*, 2003). In other words, this corresponds to a piecewise LFF field for a discrete (usually small) number of loops.

2.2.2. Non-linear Force-Free Field

The non-linear force-free (NLFF) field satisfies the following equation:

$$\nabla \times \mathbf{B} = \alpha(\mathbf{r})\mathbf{B}, \tag{4}$$

where α is the force-free function depending on the position $\mathbf{r}$. Taking the divergence of the above equation, we obtain

$$\mathbf{B} \cdot \nabla\alpha = 0 \tag{5}$$

implying that α is constant along a given magnetic field line. This fact is reinforced in the corona as the conduction along the magnetic field dominates (the conduction across field lines is negligible). The NLFF methods have been summarised by Wiegelmann and Sakurai (2012). The main methods to extrapolate the magnetic field into the corona as a NLFF field are:

Vertical integration: the method consists in propagating the boundary conditions into the corona from the bottom boundary, layer by layer (Wu and Wang, 1985; Cuperman, Ofman, and Semel, 1989, 1990a, 1990b; Wu *et al.*, 1990; Démoulin, Cuperman, and Semel, 1992; Song *et al.*, 2006, 2007).

MHD evolutionary techniques: based on the low plasma-β MHD equations, an initial configuration including electric currents is relaxed to a non-linear force-free state owing to resistivity, also know as stress-and-relax models (Yang, Sturrock, and Antiochos, 1986; Mikic, Barnes, and Schnack, 1988; Schnack *et al.*, 1990; McClymont and Mikic, 1994; Roumeliotis, 1996; Valori, Kliem, and Keppens, 2005; Valori, Kliem, and Fuhrmann, 2007; Valori *et al.*, 2010; Jiang *et al.*, 2011).

Optimisation: the basic principle is to minimise a functional containing the force-free constraint as well as the solenoidal constraint to relax an initial configuration towards a non-linear force-free state (Wheatland, Sturrock, and Roumeliotis, 2000; Wiegelmann, 2004; Wiegelmann *et al.*, 2005, 2008, 2010; Wiegelmann, Inhester, and Sakurai, 2006; Inhester and Wiegelmann, 2006; Wiegelmann and Neukirch, 2006; Tadesse, Wiegelmann, and Inhester, 2009; Mysh'yakov and Rudenko, 2009; Wiegelmann and Inhester, 2010; Fuhrmann *et al.*, 2011). In recent years, the optimisation scheme has been developed to include more constraints and thus to obtain an equilibrium closer to a force-free field.

Grad–Rubin methods: the non-linear force-free equation being a system of partial differential equations of mixed type, the method described by Grad and Rubin (1958) consists in separating the elliptic part (force-free equation) and the hyperbolic part (gradient of α) of the system, each system being then linear and easier to solve (Grad and Rubin, 1958; Sakurai, 1981; Amari *et al.*, 1997; Amari, Boulmezaoud, and Mikic, 1999; Wheatland, 2004; Amari, Boulmezaoud, and Aly, 2006; Inhester and Wiegelmann, 2006; Wheatland, 2006; Wheatland and Régnier, 2009; Malanushenko, Longcope, and McKenzie, 2009; Amari and Aly, 2010; Malanushenko *et al.*, 2012). The Grad–Rubin method requires as boundary conditions the vertical/radial component of the magnetic field on each boundary, as well as the distribution of α in a chosen polarity. This ensures that the extrapolation method is a mathematically well-posed problem in Hadamard sense.

Boundary integral: the non-linear force-free model can be describe as an exterior problem and a boundary integral equation written in which the magnetic field component within a volume can be determined by the magnetic field components on the boundary. The formulation of the boundary integrals can be found by Courant and Hilbert (1963) and recently applied to solar cases (D. Wang, Wei, and Yan, 1995; Yan and

Sakurai, 1997, 2000; Li, Yan, and Song, 2004; He and Wang, 2006; Yan and Li, 2006; He and Wang, 2008).

Force-free electrodynamics: the theory of force-free electrodynamics is applied to the modelling of coronal magnetic fields which has been applied successfully to pulsar magnetospheres (Contopoulos, Kalapotharakos, and Georgoulis, 2011; Contopoulos, 2013).

With the development of different numerical techniques, testing and comparing different algorithms has been proven to be needed. The main efforts have been done since 2004 by the international group on non-linear force-free modelling (Schrijver *et al.*, 2006, 2008; Metcalf *et al.*, 2008; De Rosa *et al.*, 2009). One aim of this series of papers has been to show that modellers need to be careful when injecting the boundary conditions into the numerical codes: the boundary conditions have to be consistent with the assumption of the model and the set-up of the numerical code. For instance, in Schrijver *et al.* (2008), it has been shown that by selecting carefully the photospheric magnetic field, the coronal magnetic field structure in the core of the reconstructed active region was similar for all NLFF methods. Several other papers have addressed quantitative differences between several algorithms (Inhester and Wiegelmann, 2006; Barnes, Leka, and Wheatland, 2006; Rudenko and Myshyakov, 2009; Mysh'yakov and Rudenko, 2009; Liu *et al.*, 2011).

2.3. Non-Force-Free Fields

The next step after the force-free field extrapolation is to solve the magnetohydrostatic (MHS) equilibrium equation, which includes the plasma pressure force and the gravitational force in addition to the magnetic forces. An algorithm has been developed by Grad and Rubin (1958) as a well-posed problem. This algorithm has been recently implemented by Gilchrist and Wheatland (2013) neglecting the gravity (see also Boulbe, Zamène Boulmezaoud, and Amari 2009). The optimisation scheme has also been adapted to solve the magnetohydrostatic equation (Wiegelmann and Neukirch, 2006; Wiegelmann *et al.*, 2007). The models usually require to define a realistic atmosphere from the photosphere to the corona. As a first order assumption (neglecting the feedback between the magnetic field and plasma properties), Régnier, Priest, and Hood (2008) derived the global properties of Alfvén speed, plasma β-values and reconnection rate in the corona by assuming a non-linear force-free equilibrium for the magnetic field and a hydrostatic equilibrium for the plasma.

A minimum dissipation rate method has been adapted to include photospheric measurements (Hu and Dasgupta, 2006, 2008; Bhattacharyya *et al.*, 2007; Hu *et al.*, 2008, 2010). The method describes a general or non-force-free magnetic field by a superimposition of one potential field and two linear force-free fields.

Gary and Alexander (1999) have developed a non-force-free model, the so-called stretched magnetic field, which combined photospheric magnetograms and the structures of coronal loops.

2.4. Miscellaneous

I will also mention several other analytical/numerical methods that have been used to access the structure of the three-dimensional coronal magnetic field, but which cannot be classified as extrapolation techniques as such.

This first method to have produced significant results is the point-charge method. A magnetogram is decomposed in a discrete number of polarities, which are reduced to points associated with the magnetic flux of the polarity (zero magnetic field outside the point charges). The magnetic field is thus given by an analytical solution. For instance, the

method has been developed and used for theorising the topology of magnetic field in different geometries (Titov, Priest, and Demoulin, 1993; Bungey, Titov, and Priest, 1996; Brown and Priest, 1999; Longcope and Klapper, 2002; Beveridge, Priest, and Brown, 2002, 2004; Barnes, Longcope, and Leka, 2005; Maclean *et al.*, 2006; Maclean, Beveridge, and Priest, 2006). The point-charge method has also been used to fit the observed 3D coronal loops following a non-linear force-free assumption (Aschwanden, 2012a, 2012b, 2013; Aschwanden and Malanushenko, 2012). Another successful model to determine the properties of the coronal magnetic field is the flux rope insertion model developed by van Ballegooijen (2004). Starting from an equilibrium state (often a potential field), a flux rope or twisted flux tube is inserted within the magnetic configuration by modifying the boundary conditions and by matching the observed X-ray sigmoid or Hα filament (see *e.g.* van Ballegooijen *et al.*, 2007).

2.5. Boundary Conditions

In order to solve a system of differential equations, it is important to define the correct boundary conditions that will lead to a mathematically well-posed problem (or not) in the Hadamard sense.

For the potential field, only the normal component of the magnetic field on the boundaries of the computational box is needed.

For the linear force-free field, the normal component is required, to which a guess for the value of α in the computational volume will be added.

For the non-linear force-free field, the normal component of the magnetic field as well as the distribution of α has to be imposed. According to Grad and Rubin (1958), imposing the distribution of α in one chosen polarity as the boundary condition will lead to a mathematically well-posed problem. It is important to notice here that in order to compute the distribution of α from vector magnetograms, the following formula is used (in Cartesian coordinates with (x, y) on the photospheric surface):

$$\alpha = \frac{1}{B_z}\left(\frac{\partial B_y}{\partial x} - \frac{\partial B_x}{\partial y}\right). \tag{6}$$

This equation is considered owing to the measurement of the magnetic field vector on the xy-plane, implying that no derivatives with respect to z can be computed. A further discussion on the implication of this formula will be done in Section 6.2.

For the minimum dissipation model, the vector magnetic field components on one or two different atmospheric layers are needed.

For the magnetostatic model, the same boundary conditions as for the non-linear force-free model are used in addition to prescribing the plasma pressure on the photospheric level in one chosen polarity. If the gravitational force is considered, then an initial atmosphere model will be needed.

3. Physical Quantities

Below, I list the important quantities that can be derived from the magnetic field extrapolations and which will lead to an in-depth physical interpretation of the magnetic field structure and coronal phenomena as described in Sections 4 and 5.

3.1. Magnetic Energy

Magnetic Energy The magnetic energy computed in a volume V is given by

$$E_{\mathrm{m}} = \int_V \frac{B^2}{2\mu_0}\,\mathrm{d}V. \tag{7}$$

The reconstruction models provide the three components of the magnetic field at discrete locations in the computational volume. The magnetic energy can then be easily computed by discretising Equation (7). The magnetic energy for the potential field is a minimum (lower bound) of magnetic energy for a force-free field computed with the same boundary conditions, *i.e.*, the same vertical/normal magnetic component on all boundaries. The LFF magnetic energy is a minimum of magnetic energy for the NLFF field if the magnetic helicity is conserved (Woltjer, 1958; Taylor, 1974).

Free Magnetic Energy The free magnetic energy is the difference in magnetic energy for a magnetic field model and for a reference field:

$$\Delta E_{\mathrm{m}} = E_{\mathrm{mod}} - E_{\mathrm{ref}}. \tag{8}$$

The reference field is often chosen to be the potential magnetic field as it is the minimum energy state (Aly, 1984). The free magnetic energy is a measure of the magnetic energy that can be stored in the magnetic configuration or released during an eruptive or reconnection event.

Magnetic Energy Density The magnetic energy density is the term $\frac{B^2}{2\mu_0}$ taken at one particular location within the volume V. The energy density can also be seen as the magnetic energy in a small volume δV (*e.g.*, a single pixel). As such, the magnetic energy density provides the distribution of magnetic energy in a small volume. However, the free magnetic energy density is of no use/meaning as the connectivity of magnetic field lines between the magnetic field and a reference field can be drastically different.

The Aly–Sturrock Conjecture Both Aly (1989) and Sturrock (1991) showed that there exists an upper bound of the magnetic energy of force-free fields when the field is totally open (unipolar field). The condition of application of this conjecture is when the magnetic field within the volume decays rapidly towards the boundaries, or when the magnetic flux through the boundaries other than the bottom boundary becomes negligible. This condition is easily satisfied when considering the half space above the photosphere, or when the boundaries are far enough from the magnetic field sources. This condition is not satisfied when magnetic flux is present near the edges of the boundaries.

Time Evolution One of the most interesting physical issues about magnetic extrapolation has been to know if the reconstructed magnetic field can describe the time evolution of solar regions. In the non-eruptive solar corona, the time of evolution is mostly given by the Alfvén transit time along individual magnetic field lines or coronal loops for active regions, and by the comparison of Alfvén transit time and granular motion for the quiet Sun. For active regions, the Alfvén transit time of a typical loop of length 200 Mm is about 10–15 min; therefore if there is no major injection of magnetic energy or magnetic helicity, the evolution of active regions can be studied by a time series of equilibria.

3.2. Magnetic Helicity

General Definition The concept of magnetic helicity has been largely used in plasma physics to describe the complexity of the magnetic field, including the twist and shear in magnetic field lines. Maxwell's equation,

$$\nabla \cdot \mathbf{B} = 0, \tag{9}$$

implies that the magnetic field is solenoidal and can be described by a vector potential $\mathbf{A}$ such that $\mathbf{B} = \nabla \times \mathbf{A}$. The definition of $\mathbf{A}$ is not unique and depends on a gauge condition. From this definition, the magnetic helicity in a volume V is defined as

$$H_{\mathrm{m}} = \int_V \mathbf{A} \cdot \mathbf{B} \, \mathrm{d}V = \int_V \mathbf{A} \cdot \nabla \times \mathbf{A} \, \mathrm{d}V. \tag{10}$$

The main concepts about magnetic helicity have been summarised by Berger (1999a).

Relative Magnetic Helicity As the definition of Equation (10) is not unique, a gauge invariant definition has been developed by Berger and Field (1984)

$$\Delta H_{\mathrm{m}} = \int_V (\mathbf{A} - \mathbf{A}_{\mathrm{ref}}) \cdot (\mathbf{B} + \mathbf{B}_{\mathrm{ref}}) \, \mathrm{d}V \tag{11}$$

and also by Finn and Antonsen (1985)

$$\Delta H_{\mathrm{m}} = \int_V (\mathbf{A} + \mathbf{A}_{\mathrm{ref}}) \cdot (\mathbf{B} - \mathbf{B}_{\mathrm{ref}}) \, \mathrm{d}V. \tag{12}$$

The definition of Berger and Field (1984) originally contained a surface term, which tends to zero when considering the half space above the photosphere (or boundaries far away from the strong magnetic field regions) or vanishes for a finite volume when the following boundary conditions are imposed: the magnetic field normal to the surface of the finite volume is the same for both magnetic fields, the divergence of the reference vector potential vanishes, and the reference vector potential is perpendicular to the surface of the finite volume. In those two cases, the Finn and Antonsen (1985) and Berger and Field (1984) formulae are equivalent.

Magnetic Helicity Conservation In ideal MHD, the magnetic helicity is invariant during the evolution of any closed flux system (Woltjer, 1958). Taylor (1974) applied this to laboratory experiments and hypothesised that, for a weak but finite resistivity, the total magnetic helicity of the flux system is invariant during the relaxation process. Taylor's theory has often been invoked to assume that the magnetic helicity in a solar atmospheric region is conserved. This latter statement is valid only if the solar region under consideration is a closed flux system. For instance, active regions in which flux emergence is taking place or a CME has originated cannot satisfy helicity conservation. The redistribution of magnetic helicity at large scale in the solar atmosphere or in the heliosphere is a basic consequence of the magnetic cycle and the sustainability of the dynamo action.

Woltjer (1958) has shown that the minimum energy of a NLFF field is a LFF field when the magnetic helicity is conserved (*i.e.*, for a closed system). This implies that the difference between the magnetic energy of the NLFF field and LFF field is a better estimate of the free magnetic energy (see Section 3.1).

Self and Mutual Helicity The magnetic helicity of a magnetic configuration can be decomposed into several components: self and mutual helicity (Berger, 1999b), or twist and writhe (Berger and Prior, 2006). As an example, for a single twisted flux tube embedded a uniform external magnetic field, the self helicity is assumed to correspond to the twist within the flux tube, while the mutual helicity corresponds to the crossing between the external field and the twisted flux tube. The definitions given by Berger (1999b) have been studied in the frame of force-free extrapolation of active regions by Régnier, Amari, and Canfield (2005): the self helicity is related to the twist of the flux bundles within the active region, while the mutual helicity contains a contribution from the crossing of field lines and the large-scale twist of the active region (large compared to the size of the computational box). Longcope and Malanushenko (2008) have defined a formula for the self helicity which describes only the twist of the field lines.

Twist in Force-Free Fields The magnetic helicity is a measure of the topology of a magnetic field configuration, and also includes a measure of the shear and twist of magnetic field lines. In the solar physics literature, the force-free parameter/function, α, is often called the twist. This is a misnomer as α is strictly equivalent to the twist in a thin flux tube approximation, which does not always apply to the magnetic field extrapolated in solar regions. Especially in a non-idealised configuration, the twist and the α-value can have opposite sign (Régnier and Amari, 2004; Prior and Berger, 2012).

Time Evolution As for the magnetic energy, the evolution of magnetic helicity injection and redistribution can be studied by a time series of equilibria. The time scale of the change in magnetic helicity is shorter than the time scale for the magnetic energy. A general equation for the rate of change of magnetic helicity has been derived by Heyvaerts and Priest (1984) for a non-ideal plasma.

Other Helicities Magnetic helicity is the integral over a given volume of the vector potential $\mathbf{A}$ and its curl, $\mathbf{B}$. This definition can be extended to other quantities such as the electric current density or the vorticity. The current helicity is

$$H_{\mathrm{c}} = \int_V \mathbf{j} \cdot \mathbf{B} \, \mathrm{d}V \tag{13}$$

with $\nabla \times \mathbf{B} = \mu_0 \mathbf{j}$, and the hydrodynamical helicity by

$$H = \int_V \mathbf{v} \cdot \omega \, \mathrm{d}V \tag{14}$$

where $\mathbf{v}$ is the flow field and $\omega = \nabla \times \mathbf{v}$ is the associated vorticity.

From vector magnetograms, the current helicity on the surface has been estimated either by assuming that the transverse components of the magnetic field and/or the electric current density are negligible, or by assuming a LFF field (*e.g.*, Abramenko, Wang, and Yurchishin, 1996). For the latter assumption, the current helicity density is $h_{\mathrm{c}} = \alpha B^2$. For a volume V, the current helicity associated with a LFF field is

$$H_{\mathrm{c}} = \int_V \alpha B^2 \, \mathrm{d}V = 2\mu_0 \alpha E_m \tag{15}$$

where E_{m} is the magnetic energy.

3.3. Magnetic Topology

As it is beyond the scope of this review to give a complete description of all topological studies, I will just mentioned that the concept and development of magnetic topology applied to coronal structures have been reviewed in Longcope (2005). The transfer of magnetic energy and magnetic helicity through topological elements is the consequence of magnetic reconnection, and thus eruptive events. In particular, the main ingredients are null points where the magnetic field vanishes, separators, separatrices, quasi-separatrices, and hyperbolic flux tubes.

The magnetic topology of the potential field is assumed to be just slightly modified compared to other magnetic field models (Hudson and Wheatland, 1999; Brown and Priest, 2000). It has recently been shown by Régnier (2012) that the location and properties of null points existing in a simple configuration for potential, LFF, and NLFF fields are similar when the spectral radius (maximum in the absolute value of the eigenvalues associated with the null point) is large, meaning that the magnetic null point is embedded in a strong field region or surrounded by strong electric currents (*i.e.*, large magnetic field gradients).

Null points have been extensively used as a proxy to the complexity of the magnetic field and the possible existence of reconnection events in a diffusion region encompassing the null points. This can be extended to the study of current sheets. The diffusion regions including a null point or being degenerated from a null point are supposed to be the more efficient in releasing magnetic energy and to convert this energy into kinetic and thermal energies. Priest, Longcope, and Heyvaerts (2005) have pointed out that the magnetic energy storage induced by slow photospheric motions is much more efficient along separators than at separatrices.

Another quantity that has been commonly used is the Q-factor or squashing degree (Titov, 2007). The Q-factor is a measure of the change of connectivity between neighbouring field lines and, as such, indicates the location where the magnetic energy could be dissipated or released. Except few quantitative studies (*e.g.*, Longcope *et al.*, 2010), only qualitative comparisons with observations have been performed.

4. Quiet Sun

4.1. Validity of the Extrapolation Methods

The complex physical behaviour of the photosphere and chromosphere makes the existence of electric currents perpendicular to the magnetic field possible, especially Hall currents described by the Hall parameter (ratio of the electron gyrofrequency to the electron-ion/neutral collision frequency), and the Pedersen currents (implied by convective electric field). These perpendicular currents will dissipate rapidly with altitude in the solar atmosphere (Gold and Hoyle, 1960; Goodman, 2000), leading to a force-free corona (only with parallel currents). The existence of such electric currents are crucial for the validity of the extrapolation methods in the quiet Sun. It is less important for active regions owing to the characteristic time scale of evolution.

Extrapolation methods such as potential fields have been applied to the quiet Sun without a real physical justification, but mostly due to the lack of observations/boundary conditions which will allow a better physical description of the system. The quiet-Sun magnetic field extrapolations can be regarded as a preliminary step towards the small scales of the solar atmosphere. It is also worth mentioning that the measurement of the magnetic field vector in the quiet-Sun regions is still challenging.

4.2. The Magnetic Carpet

The nature and structure of the magnetic field in quiet-Sun regions have been investigated with the means of magnetic field extrapolation. As currently line-of-sight magnetic field is the only reliable magnetic field component measured with high accuracy, the potential field model has been used for the quiet Sun. Note that the interest about the quiet-Sun evolution has recently been rejuvenated by non-linear force-free modelling in a theoretical context (Meyer *et al.*, 2011; Meyer, Mackay, and van Ballegooijen, 2012).

In 1999, Woodard and Chae have used a potential field model to show that the orientation of the Hα fibrils did not match the potential field lines, and thus concluding that the quiet-Sun magnetic field contains a non-potential component (see also Jing *et al.*, 2011). Hα fibril orientation has also been compared with linear force-free models by Nakagawa, Raadu, and Harvey (1973) finding that there is a value of α giving a good match between the magnetic field and the fibril direction; however, the height of the structures was the largest discrepancy between the observations and the model. This fact has been justified by the existence of perpendicular electric currents in the photosphere and chromosphere such as Pedersen and Hall currents that will be dispersed with height to vanish in the corona. The 3D modelling of the magnetic carpet has been performed based on the point charge technique (Schrijver and Title, 2002): the assumption is justified in the quiet Sun as small-scale magnetic features can be isolated and tracked in time (DeForest *et al.*, 2007; Lamb *et al.*, 2008, 2010). Schrijver and Title (2002) showed that EUV brightenings can be correlated with the change of connectivity in the small-scale magnetic field. Building on this work, Régnier, Parnell, and Haynes (2008) performed a potential field extrapolation (with continuous magnetic field) using a high-resolution *Hinode*/SOT magnetogram to describe the complexity of the quiet-Sun magnetic field. The authors showed that the complexity of the quiet Sun is located in the photosphere and chromosphere at altitude less than 2.5 Mm above the surface. In this modelling, the magnetic field in the quiet Sun has been decomposed into two components:

i) closed field lines, which characterise the complexity of the magnetic field (below several hundreds of kilometre according to Régnier, Parnell, and Haynes, 2008) and are linked to granule's boundary and part of supergranular field,
ii) open field lines ("open" meaning leaving the box of computation), which is often considered as the source of the solar wind. The amount of open flux has been measured at different height showing that a small amount of the photospheric magnetic flux is open above few megameters. The imbalance of magnetic flux increasing with latitude (towards the poles), the open magnetic flux increases also with latitude. Jin and Wang (2011) showed that the open magnetic field does not always originate from strong polarities (kG field) in the poles using vector magnetic field measurements from *Hinode*/SOT. It is worth noticing that the quiet-Sun magnetic field, and in particular the funnel structure, has been theoretically investigated using a potential field extrapolation by Aiouaz and Rast (2006).

4.3. Eruptive Events

There are several eruptive events in the quiet Sun or small-scale events which require high-resolution field extrapolations: blinkers, jets, spicules, Ellerman bombs, or mini-CMEs. There are few studies tackling the time evolution of the events themselves, but mostly analysing the structures associated with these events.

Bright points (often observed in EUV or X-rays) have been studied in detail in terms of their magnetic field structure and time evolution. Based on the point charge technique, Alexander, Del Zanna, and Maclean (2011) have shown that the observed structure of the magnetic field (or some field lines used as a proxy to the magnetic field) is close to a potential field state.

With the development of high-resolution instrumentation, the magnetic field at a granular scale becomes available, and thus also the study of photospheric and chromospheric phenomena in the quiet Sun or active regions. Based on the Flare Genesis Experiment observations (Bernasconi, Rust, and Eaton, 2001), Pariat *et al.* (2004) have studied the possibility of undulatory emergence in a small-scale field (a coherent flux tube emerging at different locations depending on the convection pattern) based on a LFF field extrapolation. The authors have noticed that the emergence locations are associated with Ellerman bombs. Guglielmino *et al.* (2010) studied reconnection events in a small-scale magnetic field within an active region during the emergence of magnetic flux. Using a LFF field extrapolation, the authors have derived the complexity associated with these events: the small-scale field exhibits a complex topology with a fan-spine structure.

From a potential extrapolation, He *et al.* (2010a) have shown that a jet occurring in a polar coronal hole is guided by the open magnetic field, and thus can be a source for the fast solar wind.

5. Active Regions

Active regions and their related structures and phenomena have been extensively studied with the advent of line-of-sight magnetographs and vector magnetographs measuring strong fields (active region fields) with high accuracy.

5.1. Structure of the Magnetic Field

As magnetic field extrapolations are based on an equilibrium, the first step is to study the static structure of the magnetic field above an active region.

General properties have been derived as follows:

- The magnetic field decays with height, but not following a bipolar magnetic field relation (Régnier, Priest, and Hood, 2008). The magnetic field can decay by several orders of magnitude with height.
- Stating the obvious, individual active regions have different structures in terms of shear and twist, which depends on their history (Régnier and Priest, 2007a, 2007b).
- Active regions have a complex distribution of electric current density generated by photospheric motions and by emergence from below the photosphere (Leka, 1996).
- In a statistical sense, the magnetic field lines are longer and higher in altitude when electric currents are present (Régnier and Priest, 2007a).
- The magnetic energy is stored mostly at the bottom of the corona (including the photosphere and chromosphere), and can also be stored in twisted flux bundles in the low corona (Régnier and Priest, 2007a).
- Active regions can be decomposed into two parts: the core, and the edge. The core is dominated by strong electric current density and thus has sheared and twisted magnetic field bundles, while the edge of the active region is less influenced by electric currents and exhibits more potential field lines (De Rosa *et al.*, 2009).

In terms of magnetic energy, active regions have been found to have a total magnetic energy between 10^{31} erg to 10^{34} erg mostly depending on the total unsigned photospheric flux and the electric currents. The magnetic helicity has a characteristic value of 10^{42} G^2 cm^4 (Régnier and Canfield, 2006).

Lots of studies have involved a comparison of the active region structures obtained using different assumptions. Hudson and Wheatland (1999) and Régnier (2012) showed that, for a simulated magnetic configuration, the magnetic topology does not change much between different force-free models, even if the geometry and the magnetic energy are significantly modified.

5.2. Filament, Sigmoid, and Twisted Flux Bundles

One of the main successes of LFF, NLFF, or MHS extrapolation methods has been to reconstruct twisted flux tubes that unambiguously exist in the corona.

Filaments/prominences are thought to be a coherent collection of twisted magnetic field lines forming a twisted flux tube/bundle. The force-free field extrapolation has been used to show that there indeed are. Using a NLFF model, Yan *et al.* (2001a) described an active-region filament as a magnetic rope or twisted flux bundle with three turns. This is a highly twisted flux tube, which has never been reproduced in magnetic field extrapolation to date. In order to store plasma/mass, the most plausible structures are magnetic dips in which magnetic curvature acts against gravity to sustain the plasma above the surface. Using a LFF approximation, Aulanier and Démoulin (1998) have identified a filament by finding the magnetic dips in the 3D magnetic field configuration (Aulanier *et al.*, 1998, 1999). Based on the same model, Dudík *et al.* (2008) showed the complexity of a filament as it can be fragmented, and not just a single coherent structure, by parasitic polarities constituting the legs or barbs of the filament. Using a NLFF method, Régnier and Amari (2004) identified a filament as a dipped twisted flux bundle with a small number of turn (see also Canou *et al.*, 2009; Canou and Amari, 2010). Guo *et al.* (2010a) showed that part of a filament was identified to a twisted flux bundle, while the rest of the filament was correlated with magnetic dips along sheared untwisted field lines.

Sigmoids are expected to play an important role in solar eruptions (Canfield, Hudson, and McKenzie, 1999). They are considered as twisted flux bundles. Régnier, Amari, and Kersalé (2002) reproduced a sigmoid as a highly twisted flux tube without magnetic dips due to the nonuniform distribution of the twist along the structure. Other studies have been performed to understand the nature and evolution of X-ray sigmoid as twisted flux tubes (Savcheva, van Ballegooijen, and DeLuca, 2012; Savcheva *et al.*, 2012; Inoue *et al.*, 2012).

5.3. Comparison with Observations

The most common way of comparing observations and magnetic field extrapolation is qualitative: overlaying or putting side-by-side images and magnetic configurations. Some quantitative methods have been developed and are mentioned in the following paragraphs.

Optical Wavelengths The main feature observed in the visible wavelengths is a filament mostly in the Hα line. The findings using field extrapolations are summarised in the previous section. Structures like fibrils are not yet extrapolated due to their small height in the chromosphere; however, their direction has been used to constrain the orientation of the transverse magnetic field in vector magnetograms (Wiegelmann *et al.*, 2008). During flares, the chromospheric brightenings (localised patches or ribbons) have been identified as the

footpoints of magnetic field lines linked to the flare process such as reconnection events or post-flare loop growth. Masson *et al.* (2009) used a potential field extrapolation to show the correlation between magnetic field lines involved in the flare process and chromospheric ribbons.

EUV-UV Using imagers, the EUV loops have been studied mostly at 171 Å and 193/195 Å due to the characteristics of EUV instruments (*e.g.*, SOHO/EIT, TRACE, STEREO/SECCHI/EUVI, SDO/AIA). A large number of studies has been performed to show the consistency of magnetic field extrapolations with observed EUV loops (Pallavicini, Sakurai, and Vaiana, 1981; Aschwanden, 2005; Zhang *et al.*, 2007; Kwon and Chae, 2008; Aschwanden *et al.*, 2008; Inhester, Feng, and Wiegelmann, 2008; Winebarger, Warren, and Falconer, 2008; Sandman *et al.*, 2009; Conlon and Gallagher, 2010; Aschwanden and Sandman, 2010; Syntelis *et al.*, 2012). The discrepancy between potential field lines and EUV loops has been used to show the existence of nonpotentiality in active regions, *i.e.*, the existence of shear and twisted magnetic fields able to store magnetic energy and to trigger eruptions. Based on observations from (imaging) spectrometers, the extrapolation methods are compared to flows/Dopplershifts in active regions (Baker *et al.*, 2009; Boutry *et al.*, 2012).

Soft X-Rays Two main solar features observed in soft X-rays have been matched to magnetic flux bundles or magnetic field lines obtained from extrapolation: sigmoids (see Section 5.2) and X-ray bright points. The latter have been extensively studied since Golub *et al.* (1974). Adding magnetic extrapolations, the X-ray bright points have been studied in more detail (Mandrini *et al.*, 1996; Brooks and Warren, 2008).

Hard X-Rays The hard X-ray sources are often observed during flares and reconnection events. The existence of sources at the footpoints of eruptive loops is well established, as well as the emission at the flare loop-top assumed to be located below the current sheet where the magnetic reconnection occurs. The magnetic field extrapolations have helped to better understand the link between the geometry of loops, the topology of the magnetic field, and the sources of hard X-ray (Takakura *et al.*, 1983; Sakurai, 1985; Yan and Huang, 2003; Xu *et al.*, 2010; Aurass *et al.*, 2010; Liu *et al.*, 2010; Guo *et al.*, 2012).

Radio The radio emission can be observed during eruptive events such as flares, CMEs or filament eruptions, and it has been often suggested that the radio emission in the high corona occurs at the interface between closed and open magnetic field regions (Klassen *et al.*, 1999; Bentley *et al.*, 2000; Paesold *et al.*, 2001; Aurass *et al.*, 2003, 2005, 2011; Grechnev *et al.*, 2006; Arzner and Vlahos, 2006; Yan *et al.*, 2006; Hofmann and Ruždjak, 2007; Wen, Wang, and Zhang, 2007; Nitta and De Rosa, 2008; Klein *et al.*, 2008; Chen *et al.*, 2011; Tun, Gary, and Georgoulis, 2011; Del Zanna *et al.*, 2011; Iwai *et al.*, 2012; Hao *et al.*, 2012). The gyroemission is also used to determine the strength of the magnetic field in the corona (Pallavicini, Sakurai, and Vaiana, 1981; Schmahl *et al.*, 1982; Hildebrandt, Seehafer, and Krueger, 1984; Brosius *et al.*, 1997, 2002; Lee *et al.*, 1998, 1999; Grebinskij *et al.*, 2000; Ryabov *et al.*, 2005; Bogod, Stupishin, and Yasnov, 2012). The comparison of those measurements and the magnetic field strength derived from extrapolation has yet not be proven to be satisfactory: the height of the radio sources does not always correlate.

Infrared Despite the development of solar observations in the infrared wavelengths, there is, to my knowledge, no study comparing the magnetic field derived from those observations (including the near-IR HeI triplet and Stokes parameter measurements in prominences by Paletou *et al.* (2001)) and the extrapolated magnetic field.

5.4. Time Evolution

The characteristic Alfvén transit time of an active region loop is of 10 – 15 min. The time evolution of an active region can thus be studied by a series of equilibria if the photospheric footpoint motions are ideal MHD motions, which do not add any topological constraints (Antiochos, 1987). The most complete study of the evolution of an active region has been performed by Sun *et al.* (2012) using a high-cadence, high-resolution time series of vector magnetograms from SDO/HMI. The authors studied the time evolution before and after a series of flares showing that the flare changes (slightly) the magnetic energy; the geometry of the magnetic field lines is also modified making the magnetic field more confined in low corona. For C-class flares, Régnier and Canfield (2006) have performed a study of the evolution of the magnetic energy and magnetic helicity. The authors showed that the start of the significant changes occurred at about 20 min before the peak of the flare. Thalmann and Wiegelmann (2008) showed that the magnetic energy build-up in an active region can be observed several days prior to the eruption.

5.5. Physics of Flares and CMEs

One of the main early study of a flare using an extrapolation method corresponds to the Bastille Day flare (Aulanier *et al.*, 2000). Using a LFF approximation, the authors showed that the flaring site was related to the existence of a null point located in the corona.

Another aspect of the physics of eruptions is the amount of magnetic energy that can be released. From a single snapshot (one extrapolation at a given time), the amount of free energy is estimated using the potential field as a minimum (lower bound) of magnetic energy. The magnetic energy of a LFF field with the same magnetic helicity can also be considered as a minimum of magnetic energy. Régnier and Priest (2007b) have demonstrated that the amount of free magnetic energy is larger than the energy of the flare associated with the active regions studied (only four active regions with very different structure have been studied). Numerous studies of flares and CMEs have been combined with magnetic field extrapolations to support the model of eruption (Schmidt, 1964; Zirin and Tanaka, 1973; Tanaka and Nakagawa, 1973; Rust, Nakagawa, and Neupert, 1975; Tanaka, 1978; Seehafer and Staude, 1979; Ma and Ai, 1979; Yang and Zhang, 1980; Su, 1980, 1982; Seehafer, 1985; Lin *et al.*, 1985; Yang, Hong, and Ding, 1988; Lin, 1990; Linke, Ioshpa, and Selivanov, 1990; Klimchuk and Sturrock, 1992; Démoulin *et al.*, 1994; McClymont and Mikic, 1994; Yan and Wang, 1995; Mandrini *et al.*, 1995; Jiao, McClymont, and Mikic, 1997; Choudhary and Gary, 1999; Delannée and Aulanier, 1999; Yurchyshyn *et al.*, 2000; Y. M. Wang, 2000; Yan *et al.*, 2001a, 2001b; T. Wang *et al.*, 2002; Yan and Huang, 2003; Moon *et al.*, 2004; Fragos, Rantsiou, and Vlahos, 2004; Gary and Moore, 2004; Berlicki *et al.*, 2004; Del Zanna *et al.*, 2006; Li *et al.*, 2007; Nitta and De Rosa, 2008; Jing *et al.*, 2008, 2009, 2010, 2012; H. Wang *et al.*, 2008; Martínez-Oliveros, Moradi, and Donea, 2008; Thalmann, Wiegelmann, and Raouafi, 2008; Guo *et al.*, 2008; Zuccarello *et al.*, 2009; Su *et al.*, 2009a, 2009b; des Jardins *et al.*, 2009; Chandra *et al.*, 2009; He *et al.*, 2010b; Xu *et al.*, 2010; Cheng *et al.*, 2010; Park *et al.*, 2010; Liu *et al.*, 2010; Guo *et al.*, 2010b; Cheng *et al.*, 2011; Inoue *et al.*, 2011; Gilchrist, Wheatland, and Leka, 2012; Shen, Liu, and Su, 2012; Vincent, Charbonneau, and Dubé, 2012; R. Wang *et al.*, 2012; Georgoulis, Tziotziou, and Raouafi, 2012; Tadesse *et al.*, 2012).

6. Improvements and Challenges

6.1. Extrapolation Techniques

Potential and LFF extrapolations are now mature techniques that are commonly used, and their physical meaning and the understanding of physical process are well established: no or limited amount of twist available in these models, and minimum energy state, for instance. However, the NLFF model is still in constant evolution/improvement. Since more than 20 years now, the NLFF assumption has been implemented in the solar community to study a large number of topics with a relatively good success. The next stages of development are:

- In Cartesian geometry, developing a reliable magnetohydrostatic equilibrium code. This corresponds to a step forward compared to the force-free field as far as the corona only is concerned. Including the thermodynamic properties of the photosphere and/or chromosphere is a challenge.
- In spherical geometry, improving the spatial resolution of the PFSS model is a first step, especially multigrids or nonuniform grids can be used. The PFSS model also currently lacks information at the poles: the improvement of the spatial resolution will need to be combined with a more accurate measure of the radial magnetic field at the poles. This will modify the dipole component of the magnetic field, which is needed to study the dynamo action.
- In spherical geometry, despite the efforts reported in the previous sections to move from the PFSS model to a NLFF assumption, the use of the NLFF model could become a standard in the community with a special care taken to the transition between the coronal magnetic field and the solar wind magnetic field. As for the NLFF field in Cartesian coordinates, a community effort should be envisioned.
- Defining constraints obtained from observations (X-rays, EUV, radio, infrared, ...) to derive a magnetic field configuration closer to reality, and thus to allow for quantitative comparison. As an example, the comparison between the density derived from MHS models and the density obtained from spectrometers should be a systematic check of the goodness of the extrapolation.

The main word for the development of extrapolation techniques using solar data as boundary conditions is quantitative. The main issue is always to find a compromise between the spatial resolution, the size of the field-of-view, the computational time, and the resources, which is the most suitable for the physical problem tackled.

6.2. Comments on Boundary Conditions

I briefly discuss the current issues encountered when using solar magnetograms as boundary conditions for magnetic field extrapolations. In the following, a "flat surface" refers to a surface of constant curvature or radius (*e.g.*, a plane or a sphere). The main issues that should be kept in mind when reconstructing a coronal magnetic field are:

- Inversion of Stokes parameters: the magnetic field components are derived from the radiative transfer equations for the four Stokes parameters. The inversion is complex and often used by reconstruction modellers as a black box. One typical assumption is to consider that the solar atmosphere as a constant optical depth. This assumption with the assumption of a local thermodynamic equilibrium is becoming less and less accurate for high resolution data.

- 180 degree ambiguity: after the inversion of the Stokes parameters, an ambiguity of 180 degrees on the orientation of the transverse magnetic field still remains. Some algorithms to resolve this ambiguity are based on a magnetic field model (potential, LFF, or NLFF field). The goodness of the ambiguity is crucial, especially when a flux rope is present in the magnetic configuration.
- Flatness of the surface: as implied by the inversion of the Stokes parameters, the measurement of the magnetic field in neighbouring pixels is certainly not at the same height in the photosphere. This fact is even more critical for chromospheric measurements. In order to currently perform a magnetic field extrapolation, it is assumed that the magnetogram corresponds to a flat surface.
- The α-distribution: the definition of α as seen in Equation (6) is given by the normal component of the force-free equation. It means that a contribution from the electric currents perpendicular to the magnetic field is included into the α-distribution when the magnetic field is not strictly normal to the photospheric surface. The effects of the electric currents have to be investigated in more detail. For extrapolation models beyond the force-free models, the components of the electric current density will be more appropriate boundary conditions (Grad and Rubin, 1958).
- Error estimate: it is still difficult to estimate the error/inaccuracy made in measuring the magnetic field:

  i) the signal in sunspot is weak (limited number of photons),
  ii) the magnetic field in quiet Sun regions is weak,
  iii) the Hanle effect can dominate the quiet-Sun field,
  iv) the linear polarisation signal leading to the transverse magnetic field is small compared to the Stokes V signal (by an order of magnitude),
  v) the properties of the spectral line such as the Landé factor can influence the threshold/saturation of the detected magnetic field strength,
  vi) a pixel is not filled uniformly by magnetic field, so the filling factor is also an important quantity.

  Error estimates from vector magnetograms can be incorporate in the extrapolation model resulting in a reliable equilibrium (Wheatland and Leka, 2011).
- Projection effect: the transverse field is strongly influenced by the projection effect, especially in the penumbra of sunspots where the magnetic field is mostly horizontal. This leads to the change of sign of observed polarities.
- Synoptic/Carrington maps: often by default, the Carrington maps have been corrected for the magnetic flux imbalance, which is good for extrapolation but do not represent correctly the physics of the solar surface magnetic field.

In the near future, we will see the development of new instruments which will provide us access to the magnetic field near the poles (*e.g.*, Solar Orbiter) and in the corona (*e.g.*, CoMP). These improved measurements will impose new constraints on the physics of magnetic field extrapolations.

7. Summary

In this review, I have summarised many different results obtained from magnetic field extrapolations combined with magnetic field observations. The extrapolations have been applied to various different issues in order to better understand the physics of the corona. Owing to the large number of observations in strong field regions, most of the studies have dealt with

the structure and evolution of the magnetic field in active regions, as well as studying the causes and consequences of flares and CMEs.

What have we learned from magnetic field extrapolations?

- The current force-free models describe relatively well the structure of the coronal magnetic above active regions.
- The amount of magnetic energy available is consistent with what is expected and observed during eruptive events, even if most of time, the studies do not specify error bars.
- The existence of twisted flux bundles which are a prime ingredient in most of the MHD models to store magnetic energy in the corona, and trigger eruptions.
- The physics of flares is closely related to the topology of the magnetic field prior to the eruption: existence of coronal null points, separators or quasi-separatrix layers.
- The large-scale connectivity of the magnetic field lines deduced from extrapolations is crucial to understanding of the redistribution of magnetic energy and magnetic helicity in the solar corona.
- The link between the broad range of observations (from hard X-ray to radio wavelengths) can be made through the structure of the magnetic field.

What have we not learned (yet) from magnetic field extrapolations?

- The "universal" ingredient responsible for triggering eruptions and which will allow us to predict flares and CMEs.
- The interaction between the different spatial scales involved in the solar atmosphere, from the quiet-Sun magnetic field to the global structure.
- The interaction between the different regions of the Sun: from the tachocline to the solar wind, englobing the whole heliosphere.
- To be specific to a particular extrapolation method, we do not yet understand the goodness of the force-free extrapolations while the imposed boundary conditions are not force-free. To achieve the goal, it is required to develop more theoretical studies based on the effects of noise or perpendicular currents on force-free magnetic configurations.

Despite this apparent success of extrapolation methods, *the improvement in the understanding of the coronal magnetic field will depend on quantitative comparisons with the observations* and not just qualitative comparisons. The quantitative success of the extrapolation method will *a posteriori* justify the physical assumptions or will drive the developments of these methods towards more physical and sophisticated techniques. The limits of these developments are the boundary conditions obtained by the observations, and the computational power available. Especially, there is a need to improve the physics incorporated into these models: the coupling between the plasma and the magnetic field playing a major role in the evolution of the magnetic fields.

Acknowledgements I would like to thank Steve Tomczyk and Marc DeRosa for inviting me to contribute to the "Coronal Magnetism – Connecting Models to Data and the Corona to the Earth" workshop held in Boulder (2012). I also thank Michael Thompson for his hospitality at HAO (Boulder) during the workshop.

References

Abramenko, V.I., Yurchishin, V.B.: 1996, *Solar Phys.* **168**, 47. doi:10.1007/BF00145824.
Abramenko, V.I., Wang, T., Yurchishin, V.B.: 1996, *Solar Phys.* **168**, 75. doi:10.1007/BF00145826.
Adams, J., Pneuman, G.W.: 1976, *Solar Phys.* **46**, 185. doi:10.1007/BF00157566.
Aiouaz, T., Rast, M.P.: 2006, *Astrophys. J.* **647**, 183. doi:10.1086/507468.

Alexander, C.E., Del Zanna, G., Maclean, R.C.: 2011, *Astron. Astrophys.* **526**, 134. doi:10.1051/0004-6361/201014045.
Alissandrakis, C.E.: 1981, *Astron. Astrophys.* **100**, 197.
Altschuler, M.D., Newkirk, G.: 1969, *Solar Phys.* **9**, 131. doi:10.1007/BF00145734.
Aly, J.J.: 1984, *Astrophys. J.* **283**, 349. doi:10.1086/162313.
Aly, J.J.: 1989, *Solar Phys.* **120**, 19. doi:10.1007/BF00148533
Amari, T., Aly, J.J.: 2010, *Astron. Astrophys.* **522**, 52. doi:10.1051/0004-6361/200913058.
Amari, T., Boulmezaoud, T.Z., Aly, J.J.: 2006, *Astron. Astrophys.* **446**, 691. doi:10.1051/0004-6361:20054076.
Amari, T., Boulmezaoud, T.Z., Maday, Y.: 1998, *Astron. Astrophys.* **339**, 252.
Amari, T., Boulmezaoud, T.Z., Mikic, Z.: 1999, *Astron. Astrophys.* **350**, 1051.
Amari, T., Aly, J.J., Luciani, J.F., Boulmezaoud, T.Z., Mikic, Z.: 1997, *Solar Phys.* **174**, 129.
Antiochos, S.K.: 1987, *Astrophys. J.* **312**, 886. doi:10.1086/164935.
Arzner, K., Vlahos, L.: 2006, *Astron. Astrophys.* **454**, 957. doi:10.1051/0004-6361:20064953.
Aschwanden, M.J.: 2005, *Solar Phys.* **228**, 339. doi:10.1007/s11207-005-2788-5.
Aschwanden, M.J.: 2012a, *Solar Phys.* doi:10.1007/s11207-012-0069-7.
Aschwanden, M.J.: 2012b, *Solar Phys.* doi:10.1007/s11207-012-0203-6.
Aschwanden, M.J.: 2013, *Astrophys. J.* **763**, 115. doi:10.1088/0004-637X/763/2/115.
Aschwanden, M.J., Malanushenko, A.: 2012, *Solar Phys.* doi:10.1007/s11207-012-0070-1.
Aschwanden, M.J., Sandman, A.W.: 2010, *Astron. J.* **140**, 723. doi:10.1088/0004-6256/140/3/723.
Aschwanden, M.J., Lee, J.K., Gary, G.A., Smith, M., Inhester, B.: 2008, *Solar Phys.* **248**, 359. doi:10.1007/s11207-007-9064-9.
Aulanier, G., Démoulin, P.: 1998, *Astron. Astrophys.* **329**, 1125.
Aulanier, G., Démoulin, P., van Driel-Gesztelyi, L., Mein, P., Deforest, C.: 1998, *Astron. Astrophys.* **335**, 309.
Aulanier, G., Démoulin, P., Mein, N., van Driel-Gesztelyi, L., Mein, P., Schmieder, B.: 1999, *Astron. Astrophys.* **342**, 867.
Aulanier, G., DeLuca, E.E., Antiochos, S.K., McMullen, R.A., Golub, L.: 2000, *Astrophys. J.* **540**, 1126. doi:10.1086/309376.
Aurass, H., Klein, K.L., Zlotnik, E.Y., Zaitsev, V.V.: 2003, *Astron. Astrophys.* **410**, 1001. doi:10.1051/0004-6361:20031249.
Aurass, H., Rausche, G., Mann, G., Hofmann, A.: 2005, *Astron. Astrophys.* **435**, 1137. doi:10.1051/0004-6361:20042199.
Aurass, H., Rausche, G., Berkebile-Stoiser, S., Veronig, A.: 2010, *Astron. Astrophys.* **515**, 1. doi:10.1051/0004-6361/200913132.
Aurass, H., Mann, G., Zlobec, P., Karlický, M.: 2011, *Astrophys. J.* **730**, 57. doi:10.1088/0004-637X/730/1/57.
Baker, D., van Driel-Gesztelyi, L., Mandrini, C.H., Démoulin, P., Murray, M.J.: 2009, *Astrophys. J.* **705**, 926. doi:10.1088/0004-637X/705/1/926.
Barnes, G., Leka, K.D., Wheatland, M.S.: 2006, *Astrophys. J.* **641**, 1188. doi:10.1086/500503.
Barnes, G., Longcope, D.W., Leka, K.D.: 2005, *Astrophys. J.* **629**, 561. doi:10.1086/431175.
Bentley, R.D., Klein, K.L., van Driel-Gesztelyi, L., Démoulin, P., Trottet, G., Tassetto, P., Marty, G.: 2000, *Solar Phys.* **193**, 227. doi:10.1023/A:1005218007132
Berger, M.A.: 1999a, *Plasma Phys. Control. Fusion* **41**, 167. doi:10.1088/0741-3335/41/12B/312.
Berger, M.A.: 1999b, In: Brown, M.R., Canfield, R.C., Pevtsov, A.A. (eds.) *Magnetic Helicity in Space and Laboratory Plasmas*, *AGU Geophys. Monogr.* **111**, 1. doi:10.1029/GM111p0001.
Berger, M.A., Field, G.B.: 1984, *J. Fluid Mech.* **147**, 133. doi:10.1017/S0022112084002019
Berger, M.A., Prior, C.: 2006, *J. Phys. A* **39**, 8321. doi:10.1088/0305-4470/39/26/005.
Berlicki, A., Schmieder, B., Vilmer, N., Aulanier, G., Del Zanna, G.: 2004, *Astron. Astrophys.* **423**, 1119. doi:10.1051/0004-6361:20040259.
Bernasconi, P.N., Rust, D.M., Eaton, H.A.C.: 2001, In: Sigwarth, M. (ed.) *Advanced Solar Polarimetry – Theory, Observation, and Instrumentation*, *ASP Conf. Ser.* **236**, 399.
Beveridge, C., Priest, E.R., Brown, D.S.: 2002, *Solar Phys.* **209**, 333. doi:10.1023/A:1021210127598.
Beveridge, C., Priest, E.R., Brown, D.S.: 2004, *Geophys. Astrophys. Fluid Dyn.* **98**, 429. doi:10.1080/03091920410001715575.
Bhattacharyya, R., Janaki, M.S., Dasgupta, B., Zank, G.P.: 2007, *Solar Phys.* **240**, 63. doi:10.1007/s11207-006-0280-5.
Bogod, V.M., Stupishin, A.G., Yasnov, L.V.: 2012, *Solar Phys.* **276**, 61. doi:10.1007/s11207-011-9850-2.
Boulbe, C., Zamène Boulmezaoud, T., Amari, T.: 2009, ArXiv e-prints.
Boutry, C., Buchlin, E., Vial, J.C., Régnier, S.: 2012, *Astrophys. J.* **752**, 13. doi:10.1088/0004-637X/752/1/13.
Brooks, D.H., Warren, H.P.: 2008, *Astrophys. J.* **687**, 1363. doi:10.1086/591834.

Brosius, J.W., Davila, J.M., Thomas, R.J., White, S.M.: 1997, *Astrophys. J.* **488**, 488. doi:10.1086/304673.
Brosius, J.W., Landi, E., Cook, J.W., Newmark, J.S., Gopalswamy, N., Lara, A.: 2002, *Astrophys. J.* **574**, 453. doi:10.1086/340923.
Brown, D.S., Priest, E.R.: 1999, *Proc. Roy. Soc. London A* **455**, 3931. doi:10.1098/rspa.1999.0484.
Brown, D.S., Priest, E.R.: 2000, *Solar Phys.* **194**, 197. doi:10.1023/A:1005221503925
Bungey, T.N., Titov, V.S., Priest, E.R.: 1996, *Astron. Astrophys.* **308**, 233.
Canfield, R.C., Hudson, H.S., McKenzie, D.E.: 1999, *Geophys. Res. Lett.* **26**, 627. doi:10.1029/1999GL900105.
Canou, A., Amari, T., Bommier, V., Schmieder, B., Aulanier, G., Li, H.: 2009, *Astrophys. J. Lett.* **693**, L27. doi:10.1088/0004-637X/693/1/L27.
Canou, A., Amari, T.: 2010, *Astrophys. J.* **715**, 1566. doi:10.1088/0004-637X/715/2/1566.
Carcedo, L., Brown, D.S., Hood, A.W., Neukirch, T., Wiegelmann, T.: 2003, *Solar Phys.* **218**, 29. doi:10.1023/B:SOLA.0000013045.65499.da.
Chandra, R., Schmieder, B., Aulanier, G., Malherbe, J.M.: 2009, *Solar Phys.* **258**, 53. doi:10.1007/s11207-009-9392-z.
Chen, B., Bastian, T.S., Gary, D.E., Jing, J.: 2011, *Astrophys. J.* **736**, 64. doi:10.1088/0004-637X/736/1/64.
Cheng, X., Ding, M.D., Guo, Y., Zhang, J., Jing, J., Wiegelmann, T.: 2010, *Astrophys. J. Lett.* **716**, L68. doi:10.1088/2041-8205/716/1/L68.
Cheng, X., Zhang, J., Ding, M.D., Guo, Y., Su, J.T.: 2011, *Astrophys. J.* **732**, 87. doi:10.1088/0004-637X/732/2/87.
Chiu, Y.T., Hilton, H.H.: 1977, *Astrophys. J.* **212**, 873. doi:10.1086/155111.
Choudhary, D.P., Gary, G.A.: 1999, *Solar Phys.* **188**, 345. doi:10.1023/A:1005165425964
Clegg, J.R., Bromage, B.J.I., Browning, P.K.: 1999, *Space Sci. Rev.* **87**, 145. doi:10.1023/A:1005190821498.
Clegg, J.R., Browning, P.K., Laurence, P., Bromage, B.J.I., Stredulinsky, E.: 2000, *Astron. Astrophys.* **361**, 743.
Conlon, P.A., Gallagher, P.T.: 2010, *Astrophys. J.* **715**, 59. doi:10.1088/0004-637X/715/1/59.
Contopoulos, I.: 2013, *Solar Phys.* **282**, 419. doi:10.1007/s11207-012-0154-y.
Contopoulos, I., Kalapotharakos, C., Georgoulis, M.K.: 2011, *Solar Phys.* **269**, 351. doi:10.1007/s11207-011-9713-x.
Courant, H.: 1963, *J. Appl. Mech.* **30**, 158. doi:10.1115/1.3630089.
Cuperman, S., Ofman, L., Semel, M.: 1989, *Astron. Astrophys.* **216**, 265.
Cuperman, S., Ofman, L., Semel, M.: 1990a, *Astron. Astrophys.* **227**, 583.
Cuperman, S., Ofman, L., Semel, M.: 1990b, *Astron. Astrophys.* **230**, 193.
De Rosa, M.L., Schrijver, C.J., Barnes, G., Leka, K.D., Lites, B.W., Aschwanden, M.J., Amari, T., Canou, A., McTiernan, J.M., Régnier, S., Thalmann, J.K., Valori, G., Wheatland, M.S., Wiegelmann, T., Cheung, M.C.M., Conlon, P.A., Fuhrmann, M., Inhester, B., Tadesse, T.: 2009, *Astrophys. J.* **696**, 1780. doi:10.1088/0004-637X/696/2/1780.
DeForest, C.E., Hagenaar, H.J., Lamb, D.A., Parnell, C.E., Welsch, B.T.: 2007, *Astrophys. J.* **666**, 576. doi:10.1086/518994.
Del Zanna, G., Berlicki, A., Schmieder, B., Mason, H.E.: 2006, *Solar Phys.* **234**, 95. doi:10.1007/s11207-006-0016-6.
Del Zanna, G., Aulanier, G., Klein, K.L., Török, T.: 2011, *Astron. Astrophys.* **526**, 137. doi:10.1051/0004-6361/201015231.
Delannée, C., Aulanier, G.: 1999, *Solar Phys.* **190**, 107. doi:10.1023/A:1005249416605.
Démoulin, P., Cuperman, S., Semel, M.: 1992, *Astron. Astrophys.* **263**, 351.
Démoulin, P., Mandrini, C.H., Rovira, M.G., Hénoux, J.C., Machado, M.E.: 1994, *Solar Phys.* **150**, 221. doi:10.1007/BF00712887.
des Jardins, A., Canfield, R., Longcope, D., McLinden, E., Dillman, A.: 2009, *Astrophys. J.* **693**, 886. doi:10.1088/0004-637X/693/1/886.
Dudík, J., Aulanier, G., Schmieder, B., Bommier, V., Roudier, T.: 2008, *Solar Phys.* **248**, 29. doi:10.1007/s11207-008-9155-2.
Durrant, C.J.: 1989, *Aust. J. Phys.* **42**, 317.
Finn, J.M., Antonsen, T.M.: 1985, *Comments Plasma Phys. Control. Fusion* **9**, 111.
Fragos, T., Rantsiou, E., Vlahos, L.: 2004, *Astron. Astrophys.* **420**, 719. doi:10.1051/0004-6361:20034570.
Fuhrmann, M., Seehafer, N., Valori, G., Wiegelmann, T.: 2011, *Astron. Astrophys.* **526**, 70. doi:10.1051/0004-6361/201015453.
Gary, G.A.: 1989, *Astrophys. J. Suppl.* **69**, 323. doi:10.1086/191316.
Gary, G.A., Alexander, D.: 1999, *Solar Phys.* **186**, 123. doi:10.1023/A:1005147921110.
Gary, G.A., Moore, R.L.: 2004, *Astrophys. J.* **611**, 545. doi:10.1086/422132.
Georgoulis, M.K., Tziotziou, K., Raouafi, N.E.: 2012, *Astrophys. J.* **759**, 1. doi:10.1088/0004-637X/759/1/1.
Gilchrist, S.A., Wheatland, M.S.: 2013, *Solar Phys.* **282**, 283. doi:10.1007/s11207-012-0144-0.

Gilchrist, S.A., Wheatland, M.S., Leka, K.D.: 2012, *Solar Phys.* **276**, 133. doi:10.1007/s11207-011-9878-3.
Gold, T., Hoyle, F.: 1960, *Mon. Not. Roy. Astron. Soc.* **120**, 89.
Golub, L., Krieger, A.S., Silk, J.K., Timothy, A.F., Vaiana, G.S.: 1974, *Astrophys. J. Lett.* **189**, L93. doi:10.1086/181472.
Goodman, M.L.: 2000, *Astrophys. J.* **533**, 501. doi:10.1086/308635.
Grad, H., Rubin, H.: 1958, In: *Proc. 2nd Int. Conf. on Peaceful Uses of Atomic Energy* **31**, 190.
Grebinskij, A., Bogod, V., Gelfreikh, G., Urpo, S., Pohjolainen, S., Shibasaki, K.: 2000, *Astron. Astrophys. Suppl.* **144**, 169. doi:10.1051/aas:2000202.
Grechnev, V.V., Uralov, A.M., Zandanov, V.G., Rudenko, G.V., Borovik, V.N., Grigorieva, I.Y., Slemzin, V.A., Bogachev, S.A., Kuzin, S.V., Zhitnik, I., Pertsov, A.A., Shibasaki, K., Livshits, M.A.: 2006, *Publ. Astron. Soc. Japan* **58**, 55.
Guglielmino, S.L., Bellot Rubio, L.R., Zuccarello, F., Aulanier, G., Vargas Domínguez, S., Kamio, S.: 2010, *Astrophys. J.* **724**, 1083. doi:10.1088/0004-637X/724/2/1083.
Guo, Y., Ding, M.D., Wiegelmann, T., Li, H.: 2008, *Astrophys. J.* **679**, 1629. doi:10.1086/587684.
Guo, Y., Schmieder, B., Démoulin, P., Wiegelmann, T., Aulanier, G., Török, T., Bommier, V.: 2010a, *Astrophys. J.* **714**, 343. doi:10.1088/0004-637X/714/1/343.
Guo, Y., Ding, M.D., Schmieder, B., Li, H., Török, T., Wiegelmann, T.: 2010b, *Astrophys. J. Lett.* **725**, L38. doi:10.1088/2041-8205/725/1/L38.
Guo, Y., Ding, M.D., Schmieder, B., Démoulin, P., Li, H.: 2012, *Astrophys. J.* **746**, 17. doi:10.1088/0004-637X/746/1/17.
Hakamada, K.: 1995, *Solar Phys.* **159**, 89. doi:10.1007/BF00733033.
Hao, Q., Guo, Y., Dai, Y., Ding, M.D., Li, Z., Zhang, X.Y., Fang, C.: 2012, *Astron. Astrophys.* **544**, 17. doi:10.1051/0004-6361/201219941.
He, H., Wang, H.: 2006, *Mon. Not. Roy. Astron. Soc.* **369**, 207. doi:10.1111/j.1365-2966.2006.10288.x.
He, H., Wang, H.: 2008, *J. Geophys. Res.* **113**, 5. doi:10.1029/2007JA012441.
He, J.S., Marsch, E., Curdt, W., Tian, H., Tu, C.Y., Xia, L.D., Kamio, S.: 2010a, *Astron. Astrophys.* **519**, 49. doi:10.1051/0004-6361/201014709.
He, J.S., Marsch, E., Tu, C.Y., Tian, H., Guo, L.J.: 2010b, *Astron. Astrophys.* **510**, 40. doi:10.1051/0004-6361/200913059.
Heyvaerts, J., Priest, E.R.: 1984, *Astron. Astrophys.* **137**, 63.
Hildebrandt, J., Seehafer, N., Krueger, A.: 1984, *Astron. Astrophys.* **134**, 185.
Hofmann, A., Ruždjak, V.: 2007, *Solar Phys.* **240**, 107. doi:10.1007/s11207-006-0228-9.
Hu, Q., Dasgupta, B.: 2006, *Geophys. Res. Lett.* **33**, 15106. doi:10.1029/2006GL026952.
Hu, Q., Dasgupta, B.: 2008, *Solar Phys.* **247**, 87. doi:10.1007/s11207-007-9090-7.
Hu, Q., Dasgupta, B., Choudhary, D.P., Büchner, J.: 2008, *Astrophys. J.* **679**, 848. doi:10.1086/587639.
Hu, Q., Dasgupta, B., Derosa, M.L., Büchner, J., Gary, G.A.: 2010, *J. Atmos. Solar-Terr. Phys.* **72**, 219. doi:10.1016/j.jastp.2009.11.014.
Hudson, T.S., Wheatland, M.S.: 1999, *Solar Phys.* **186**, 301. doi:10.1023/A:1005176500346.
Inhester, B., Wiegelmann, T.: 2006, *Solar Phys.* **235**, 201. doi:10.1007/s11207-006-0065-x.
Inhester, B., Feng, L., Wiegelmann, T.: 2008, *Solar Phys.* **248**, 379. doi:10.1007/s11207-007-9027-1.
Inoue, S., Kusano, K., Magara, T., Shiota, D., Yamamoto, T.T.: 2011, *Astrophys. J.* **738**, 161. doi:10.1088/0004-637X/738/2/161.
Inoue, S., Magara, T., Watari, S., Choe, G.S.: 2012, *Astrophys. J.* **747**, 65. doi:10.1088/0004-637X/747/1/65.
Iwai, K., Miyoshi, Y., Masuda, S., Shimojo, M., Shiota, D., Inoue, S., Tsuchiya, F., Morioka, A., Misawa, H.: 2012, *Astrophys. J.* **744**, 167. doi:10.1088/0004-637X/744/2/167.
Jiang, C., Feng, X., Fan, Y., Xiang, C.: 2011, *Astrophys. J.* **727**, 101. doi:10.1088/0004-637X/727/2/101.
Jiao, L., McClymont, A.N., Mikic, Z.: 1997, *Solar Phys.* **174**, 311. doi:10.1023/A:1004927101300.
Jin, C., Wang, J.: 2011, *Astrophys. J.* **732**, 4. doi:10.1088/0004-637X/732/1/4.
Jing, J., Wiegelmann, T., Suematsu, Y., Kubo, M., Wang, H.: 2008, *Astrophys. J. Lett.* **676**, L81. doi:10.1086/587058.
Jing, J., Chen, P.F., Wiegelmann, T., Xu, Y., Park, S.H., Wang, H.: 2009, *Astrophys. J.* **696**, 84. doi:10.1088/0004-637X/696/1/84.
Jing, J., Tan, C., Yuan, Y., Wang, B., Wiegelmann, T., Xu, Y., Wang, H.: 2010, *Astrophys. J.* **713**, 440. doi:10.1088/0004-637X/713/1/440.
Jing, J., Yuan, Y., Reardon, K., Wiegelmann, T., Xu, Y., Wang, H.: 2011, *Astrophys. J.* **739**, 67. doi:10.1088/0004-637X/739/2/67.
Jing, J., Park, S.H., Liu, C., Lee, J., Wiegelmann, T., Xu, Y., Deng, N., Wang, H.: 2012, *Astrophys. J. Lett.* **752**, L9. doi:10.1088/2041-8205/752/1/L9.
Klassen, A., Aurass, H., Klein, K.L., Hofmann, A., Mann, G.: 1999, *Astron. Astrophys.* **343**, 287.
Klein, K.L., Krucker, S., Lointier, G., Kerdraon, A.: 2008, *Astron. Astrophys.* **486**, 589. doi:10.1051/0004-6361:20079228.

Klimchuk, J.A., Sturrock, P.A.: 1992, *Astrophys. J.* **385**, 344. doi:10.1086/170943.
Kusano, K., Nishikawa, K.: 1996, *Astrophys. J.* **461**, 415. doi:10.1086/177070.
Kwon, R.Y., Chae, J.: 2008, *Astrophys. J. Lett.* **677**, L141. doi:10.1086/587981.
Lamb, D.A., DeForest, C.E., Hagenaar, H.J., Parnell, C.E., Welsch, B.T.: 2008, *Astrophys. J.* **674**, 520. doi:10.1086/524372.
Lamb, D.A., DeForest, C.E., Hagenaar, H.J., Parnell, C.E., Welsch, B.T.: 2010, *Astrophys. J.* **720**, 1405. doi:10.1088/0004-637X/720/2/1405.
Lee, J., McClymont, A.N., Mikic, Z., White, S.M., Kundu, M.R.: 1998, *Astrophys. J.* **501**, 853. doi:10.1086/305851.
Lee, J., White, S.M., Kundu, M.R., Mikić, Z., McClymont, A.N.: 1999, *Astrophys. J.* **510**, 413. doi:10.1086/306556.
Leka, K.D.: 1996, *Astrophys. J.* **462**, 547. doi:10.1086/177171.
Leka, K.D.: 1999, *Solar Phys.* **188**, 21. doi:10.1023/A:1005130630873.
Leka, K.D., Skumanich, A.: 1999, *Solar Phys.* **188**, 3. doi:10.1023/A:1005108632671.
Levine, R.H., Altschuler, M.D.: 1974, *Solar Phys.* **36**, 345. doi:10.1007/BF00151204.
Levine, R.H., Schulz, M., Frazier, E.N.: 1982, *Solar Phys.* **77**, 363. doi:10.1007/BF00156118.
Li, H., Schmieder, B., Song, M.T., Bommier, V.: 2007, *Astron. Astrophys.* **475**, 1081. doi:10.1051/0004-6361:20077500.
Li, Y., Song, G., Li, J.: 2009, *Solar Phys.* **260**, 109. doi:10.1007/s11207-009-9431-9.
Li, Z., Yan, Y., Song, G.: 2004, *Mon. Not. Roy. Astron. Soc.* **347**, 1255. doi:10.1111/j.1365-2966.2004.07309.x.
Lin, Y.: 1990, *Comput. Phys. Commun.* **59**, 139. doi:10.1016/0010-4655(90)90163-U.
Lin, Y.Z., Wang, Z.Z., Wu, F., Ding, Y.J., Hong, Q.F.: 1985, *Acta Astrophys. Sin.* **5**, 19.
Linke, J., Ioshpa, B.A., Selivanov, V.L.: 1990, *Astron. Nachr.* **311**, 309.
Liu, C., Lee, J., Jing, J., Liu, R., Deng, N., Wang, H.: 2010, *Astrophys. J. Lett.* **721**, L193. doi:10.1088/2041-8205/721/2/L193.
Liu, S., Zhang, H.Q., Su, J.T., Song, M.T.: 2011, *Solar Phys.* **269**, 41. doi:10.1007/s11207-010-9691-4.
Longcope, D.W.: 2005, *Living Rev. Solar Phys.* **2**(7). doi:10.12942/lrsp-2005-7. http://solarphysics.livingreviews.org/Articles/lrsp-2005-7/.
Longcope, D.W., Des Jardins, A.C., Carranza-Fulmer, T., Qiu, J.: 2010, *Solar Phys.* **267**, 107. doi:10.1007/s11207-010-9635-z.
Longcope, D.W., Klapper, I.: 2002, *Astrophys. J.* **579**, 468. doi:10.1086/342750.
Longcope, D.W., Malanushenko, A.: 2008, *Astrophys. J.* **674**, 1130. doi:10.1086/524011.
Ma, E., Ai, G.X.: 1979, *Acta Astron. Sin.* **20**, 374.
Mackay, D., Yeates, A.: 2012, *Living Rev. Solar Phys.* **6**(9). doi:10.12942/lrsp-2012-6. http://solarphysics.livingreviews.org/Articles/lrsp-2012-6/.
Maclean, R.C., Beveridge, C., Priest, E.R.: 2006, *Solar Phys.* **238**, 13. doi:10.1007/s11207-006-0179-1.
Maclean, R.C., Beveridge, C., Hornig, G., Priest, E.R.: 2006, *Solar Phys.* **237**, 227. doi:10.1007/s11207-006-9002-2.
Malanushenko, A., Schrijver, C.J., DeRosa, M.L., Wheatland, M.S., Gilchrist, S.A.: 2012, *Astrophys. J.* **756**, 153. doi:10.1088/0004-637X/756/2/153.
Malanushenko, A., Longcope, D.W., McKenzie, D.E.: 2009, *Astrophys. J.* **707**, 1044. doi:10.1088/0004-637X/707/2/1044.
Mandrini, C.H., Demoulin, P., Rovira, M.G., de La Beaujardiere, J.F., Henoux, J.C.: 1995, *Astron. Astrophys.* **303**, 927.
Mandrini, C.H., Démoulin, P., van Driel-Gesztelyi, L., Schmieder, B., Cauzzi, G., Hofmann, A.: 1996, *Solar Phys.* **168**, 115. doi:10.1007/BF00145829.
Martínez-Oliveros, J.C., Moradi, H., Donea, A.C.: 2008, *Solar Phys.* **251**, 613. doi:10.1007/s11207-008-9122-y.
Masson, S., Pariat, E., Aulanier, G., Schrijver, C.J.: 2009, *Astrophys. J.* **700**, 559. doi:10.1088/0004-637X/700/1/559.
McClymont, A.N., Mikic, Z.: 1994, *Astrophys. J.* **422**, 899. doi:10.1086/173781.
Metcalf, T.R., De Rosa, M.L., Schrijver, C.J., Barnes, G., van Ballegooijen, A.A., Wiegelmann, T., Wheatland, M.S., Valori, G., McTtiernan, J.M.: 2008, *Solar Phys.* **247**, 269. doi:10.1007/s11207-007-9110-7.
Meyer, K.A., Mackay, D.H., van Ballegooijen, A.A.: 2012, *Solar Phys.* **278**, 149. doi:10.1007/s11207-011-9924-1.
Meyer, K.A., Mackay, D.H., van Ballegooijen, A.A., Parnell, C.E.: 2011, *Solar Phys.* **272**, 29. doi:10.1007/s11207-011-9809-3.
Mikic, Z., Barnes, D.C., Schnack, D.D.: 1988, *Astrophys. J.* **328**, 830. doi:10.1086/166341.
Molodensky, M.M.: 1974, *Solar Phys.* **39**, 393. doi:10.1007/BF00162432.
Moon, Y.J., Chae, J., Choe, G.S., Wang, H., Park, Y.D., Cheng, C.Z.: 2004, *J. Korean Astron. Soc.* **37**, 41.

Mysh'yakov, I.I., Rudenko, G.V.: 2009, *Geomagn. Aeron.* **49**, 940. doi:10.1134/S0016793209070184.
Nakagawa, Y., Raadu, M.A.: 1972, *Solar Phys.* **25**, 127. doi:10.1007/BF00155751.
Nakagawa, Y., Raadu, M.A., Harvey, J.W.: 1973, *Solar Phys.* **30**, 421. doi:10.1007/BF00152673.
Nakagawa, Y., Wu, S.T., Tandberg-Hanssen, E.: 1978, *Astron. Astrophys.* **69**, 43.
Nitta, N.V., De Rosa, M.L.: 2008, *Astrophys. J. Lett.* **673**, L207. doi:10.1086/527548.
Paesold, G., Benz, A.O., Klein, K.L., Vilmer, N.: 2001, *Astron. Astrophys.* **371**, 333. doi:10.1051/0004-6361:20010358.
Paletou, F., López Ariste, A., Bommier, V., Semel, M.: 2001, *Astron. Astrophys.* **375**, 39. doi:10.1051/0004-6361:20010927.
Pallavicini, R., Sakurai, T., Vaiana, G.S.: 1981, *Astron. Astrophys.* **98**, 316.
Pariat, E., Aulanier, G., Schmieder, B., Georgoulis, M.K., Rust, D.M., Bernasconi, P.N.: 2004, *Astrophys. J.* **614**, 1099. doi:10.1086/423891.
Park, S.H., Chae, J., Jing, J., Tan, C., Wang, H.: 2010, *Astrophys. J.* **720**, 1102. doi:10.1088/0004-637X/720/2/1102.
Priest, E.R., Longcope, D.W., Heyvaerts, J.: 2005, *Astrophys. J.* **624**, 1057. doi:10.1086/429312.
Prior, C., Berger, M.A.: 2012, *Solar Phys.* **278**, 323. doi:10.1007/s11207-012-9938-3.
Régnier, S.: 2012, *Solar Phys.* **277**, 131. doi:10.1007/s11207-011-9830-6.
Régnier, S., Amari, T.: 2004, *Astron. Astrophys.* **425**, 345. doi:10.1051/0004-6361:20034383.
Régnier, S., Canfield, R.C.: 2006, *Astron. Astrophys.* **451**, 319. doi:10.1051/0004-6361:20054171.
Régnier, S., Priest, E.R.: 2007a, *Astron. Astrophys.* **468**, 701. doi:10.1051/0004-6361:20077318.
Régnier, S., Priest, E.R.: 2007b, *Astrophys. J.* **669**, 53. doi:10.1086/523269.
Régnier, S., Amari, T., Canfield, R.C.: 2005, *Astron. Astrophys.* **442**, 345. doi:10.1051/0004-6361:20053509
Régnier, S., Amari, T., Kersalé, E.: 2002, *Astron. Astrophys.* **392**, 1119. doi:10.1051/0004-6361:20020993.
Régnier, S., Parnell, C.E., Haynes, A.L.: 2008, *Astron. Astrophys.* **484**, 47. doi:10.1051/0004-6361:200809826.
Régnier, S., Priest, E.R., Hood, A.W.: 2008, *Astron. Astrophys.* **491**, 297. doi:10.1051/0004-6361:200810362.
Roumeliotis, G.: 1996, *Astrophys. J.* **473**, 1095. doi:10.1086/178219.
Rudenko, G.V.: 2001, *Solar Phys.* **198**, 5. doi:10.1023/A:1005270431628.
Rudenko, G.V., Myshyakov, I.I.: 2009, *Solar Phys.* **257**, 287. doi:10.1007/s11207-009-9389-7.
Rust, D.M., Nakagawa, Y., Neupert, W.M.: 1975, *Solar Phys.* **41**, 397. doi:10.1007/BF00154077.
Ryabov, B.I., Maksimov, V.P., Lesovoi, S.V., Shibasaki, K., Nindos, A., Pevtsov, A.: 2005, *Solar Phys.* **226**, 223. doi:10.1007/s11207-005-2691-0.
Sakurai, T.: 1981, *Solar Phys.* **69**, 343. doi:10.1007/BF00149999.
Sakurai, T.: 1985, *Solar Phys.* **95**, 311. doi:10.1007/BF00152408.
Sandman, A.W., Aschwanden, M.J., Derosa, M.L., Wülser, J.P., Alexander, D.: 2009, *Solar Phys.* **259**, 1. doi:10.1007/s11207-009-9383-0.
Savcheva, A.S., van Ballegooijen, A.A., DeLuca, E.E.: 2012, *Astrophys. J.* **744**, 78. doi:10.1088/0004-637X/744/1/78.
Savcheva, A., Pariat, E., van Ballegooijen, A., Aulanier, G., DeLuca, E.: 2012, *Astrophys. J.* **750**, 15. doi:10.1088/0004-637X/750/1/15.
Schatten, K.H., Wilcox, J.M., Ness, N.F.: 1969, *Solar Phys.* **6**, 442. doi:10.1007/BF00146478.
Schmahl, E.J., Kundu, M.R., Strong, K.T., Bentley, R.D., Smith, J.B. Jr., Krall, K.R.: 1982, *Solar Phys.* **80**, 233. doi:10.1007/BF00147971.
Schmidt, H.U.: 1964, In: Hess, W.N. (ed.) *The Physics of Solar Flares*, *NASA SP-50*, 107.
Schnack, D.D., Mikić, Z., Barnes, D.C., van Hoven, G.: 1990, *Comput. Phys. Commun.* **59**, 21. doi:10.1016/0010-4655(90)90153-R.
Schrijver, C.J., Title, A.M.: 2002, *Solar Phys.* **207**, 223. doi:10.123/A:1016295516408.
Schrijver, C.J., De Rosa, M.L., Metcalf, T.R., Liu, Y., McTiernan, J., Régnier, S., Valori, G., Wheatland, M.S., Wiegelmann, T.: 2006, *Solar Phys.* **235**, 161. doi:10.1007/s11207-006-0068-7.
Schrijver, C.J., De Rosa, M.L., Metcalf, T., Barnes, G., Lites, B., Tarbell, T., McTiernan, J., Valori, G., Wiegelmann, T., Wheatland, M.S., Amari, T., Aulanier, G., Démoulin, P., Fuhrmann, M., Kusano, K., Régnier, S., Thalmann, J.K.: 2008, *Astrophys. J.* **675**, 1637. doi:10.1086/527413.
Seehafer, N.: 1975, *Astron. Nachr.* **296**, 177.
Seehafer, N.: 1982, *Solar Phys.* **81**, 69. doi:10.1007/BF00151981.
Seehafer, N.: 1985, *Solar Phys.* **96**, 307. doi:10.1007/BF00149686.
Seehafer, N., Staude, J.: 1979, *Astron. Nachr.* **300**, 151.
Semel, M.: 1988, *Astron. Astrophys.* **198**, 293.
Shen, Y., Liu, Y., Su, J.: 2012, *Astrophys. J.* **750**, 12. doi:10.1088/0004-637X/750/1/12.
Song, M.T., Fang, C., Tang, Y.H., Wu, S.T., Zhang, Y.A.: 2006, *Astrophys. J.* **649**, 1084. doi:10.1086/506249.
Song, M.T., Fang, C., Zhang, H.Q., Tang, Y.H., Wu, S.T., Zhang, Y.A.: 2007, *Astrophys. J.* **666**, 491. doi:10.1086/519829.

Sturrock, P.A.: 1991, *Astrophys. J.* **380**, 655. doi:10.1086/170620.
Su, Q.R.: 1980, *Acta Astron. Sin.* **21**, 152.
Su, Q.R.: 1982, *Solar Phys.* **75**, 229. doi:10.1007/BF00153473.
Su, Y., van Ballegooijen, A., Schmieder, B., Berlicki, A., Guo, Y., Golub, L., Huang, G.: 2009a, *Astrophys. J.* **704**, 341. doi:10.1088/0004-637X/704/1/341.
Su, Y., van Ballegooijen, A., Lites, B.W., Deluca, E.E., Golub, L., Grigis, P.C., Huang, G., Ji, H.: 2009b, *Astrophys. J.* **691**, 105. doi:10.1088/0004-637X/691/1/105.
Sun, X., Hoeksema, J.T., Liu, Y., Wiegelmann, T., Hayashi, K., Chen, Q., Thalmann, J.: 2012, *Astrophys. J.* **748**, 77. doi:10.1088/0004-637X/748/2/77.
Syntelis, P., Gontikakis, C., Georgoulis, M.K., Alissandrakis, C.E., Tsinganos, K.: 2012, *Solar Phys.* **280**, 475. doi:10.1007/s11207-012-0026-5.
Tadesse, T., Wiegelmann, T., Inhester, B.: 2009, *Astron. Astrophys.* **508**, 421. doi:10.1051/0004-6361/200912529.
Tadesse, T., Wiegelmann, T., Inhester, B., Pevtsov, A.: 2012, *Solar Phys.* **281**, 53. doi:10.1007/s11207-012-9961-4.
Takakura, T., Tsuneta, S., Nitta, N., Ohki, K.: 1983, *Solar Phys.* **86**, 323. doi:10.1007/BF00157205.
Tanaka, K.: 1978, *Solar Phys.* **58**, 149. doi:10.1007/BF00152561.
Tanaka, K., Nakagawa, Y.: 1973, *Solar Phys.* **33**, 187. doi:10.1007/BF00152390.
Taylor, J.B.: 1974, *Phys. Rev. Lett.* **33**, 1139. doi:10.1103/PhysRevLett.33.1139.
Thalmann, J.K., Wiegelmann, T.: 2008, *Astron. Astrophys.* **484**, 495. doi:10.1051/0004-6361:200809508.
Thalmann, J.K., Wiegelmann, T., Raouafi, N.E.: 2008, *Astron. Astrophys.* **488**, 71. doi:10.1051/0004-6361:200810235.
Titov, V.S.: 2007, *Astrophys. J.* **660**, 863 doi:10.1086/512671.
Titov, V.S., Priest, E.R., Demoulin, P.: 1993, *Astron. Astrophys.* **276**, 564.
Tun, S.D., Gary, D.E., Georgoulis, M.K.: 2011, *Astrophys. J.* **728**, 1. doi:10.1088/0004-637X/728/1/1.
Valori, G., Kliem, B., Fuhrmann, M.: 2007, *Solar Phys.* **245**, 263. doi:10.1007/s11207-007-9046-y.
Valori, G., Kliem, B., Keppens, R.: 2005, *Astron. Astrophys.* **433**, 335. doi:10.1051/0004-6361:20042008.
Valori, G., Kliem, B., Török, T., Titov, V.S.: 2010, *Astron. Astrophys.* **519**, 44. doi:10.1051/0004-6361/201014416.
van Ballegooijen, A.A.: 2004, *Astrophys. J.* **612**, 519. doi:10.1086/422512.
van Ballegooijen, A.A., Deluca, E.E., Squires, K., Mackay, D.H.: 2007, *J. Atmos. Solar-Terr. Phys.* **69**, 24. doi:10.1016/j.jastp.2006.06.007.
Vincent, A., Charbonneau, P., Dubé, C.: 2012, *Solar Phys.* **278**, 367. doi:10.1007/s11207-012-9953-4.
Wang, D., Wei, F., Yan, Y.: 1995, *Acta Astrophys. Sin.* **15**, 359.
Wang, H., Jing, J., Tan, C., Wiegelmann, T., Kubo, M.: 2008, *Astrophys. J.* **687**, 658. doi:10.1086/592082.
Wang, R., Tan, B., Tan, C., Yan, Y.: 2012, *Solar Phys.* **278**, 411. doi:10.1007/s11207-012-9937-4.
Wang, T., Yan, Y., Wang, J., Kurokawa, H., Shibata, K.: 2002, *Astrophys. J.* **572**, 580. doi:10.1086/340189.
Wang, Y.M.: 2000, *Astrophys. J. Lett.* **543**, L89. doi:10.1086/318178.
Wen, Y.Y., Wang, J.X., Zhang, Y.Z.: 2007, *Chin. J. Astron. Astrophys.* **7**, 265. doi:10.1088/1009-9271/7/2/11.
Wheatland, M.S.: 2004, *Solar Phys.* **222**, 247. doi:10.1023/B:SOLA.0000043579.93988.6f.
Wheatland, M.S.: 2006, *Solar Phys.* **238**, 29. doi:10.1007/s11207-006-0232-0.
Wheatland, M.S., Leka, K.D.: 2011, *Astrophys. J.* **728**, 112. doi:10.1088/0004-637X/728/2/112.
Wheatland, M.S., Régnier, S.: 2009, *Astrophys. J. Lett.* **700**, L88. doi:10.1088/0004-637X/700/2/L88.
Wheatland, M.S., Sturrock, P.A., Roumeliotis, G.: 2000, *Astrophys. J.* **540**, 1150. doi:10.1086/309355.
Wiegelmann, T.: 2004, *Solar Phys.* **219**, 87. doi:10.1023/B:SOLA.0000021799.39465.36.
Wiegelmann, T., Inhester, B.: 2010, *Astron. Astrophys.* **516**, 107. doi:10.1051/0004-6361/201014391.
Wiegelmann, T., Neukirch, T.: 2002, *Solar Phys.* **208**, 233. doi:10.1023/A:1020537403934.
Wiegelmann, T., Neukirch, T.: 2006, *Astron. Astrophys.* **457**, 1053. doi:10.1051/0004-6361:20065281.
Wiegelmann, T., Sakurai, T.: 2012, *Living Rev. Solar Phys.* **9**(5). doi:10.12942/lrsp-2012-5. http://solarphysics.livingreviews.org/Articles/lrsp-2012-5/.
Wiegelmann, T., Inhester, B., Sakurai, T.: 2006, *Solar Phys.* **233**, 215. doi:10.1007/s11207-006-2092-z.
Wiegelmann, T., Inhester, B., Lagg, A., Solanki, S.K.: 2005, *Solar Phys.* **228**, 67. doi:10.1007/s11207-005-2511-6.
Wiegelmann, T., Neukirch, T., Ruan, P., Inhester, B.: 2007, *Astron. Astrophys.* **475**, 701. doi:10.1051/0004-6361:20078244.
Wiegelmann, T., Thalmann, J.K., Schrijver, C.J., De Rosa, M.L., Metcalf, T.R.: 2008, *Solar Phys.* **247**, 249. doi:10.1007/s11207-008-9130-y.
Wiegelmann, T., Yelles Chaouche, L., Solanki, S.K., Lagg, A.: 2010, *Astron. Astrophys.* **511**, 4. doi:10.1051/0004-6361/200912812.
Winebarger, A.R., Warren, H.P., Falconer, D.A.: 2008, *Astrophys. J.* **676**, 672. doi:10.1086/527291.
Woltjer, L.: 1958, *Proc. Natl. Acad. Sci.* **44**, 489.

Woodard, M.F., Chae, J.: 1999, *Solar Phys.* **184**, 239. doi:10.1023/A:1005088232234.
Wu, F., Wang, Z.Z.: 1984, *Acta Astrophys. Sin.* **4**, 272.
Wu, F., Wang, Z.Z.: 1985, *Chin. J. Astron. Astrophys.* **9**, 44. doi:10.1016/0275-1062(85)90057-8.
Wu, S.T., Sun, M.T., Chang, H.M., Hagyard, M.J., Gary, G.A.: 1990, *Astrophys. J.* **362**, 698. doi:10.1086/169307.
Xu, Y., Jing, J., Cao, W., Wang, H.: 2010, *Astrophys. J. Lett.* **709**, L142. doi:10.1088/2041-8205/709/2/L142.
Yan, Y.: 1995, *Solar Phys.* **159**, 97. doi:10.1007/BF00733034.
Yan, Y., Huang, G.: 2003, *Space Sci. Rev.* **107**, 111. doi:10.1023/A:1025515504413.
Yan, Y., Li, Z.: 2006, *Astrophys. J.* **638**, 1162. doi:10.1086/499064.
Yan, Y., Sakurai, T.: 1997, *Solar Phys.* **174**, 65. doi:10.1023/A:1004943409775.
Yan, Y., Sakurai, T.: 2000, *Solar Phys.* **195**, 89. doi:10.1023/A:1005248128673.
Yan, Y., Wang, J.: 1995, *Astron. Astrophys.* **298**, 277.
Yan, Y., Deng, Y., Karlický, M., Fu, Q., Wang, S., Liu, Y.: 2001a, *Astrophys. J. Lett.* **551**, L115. doi:10.1086/319829.
Yan, Y., Liu, Y., Akioka, M., Wei, F.: 2001b, *Solar Phys.* **201**, 337. doi:10.1023/A:1017934615013.
Yan, Y., Pick, M., Wang, M., Krucker, S., Vourlidas, A.: 2006, *Solar Phys.* **239**, 277. doi:10.1007/s11207-006-0202-6.
Yang, H.S., Zhang, H.M.: 1980, *Acta Astron. Sin.* **21**, 136.
Yang, H.S., Hong, Q.F., Ding, Y.J.: 1988, *Solar Phys.* **117**, 57. doi:10.1007/BF00148572.
Yang, W.H., Sturrock, P.A., Antiochos, S.K.: 1986, *Astrophys. J.* **309**, 383. doi:10.1086/164610.
Yurchyshyn, V.B., Wang, H., Qiu, J., Goode, P.R., Abramenko, V.I.: 2000, *Astrophys. J.* **540**, 1143. doi:10.1086/309359.
Zhang, Y., Wang, J., Attrill, G.D.R., Harra, L.K., Yang, Z., He, X.: 2007, *Solar Phys.* **241**, 329. doi:10.1007/s11207-007-0229-3.
Zirin, H., Tanaka, K.: 1973, *Solar Phys.* **32**, 173. doi:10.1007/BF00152736.
Zuccarello, F., Romano, P., Farnik, F., Karlicky, M., Contarino, L., Battiato, V., Guglielmino, S.L., Comparato, M., Ugarte-Urra, I.: 2009, *Astron. Astrophys.* **493**, 629. doi:10.1051/0004-6361:200809887.

DOI 10.1007/978-1-4939-2038-9_4
Reprinted from *Solar Physics* Journal, DOI 10.1007/s11207-013-0422-5

Three-Dimensional Nonlinear Force-Free Field Reconstruction of Solar Active Region 11158 by Direct Boundary Integral Equation

Rui Wang · Yihua Yan · Baolin Tan

Received: 24 February 2013 / Accepted: 23 September 2013 / Published online: 30 October 2013

Abstract A three-dimensional coronal magnetic field is reconstructed for the NOAA active region 11158 on 14 February 2011. A GPU-accelerated direct boundary integral equation (DBIE) method is implemented which is approximately 1000 times faster than the original DBIE used on solar non-linear force-free field modeling. Using the SDO/HMI vector magnetogram as the bottom boundary condition, the reconstructed magnetic field lines are compared with the projected EUV loop structures as observed in the front-view (SDO/AIA) and the side-view (STEREO-A/B) images for the first time; they show very good agreement three-dimensionally. A quantitative comparison with some stereoscopically reconstructed coronal loops shows that the average misalignment angles in our model are at the same order as the state-of-the-art results obtained from reconstructed coronal loops. It is found that the observed coronal loop structures can be grouped into a number of closed and open field structures with some central bright coronal loop features around the polarity inversion line. The reconstructed highly sheared magnetic field lines agree very well with the low-lying sigmoidal filament along the polarity inversion line. This central low-lying magnetic field loop system must have played a key role in powering the flare. It should be noted that while a strand-like coronal feature along the polarity inversion line may be related to the filament, one cannot simply interpret all the coronal bright features along the polarity inversion line as manifestation of the filament without any stereoscopic information.

Keywords Magnetic fields, corona · Magnetic fields, extrapolation · Solar active regions

Coronal Magnetometry
Guest Editors: S. Tomczyk, J. Zhang, and T.S. Bastian

R. Wang (✉) · Y. Yan · B. Tan
Key Laboratory of Solar Activity, National Astronomical Observatories, Chinese Academy of Sciences, Beijing 100012, China
e-mail: spiderscorpionman@163.com

Y. Yan
e-mail: yyh@nao.cas.cn

B. Tan
e-mail: bltan@nao.cas.cn

1. Introduction

It is well-known that the magnetic field plays a key role in almost all solar activities, such as solar flares, filament eruptions, coronal mass ejections, *etc*. Many structures in the solar corona are shaped by the magnetic field, due to its pervasive nature. Therefore, a thorough knowledge of the coronal magnetic field topology will help us to understand the physical processes taking place in various solar activities. However, so far the routine measurement of solar magnetic field is mainly based on the Zeeman effect, which can produce measurable polarization of sharp and strong absorption lines in the photosphere, but failed to measure the coronal magnetic field for its low polarization, faint intensities, and broad line widths of coronal emission lines. Although some techniques using infrared and radio observations have been proposed to solve this problem, (Lin, Kuhn, and Coulter, 2004; Gary and Hurford, 1994), they have not reached full maturity yet and have many limitations. Normally, one has to obtain the solar coronal magnetic fields from modeling by extrapolation using the observations made on the underlying photosphere.

At present, the non-linear force-free field (NLFFF) model has been thought to be a good approximation to the actual physical state of the coronal magnetic fields. Available NLFFF extrapolation methods can be classified into five types:

i) the upward integration method (Nakagawa, 1974; Wu *et al.*, 1990; Song *et al.*, 2006),
ii) the Grad–Rubin method (Grad and Rubin, 1958; Sakurai, 1981; Amari, Boulmezaoud, and Mikic, 1999; Amari, Boulmezaoud, and Aly, 2006; Wheatland, 2006),
iii) the MHD relaxation method (Chodura and Schlueter, 1981; Yang, Sturrock, and Antiochos, 1986; Mikic and McClymont, 1994; Roumeliotis, 1996; Valori, Kliem, and Keppens, 2005; Valori, Kliem, and Fuhrmann, 2007; Jiang *et al.*, 2011; Jiang and Feng, 2012),
iv) the optimization approach (Wheatland, Sturrock, and Roumeliotis, 2000; Wiegelmann 2004, 2007; Inhester and Wiegelmann, 2006; Wiegelmann and Neukirch, 2006), and
v) the boundary integral equation method (Yan and Sakurai 1997, 2000; Yan and Li, 2006; He and Wang, 2008; He, Wang, and Yan, 2011).

As a stand-alone method, the boundary integral equation (BIE) method is the one that allows us to evaluate the NLFFF field at an arbitrary point within the domain from the boundary data, without the requirement to solve the field in the entire domain. Moreover, because the BIE model takes into account the asymptotic condition at infinity consistently, it allows us to use only the bottom boundary data as the boundary condition. This satisfies the current observational condition and avoids assuming arbitrarily prescribed lateral and top boundary conditions. The BIE method for NLFFF was first proposed by Yan and Sakurai (1997, 2000), and many applications of BIE to solar events have been implemented (*e.g.*, Yan and Sakurai, 1997; Yan *et al.*, 2001; Liu *et al.*, 2002; Yan, 2003). Later a new direct boundary integral equation (DBIE) method was proposed as an improvement to the BIE method. An optimization technique has been applied to approximate the non-linear force-free field at any position numerically. Compared with BIE, the complicated volume integration in Equations (17) and (19) of Yan and Li (2006) was avoided. A series of test cases and practical applications (Yan and Li, 2006; Liu *et al.*, 2011; Liu, Zhang, and Su, 2012; He and Wang, 2008; He, Wang, and Yan, 2011) have been studied to demonstrate the reliability and feasibility of DBIE.

Recently, with the launch of *Solar Dynamic Observatory* (SDO), the *Helioseismic and Magnetic Imager* (HMI; Schou *et al.*, 2012) provides the vector magnetograms which can be used as high quality boundary data for coronal magnetic field reconstruction.

The *Atmospheric Imaging Assembly* (AIA; Lemen *et al.*, 2012) simultaneously provides high resolution coronal images for the evaluation of any modeling technique. Therefore, it is now possible to apply the DBIE method to real data by using high resolution boundary data as validation. The previous BIE method was thought to be slow when carried out on an entire three-dimensional (3-D) domain (Schrijver *et al.*, 2006; Wiegelmann, 2008) as the parallel algorithm was not implemented though the BIE technique itself is suitable for parallel computation. In order to solve this problem, we implemented a graphics processing unit (GPU) technique into our program to accelerate the computing processes. The results show that this method is effective and promising.

The NOAA region 11158 was the first active region that produced an X-class event in the current 24th solar cycle. An X2.2 flare event occurred on 15 February 2011 at 01:44 UT. Many studies have been carried out on this event, such as on the evolution of the magnetic field (Sun *et al.*, 2012), research focusing on solar features (Schrijver *et al.*, 2011), extrapolations using the HMI, vector magnetograms (Wiegelmann *et al.*, 2012), evolution of relative magnetic helicity and current helicity (Jing *et al.*, 2012), non-potentiality of active region (Song *et al.*, 2013), and on the rotating sunspots of this region (Vemareddy, Ambastha, and Maurya, 2012). Although most of these studies have the aid of extrapolation methods, none of them have demonstrated the 3-D view of the reconstructed coronal magnetic fields in this active region. The twin STEREO-A(head) and B(ehind) spacecraft (Kaiser *et al.*, 2008) observe the Sun from multi-directions, which provides us with a good opportunity for a comprehensive comparison so that the physical process in the corona can be understood correctly. It should be mentioned that Su and van Ballegooijen (2012) compared a NLFFF model with bright EUV features on the two sides of a solar polar crown prominence that erupted on 6 December 2010 observed by STEREO-B and AIA; the filament channel was on the backside of the Sun in STEREO-A observations. Derosa *et al.* (2009) compared other NLFFF models with observations including STEREO-A/B data for AR 10953 on 30 April 2007 but no comparison with STEREO images was shown. Sandman and Aschwanden (2011) proposed a forward-fitting method with the stereoscopically reconstructed STEREO loops as known conditions.

In this work, we apply the DBIE method to active region NOAA 11158 observed on 14 February 2011 with the HMI vector magnetogram taken at 20:12 UT as the boundary condition in order to understand the 3-D magnetic configuration before the X2.2 flare event. We will present our reconstructed configuration of magnetic fields in the whole volume of the studied region and electric current distribution in its central region. We then compare them with both front-view (SDO/AIA) and side-view (STEREO-A/B) images.

This paper is arranged as follows. Section 2 briefly introduces the DBIE method and GPU technique. Section 3 shows the observations and Section 4 presents the reconstructed results. Finally in Section 5 we draw our conclusions.

2. Methods

2.1. Principle of DBIE

As an improvement of the BIE method, the DBIE method also needs to satisfy the force-free field and divergence-free conditions (Yan and Li, 2006):

$$\nabla \times \mathbf{B} = \alpha \mathbf{B} \tag{1}$$

$$\nabla \cdot \mathbf{B} = 0 \tag{2}$$

with the boundary condition at $z = 0$ specified by a magnetogram (outside this magnetogram region a vanishing field is assumed):

$$\mathbf{B} = \mathbf{B}_0. \tag{3}$$

At infinity, an asymptotic constraint should be employed to ensure a finite energy content in the semispace above the Sun,

$$\mathbf{B} = O\left(R^{-2}\right) \quad \text{when } R \longrightarrow \infty \tag{4}$$

where R is the radial distance. A reference function Y is introduced in this method

$$Y = \frac{\cos(\lambda\rho)}{4\pi\rho} - \frac{\cos(\lambda\rho')}{4\pi\rho'} \tag{5}$$

where λ is a pseudo-force-free factor depending on the location of point i only, and $\rho = [(x - x_i)^2 + (y - y_i)^2 + (z - z_i)^2]^{1/2}$ is the distance between a variable point (x, y, z) and a fixed point (x_i, y_i, z_i), and $\rho' = [(x - x_i)^2 + (y - y_i)^2 + (z + z_i)^2]^{1/2}$.

Combining the force-free, divergence-free, boundary, and asymptotic conditions, we obtain a direct boundary integral formulation (Yan and Li, 2006):

$$B_p(x_i, y_i, z_i) = \int_\Gamma \frac{z_i[\lambda_{pi} r \sin(\lambda_{pi} r) + \cos(\lambda_{pi} r)]B_{p0}(x, y, 0)}{2\pi[(x - x_i)^2 + (y - y_i)^2 + z_i^2]^{3/2}}\,\mathrm{d}x\,\mathrm{d}y \tag{6}$$

where $r = [(x - x_i)^2 + (y - y_i)^2 + z_i^2]^{1/2}$, $p = x$, y, or z. B_{p0} is the magnetic field on the photospheric surface. In place of λ in Equation (5), we have introduced $\lambda_{pi} = \lambda_p(x_i, y_i, z_i)$ which is in principle determined implicitly by the following equation:

$${\lambda_{pi}}^2 = \frac{\int_\Omega Y(x, y, z; x_i, y_i, z_i, \lambda_{pi})[\alpha^2 B_p + (\nabla\alpha \times \mathbf{B})_p]\,\mathrm{d}x\,\mathrm{d}y\,\mathrm{d}z}{\int_\Omega Y(x, y, z; x_i, y_i, z_i, \lambda_{pi}) B_p\,\mathrm{d}x\,\mathrm{d}y\,\mathrm{d}z}. \tag{7}$$

Here λ (meaning λ_{pi} for short) has the same dimension as the force-free factor α; hence it is called the pseudo-force-free factor. From Equation (6), we can obtain the magnetic field $\mathbf{B}$ if λ is known. Previously a study was done for the BIE method (Li, Yan, and Song, 2004) on the property of λ distribution by substituting Low and Lou's (1990) solution into the rigorous expression similar to Equation (7). It was found that the λ values that satisfy the condition at some given point are not unique. However, this non-uniqueness in the λ solutions does not influence the computation of the field at that location, as demonstrated by numerical results. Obviously, it is not practical to determine λ from such an implicit expression [Equation (7)]. Yan and Li (2006) suggested to make use of the downhill simplex method of nonlinear programming (Nelder and Mead, 1965) to find a suitable value of λ. In this way the value of λ is not obtained from Equation (7) exactly but instead we look for a numerical solution of the magnetic field. This is calculated from the given boundary condition [Equation (3)] together with the assumed asymptotic condition [Equation (4)] and satisfies the original force-free [Equation (1)] and divergence-free [Equation (2)] conditions approximately. Here the two stopping criteria of the procedure for the approximation of Equations (1) and (2) are

$$f_i(\lambda_{xi}, \lambda_{yi}, \lambda_{zi}) = \frac{|\mathbf{J} \times \mathbf{B}|}{|\mathbf{J}||\mathbf{B}|}, \quad \text{with } \mathbf{J} = \nabla \times \mathbf{B} \tag{8}$$

$$g_i(\lambda_{xi}, \lambda_{yi}, \lambda_{zi}) = \frac{|\delta\mathbf{B}_i|}{|\mathbf{B}_i|} = \frac{|\nabla \cdot \mathbf{B}|\Delta V_i}{|\mathbf{B}|\Delta\sigma_i} \tag{9}$$

and

$$f_i\left(\lambda_{xi}^*, \lambda_{yi}^*, \lambda_{zi}^*\right) = \min\left\{f_i(\lambda_{xi}, \lambda_{yi}, \lambda_{zi})\right\} \tag{10}$$

$$g_i\left(\lambda_{xi}^*, \lambda_{yi}^*, \lambda_{zi}^*\right) = \min\left\{g_i(\lambda_{xi}, \lambda_{yi}, \lambda_{zi})\right\}. \tag{11}$$

We set the constraints as follows:

$$f_i\left(\lambda_{xi}^*, \lambda_{yi}^*, \lambda_{zi}^*\right) \leq \epsilon_f, \qquad g_i\left(\lambda_{xi}^*, \lambda_{yi}^*, \lambda_{zi}^*\right) \leq \epsilon_g \tag{12}$$

where ϵ_f and ϵ_g are sufficiently small thresholds. Basically, $f_i(\lambda_{xi}, \lambda_{yi}, \lambda_{zi})$ is the angle between $\mathbf{B}$ and $\mathbf{J}$, which is used to evaluate the force-freeness. Similarly, $g_i(\lambda_{xi}, \lambda_{yi}, \lambda_{zi})$ stands for the divergence of $\mathbf{B}$.

Since we have only given a simple description about the approximation of λ in the previous work (Yan and Li, 2006), one might have misunderstood about our method. Therefore, we will provide a thorough description on our assumptions here. As stated above, in the numerical procedure of Yan and Li (2006), we only need to control the force-freeness and divergence-freeness of the magnetic field through Equations (8) and (9) approaching a minimum. The DBIE numerical procedure is possible if the function f_i can be calculated analytically. In order to evaluate the right-hand side of Equations (8) and (9), we need to know the spatial derivative of $\mathbf{B}$ from Equation (6) and hence of λ. This derivative is approximated by a first order finite difference. We evaluate λ in the δ-neighborhood of the point $r_i = (x_i, y_i, z_i)$, where δ is a very small positive number (typically one thousandth of the pixel size). At an arbitrary point in this small neighborhood it can be expressed as

$$\lambda_p(r) = \lambda_p(r_i) + \lambda_p'(\xi)(r - r_i) \tag{13}$$

which satisfies the Lagrange mean value theorem and $r_i < \xi < r$. Since $|\delta| \ll 1$ and $|r - r_i| \leq \delta$, the zeroth-order approximation is adopted. In our difference domain, we obtain $\lambda_p(r) \approx \lambda_p(r_i)$. Here $\lambda_p(r_i)$ is a value of $\lambda_p(r)$ at the center of the small domain. Then, any value of the function $\lambda_p(r_i)$ in the infinitesimal neighborhood is known. The field $\mathbf{B}$ and the current $\nabla \times \mathbf{B}$ can then be evaluated around the point i. This is a practical and rigorous numerical procedure.

Rudenko and Myshyakov (2009) wrote that they "think that this method for solving the extrapolation problem is incorrect" because they found that Yan and Li (2006) "unreasonably drop these space derivative" of λ functions and "the resulting magnetic field will not be free-force". The comments in Rudenko and Myshyakov (2009) are incorrect as they have confused the DBIE representation of the force-free-field solution and the numerical approximation to the force-free field. It should be pointed out that the derivation of DBIE is mathematically valid and rigorous. The problem is to find how to obtain a numerical solution with the help of DBIE.

As explained above, the strategy is not to solve Equations (6) and (7) exactly but to find a numerical solution that satisfies Equation (12) and the boundary and asymptotic conditions [Equations (3) and (4)]. Alternatively the original force-free and divergence-free equations [Equations (1) and (2)] together with boundary and asymptotic conditions [Equations (3) and (4)] are solved approximately. Therefore if one can construct numerically the magnetic field distribution pointwise at any position that satisfies Equation (12) with the boundary and asymptotic conditions [Equations (3) and (4)], one has already obtained a set of numerical solutions that are force-free and divergence-free with the given boundary conditions approximately. In the present work, our calculated results will further demonstrate the feasibility and validity of DBIE.

At the same time, the current density can be obtained pointwise:

$$\mathbf{J} = \nabla \times \mathbf{B} \tag{14}$$

As one of the advantages of DBIE, it is a pointwise method, which can calculate the magnetic field and current density at any point above the photospheric boundary from the proce-

dure. However, it should be noted that a vector magnetogram with all three field components is more than what a force-free field is to be uniquely determined. The present DBIE employs the vector field in the reconstruction. Therefore the boundary data should satisfy compatibility relations in order to be consistent with a force-free corona. The inconsistency and errors contained in the vector magnetogram data will cause errors in the reconstructed field. The ignorance of the boundary field $\mathbf{B}_0$ outside of the magnetogram area would also have influence on the reconstructed field. In practice, the truncation of the magnetogram data should be chosen to approach zero as $\mathbf{B}_0$ vanishes outside of the magnetogram area. Nevertheless, the net flux of $\mathbf{B}_0$ in Equation (3) over the boundary area of the magnetogram does not need to be zero as shown in the derivation of the BIE (Yan and Sakurai, 2000) or DBIE (Yan and Li, 2006).

2.2. GPU Technique

With more and more advanced telescopes launched into space, higher quality images have become available. On one hand, high resolution images provide more clarity to the detail of the Sun and this will help us to study the nature of the Sun in more detail. On the other hand, the vector magnetogram used as the boundary condition in the NLFFF modeling is getting larger which will vastly increase the amount of computation in numerical solutions. For the BIE method, it is necessary to solve the computing speed problem and apply it to real data by using high resolution boundary data. The BIE or DBIE methods are in principle suitable for high-performance parallel computing. However, in the previous work, the implementation of BIE with parallel computing on high-performance computers was not carried out. Therefore BIE would be slow when extrapolating NLFFF from boundary data with computing grids compatible with current observations. DBIE is expected to make an improvement in this respect (Schrijver *et al.*, 2006; Wiegelmann, 2008). Hence we will adopt a suitable parallel computing technique for DBIE.

In recent years, the graphic processing technique has become prevalent in general purpose calculations. We utilized graphics processing units (GPUs) in our computation. The results have turned out to be effective and promising. We can replace a CPU cluster consisting of tens of CPUs with just one GPU board installed in a personal computer. This convenience profoundly promotes the application of the DBIE method.

A GPU is composed of high-performance multi-core processors capable of very high computation speed and data throughput (Zhang *et al.*, 2009). GPU's powerful parallel computing ability to process the integration operation can be applied to the DBIE method. Parallel computation of the DBIE-NLFFF extrapolation algorithm is performed through a GPU with shared memory accessing optimization under a Linux system and a Compute Unified Device Architecture (CUDA) compiler. The calculation is operated through an Intel CPU (3.40 GHz) and NVIDIA Geforce GTX 480 graphics device with NVIDIA CUDA 4.2 on a personal computer.

The platform employed in this work is a 4 core CPU and one GPU machine. The main part of the program is the integral operation in Equation (6). The iteration part is executed mostly in the CPU cores and the data are transferred between CPU and GPU. In order to reduce the latency and improve the occupancy of the procedure, we need to reduce the data exchange in the global memory between CPU and GPU, and make reasonable allocations of multiple *threads* and *blocks*. The number of threads and blocks is not fixed and there are some allocation rules which may improve the speed. The number of thread is a multiple of 32, which can improve the memory coalescing of the procedure. For different sizes of data, the number of threads is different; the larger the better, since it can improve the occupancy.

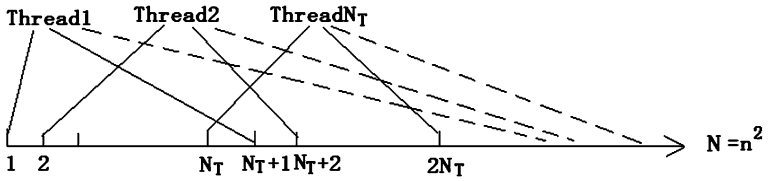

Figure 1 The stretch of the allocation of the GPU. The data size is $N = n \times n$ (n is the number of boundary grids). N_T indicates the number of GPU threads. The lines represent the parts of assignment that are put into the corresponding GPU threads.

We can adjust the number of threads between 128 and 256, and then change the number of blocks gradually. Meanwhile, we should make sure the number of blocks is larger than the number of processors, which can guarantee that no processor is left empty. In our work, the numbers of threads and blocks are 128 and 80, respectively, which provide good allocation in our procedure. In addition, we utilize the shared memory for optimizing our program to improve the computational speed. This can reduce the volume of the data transmission from GPU to CPU.

According to Equation (6), in the numerical procedure the magnetic field of an arbitrary point i in the semispace above the boundary can be expressed as follows (Yan and Sakurai, 2000):

$$\mathbf{B}_i = \sum_{e=1}^{N_e} \sum_{j=1}^{9} \left[\int_{-1}^{+1} \int_{-1}^{+1} Y N_k(\xi, \eta) J(\xi, \eta) \, \mathrm{d}\xi \, \mathrm{d}\eta \right] \mathbf{B}_j^e \tag{15}$$

where the boundary has been subdivided into N_e pieces of 9-node elements with boundary data known over each node, $N_k(\xi, \eta)$ is the shape function, $J(\xi, \eta)$ denotes the Jacobian, and $\mathbf{B}_j^e$ indicates known nodal field values as provided by the boundary condition similar to B_{p0} in Equation (6).

For clarity, we simplify this equation as Equation (16), where $N = n \times n$ is the number of grid nodes on the boundary. We allocate our GPU assignment like Figure 1, where the number of threads is expressed by N_T, and the boundary grids are marked $1, 2, \ldots, N_T, N_{T+1}, N_{T+2}, \ldots, 2N_T, \ldots, N$. The boundary data are put into each thread, and the threads are put into blocks, and our data parallelization is realized. Then we carry out the summation of the data in each thread, then add the summation results in each block.

$$\mathbf{B}_i = \sum_{k=1}^{N} a_{ik} \mathbf{B}_k. \tag{16}$$

A series of numerical tests indicate that the GPU-accelerated DBIE program is almost 1000 times faster than the original DBIE, which includes the hardware update, difference in the compiler, instruction optimization, and GPU's effect. The total computation cost can be expressed as $O(n^2 m^3)$ (Yan and Li, 2006), which has to be multiplied by the number of iterations to minimize f_i and g_i in Equation (12), where $n \times n$ is the number of boundary nodes and $m \times m \times m$ expresses the cubic grids. As Figure 1 shows us that point i in the semispace above the boundary requires the integral operation to the $n \times n$ boundary grids B_{p0} [Equation (6)]. We only apply the GPU acceleration into making this n^2 part parallelized. However, the parallelization of the internal grids (or m^3 part), namely the number of points r_i, is not involved yet. Therefore, further acceleration is possible by combining CUDA with other parallel computing techniques such as Message Passing Interface (MPI) to realize multi-GPU parallelization.

Table 1 Evaluation of metrics for the present DBIE and other methods.

Only lower boundary provided, entire volume[a]	$C_{\rm vec}$	$C_{\rm cs}$	$E_{\rm n}$	$E_{\rm m}$	ϵ
Exact solution (Low and Lou, 1990)	1	1	1	1	1
Weighted optimization method (Wiegelmann)[b]	1.00	0.57	0.86	−0.25	1.04
Optimization method (McTiernan)[b]	1.00	0.51	0.84	−0.38	1.04
Magnetofrictional method (Valori)[b]	0.99	0.55	0.75	−0.15	1.02
Grad–Rubin-like method (Wheatland)[b]	0.99	0.58	0.69	0.13	0.96
Grad–Rubin-like method (Régnier)[b]	0.94	0.28	0.49	−1.7	0.74
Boundary integral method (no iteration)[b]	0.97	0.41	−0.02	−14	1.00
Upward-layered DBIE method (He)[c]	0.97	0.65	0.077	12.4	1.06
Present DBIE method	0.99	0.52	0.83	−0.53	1.08

[a]The parameters are the same as in Case II in Schrijver *et al.* (2006) with Low and Lou's (1990) solution: $n = 3, m = 1, l = 0.3$, $\Phi = 4\pi/5$ on a 192×192 pixel grid centered at the $64 \times 64 \times 64$-pixel test region.

[b]Data from Table I of Schrijver *et al.* (2006).

[c]Data from Table 4 of He and Wang (2008).

Before we apply the present DBIE method to analyze the practical problems, we first compare it with a semi-analytical solution for NLFFF. In this case no iteration was performed to determine the set of λ factors by the BIE method in the comparison against the analytical force-free-field models of Low and Lou (1990). It was expected that DBIE will greatly reduce the computation time and iterative determination of λ becomes feasible (Schrijver *et al.*, 2006). Here we just adopt the Case II of Schrijver *et al.* (2006), *i.e.*, only the bottom boundary data are used because this type of boundary condition is close to the case of the Sun. The boundary size and the five evaluation metrics; vector correlation $C_{\rm vec}$, Cauchy–Schwarz $C_{\rm cs}$, normalized vector error $E_{\rm n}$, mean vector error $E_{\rm m}$, and the quality of fit ϵ, are the same as in Schrijver *et al.* (2006). The results and the comparison with other methods are shown in Table 1. It can be seen that after iteration by the present DBIE method, the metrics have been significantly improved as compared with the boundary integral method without iteration and are comparable to the best results from other methods.

3. Observations

NOAA 11158 was the first active region that produced an X-class event in the current 24th solar cycle. Many C-class and M-class flares were observed in this active region during its passage over the solar disk in February 2011. The largest, the X2.2 flare event occurred on 15 February at 01:44 UT. Several studies have been carried out on NOAA 11158 (Schrijver *et al.*, 2011; Sun *et al.*, 2012; Wiegelmann *et al.*, 2012). The proposed GPU-accelerated DBIE is applied to reconstruct the coronal magnetic field from the vector magnetogram taken on 14 February 2011 at 20:12 UT from SDO/HMI. This is combined with observations from the SDO/AIA and two STEREO/*Extreme Ultraviolet Imager* (EUVI) instruments (Howard *et al.*, 2008; Wülser *et al.*, 2004) to pursue a stereoscopic investigation of the coronal magnetic fields in order to understand the X2.2 flare event. We average the boundary data from 360 km pix^{-1} (0.5″) to 720 km pix^{-1} (about 1″), leading to 300×300 grid points to be used as the boundary condition. In order to compare with the previous work, we also

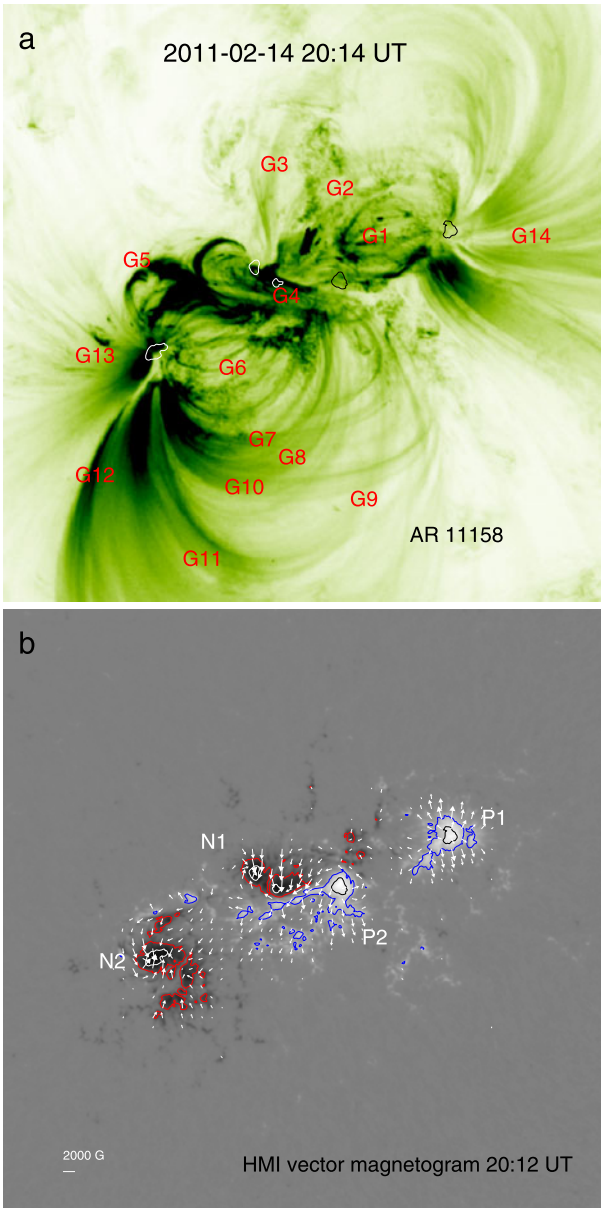

Figure 2 (a) EUV image in 171 Å of NOAA AR 11158 from SDO/AIA on 14 February 2011 at 20:14 UT. The EUV loops are divided into 14 groups and marked from G1 to G14. The field of view is about $300'' \times 300''$. (b) Vector magnetogram from SDO/HMI at 20:12 UT. The horizontal fields are presented by using arrows with a length scale of 2000 gauss (G) shown by the white bar. The vertical fields are plotted with contour levels at ± 1000 and ± 2000 G. (P1, N1), and (P2, N2) represent two pairs of opposite polarities. Red indicates negative polarity and blue is positive.

pay attention to the central 250×200-pixel area covering the main features of the active region, with the vertical grid spacing matching the horizontal spacing.

Here, we used the HMI vector magnetogram as the boundary data with three components of the magnetic field shown in Figure 2(b), and the two main bi-polar pairs are marked as (P1, N1) and (P2, N2) there. The cutout data used for the force-free field modeling has been mapped to local Cartesian coordinates.

Considering that the success of our method largely depends on the quality of boundary data, we must recognize that solar magnetic field measurements suffer from several uncer-

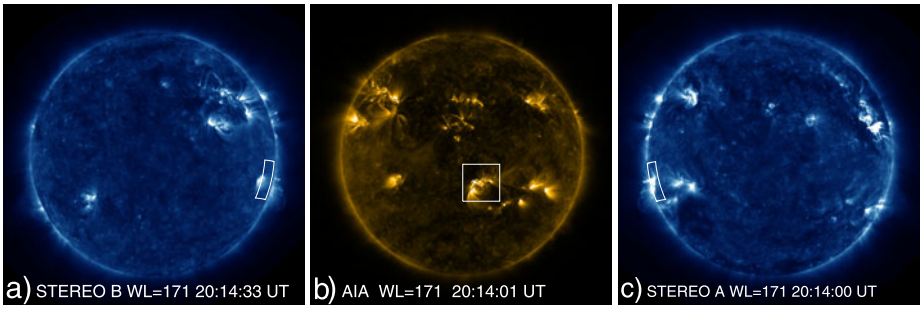

Figure 3 Full-disk maps from (a) STEREO-B, (b) AIA, and (c) STEREO-A in 171 Å. The region of interest for extrapolation is marked by a white square in (b), and the corresponding domain is marked in (a) and (c).

tainties (McClymont, Jiao, and Mikic, 1997). Wang, Yan, and Sakuari (2001) proposed a method to remove the 180° azimuth ambiguity and to make the boundary data for the BIE method. Here we apply this data reduction method to the boundary data in the present study.

After reconstructing the coronal magnetic field using the GPU-accelerated DBIE method, we compare the modeling results with the EUV images of AIA and STEREO/EUVI from three view directions in order to quantify to what extent they correctly reproduce the coronal magnetic field configuration. To co-align the cutout vector magnetogram with AIA images we carried out a correlation analysis between B_z from the original vector magnetogram and line-of-sight (LOS) from the full-disk LOS magnetogram. Then the location of the rectangular region of interest (ROI, shown as the white squares in Figure 3) is determined in the full-disk SDO/HMI magnetogram. According to the SDO data analysis guide, we align HMI data with AIA data and obtain the cutout AIA image (Figure 2(a)) and the location of our ROI. In order to determine the location of the ROI in STEREO images, the transformations between Stonyhurst heliographic and heliocentric Cartesian coordinates are applied (Thompson, 2006). Thus the reconstructed field lines viewed from three different directions are shown aligned with the EUV background accurately.

Before we compare our reconstruction results with the observed EUV loops, we need to determine the corresponding features in an AIA image and two STEREO/EUVI images. For a coronal loop in the STEREO-A image shown as the light blue line at the bottom of Figure 4(c), we apply a Gaussian fitting to the cross sectional intensity profile of the loop and find the brightest point along this cross section. Then we select a number of cross sections along this loop and connected these points together. Thus, we get the *skeleton* of the loop. If we assume the z-coordinates (along the line-of-sight of STEREO-A) of the selected points along the skeleton line, these points can be mapped onto the image of STEREO-B in Figure 4(a) as short black bars through the coordinate transformation (Thompson, 2006). Here the assumed range of the z-coordinates had been iteratively adjusted until the mapped points fall onto the corresponding loop structure in Figure 4(a). By using the same method, we get the skeleton line of the loop in the image of STEREO-B. We then map the points along the skeleton lines in STEREO-A and B images to the AIA image in Figure 4(b) as crosses. We thus obtained the stereoscopically reconstructed coronal loop. We have applied this method to several loop structures which were at higher altitudes and could be seen from both STEREO-A/B EUVI instruments. Therefore, the comparisons below will take into account these obvious higher altitude structures.

We present some selected EUV bright loop structures in 171 Å, and divide the EUV features into groups marked from G1 to G14 (Figure 2(a)). G1, G2, and G3 are three groups

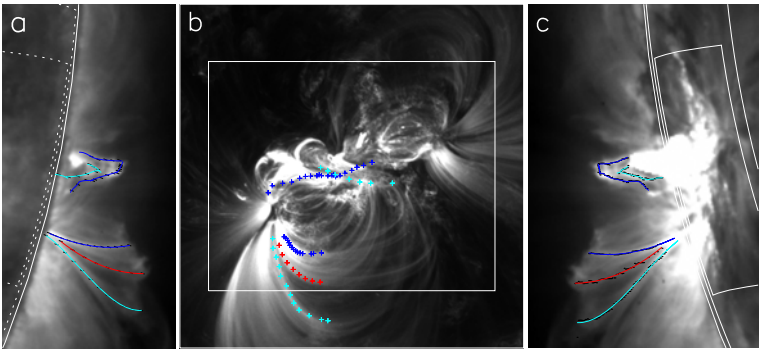

Figure 4 Stereoscopically reconstructed coronal loops from three different view directions representing the loop features in the southern part (blue, red, and light blue crosses) and the middle part (blue and light blue crosses) of the AIA image (b). The corresponding loop features are denoted by the same color lines in the STEREO-B (a) and A (c) images.

corresponding to the EUV loops in the northern part of the ROI and connect the magnetic polarities P1 and N1. When we determine the EUV structures rooted at the edge of the solar disk and stretching vertically out of the disk in the side views, we often find after 3-D reconstruction that they are out of the ROI. For example, loops G1 could not be seen from the side views and they must be at a lower altitude. G4 is the kernel region where loops stretched along the polarity inversion line (PIL) are observed and the flare event occurred. Therefore, we present not only the reconstructed magnetic field lines but also the electric current lines. G5 and G6 are lower small loops which can be only distinguished in the front view (on the solar disk). G7, G8, and G9 are large loops connecting N2 and P2. G10 and G11 are also large loops connecting N2 and P1. These bundles of loops could be seen from three different view directions. G12, G13, and G14 are open loops extending beyond the ROI and rooted at N2 and P1, respectively.

4. Reconstructed Field Lines

The extrapolation code is based on the GPU-accelerated DBIE method. Alignments between the extrapolated field lines and EUV images in 171 Å from SDO/AIA and twin STEREO/EUVI instruments are shown in Figure 5. We ran the DBIE code to reconstruct the 3-D magnetic field structures of the region NOAA 11158 in the corona. The red lines in Figure 5(e) show the calculated closed magnetic field lines. Blue lines present the calculated open magnetic field lines which extend beyond our ROI. Figures 5(d) and (f) show the reconstructed field structures from the view directions of STEREO-B and A, respectively.

Figure 6 presents a comparison between EUV loop groups G1, G2, G3 and our reconstructed magnetic field lines L1, L2, L3. The first row of Figure 6 shows the EUV loop structures in 171 Å. G1 consists of a series of small lower loop structures which are not seen from STEREO-B, and shows really good agreement with our reconstructed field lines L1 in the front view on the solar disk. This bundle of loops connects P1 to the relatively weaker negative magnetic polarities between P1 and N1. G2 is the same as G1 and can also be seen from STEREO-A. It is worth mentioning that the eastern (toward left) footpoints of calculated field lines L2 show a helical structure and this agrees well with the EUV structure G2 around the negative polarity N1. According to the method formulated in Section 3, the

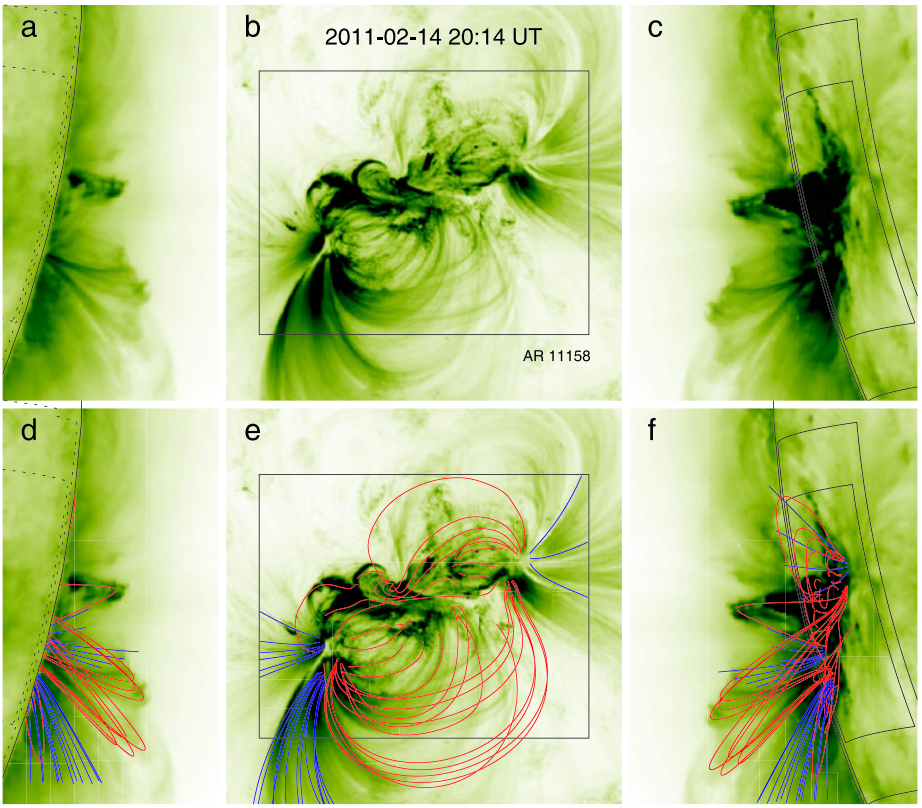

Figure 5 Comparison between EUV images and reconstructed field lines. The first row presents the EUV images in 171 Å from STEREO-B (a), AIA (b), and STEREO-A (c). The same images superimposed with extrapolated magnetic field lines are presented in the bottom row. The red lines show the closed field lines while the blue lines are the open field lines which extend beyond the boundary area that is $300'' \times 300''$. The black squares in panels (b) and (e) represent the $250'' \times 200''$ domain which contains the main features of EUV structures. The outer square in panels (c) and (f) represents the boundary area and inner one is the same as the squares on the AIA images. The same region in the backside of the Sun in panels (a) and (d) are represented by dotted lines.

EUV loops G3 are lower than the vertical structures stretching out of the solar disk. This is consistent with the calculated magnetic field lines in L3, namely they have a lower altitude seen from STEREO-A and could not be seen from STEREO-B. It is the largest loop bundle connecting P1 with N1.

G4 is a group of EUV loops in the region around PIL and between magnetic polarities P2 and N1 (Figure 7). There is strong magnetic shear indicating a large amount of magnetic free energy around the PIL, which is the most important region for understanding the physical processes of solar eruptions (see the blue box in the first row images of Figure 7). This region shows relatively complex structures in the AIA images, and there are also vertical structures stretching out of the edge of the solar disk (seen in the boxes in the STEREO side-view images). We determine the correspondence among the features in all three images. Around the PIL, there are some observed EUV loops connecting P2 and N1. Our extrapolation has obtained a series of small and low field lines along the PIL connecting the regions on both sides. These field lines agree with the EUV loop structures in general

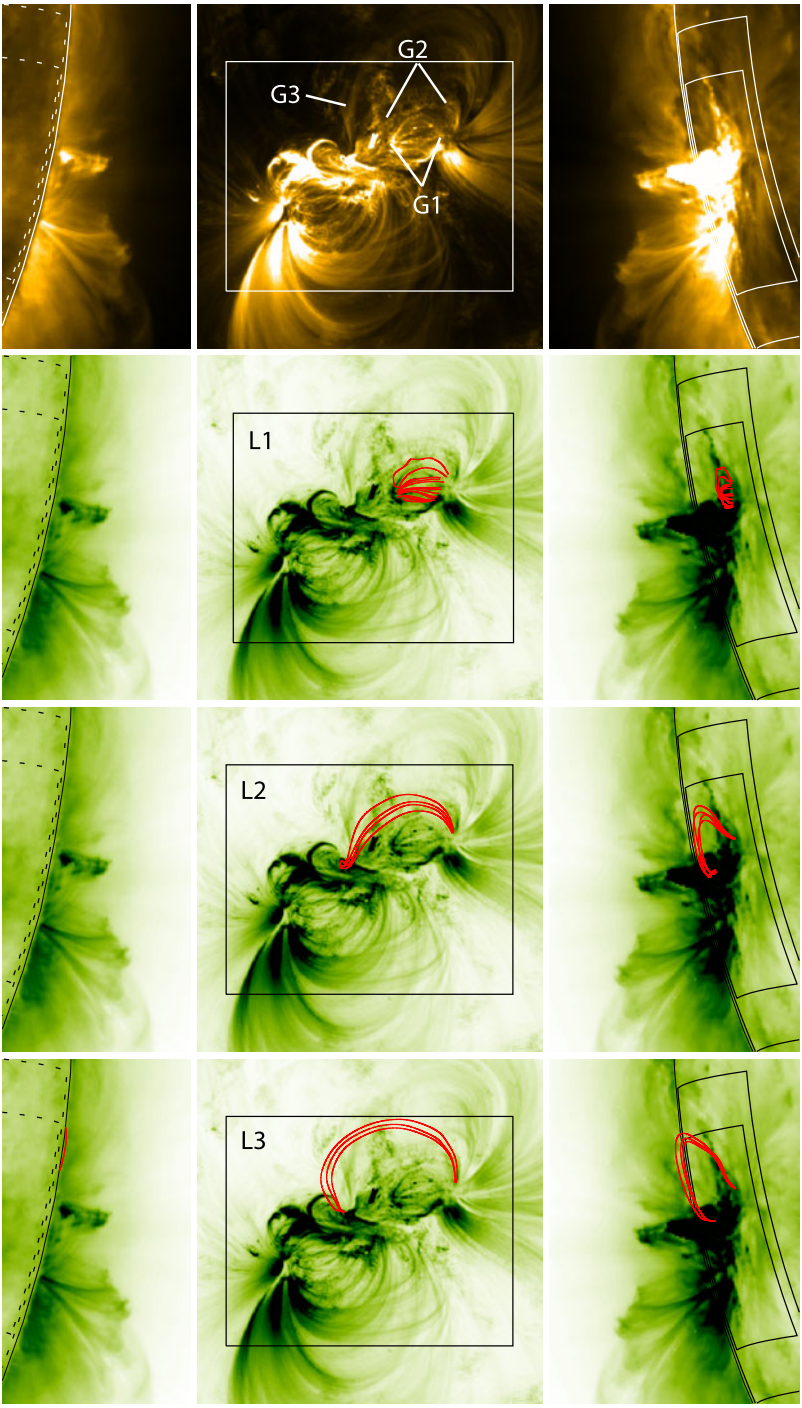

Figure 6 Calculated magnetic field lines L1, L2, and L3 and their counterparts G1, G2, and G3 in the EUV 171 Å images.

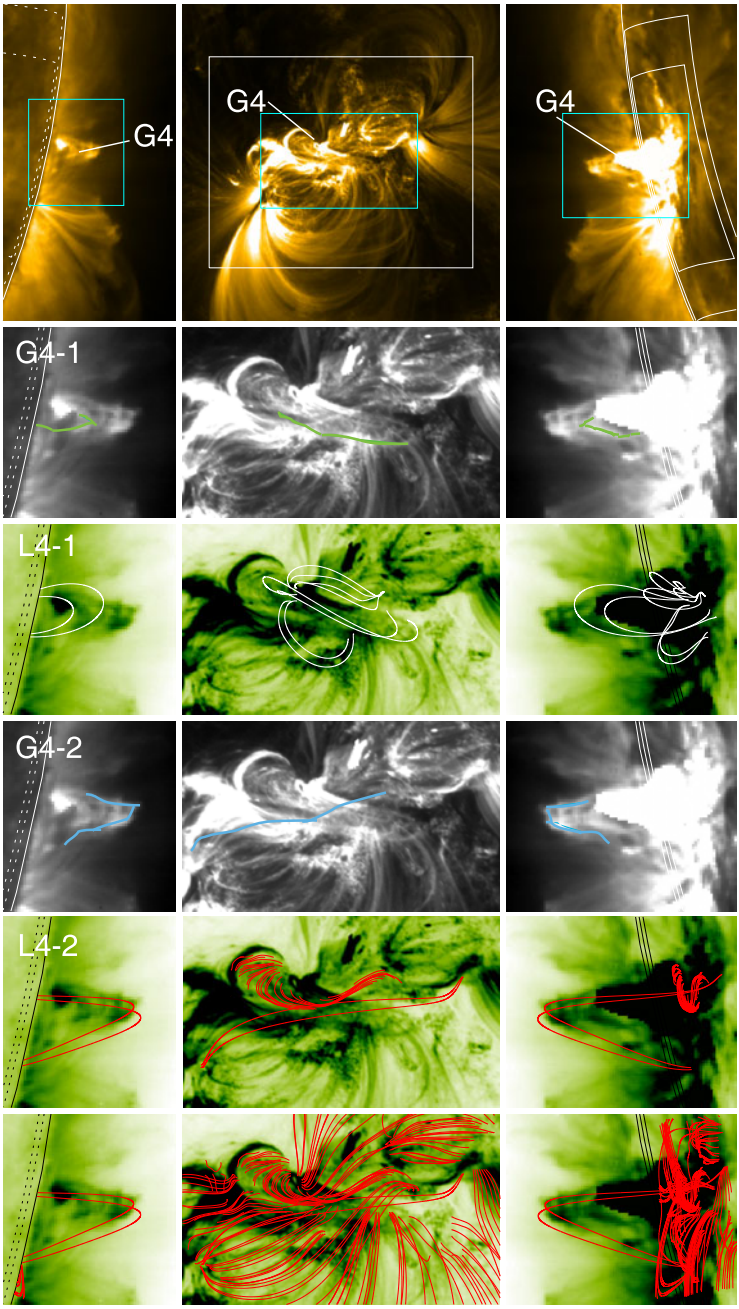

Figure 7 Loop group G4 around the polarity inversion line (PIL) seen from three different view directions (top panel); the three blue squares represent the region within which the results are displayed in the following panels. G4-1 and G4-2 are close-up views of G4. The green lines in G4-1 agree with the calculated electric current lines (white) in L4-1. The blue lines in G4-2 agree with the taller magnetic field lines (red) in L4-2. The short and low-lying field lines in L4-2 form an S-shape co-spatial with a filament channel there along the PIL. In the bottom panel the calculated magnetic field lines are shown in detail to demonstrate the location of L4-2 with respect to all the other surrounding field lines.

and the filament structure marked in Figure 1 of Sun *et al.* (2012), as shown in the last two rows in Figure 7. However, we did not obtain high field lines lying over the filament channel connecting opposite magnetic polarities P2 and N1. Nevertheless, the current lines (which can be calculated from Equation (14)) connecting P2 and N1 are found and plotted in white marked as L4-1. The locations of the corresponding EUV loops in three view directions are also shown in G4-1 as green lines. In the STEREO-A image, the half of this loop structure is blocked by saturation in the detector, but the other visible part is in good agreement with the central electric current lines in L4-1. The highest structure above the one in G4-1 is shown as the blue line in G4-2 representing large-scale loops connecting P1 and N2 along the PIL in the center region of G4 loops. L4-2 shows two bundles of magnetic field lines in the kernel region. One bundle of field lines is located higher than the electric current lines and it shows very good agreement with the coronal loop denoted as the blue line in G4-2 in both front and side views. Another bundle of low-lying and short, twisted field lines in L4-2 connects P2 and N1 along the PIL and is co-spatial with the S-shaped filament channel, where some EUV strands in the dark filament channel were also shown in Sun *et al.* (2012). The highly twisted short and low-lying field lines in L4-2 are at the pivotal location with respect to all the other surrounding field lines L1, L2, L3, L5, L6 and one ends of field lines L7, L8, ..., L12, and L14. Therefore they must have played a key role for the occurrence of the X2.2 flare event. In the STEREO-A image, it can be seen that those low-lying field lines in L4-2 form a twisted arcade structure along the PIL where the filament is located. It should be noted that while the strand in the eastern part of the S-shaped filament channel may be a low-altitude structure related to the filament, the western part of the EUV bright features along the PIL, marked as a filament in Figures 1 and 2 of Sun *et al.* (2012), may not be necessarily located at low altitude. As a matter of fact, they are almost identical to the coronal loop in G4-2 that is clearly stereoscopically resolved as a high-lying coronal bright feature seen in STEREO A/B EUV images. One cannot simply interpret all those EUV bright features along the PIL in the filament channel as manifestation of a filament although the filament could be located there.

Theoretically the field and current lines should be identical in a force-free field, but in a practical situation there may exist a discrepancy. This may be due to the inconsistency, in the computed results with the force-free condition, or to errors contained in the boundary data in the PIL region. It should be pointed out that by the DBIE method the angle between the current **J** and the field **B** is mostly less than 5° with an average value of 4°, but there do exist some points where the angles are large. On the other hand the relative flux error factor g_i always has a maximum value of about 0.5 % when comparing with the exact solution (*e.g.*, Figure 5 of Yan and Li, 2006). In the present case for $250 \times 200 \times 100$ internal grid points, the average values are, respectively, $\langle f_i \rangle = 0.078$ (or the average angle between **B** and **J** is less than 4.5°) and $\langle g_i \rangle = 0.00067$. Physically coronal EUV loops are controlled by the photospheric vector magnetic fields which are not necessarily force-free. Therefore there is no guarantee that the observed coronal EUV loops are always consistent with a force-free field solution, especially for the solar flare or coronal mass ejection events. Nevertheless the comparison between the calculated field lines and the observed coronal loops would reveal the quality of the extrapolation.

G5 and G6 are relatively low-lying EUV bright loops (Figure 8). In the STEREO-A images, G5 is seen as a bright structure which we cannot distinguish the details. The corresponding magnetic field lines L5 connect negative polarity N2 and the positive polarity between N1 and N2. These low-lying field lines cannot be seen from STEREO-B. It is important to note that there were a series of drastic activities before our selected extrapolated time in this region of G5. There was a large CME on 14 February at 18:00 UT, with the

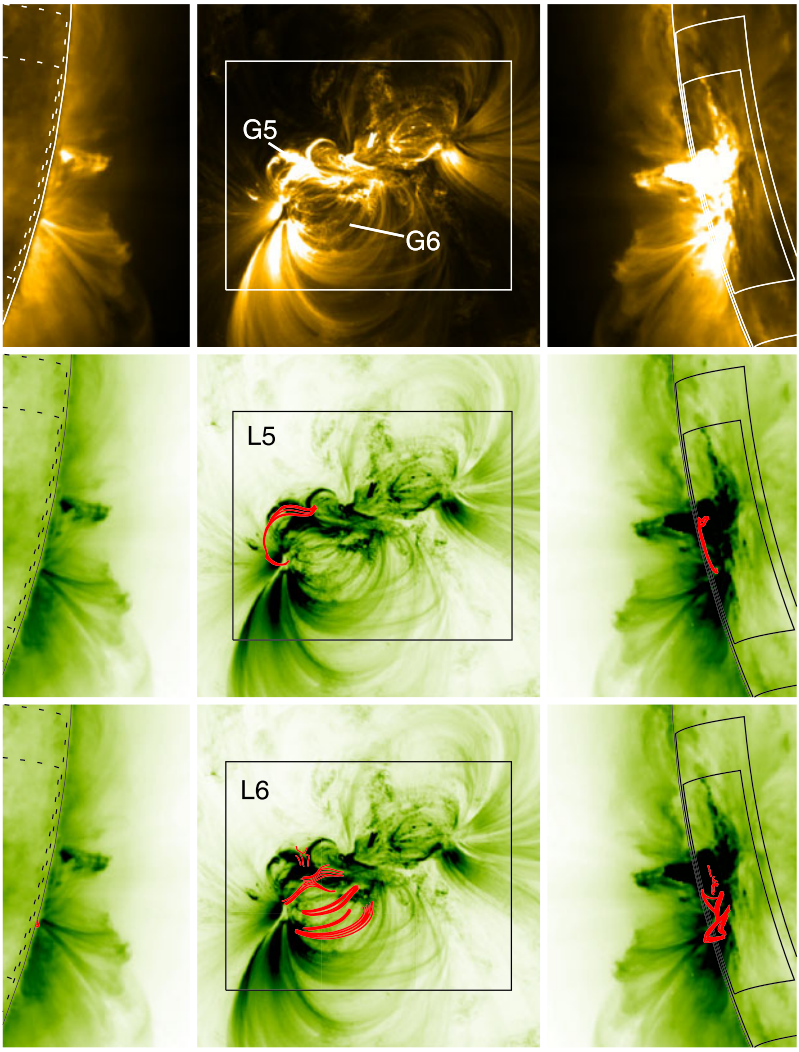

Figure 8 Calculated magnetic field lines L5 and L6, and their counterparts G5 and G6 in the EUV 171 Å images.

associated M2.2 flare at 17:20 UT from this site. G6 corresponds to a series of low-lying loops. The calculated field lines L6 are qualitatively in good agreement with G6 in the front view from AIA. In the side views from STEREO, they mix with the background and no obvious features could be seen.

G7, G8, and G9 consist of a series of coronal loops with different lengths (Figure 9). These loops all originate from polarity N2 and their end points are around polarity P2. The calculated field lines L7, L8, and L9 are all in good spatial agreement with the EUV loops G7, G8, and G9 in the front view from AIA. The calculated field lines L7-1 and L7-2 are lower and shorter, which can be seen only from STEREO-A but not from STEREO-B. L8 connects N2 to P2 and has good spatial co-alignment with G8 in the AIA image, but their side views from STEREO still mix with the background and cannot be distinguished. L8 also

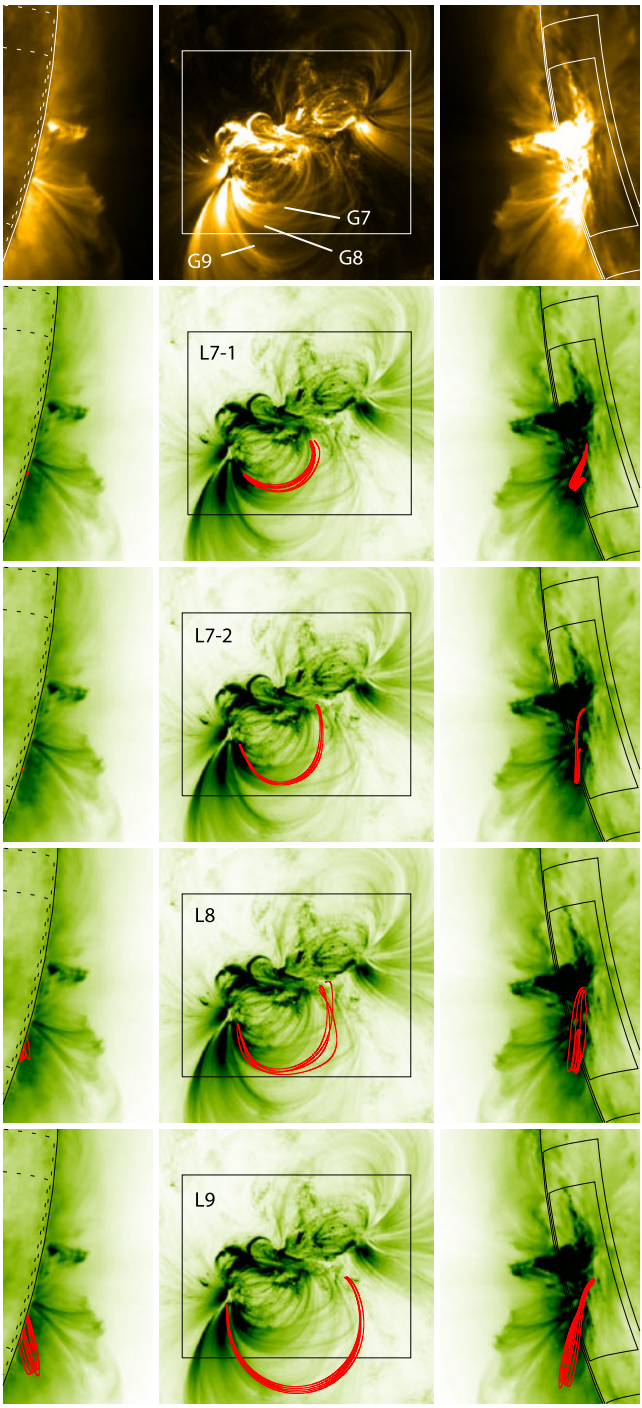

Figure 9 Calculated magnetic field lines L7-1, L7-2, L8, and L9, and their counterparts G7, G8, and G9 in the EUV 171 Å images.

shows poor spatial co-alignment with the high altitude STEREO-A/B EUV loops. G9 is one of the largest loop bundles in the southern part of this region. As their altitude increases, the loop thickness grows. This could be seen from the side view in the last row of Figure 9. L9 is in good agreement with G9 in the front view from AIA but shows poor spatial co-alignment with the high altitude STEREO-A/B EUV loops.

We may find the cases where the coronal loops are better defined in STEREO EUV images than in AIA images. Figure 10 shows a series of loops connecting N2 and P1; their structures are shown, from different view directions, in the first row of Figure 10. The correspondence among these EUV loops are confirmed by our method formulated in Section 3 and shown in the last row of Figure 10 in different colored lines. It is true that we just confirm the correspondence of half loops and the other half cannot be determined, but nevertheless this comparison validates our reconstructed results. We can see that the calculated magnetic field lines L10 agree well with the eastern part of the EUV loops G10. They overlap with some parts of G7 and G8, but their end points do not match those of G10. G11 also connects N2 and P1 and has the same situation with G10; it overlaps with some parts of G9. It can be seen that the overall configurations of the calculated field lines L10 and L11 are consistent with the coronal loops G10 and G11 in both front view from AIA and STEREO A/B side views. However, they do not always follow the same trajectories. In order to make a quantitative comparison for the three stereoscopically reconstructed loops, we calculated the angles between the tangent vectors along the reconstructed loops and the calculated fields lines. The average misalignment angles of the three reconstructed loops in the middle panel of the bottom row in Figure 10 are 16.6° (light blue), 17.8° (red), and 18.3° (blue). These values demonstrate the deviation from the force-free condition along these loops, which are quite good with a factor of about two smaller than those given by other NLFFF models yielding overall misalignment angles of $4° - 24°$ (Derosa *et al.*, 2009). They are at the same order as given by the forward-fitting model using stereoscopically reconstructed loops as constraints (Sandman and Aschwanden, 2011).

G12, G13, and G14 consist of a series of large coronal loops which are open to the outside of the computing region (Figure 11). It should be noted that they are not necessarily open to the interplanetary space but may be connected to other places in the solar surface. L12 represents a bundle of magnetic field lines rooted in N2. The bright portion of G12 near the footpoint shows good agreement with L12 both in the front view from AIA and STEREO-A/B side views. L13 are also magnetic field lines rooted in N2. There are two bundles of field lines that extend beyond the region. These two bundles of field lines in L13 are consistent with the diffuse EUV structure G13 from all view directions. The next group is L14 which displays a radial pattern originating from P1. These structures spread to the outside of the computing area and are in good agreement with northern part of G14 in the middle panel of the top row of Figure 11. Some open coronal loops in the southern part of G14 in the middle panel are actually connected to a southern pore region outside AR 11158 as shown in Figure 3(b), which are not included in the present boundary data. Therefore the southern bundle of field lines of L14 at first follows the EUV loop, but at higher altitudes they bend back to deviate from the real coronal loops. This should be due to the ignorance of the boundary field outside of the magnetogram area.

5. Conclusions

The configurations of the magnetic fields in NOAA 11158 computed under the assumption of the force-free field were compared for the first time with the coronal loop structures

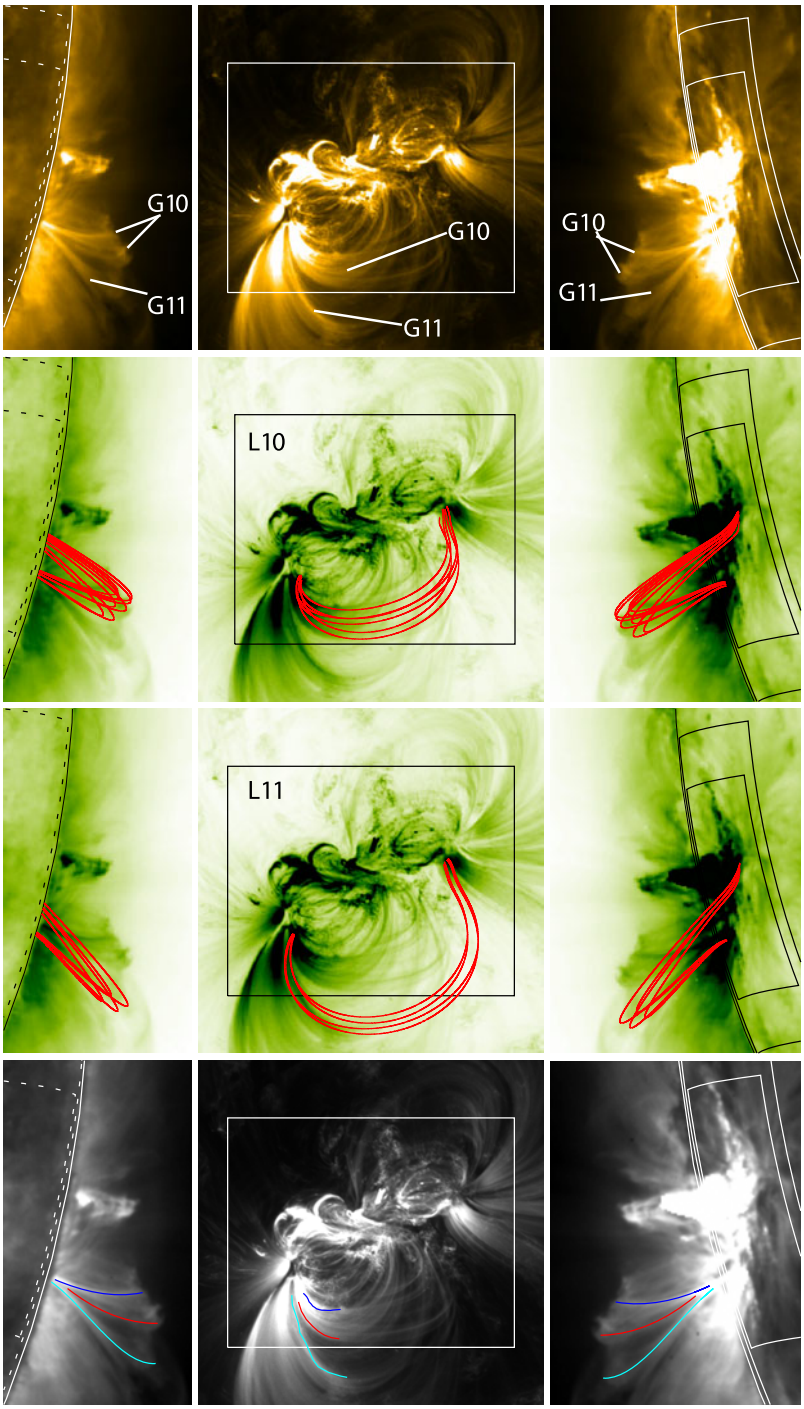

Figure 10 Calculated magnetic field lines L10 and L11, and their counterparts G10 and G11 in the EUV 171 Å images. On the bottom row images are superimposed the skeletons of identified loops G10 (blue and red) and G11 (light blue) from three different view directions.

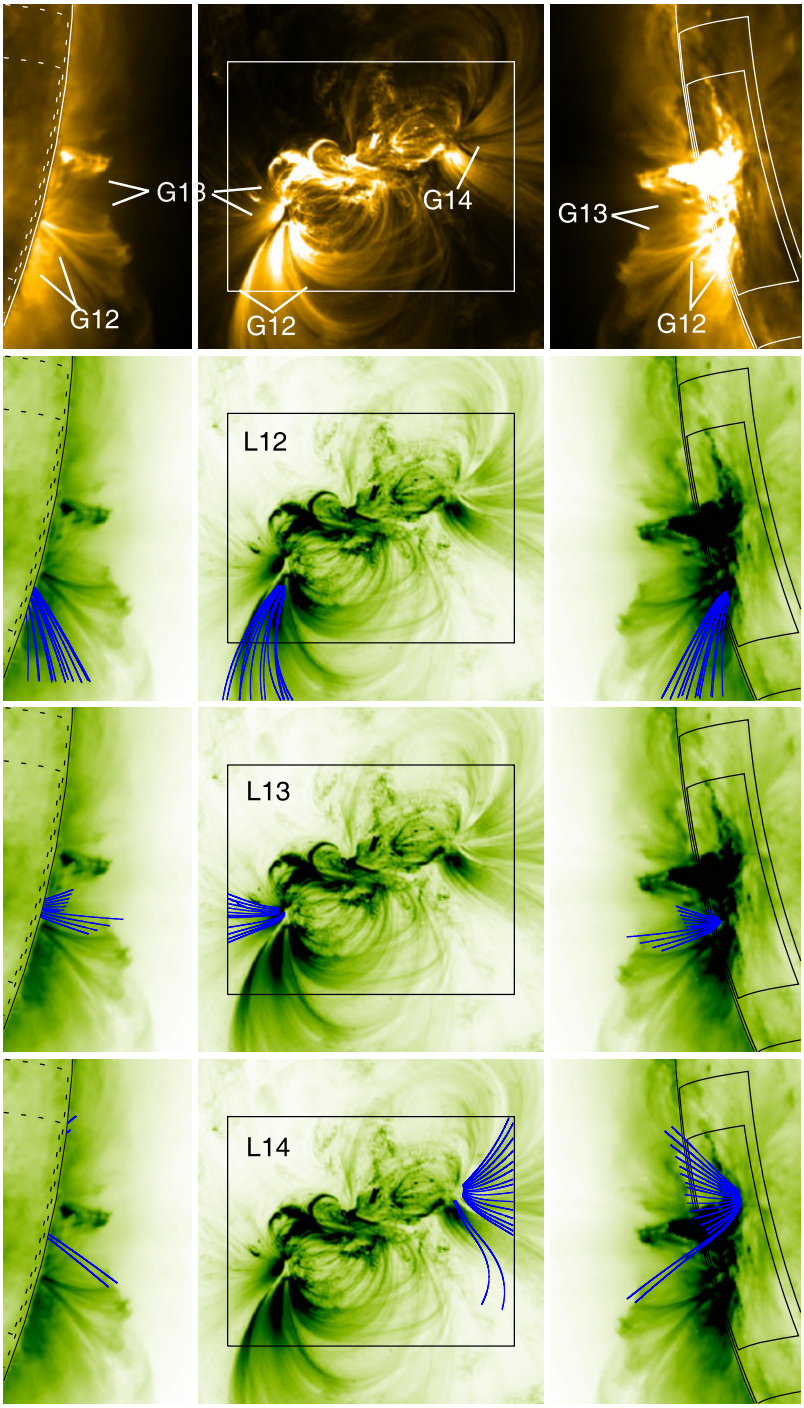

Figure 11 Calculated magnetic field lines L12, L13, and L14 that extend beyond the boundary box, and their counterparts G12, G13, and G14 in the EUV 171 Å images.

stereoscopically reconstructed from observations. This allows us to understand this active region more comprehensively. The calculated magnetic field lines replicated well the EUV loop patterns observed from different view directions. These results demonstrate clearly that the DBIE method is effective when it is applied to actual photospheric magnetograms. The GPU acceleration makes DBIE tractable even if applied to large-scale domains. From the reconstructed coronal field structures, we can estimate the altitude of EUV loop patterns which we found to be below 86 Mm, or 40 % of the size of the magnetogram area. They also matched the actual EUV features as estimated from stereoscopic observations. In this region the DBIE can achieve very high numerical accuracy. In the present case for $250 \times 200 \times 100$ internal grid points, the average angle between $\mathbf{B}$ and $\mathbf{J}$ is less than 4.5° and the average relative flux error is $\bar{g}_i = 0.00067$.

In the central area of this active region, the current density is very strong along the filament in the PIL, and the current density distribution on a vertical cross section was plotted by Sun *et al.* (2012). Our results agree very well with theirs, in that there are strong currents across the PIL, and we also found elongated low-lying twisted field lines co-spatial with the S-shaped filament along the PIL. However, we argue that one cannot simply interpret all the EUV bright features along the PIL as manifestation of a filament although the filament could be located there. Furthermore, we have obtained the electric current lines three-dimensionally at a higher altitude across the PIL in this region from three view directions. According to their agreement with the bright EUV loop structures there, we claim that the features dominated by the strong currents really existed above the PIL. Generally speaking, the region with strong currents contains a large amount of accumulated free energy and will eventually release it quickly as a flare. It is most possible that the extrapolated magnetic field lines resembling the S-shaped filament channel and the electric current lines coinciding with the bright and twisted EUV loops overlying the filament are associated with the occurrence of the X2.2 flare.

It should be noted that even when the line-of-sight (from the Earth direction) co-alignments between the calculated field lines and the observed coronal loops are successful, the views from other directions may show that they do not actually agree three-dimensionally and belong to other groups. This indicates that co-alignment in an image taken from one direction (*e.g.* from the Earth direction) alone may not provide the accurate coronal configuration; real 3-D information is vital in understanding the coronal magnetic field structures and their association with solar activities. For the three stereoscopically reconstructed coronal loops, we quantitatively obtained the average misalignment angles of $16 - 18°$, which are quite good being a factor of about two smaller than those given by other NLFFF models.

As a method different from others while it demonstrates similar computational capability, DBIE has the advantage that it requires photospheric data as the boundary condition and allows us to evaluate the NLFFF field at any point within the domain from the boundary data instead of having to solve the entire domain. The DBIE code can be accelerated by a parallel algorithm utilizing GPU hardware, which makes the DBIE method applicable to larger boundary data. The present study validates that the DBIE method is rigorous and practical.

In addition, further acceleration of the DBIE method could be possible by combining CUDA with MPI to realize multi-GPU parallelization. As the first images of Chinese Spectral Radioheliograph (CSRH; Yan *et al.*, 2009) have been obtained, the comparison between our extrapolation and the tomography observation from CSRH will be carried out in the near future.

Acknowledgements The authors would like to thank the referee for the helpful and valuable comments on this paper. Dr. Yingna Su is acknowledged for improving the English of the manuscript and helpful comments. Mr. L.A. Selzer is acknowledged for improving the English of the manuscript as well. We thank the SDO and STEREO team for providing the magnetic field data and EUV images used in this investigation. We also wish to thank Dr. W.T. Thompson for his efficient support in the routine for correcting the STEREO data error. This work is supported by NSFC Grants No. 11221063, 11273030, and 11211120147, MOST Grant No. 2011CB811401, and the National Major Scientific Equipment R&D Project ZDYZ2009-3. Part of experiments were implemented on the ScGrid and GPU cluster of Supercomputing Center, Computer Network Information Center of Chinese Academy of Sciences.

References

Amari, T., Boulmezaoud, T.Z., Mikic, Z.: 1999, *Astron. Astrophys.* **350**, 1051.
Amari, T., Boulmezaoud, T.Z., Aly, J.J.: 2006, *Astron. Astrophys.* **446**, 691.
Chodura, R., Schlueter, A.: 1981, *J. Comput. Phys.* **41**, 68.
Derosa, M.L., Schrijver, C.J., Barnes, G., Leka, K.D., Lites, B.W., Aschwanden, M.J., *et al.*: 2009, *Astrophys. J.* **696**, 1870.
Gary, D.E., Hurford, G.J.: 1994, *Astrophys. J.* **420**, 903.
Grad, H., Rubin, H.: 1958, In: *Proc. 2nd Int. Conf. Peaceful Uses of Atomic Energy* **31**, United Nations, Geneva, 190.
He, H., Wang, H.: 2008, *J. Geophys. Res.* **113**, A05S90.
He, H., Wang, H., Yan, Y.: 2011, *J. Geophys. Res.* **116**, 01101.
Howard, R.A., Moses, J.D., Vourlidas, A., Newmark, J.S., Socker, D.G., Plunkett, S.P., *et al.*: 2008, *Space Sci. Rev.* **136**, 67.
Inhester, B., Wiegelmann, T.: 2006, *Solar Phys.* **235**, 201.
Jiang, C.W., Feng, X.S.: 2012, *Astrophys. J.* **749**, 135.
Jiang, C.W., Feng, X.S., Fan, Y.L., Xiang, C.Q.: 2011, *Astrophys. J.* **727**, 101.
Jing, J., Park, S.H., Liu, C., Lee, J., Wiegelmann, T., Xu, Y., Deng, N., Wang, H.M.: 2012, *Astrophys. J.* **752**, L9.
Kaiser, M.L., Kucera, T.A., Davila, J.M., St. Cyr, O.C., Guhathakurta, M., Christian, E.: 2008, *Space Sci. Rev.* **136**, 5.
Lemen, J.R., Title, A.M., Akin, D.J., Boerner, P.F., Chou, C., Drake, J.F., *et al.*: 2012, *Solar Phys.* **275**, 17.
Li, Z., Yan, Y., Song, G.: 2004, *Mon. Not. Roy. Astron. Soc.* **347**, 1255.
Lin, H., Kuhn, J.R., Coulter, R.: 2004, *Astrophys. J.* **9**, 611.
Liu, S., Zhang, H.Q., Su, J.T.: 2012, *Astrophys. Space Sci.* **337**, 665.
Liu, Y., Zhao, X.P., Hoeksema, J.T., Scherrer, P.H., Wang, J., Yan, Y.: 2002, *Solar Phys.* **206**, 333.
Liu, S., Zhang, H.Q., Su, J.T., Song, M.T.: 2011, *Solar Phys.* **269**, 41.
Low, B.C., Lou, Y.Q.: 1990, *Astrophys. J.* **352**, 343.
McClymont, A.N., Jiao, L., Mikic, Z.: 1997, *Solar Phys.* **174**, 191.
Mikic, Z., McClymont, A.N.: 1994, In: Balasubramanian, K.S., Simon, G.W. (eds.) *Solar Active Region Evolution: Comparing Models with Observations*, *ASP Conf. Ser.* **68**, 225.
Nakagawa, Y.: 1974, *Astrophys. J.* **190**, 437.
Nelder, J.A., Mead, R.: 1965, *Comput. J.* **7**, 308.
Roumeliotis, G.: 1996, *Astrophys. J.* **473**, 1095.
Rudenko, G.V., Myshyakov, I.I.: 2009, *Solar Phys.* **257**, 287.
Sakurai, T.: 1981, *Solar Phys.* **69**, 343.
Sandman, A.W., Aschwanden, M.J.: 2011, *Solar Phys.* **270**, 503.
Schou, J., Scherrer, P.H., Bush, R.I., Tomczyk, S., Elmore, D., Card, G.L.: 2012, *Solar Phys.* **275**, 229.
Schrijver, C.J., DeRosa, M.L., Metcalf, T.R., Liu, Y., McTiernan, J., Régnier, S., *et al.*: 2006, *Solar Phys.* **235**, 161.
Schrijver, C.J., Aulanier, G., Title, A.M., Pariat, E., Delannée, C.: 2011, *Astrophys. J.* **738**, 167.
Song, M.T., Fang, C., Tang, Y.H., Wu, S.T., Zhang, Y.A.: 2006, *Astrophys. J.* **649**, 1084.
Song, Q., Zhang, J., Yang, S.H., Liu, Y.: 2013, *Res. Astron. Astrophys.* **13**, 226.
Su, Y., van Ballegooijen, A.: 2012, *Astrophys. J.* **757**, 168.
Sun, X., Hoeksema, J.T., Liu, Y., Wiegelmann, T., Hayashi, K., Chen, Q., Thalmann, J.: 2012, *Astrophys. J.* **748**, 77.
Thompson, W.T.: 2006, *Astron. Astrophys.* **449**, 791.
Valori, G., Kliem, B., Keppens, R.: 2005, *Astron. Astrophys.* **433**, 335.
Valori, G., Kliem, B., Fuhrmann, M.: 2007, *Solar Phys.* **245**, 263.

Vemareddy, P., Ambastha, A., Maurya, R.A.: 2012, *Astrophys. J.* **761**, 60.
Wang, H., Yan, Y., Sakuari, T.: 2001, *Solar Phys.* **201**, 323.
Wheatland, M.S.: 2006, *Solar Phys.* **238**, 29.
Wheatland, M.S., Sturrock, P.A., Roumeliotis, G.: 2000, *Astrophys. J.* **540**, 1150.
Wiegelmann, T.: 2004, *Solar Phys.* **219**, 87.
Wiegelmann, T.: 2007, *Solar Phys.* **240**, 227.
Wiegelmann, T.: 2008, *J. Geophys. Res.* **113**, 3.
Wiegelmann, T., Neukirch, T.: 2006, *Astron. Astrophys.* **457**, 1053.
Wiegelmann, T., Thalmann, J.K., Inhester, B., Tadesse, T., Sun, X., Hoeksema, J.T.: 2012, *Solar Phys.* **281**, 37.
Wu, S.T., Sun, M.T., Chang, H.M., Hagyard, M.J., Gary, G.A.: 1990, *Astrophys. J.* **362**, 698.
Wülser, J.P., Lemen, J.R., Tarbell, T.D., Wolfson, C.J., Cannon, J.C., Carpenter, B.A., *et al.*: 2004, In: Fineschi, S., Gummin, M.A. (eds.) *Telescope and Instrumentation for Solar Astrophysics*, *Proc. SPIE* **5171**, 111.
Yan, Y.: 2003, *Space Sci. Rev.* **107**, 119.
Yan, Y., Li, Z.: 2006, *Astrophys. J.* **638**, 1162.
Yan, Y., Sakurai, T.: 1997, *Solar Phys.* **174**, 65.
Yan, Y., Sakurai, T.: 2000, *Solar Phys.* **195**, 89.
Yan, Y., Liu, Y., Akioka, M., Wei, F.: 2001, *Solar Phys.* **201**, 337.
Yan, Y., Zhang, J., Wang, W., Liu, F., Chen, Z., Ji, G.: 2009, *Earth Moon Planets* **104**, 97.
Yang, W.H., Sturrock, P.A., Antiochos, S.K.: 1986, *Astrophys. J.* **309**, 383.
Zhang, S., Zhu, Y., Zhao, K., Zhang, Y.: 2009, *The High Performance Computing of GPU: CUDA*, China Water and Power Press, Beijing, 2 – 3.

DOI 10.1007/978-1-4939-2038-9_5
Reprinted from *Solar Physics* Journal, DOI 10.1007/s11207-013-0270-3

Magnetic Field Diagnostics and Spatio-Temporal Variability of the Solar Transition Region

H. Peter

Received: 18 December 2012 / Accepted: 6 March 2013 / Published online: 4 April 2013

Abstract Magnetic field diagnostics of the transition region from the chromosphere to the corona faces us with the problem that one has to apply extreme-ultraviolet (EUV) spectro-polarimetry. While for the coronal diagnostics techniques already exist in the form of infrared coronagraphy above the limb and radio observations on the disk, one has to investigate EUV observations for the transition region. However, so far the success of such observations has been limited, but various current projects aim to obtain spectro-polarimetric data in the extreme UV in the near future. Therefore it is timely to study the polarimetric signals we can expect from these observations through realistic forward modeling.

We employ a 3D magneto-hydrodynamic (MHD) forward model of the solar corona and synthesize the Stokes I and Stokes V profiles of C IV (1548 Å). A signal well above 0.001 in Stokes V can be expected even if one integrates for several minutes to reach the required signal-to-noise ratio, and despite the rapidly changing intensity in the model (just as in observations). This variability of the intensity is often used as an argument against transition region magnetic diagnostics, which requires exposure times of minutes. However, the magnetic field is evolving much slower than the intensity, and therefore the degree of (circular) polarization remains rather constant when one integrates in time. Our study shows that it is possible to measure the transition region magnetic field if a polarimetric accuracy on the order of 0.001 can be reached, which we can expect from planned instrumentation.

Keywords Sun: transition region · Sun: corona · Sun: UV radiation · Magnetic field · Techniques: polarimetric · Magnetohydrodynamics (MHD)

1. Introduction

There is a general consensus that the outer atmosphere of the Sun (and of other cool stars) is heated by one or several mechanisms related to the magnetic field (*e.g.* Schrijver and

Coronal Magnetometry
Guest Editors: S. Tomczyk, J. Zhang, and T.S. Bastian

H. Peter (✉)
Max Planck Institute for Solar System Research, 37191 Katlenburg-Lindau, Germany
e-mail: peter@mps.mpg.de

Zwaan, 2000). Despite the pivotal importance of the magnetic field for our understanding of the corona, actual measurements of the magnetic field are scarce – mostly we have to rely on extrapolations of the magnetic field from the photosphere (*e.g.* De Rosa *et al.*, 2009). Because the extrapolations are based on assumptions that might or might not be fulfilled in regions of interest in the corona, it is necessary to actually measure the coronal magnetic field.

Some measurements in the corona have been performed in active-region loops above the limb using the Zeeman effect for infrared coronagraphic observations (Lin, Penn, and Tomczyk, 2000). These and also radio measurements (*e.g.* White, 2005) suffer from low spatial and temporal resolution. A very promising project for diagnostics of the magnetic field in the upper chromosphere is the rocket experiment chromospheric Lyman-alpha spectropolarimeter (CLASP; Kobayashi *et al.*, 2012), planned to be launch in Dec 2014. This is based on diagnostics using the Hanle effect in Ly-α (Trujillo Bueno, Štěpán, and Casini, 2011).

The first attempt to measure the magnetic field on the solar disk at high resolution in the transition region from the chromosphere to the corona was made with the *Solar Maximum Mission* (SMM) ultraviolet spectrometer and polarimeter (UVSP; Woodgate *et al.*, 1980). The polarimetric accuracy of just below 1 % in the C IV line at 1548 Å (Henze *et al.*, 1982; Hagyard *et al.*, 1983) gave no conclusive results, except possibly in sunspots (Lites, 2001). As we found in our investigation, an accuracy of 0.1 % would be needed to derive useful information on the magnetic field with the C IV line. This accuracy is provided by the *Solar Ultraviolet Magnetograph Investigation* (SUMI; West *et al.*, 2004), which has been flown twice on a rocket. The C IV data from the latest flight in summer 2012 await calibration and analysis.

We present a forward model that provides synthesized polarimetric data as they are recorded, *e.g.*, by SUMI. This will allow a direct comparison between model and observations and will (hopefully) provide some guidance for the interpretation of the acquired polarimetric observations. A 3D model is prerequisite to investigate the transition region, because of its highly complex spatial structuring (*e.g.* Peter, 2000, 2001). Consequently, this study is based on a 3D magnetohydrodynamic (MHD) numerical experiment that provides temperature, density, velocity, and of course the magnetic field in the corona above a small active region. The model produces a loop-dominated corona (Gudiksen and Nordlund, 2002; Gudiksen and Nordlund, 2005a, 2005b). In a statistical sense, it reproduces various observational properties (Peter, Gudiksen, and Nordlund, 2004, 2006), in particular the persistent transition region redshifts (Peter and Judge, 1999; Peter, 1999). Based on the success of previous models, we here advance to investigate not only the profiles of the emission lines, but also the circular polarization due to the Zeeman effect. Another forward-modeling investigation of the polarization of the emerging radiation in a magneto-hydrodynamic (MHD) model of the extended solar atmosphere, but for the (optically thick) hydrogen Ly-α line, has been carried out by Štěpán *et al.* (2012), paying particular attention to the linear polarization produced by scattering processes and the Hanle effect.

Once the instruments provide the required polarimetric sensitivity, we will have to interpret the data properly. The extreme UV lines formed in the transition region (or in hotter parts of the atmosphere) originate from a spatially complex volume, comparable to highly corrugated surfaces. This is a fundamental difference to photospheric magnetic field observations, where the height of the source surface remains at a roughly constant altitude, within one barometric scale height. This more complex source region of transition region lines enormously complicates possible inversions. Furthermore, the high temporal variability of the intensity will be a major problem for the interpretation of the polarimetric data. The forward-model approach presented here provides insight into these problems by accounting for the whole spatial and temporal complexity.

In Section 2 the basic concept of the 3D MHD model and the spectral synthesis including the calculation of the Stokes V profile are introduced. Based on this, we synthesize the observable quantities in Section 3 and present some sample Stokes V profiles in Section 4. The observational requirements for the exposure times are discussed in Section 5 along with the spatio-temporal variability found in observations and in synthesized model data. In Section 6 we construct a realistic Stokes V observation of C IV and show that we can afford comparatively long exposure times for the observations – and why. Finally, in Section 7 we discuss some simple inversions and their reliability, before we conclude in Section 8.

2. Synthetic Spectra from a 3D MHD Model

In general, the state of polarization of the light can be described by the Stokes vector (I, Q, U, V). Stokes I represents the integral over all polarization states, while Stokes V is the difference of right- and left-circularly polarized light, and hence carries information on the longitudinal component of the magnetic field based on the Zeeman effect. For an observation near disk center and assuming that the magnetic field will be predominantly vertical, we can expect Stokes Q and U, which characterize the linear polarization, to be much weaker than Stokes V, just as found in photospheric observations in the visible. Because we found that already the Stokes V signal will be at the edge of observability, we concentrate on Stokes I and V only.

2.1. 3D MHD Model

To calculate the Stokes profiles, one needs the temperature T, density n, velocity vector $\mathbf{v}$, and magnetic field vector $\mathbf{B}$. These are provided by a 3D MHD model that solves for the induction equation, the conservation of mass, and the momentum and energy balance. Most importantly, the energy balance has to include heat conduction and radiative losses. This is pivotal to set the proper coronal pressure and therefore a prerequisite to synthesize coronal emission lines, which are very sensitive to the temperature and density.

The MHD model used for this study has been published previously by Gudiksen and Nordlund (2002, 2005a, 2005b), and an analysis of this model in terms of Doppler shifts and emission measure and a comparison with observations was presented by Peter, Gudiksen, and Nordlund (2004, 2006). In the model the plasma is heated through Ohmic dissipation of currents that are induced by the braiding of magnetic field lines through the horizontal photospheric granular motions. The good match to the observations showed that this model provides a realistic way to describe the corona in an active region, accounting for the spatial and temporal variability. Subsequently, more models of a similar type solidified these results, discussing details of the heat input (Bingert and Peter, 2011, 2013), providing further insight into the persistent transition-region Doppler shifts (Hansteen *et al.*, 2010; Zacharias, Bingert, and Peter, 2011b), transient events in the corona (Zacharias, Bingert, and Peter, 2011a), or the constant cross-section of loops (Peter and Bingert, 2012). All these results make us confident that this type of model will also provide a reliable and realistic determination of the Stokes V profiles in a transition region extreme-ultraviolet (EUV) line.

2.2. Intensity Spectra: Stokes I Profiles

To calculate the Stokes profile $I(\lambda)$ we exactly followed the procedure of Peter, Gudiksen, and Nordlund (2004, 2006). Assuming ionization equilibrium, we calculated the emissivity (energy loss per time and volume) at each grid point in the computational domain in the C IV

(1548 Å) line using the CHIANTI atomic data base (Dere *et al.*, 1997; Young *et al.*, 2003). To avoid aliasing effects we interpolated the mesh in the vertical direction. The line width was assumed to be the thermal width, $\Delta\lambda_{\rm D}$, and the Doppler shift is given by the line of sight component of the velocity vector (here the vertical component). This provides a line profile $I(\lambda)$ at each grid point.

2.3. Stokes V Profiles: Weak-Field Approximation

In a magnetic field a spectral line will be affected by the Zeeman effect. The Zeeman splitting is given by

$$\Delta\lambda_B = \frac{e}{4\pi cm_{\rm e}}\bar{g}\lambda_0^2 B_{\rm los}, \tag{1}$$

with the elementary charge e, the speed of light c, the electron mass $m_{\rm e}$, the rest wavelength λ_0, the effective Landé factor $\bar{g}$, and the component of the magnetic field along the line of sight $B_{\rm los}$.

In the weak-field limit the Stokes V signal is given by a Fourier expansion up to first order of the Stokes I line profile (*e.g.*, Stenflo, 1994, Section 11.9),

$$V(\lambda) \approx -\Delta\lambda_B \frac{\partial I}{\partial\lambda} \approx -4.67{\cdot}10^{-13}\bar{g}\left(\lambda_0[\text{Å}]\right)^2 B_{\rm los}[\text{G}]\frac{\partial I}{\partial\lambda[\text{Å}]}. \tag{2}$$

We concentrated here on the C IV line at 1548 Å to investigate the transition region magnetic field, because it has a high diagnostic potential: it is a strong line at a long wavelength λ_0 (for transition region EUV lines) with a decent effective Landé factor $\bar{g}$. This combination provides the best potential among the transition region lines.

The effective Landé factor for the 1548 Å line ($^2{\rm P}_{3/2} \rightarrow {}^2{\rm S}_{1/2}$) is $\bar{g} = 7/6 \approx 1.167$ (for details on the calculation of $\bar{g}$ see *e.g.* Stenflo, 1994, Sections 6.4 & 6.5). While the 1550 Å line of the C IV doublet has a slightly higher effective Landé factor ($\bar{g} = 4/3$), its radiance is lower by a factor of about two, which is why we concentrated on the 1548 Å line.

Even for a very strong magnetic field in the transition region of 1000 G the splitting for the C IV lines would be below $\Delta\lambda_B < 0.15$ pm, corresponding to less than 0.3 km s^{-1} in Doppler shift units. This can be considered as an upper limit. Consequently, the Zeeman splitting for C IV is much smaller than the Doppler broadening of the line, $\Delta\lambda_B \ll \Delta\lambda_{\rm D}$, the latter being about 6 pm, corresponding to 12 km s^{-1} at the line formation temperature of C IV of about 10^5 K. This justifies the application of the weak-field limit for Equation (2).

From Equation (2) we can roughly estimate the Stokes V/I signal to be expected in C IV. For this we assumed a magnetic field of 100 G (above a pore or a strong network patch) in the transition region some 3 Mm above the photosphere.

For a line width of the order of the thermal width the expected signal is about $V/I \approx 0.002$, which would be measurable with planned instrumentation (*cf.* Section 8).

With the line-of-sight magnetic field from the 3D model and the Stokes I profile from Section 2.2 we can compute the Stokes V profile according to Equation (2) at each grid point on the interpolated mesh of the computational domain.

We concentrate here on the C IV line formed at about 10^5 K. We could as easily have chosen any other extreme UV emission line, *e.g.*, the O VI line at 1032 Å formed at some 300 000 K, or the Mg X line at 625 Å formed at 10^6 K to study the coronal magnetic field. However, at these shorter wavelengths the Stokes V signal will be weaker. Furthermore, the magnetic field will be weaker at the higher temperatures that are found on average at higher heights. To detect a Stokes V signal from these lines, the sensitivity of future instruments would have to be well below 0.1 %.

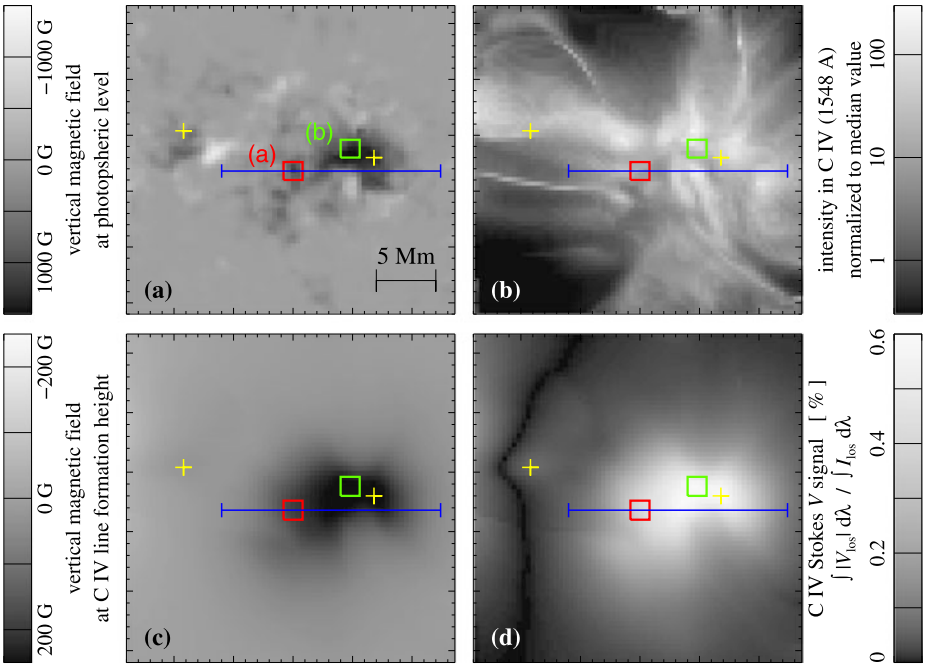

Figure 1 Snapshot of a view when looking from straight above at the computational box (along the vertical direction). Panel (a) shows the line-of-sight magnetic field at the bottom of the box defined by the boundary condition. Panel (b) displays the synthesized emission of the C IV line, integrated along the line of sight. The line-of-sight component of the transition region magnetic field at the height of the formation of C IV is plotted in panel (c). Panel (d) shows the resulting integrated Stokes V signal normalized by the line intensity (see Equation (4)). The field of view shown here is about 27×27 Mm^2 and represents part of the whole computational domain. The two yellow crosses denote the locations for which the sample Stokes V spectra are plotted in Figure 3(a). The red and green boxes show the regions over which realistic Stokes profiles are synthesized (Figure 8) and in which the temporal variation is analyzed (Figure 6). The long blue bar indicates the line along which the spatial variation is analyzed (Figure 7).

3. Synthetic Observation and Diagnostics

We here restrict the discussion to a part of the computational domain that covers about 27×27 Mm^2 in the horizontal directions. This region of interest contains a magnetic structure at the bottom boundary that resembles a pore on the real Sun. The (vertical component of) the magnetic field at the bottom boundary, *i.e.*, the photosphere, in this area is shown in Figure 1(a). In this region the photospheric magnetic field is predominantly of one sign.

We investigated synthetic EUV observations for which the line of sight is aligned with the vertical. For this we integrated the Stokes $I(\lambda)$ and $V(\lambda)$ profiles along the vertical direction,

$$I_{\rm los}(\lambda) = \int I(\lambda)\,{\rm d}z; \qquad V_{\rm los}(\lambda) = \int V(\lambda)\,{\rm d}z. \tag{3}$$

This produces observables as they would be found in actual observations of the Sun close to disk center when employing an EUV spectro-polarimeter. These data were analyzed in the same way as actual observations of the Sun would be handled. For instance, one can derive maps of the total line intensity, Doppler shifts, or the wavelength-integrated Stokes V signal.

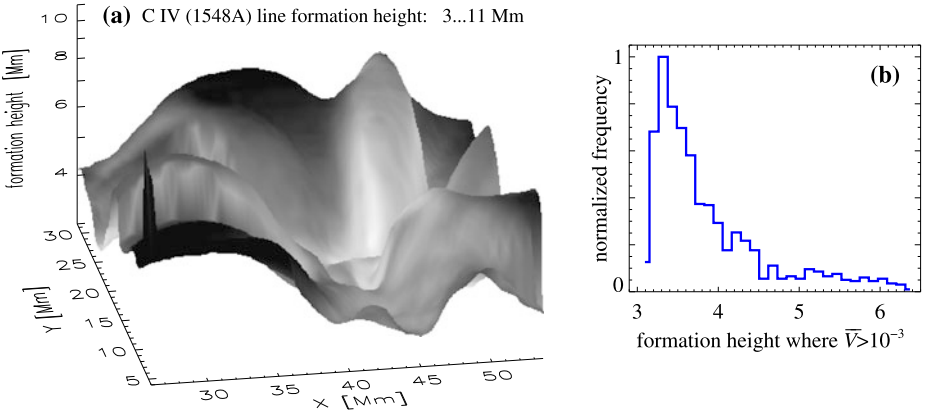

Figure 2 Line-formation height of C IV. The surface in panel (a) shows the height from which C IV is originating. We display the emission from C IV on that surface to show the (inverse) relation of emission and formation height. The horizontal extent of the field of view is the same as in Figure 1. Panel (b) presents the distribution of formation heights in the areas where the Stokes signal $\overline{V}$ as defined in Equation (4) exceeds 10^{-3}.

In particular, we define the total intensity and the integrated Stokes V signal as

$$\overline{I} = \int I_{\rm los}(\lambda)\,{\rm d}\lambda; \qquad \overline{V} = \frac{1}{\overline{I}} \int |V_{\rm los}|(\lambda)\,{\rm d}\lambda. \tag{4}$$

The latter gives the fraction of the (unsigned) Stokes signal along the line of sight compared to the total line emission. In Figures 1(b) and 1(d) we show the resulting maps of $\overline{I}$ and $\overline{V}$ for the part of the computational domain investigated here.

From the three-dimensional distribution of the C IV emission in the computational domain we can derive at each horizontal location (x, y) at which height z the main contribution of C IV originates. This defines the line-formation height, which we show in Figure 2(a). As noted above, this is a highly corrugated surface. Typically, the line-formation height is lowest where the intensity is highest – where the heating is particularly high, the transition will move to lower heights and produce more emission. Even when considering only regions with considerable field strength, where the Stokes signal $\overline{V}$ as defined in Equation (4) exceeds 10^{-3}, there is a wide range of heights of the C IV source region. The histogram in Figure 2(b) shows that there the formation of C IV is mostly found between 3 Mm and 4 Mm, sometimes reaching up to 6 Mm. This corresponds to several chromospheric pressure scale heights ($\approx$300 km).

From the line-formation height we can now extract the magnetic field at the source region of C IV. We plot the vertical component of this, *i.e.*, the line-of-sight component, in Figure 1(c). This map of the transition region magnetic field is *not* just a horizontal cut, but shows the magnetic field at the actual height of the main transition region emission for each horizontal location, *i.e.*, on the corrugated surface shown in Figure 2(a).

This surface of the maximum contribution of C IV coincides with the location of the temperature jump into the corona. However, the spatial structure of the transition region is even more complicated than this. The emission of the optically thin C IV line is not restricted to this surface, but pockets of 10^5 K cool plasma are also found higher up in the (generally) hotter volume of the corona, as can be seen from the images and movies of Peter, Gudiksen,

and Nordlund (2006). One should keep this in mind when interpreting the data – along the line of sight various structures can contribute to the emission seen in transition region lines.

Comparing the photospheric and transition region magnetic field in Figures 1(a) and 1(c), the transition region field is clearly much smoother and no longer shows any signs of (small-scale) mixed polarities. The opposite polarities in the photosphere are several Mm apart, which means that at a height of 3 Mm and higher, where C IV is formed, all these mixed polarities are closed already. Similar to a simple potential field expansion, the 3D MHD model shows the expansion and smoothing of the magnetic field with height.

4. Stokes *V* Line Profiles

Two examples of Stokes *V* profiles are shown in Figure 3(a). The sample from the location close to the center of the magnetic field concentration in the photosphere shows a peak-to-peak signal in Stokes *V* of C IV normalized to the peak intensity of almost 1 %. This profile is among the strongest Stokes *V* signals in the field of view (right cross in Figure 1). The signal is symmetric and close to a Stokes *V* signal in an idealized situation. In regions where the magnetic field is weak, but significant emission in C IV is still present (left cross in Figure 1), the Stokes *V* signal is typically weaker than 0.1 %.

The distribution of the C IV Stokes *V* signals in the field of view displayed in Figure 3(b) reveals that about one third of the area shows a signal higher than 0.1 %. This is within the detection limit of the SUMI rocket (West *et al.*, 2004). Likewise, the future rocket mission CLASP (Kobayashi *et al.*, 2012) will achieve this accuracy in the EUV (albeit at Ly-α). Furthermore, the space-based observatory SolmeX, which was proposed to ESA (Peter *et al.*, 2012), would have included a spectro-polarimeter with the required capabilities for C IV observations (see also Section 8).

Most of the area in the field of view visible in Figure 1 shows signals much weaker than 0.1 % (*cf.* Figure 3(b)) that will not be detectable. These weak signals mostly originate from regions with very low emission in C IV. Therefore in addition to the weak Stokes *V* signal,

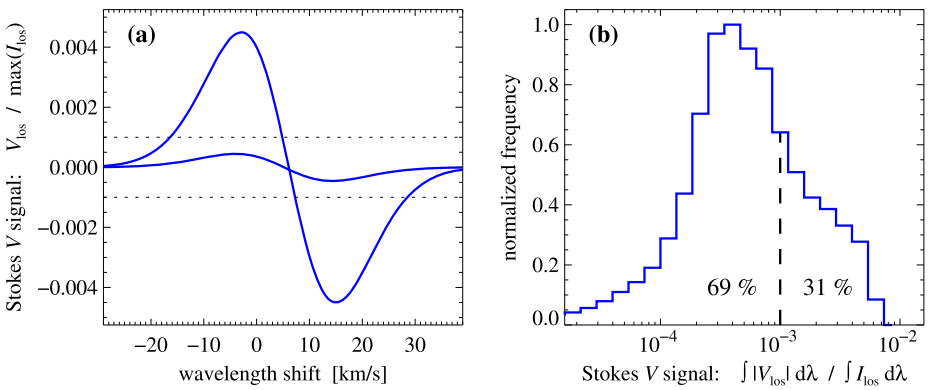

Figure 3 Synthesized Stokes *V* profiles and histogram of the distribution of Stokes *V* signals. Panel (a) shows two sample Stokes *V* profiles normalized to the peak line-intensity for the locations marked by crosses in Figure 1 (the stronger signal corresponds to the right cross). Panel (b) displays the distribution of Stokes *V* signals as defined in Equation (4) for the field of view shown in Figure 1. About one third of the area shows a Stokes *V* signal higher than 0.1 %. Alternatively, one could also plot the histogram of the peak values of the Stokes *V* profiles, which would show a very similar result. See Section 4.

the low intensity would also prevent the detection of a signal here because of the limitation in signal to noise.

The distribution in Figure 3(b) shows the Stokes signal as defined in Equation (4), *i.e.*, the total unsigned Stokes V normalized by the total intensity. The distribution for the peak values of Stokes V normalized by the peak intensity would show a very similar distribution.

5. Variability of the Transition Region Intensity and Magnetic Field

5.1. Observational Requirements for Exposure Times

Based on the discussion of Figures 1(d) and 3(b) in Section 4, and considering the order-of-magnitude arguments in Section 2.3, instruments clearly would have to detect a Stokes V signal (normalized to I) of 0.001 or better. This implies that the signal-to-noise ratio of the recorded data has to be better than 1000. Assuming Poisson statistics, we conclude that the detector has to acquire at least 10^6 counts (or 10^7 counts for a 3σ detection). This will set a limit for the required exposure time.

As a simple experiment, one can investigate a time series of actual observations to obtain an estimate of the exposure time. The most recent instrument that recorded high-quality solar data in C IV is SUMER (Wilhelm *et al.*, 1995). Because of the lack of a well-suited time series in C IV, we used data from Si IV, a line that forms at similar temperatures as C IV. The two lines share the main observational properties, *e.g.*, variability, line shifts, contrast, *etc.*

To investigate the noise level, a time series with high temporal cadence was analyzed and the acquired counts were accumulated. This is possible with a photon-counting device such as SUMER. Assuming Poisson statistics, which is a good approximation for the SUMER detector, the noise-to-signal ratio was derived. This is simply the inverse of the square root of the accumulated counts. In Figure 4 this noise-to-signal ratio based on the accumulated counts is shown as a function of the observational time. As expected, the noise level generally drops with time. The details depend on the time-variable emission, of course. For the particular example shown in Figure 4 a noise level of 0.001 was reached after 12 minutes.

Therefore, to reach a signal-to-noise level from which a Stokes V signal of 0.001 is detectable, one would have to integrate for about 12 minutes, as well. The data shown here are for a bright patch in the network, *i.e.*, for regions with a higher magnetic field, *e.g.*, in the vicinity of a pore, where we can expect higher emission in the transition region lines, and thus a shorter exposure time would be sufficient. A more modern instrument could also have a higher throughput and larger aperture, which would in part be counterweighted by the additional optics needed to analyze the state of polarization of the incoming light. Accordingly, one might need exposure times of the order of minutes as a very rough estimate.

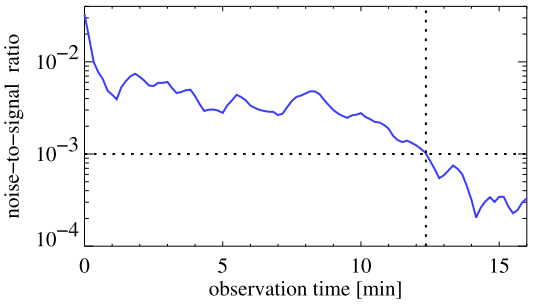

Figure 4 Noise-to-signal ratio for a photon-counting detector (SUMER/SOHO) from an actual observation. The data show Si IV at 140.3 nm observed in the quiet-Sun network. After ≈ 12 minutes 10^6 counts were reached and the noise level dropped to 10^{-3}. See Section 5.1.

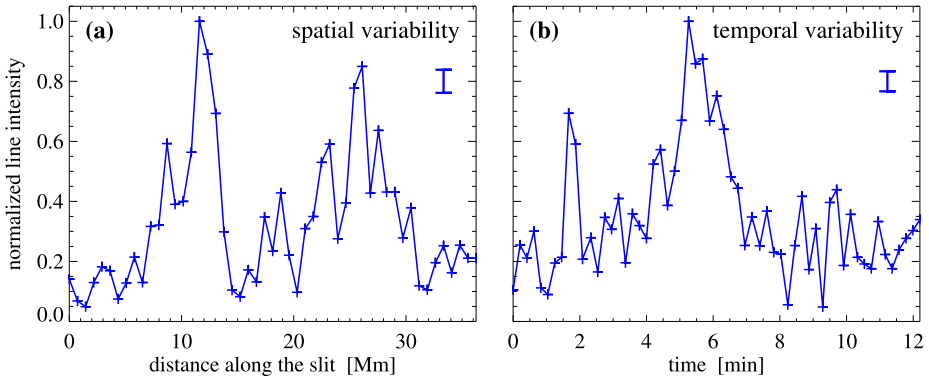

Figure 5 Observed actual spatial and temporal variability of the transition region. Example of SUMER data showing the intensity of the O VI line at 1038 Å observed on 16 May 1998. They represent a region with strong network activity. The left panel (a) displays the spatial variation (along the slit), with a pixel size of $1''$ (crosses), *i.e.*, at the highest possible spatial sampling, at an exposure time of 10 s. The right panel (b) shows the temporal variation in a single $1'' \times 1''$ spatial pixel (crosses). The bars in the panels indicate the average uncertainty for the line intensity (Poisson noise). The crosses indicate the spatial pixels (left) and times of exposures (right). The temporal and the spatial variability is down to the resolution limit of SUMER. See Section 5.2.

Considering the high variability of the transition region emission, this poses the question whether Stokes V observations with such comparatively long exposure times are meaningful. After presenting the transition region variability in actual observations (Section 5.2) and in the synthesized model data (Section 5.3), we return to this question in Section 6.

5.2. Actually Observed Transition Region Variability

As one possible example, Figure 5 shows the temporal and spatial variability of the transition region emission. The spectra were acquired in the quiet-Sun in a region with strong network activity. The spatial variation (panel a) shows a 35 Mm ($\approx 48''$) long cut through two network patches with enhanced emission. In addition to this spatial variation on a scale of some 10 Mm, variations down to the resolution limit ($1''$ spatial sampling) can be seen. We emphasize that this pixel-to-pixel variation is *not* noise, but represents real variability not fully resolved by the instrument.

For the temporal variation (Figure 5(b)) one can identify fluctuations also down to the sampling of the instrument (here 10 s). Again, these fast fluctuations are real, and consistent with the very short cooling times in the transition region. Stronger fluctuations well above a factor of two occur on time scales of minutes; they are ubiquitous on the Sun. In this example one shorter and one longer fluctuation can be identified. These brightenings can be classified as blinkers, which have been abundantly studied (Harrison *et al.*, 1999, 2003; Peter and Brković, 2003; Brković and Peter, 2004).

This strong variability in time (and space) raises the question to which extent spectro-polarimetric data will be useful for investigating the transition region magnetic field with instruments that will have limited spatial and temporal resolution. This can be explored by observations synthesized from a model for which the magnetic field is known.

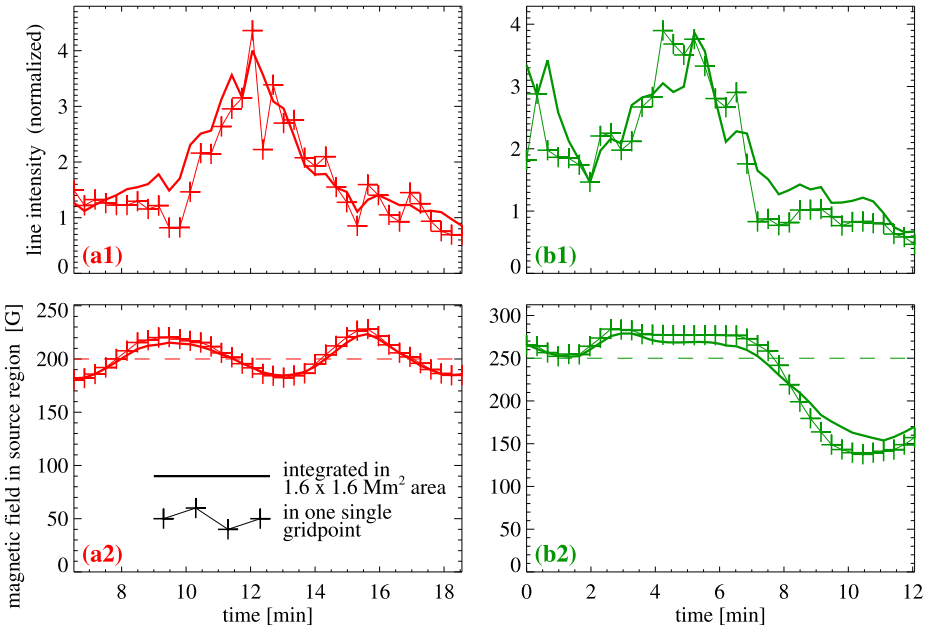

Figure 6 Temporal variability of synthesized transition region emission and magnetic field. The top panels (a1) and (b1) show the temporal variation in the two 1.6×1.6 Mm^2 squares labeled (a) and (b) in Figure 1(a). The thick solid lines show the variation of the average intensity in the respective square, while the thin lines with the crosses show the variation at the central grid point in that square. The bottom panels (a2) and (b2) show the variation of the magnetic field at the line formation height of C IV, *i.e.*, the source region of the transition region emission. Again, this is plotted for the average within the respective square (thick) and the central grid point (thin with crosses). The dashed lines indicate the magnetic field inverted from the average Stokes V signal as discussed in Section 7. See Section 5.3.

5.3. Spatio-Temporal Variability in Synthesized Observations

Examples for the temporal variability of the transition region emission synthesized from the 3D MHD model are shown in Figure 6 (top panels) for the squares labeled (a) and (b) in Figure 1. These regions were selected to be in regions near the main polarity with medium (a) and high (b) intensity in C IV. In the figure the variation integrated over an area of 1.6×1.6 Mm^2 (roughly $2'' \times 2''$) is plotted along with the intensity of the simulation in the center of that square. As expected, the variation integrated over the square is smoother than the one in its center, with the variation being quite similar in both cases.

In the two examples shown in Figure 6 transient brightenings are visible that last a few minutes with an intensity enhancement of about a factor four. These brightenings are induced by short increases of the heating rate, which are ubiquitously present in these 3D MHD models (see also Bingert and Peter, 2011, 2013). The brightenings shown here have properties similar to the observed ones in Figure 5, and could therefore be considered as a valid model for blinkers (Harrison *et al.*, 1999, 2003). However, the relation of the observed blinkers to the brightenings in these 3D MHD models is beyond the scope of this article.

In contrast to the spectroscopic observations, in the model one can compare the intensity variation with the magnetic field $B_{\rm TR}$ in the source region of the transition region emission (bottom row of Figure 6). The magnetic field strength in the source region obviously changes

only slightly, while the intensity changes dramatically. Because the plasma-β parameter is much smaller than unity in the source region of C IV (*cf.* Peter, Gudiksen, and Nordlund, 2006 their Figure 12), very strong and rapid intensity variations emerge, while the magnetic field remains mostly unaffected. This opens up the possibility of inferring the transition region magnetic field despite the high temporal variability of the emission (*cf.* Section 6).

In example (a) in the left column, the magnetic field strength changes only by about 20 %, while the intensity increases by a factor of three. With the increased heating the transition region moves downward to higher densities to be able to radiate the increased amount of heat input. Because the scale height in the chromosphere is only about 300 km, moving down by about 150 km is sufficient to relocate the transition region to densities a factor of about 1.7 higher. The emission evolves with the density squared and thus this change of height of the source region by 150 km will change the intensity (and thus the radiative losses) by a factor of three. Over this small change in height the magnetic field is changing only slightly, hence the small decrease of B by some 30 G at the time of the emission peak in example (a).

Example (b) in the right column of Figure 6 also shows only a small change in magnetic field while the intensity changes significantly. Here the magnetic field in the area drops toward the end of the time frame shown because of the (comparably slow) changes induced by the footpoint motions. This leads to weaker currents, lower heating, and consequently lower transition region emission.

In Figure 6 only $\int I_{\rm los}\,{\rm d}\lambda$ and the magnetic field in the source region, $B_{\rm TR}$ are plotted. Because according to Equation (2) Stokes V is basically proportional to I and $B_{\rm TR}$, and because $B_{\rm TR}$ is quite constant, Stokes V is changing in a manner very similar to I. This is why $\int |V_{\rm los}|\,{\rm d}\lambda$ is not plotted in Figure 6. Normalizing $\int |V_{\rm los}|\,{\rm d}\lambda$ by $\int I_{\rm los}\,{\rm d}\lambda$, *i.e.,* $\overline{V}$ as defined in Equation (4), basically gives the magnetic field, see also Section 7 and Equation (5). Therefore the variation of the (normalized) Stokes V signal $\overline{V}$ closely follows the magnetic field in the source region $B_{\rm TR}$. Accordingly, we plotted only $B_{\rm TR}$ but not $\overline{V}$ in Figure 6.

The spatial variation basically shows the same properties as the temporal variation: strong intensity variation with only small changes of the magnetic field in the source region. To illustrate this, Figure 7 shows the variation along the blue bar in Figure 1. Despite the large-scale variation of the magnetic field across the pore region, in the region of strongest magnetic field (x from about 40 Mm to 50 Mm) there is only a weak variation in magnetic field, while the C IV intensity changes by a factor of 4 to 5. This documents the close relation between the decreased emission and magnetic field near $x \approx 46$ Mm to the increase in formation height. The small increase in formation height (due to lower heating) by some 300 km leads to only a small change in magnetic field. Because the (chromospheric) scale height is comparable to this change in formation height, the change in emission is quite dramatic.

6. A Realistic Synthetic Observation: Can We Afford Long Exposure Times?

The above discussion shows that the observations and the synthesized emission from the 3D model show very strong variations in the emissivity. A future spectro-polarimetric instrument would have only a limited resolution in space *and* time because of the limitations in count rate and signal-to-noise ratio to detect the weak Stokes V signal. To obtain a realistic estimate for a possible spectro-polarimetric observation of C IV, we used the estimate for the exposure time from Section 5.1 and Figure 4 adapted for specifications similar to SUMER. Specifically, we adopted a resolution element of about $2''$ and an exposure time of 12 minutes. This can be considered a worst case because more modern instruments (will) have a

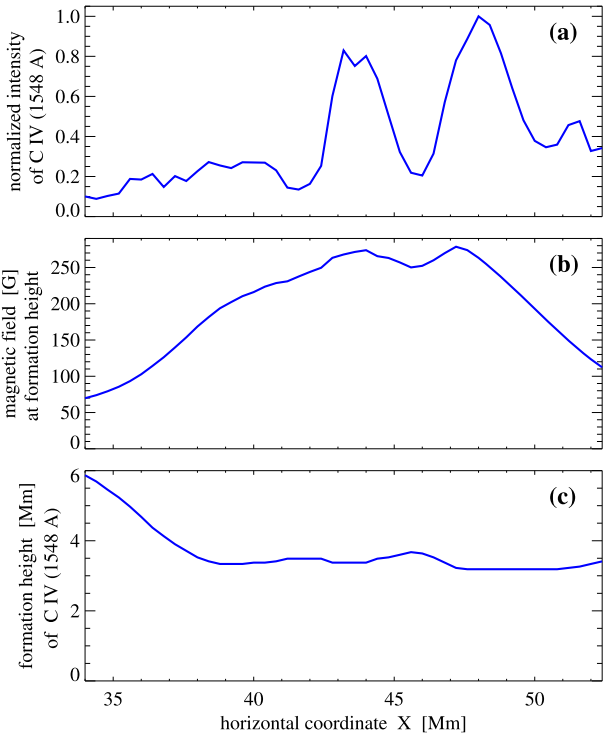

Figure 7 Spatial variation of the synthesized transition region emission, magnetic field, and line formation height. The spatial variation is plotted along the long blue horizontal bar marked in Figure 1 and is shown for the same time as the snapshot displayed there. See Section 5.3.

significantly higher efficiency. If a Stokes V signal is visible with such a long exposure, clearly it will be visible for the shorter exposure times of more modern instruments.

Figure 8 shows synthesized Stokes V profiles integrated in space over a square of 1.6×1.6 Mm^2 (boxes in Figure 1) and in time over the 12 minutes for which the temporal intensity variation is shown in the squares in Figure 6. To achieve a more realistic representation, the Stokes V spectra are shown as bars with a spectral sampling comparable to the SUMER instrument and with the addition of a noise level of 10^{-3}.

This shows that in the two regions selected here, close to the pore and in its vicinity, one can detect a Stokes V signal with an instrument with a detection limit in Stokes V over I of about 10^{-3}. The main result from this experiment is that a Stokes V signal survives even when integrating in space and time, although the spatial and temporal fluctuations of the intensity on scales shorter than the length- and time scales the spectrum are integrated during the exposure. This is basically because the magnetic field is comparatively constant (in time and space), at least much smoother than the intensity (see Section 5.3). In conclusion, this model shows that the question posed in the heading of the current section can be answered: yes, we can afford long exposure times to obtain information on the magnetic field.

It might be that one can extrapolate this conclusion to existing measurements of the magnetic field in the upper atmosphere by spectro-polarimetry in the infrared. For example, the signals of forbidden and optically thin lines detected in active-region coronal loops with a coronagraph (*e.g.* Lin, Penn, and Tomczyk, 2000) might represent the background magnetic field. The polarization signals of the allowed He I 10830 Å triplet, which is not optically thin, observed in spicules above the limb (Centeno, Trujillo Bueno, and Asensio Ramos, 2010) may well represent the magnetic field of the spicular plasma itself, as argued by these authors.

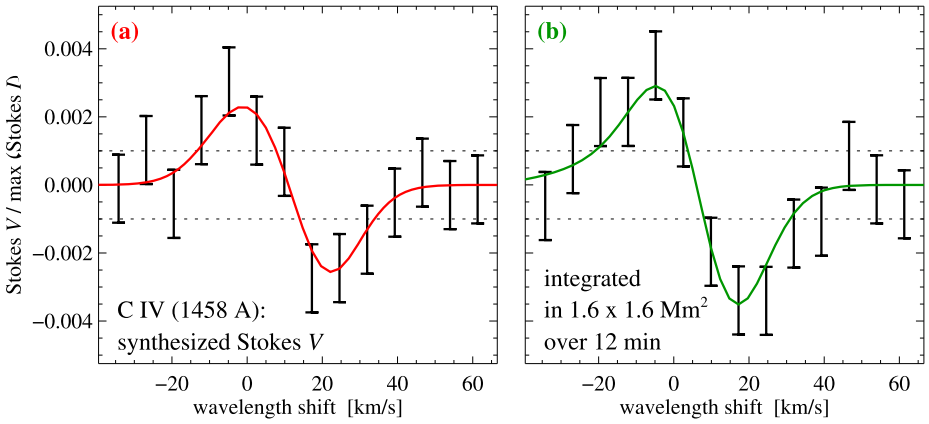

Figure 8 Realistic synthetic Stokes V observation. The two panels show the synthesized Stokes V profiles in the 1.6×1.6 Mm^2 squares labeled in Figure 1 accordingly. The synthetic observation was integrated in space over the square and in time for 12 min. The bars show a potential observation at a spectral sampling comparable to that of the SUMER instrument with a noise level of 10^{-3}. See Section 6.

7. How Reliable Is an Inversion of the Transition Region Magnetic Field?

Even if one can detect a Stokes V signal in C IV, it is not clear to what extent one can invert the longitudinal component of the magnetic field in the source region of the transition region emission. To test this, as a first step we derived a very simple magnetograph equation from Equation (2) and compared the resulting inverted magnetic field with the magnetic field in the 3D model. Using the wavelength and the effective Landé factor for the C IV line, $\lambda = 1548$ Å and $\bar{g} = 1.167$, and assuming that the line width is comparable with the thermal width, $\Delta\lambda \approx 0.06$ Å, one can rewrite Equation (2) as

$$B_{\rm me}[\mathrm{G}] \approx 46\,000 \overline{V}. \tag{5}$$

Because in the 3D model the magnetic field B is known at each grid point, one can now compare the inverted magnetic field $B_{\rm me}$ with the actual magnetic field in the source region to test this very simple inversion procedure.

As a first step we investigate the two realistic sample spectra shown in Figure 8. Here the Stokes V signals for regions (a) and (b) are $\overline{V} \approx 0.45$ % and 0.55 %. According to Equation (5), this corresponds to inverted magnetic field strengths of $B_{\rm me} \approx 200$ G and 250 G. These inverted values are plotted as dashed lines in Figure 6 on top of the magnetic field variation during the exposure of these spectra. In these two cases the simple inversion apparently works and represents some average value of the (line-of-sight) magnetic field in the source region of the transition region emission. Comparing the actual and inverted magnetic field in the bottom panels of Figure 6, we estimate the error of this procedure to be about 20 %.

To test if the simple inversion also works in a statistical sense, we considered the scatter of the ratio of the inverted field $B_{\rm me}$ to the actual (line-of-sight) magnetic field B in the C IV source region. This is shown in Figure 9(a) as a function of the Stokes V signal. At least in areas with a Stokes V signal higher than a noise level of 10^{-3}, the inverted and the actual magnetic field are closely correlated: the inverted signal is within about 5 % of the value

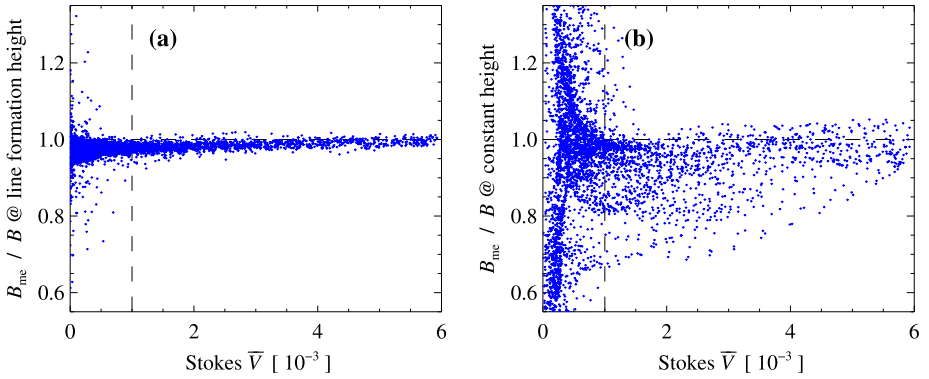

Figure 9 Relation of a simple magnetic field reconstruction to the synthesized Stokes signal $\overline{V}$ of C IV as defined in Equation (4). Panel (a) shows the ratio of the magnetic field strength $B_{\rm me}$ reconstructed by the magnetograph equation (5) to the magnetic field at the line formation height, *i.e.*, on the corrugated source surface of C IV. In contrast, panel (b) shows the ratio of $B_{\rm me}$ to the magnetic field at a fixed height ($z = 3.3$ Mm), where the horizontally averaged temperature is 10^5 K. See Section 7.

from the 3D model. However, we recall that this excludes any noise, which will (in part) degrade the nice correlation.

From Figure 2(a) it is clear that the C IV source region is anything but close to a flat plane. Of course, this raises the question on the usability of the inverted values of the magnetic field, which mainly reflect the field on the highly corrugated source surface of the transition region emission in C IV, as shown in Figure 9(a). Therefore we compare in Figure 9(b) the inverted magnetic field $B_{\rm me}$ with the magnetic field at a constant height in the computational box. Here we chose a height of $z = 3.3$ Mm, which in this model represents the height where the *horizontally averaged* temperature reaches 10^5 K. This shows a much stronger scatter. Still, if one assumes that the measurement were to represent the magnetic field at a constant height, one would be able to invert the magnetic field within some 20 % to 30 % (most values in Figure 9(b) higher than a Stokes V signal of 0.1 % have a ratio of between 0.75 to 1.05). Of course, this is again excluding noise of the measurement.

Certainly, the community will have to develop more elaborate inversion procedures to interpret the Stokes V measurements in C IV in the future. However, even with the simple magnetograph-type inversion presented here one can hope to measure the transition region magnetic field within some 30 %.

8. Conclusions

We presented a forward modeling of the Stokes profiles in the EUV to explore the diagnostic potential of emission lines for investigations of the magnetic field in the transition region and low corona. We showed that with instruments providing a polarimetric sensitivity of Stokes V/I of about 0.1 % this task of measuring the transition region magnetic field can be achieved; probably within some 20 % to 30 % using simple magnetograph-type inversions as a first step.

We employed a realistic 3D MHD model that self-consistently solves for the magnetic structure *and* the transition region and coronal plasma properties. The emission synthesized from the model is highly structured in space and shows a strong temporal variability, just as

actual observations. Naively, one could expect that this high level of variation would destroy any significant polarization signal of the magnetic field. However, because the magnetic field structure is rather stable and smooth, the Stokes V signal survives even when integrating in space and time.

Therefore spectro-polarimeters operating in the EUV will be able to provide reliable diagnostics of the transition region magnetic field. During its first flight in summer 2010, the SUMI rocket acquired several minutes worth of polarization data in Mg II (West *et al.*, 2011). A second flight took place in summer 2012. The C IV data of this last flight are currently being calibrated and analyzed, and it will be very interesting to see how they compare to the synthesized model data shown in this study – in particular if the field of view of SUMI were to include some regions comparable with the magnetic structures shown here.

Of course, it would be desirable to obtain measurements of the magnetic field in the transition region as proposed here from a space-based observatory and embedded into a suite of instruments that provide information on the magnetic field in the chromosphere and the corona as well. The SolmeX space mission (Peter *et al.*, 2012) would have provided such comprehensive measurements of the coronal magnetic field in the solar upper atmosphere, and was proposed to ESA recently. Continuing the theoretical and instrumental efforts, an opportunity might open up to compare the synthetic Stokes V data from the transition region presented here with actual observations.

Acknowledgements The author gratefully acknowledges the collaboration with B. Gudiksen and Å. Nordlund, which stood at the beginning of this project with the aim of deriving synthetic observations from coronal models. The author is particularly grateful to B. Gudiksen for sharing data used in this study. It is a pleasure to thank J. Trujillo Bueno for his comments on the manuscript.

References

Bingert, S., Peter, H.: 2011, Intermittent heating in the solar corona employing a 3D MHD model. *Astron. Astrophys.* **530**, A112.

Bingert, S., Peter, H.: 2013, Nanoflare heating in an active region 3D MHD coronal model. *Astron. Astrophys.* **550**, A30.

Brković, A., Peter, H.: 2004, Statistical comparison of transition region blinkers and explosive events. *Astron. Astrophys.* **422**, 709 – 716.

Centeno, R., Trujillo Bueno, J., Asensio Ramos, A.: 2010, On the magnetic field of off-limb spicules. *Astrophys. J.* **708**, 1579 – 1584.

De Rosa, M.L., Schrijver, C.J., Barnes, G., Leka, K.D., Lites, B.W., Aschwanden, M.J., Amari, T., Canou, A., McTiernan, J.M., Régnier, S., Thalmann, J.K., Valori, G., Wheatland, M.S., Wiegelmann, T., Cheung, M.C.M., Conlon, P.A., Fuhrmann, M., Inhester, B., Tadesse, T.: 2009, A critical assessment of nonlinear force-free field modeling of the solar corona for active region 10953. *Astrophys. J.* **696**, 1780 – 1791.

Dere, K.P., Landi, E., Mason, H.E., Monsignori Fossi, B.C., Young, P.R.: 1997, CHIANTI–an atomic database for emission lines. *Astron. Astrophys. Suppl.* **125**, 149 – 173.

Gudiksen, B., Nordlund, Å.: 2002, Bulk heating and slender magnetic loops in the solar corona. *Astrophys. J. Lett.* **572**, L113 – L116.

Gudiksen, B., Nordlund, Å.: 2005a, An *ab initio* approach to the solar coronal heating problem. *Astrophys. J.* **618**, 1020 – 1030.

Gudiksen, B., Nordlund, Å.: 2005b, An *ab initio* approach to solar coronal loops. *Astrophys. J.* **618**, 1031 – 1038.

Hagyard, M.J., Teuber, D., West, E.A., Tandberg-Hanssen, E., Henze, W. Jr., Beckers, J.M., Bruner, M., Hyder, C.L., Woodgate, B.E.: 1983, Vertical gradients of sunspot magnetic fields. *Solar Phys.* **84**, 13 – 31.

Hansteen, V.H., Hara, H., De Pontieu, B., Carlsson, M.: 2010, On redshifts and blueshifts in the transition region and corona. *Astrophys. J.* **718**, 1070 – 1078.

Harrison, R.A., Lang, J., Brooks, D.H., Innes, D.E.: 1999, A study of extreme ultraviolet blinker activity. *Astron. Astrophys.* **351**, 1115 – 1132.

Harrison, R.A., Harra, L.K., Brković, A., Parnell, C.E.: 2003, A study of the unification of quiet-Sun transient-event phenomena. *Astron. Astrophys.* **409**, 755 – 764.

Henze, W. Jr., Tandberg-Hanssen, E., Hagyard, M.J., West, E.A., Woodgate, B.E., Shine, R.A., Beckers, J.M., Bruner, M., Hyder, C.L., West, E.A.: 1982, Observations of the longitudinal magnetic field in the transition region and photosphere of a sunspot. *Solar Phys.* **81**, 231 – 244.

Kobayashi, K., Kano, R., Trujillo-Bueno, J., Ramos, A.A., Bando, T., Belluzzi, L., Carlsson, M., De Pontieu, R.C.B., Hara, H., Ichimoto, K., Ishikawa, R., Katsukawa, Y., Kubo, M., Sainz, R.M., Narukage, N., Sakao, T., Stepan, J., Suematsu, Y., Tsuneta, S., Watanabe, H., Winebarger, A.: 2012, The chromospheric Lyman-alpha SpectroPolarimeter: CLASP. In: Golub, L., De Moortel, I., Shimizu, T. (eds.) *Fifth Hinode Science Meeting* **CS-456**, 233 – 240.

Lin, H., Penn, M.J., Tomczyk, S.: 2000, A new precise measurement of the coronal magnetic field strength. *Astrophys. J.* **541**, L83 – L86.

Lites, B.W.: 2001, Space-based instrumentation for inference of the solar magnetic field. In: Mathys, G., Solanki, S.K., Wickramasinghe, D.T. (eds.) *Magnetic Fields Across the Hertzsprung-Russell Diagram* **CS-248**, 553 – 562.

Peter, H.: 1999, Analysis of transition-region emission line profiles from full-disk scans of the Sun using the sumer instrument on SOHO. *Astrophys. J.* **516**, 490 – 504.

Peter, H.: 2000, Multi-component structure of solar and stellar transition regions. *Astron. Astrophys.* **360**, 761 – 776.

Peter, H.: 2001, On the nature of the transition region from the chromosphere to the corona of the Sun. *Astron. Astrophys.* **374**, 1108 – 1120.

Peter, H., Bingert, S.: 2012, Constant cross section of loops in the solar corona. *Astron. Astrophys.* **548**, A1.

Peter, H., Brković, A.: 2003, Explosive events and transition region blinkers: time variability of non-Gaussian quiet Sun EUV spectra. *Astron. Astrophys.* **403**, 287 – 295.

Peter, H., Judge, P.G.: 1999, On the Doppler shifts of solar UV emission lines. *Astrophys. J.* **522**, 1148 – 1166.

Peter, H., Gudiksen, B., Nordlund, Å.: 2004, Coronal heating through braiding of magnetic field lines. *Astrophys. J. Lett.* **617**, L85 – L88.

Peter, H., Gudiksen, B., Nordlund, Å.: 2006, Forward modeling of the corona of the Sun and solar-like stars: from a three-dimensional magnetohydrodynamic model to synthetic extreme-ultraviolet spectra. *Astrophys. J.* **638**, 1086 – 1100.

Peter, H., Abbo, L., Andretta, V., Auchère, F., Bemporad, A., Berrilli, F., Bommier, V., Braukhane, A., Casini, R., Curdt, W., Davila, J., Dittus, H., Fineschi, S., Fludra, A., Gandorfer, A., Griffin, D., Inhester, B., Lagg, A., Degl'Innocenti, E.L., Maiwald, V., Sainz, R.M., Pillet, V.M., Matthews, S., Moses, D., Parenti, S., Pietarila, A., Quantius, D., Raouafi, N.-E., Raymond, J., Rochus, P., Romberg, O., Schlotterer, M., Schühle, U., Solanki, S., Spadaro, D., Teriaca, L., Tomczyk, S., Bueno, J.T., Vial, J.-C.: 2012, Solar magnetism eXplorer (SolmeX). Exploring the magnetic field in the upper atmosphere of our closest star. *Exp. Astron.* **33**, 271 – 303.

Schrijver, C.J., Zwaan, C.: 2000, *Solar and Stellar Magnetic Activity*, Cambridge Univ. Press, Cambridge.

Stenflo, J.O.: 1994, *Solar Magnetic Fields*, Kluwer, Dordrecht.

Trujillo Bueno, J., Štěpán, J., Casini, R.: 2011, The Hanle effect of the hydrogen Lyα line for probing the magnetism of the solar transition region. *Astrophys. J. Lett.* **738**, L11.

Štěpán, J., Trujillo Bueno, J., Carlsson, M., Leenaarts, J.: 2012, The Hanle effect of Lyα in a magnetohydrodynamic model of the solar transition region. *Astrophys. J. Lett.* **758**, L43.

West, E.A., Porter, J.G., Davis, J.M., Gary, G.A., Noble, M.W., Lewis, M., Thomas, R.J.: 2004, The Marshall Space Flight Center solar ultraviolet magnetograph. In: Hasinger, G., Turner, M.J.L. (eds.) *Society of Photo-Optical Instrumentation Engineers (SPIE) Conference Series* **5488**, 801 – 812.

West, E., Cirtain, J., Kobayashi, K., Davis, J., Gary, A., Adams, M.: 2011, MgII linear polarization measurements using the MSFC solar ultraviolet magnetograph. In: *Society of Photo-Optical Instrumentation Engineers (SPIE) Conference Series* **8160**, 816010.

White, S.M.: 2005, Radio measurements of coronal magnetic fields. In: *Chromospheric and Coronal Magnetic Fields* **SP-596**, ESA, Noordwijk, CDROM 10.1.

Wilhelm, K., Curdt, W., Marsch, E., Schühle, U., Lemaire, P., Gabriel, A., Vial, J.-C., Grewing, M., Huber, M.C.E., Jordan, S.D., Poland, A.I., Thomas, R.J., Kühne, M., Timothy, J.G., Hassler, D.M., Siegmund, O.H.W.: 1995, SUMER – solar ultraviolet measurements of emitted radiation. *Solar Phys.* **162**, 189 – 231.

Woodgate, B.E., Brandt, J.C., Kalet, M.W., Kenny, P.J., Tandberg-Hanssen, E.A., Bruner, E.C., Beckers, J.M., Henze, W., Knox, E.D., Hyder, C.L.: 1980, The ultraviolet spectrometer and polarimeter on the solar maximum mission. *Solar Phys.* **65**, 73 – 90.

Young, P.R., Del Zanna, G., Landi, E., Dere, K.P., Mason, H.E., Landini, M.: 2003, CHIANTI – an atomic database for emission lines. VI. Proton rates and other improvements. *Astrophys. J. Suppl.* **144**, 135 – 152.

Zacharias, P., Bingert, S., Peter, H.: 2011a, Ejection of cool plasma into the hot corona. *Astron. Astrophys.* **532**, A112.

Zacharias, P., Bingert, S., Peter, H.: 2011b, Investigation of mass flows in the transition region and corona in a three-dimensional numerical model approach. *Astron. Astrophys.* **531**, A97.

DOI 10.1007/978-1-4939-2038-9_6
Reprinted from *Solar Physics* Journal, DOI 10.1007/s11207-013-0299-3

Magnetography of Solar Flaring Loops with Microwave Imaging Spectropolarimetry

D.E. Gary · G.D. Fleishman · G.M. Nita

Received: 31 December 2012 / Accepted: 2 April 2013 / Published online: 26 April 2013

Abstract We have developed a general framework for modeling gyrosynchrotron and free–free emission from solar flaring loops and used it to test the premise that 2D maps of source parameters, particularly the magnetic field, can be deduced from spatially resolved microwave spectropolarimetry data. We show quantitative results for a flaring loop with a realistic magnetic geometry, derived from a magnetic-field extrapolation, and containing an electron distribution with typical thermal and nonthermal parameters, after folding through the instrumental profile of a realistic interferometric array. We compare the parameters generated from forward-fitting a homogeneous source model to each line of sight through the folded image data cube both with the original parameters used in the model and with parameters generated from forward-fitting a homogeneous source model to the original (unfolded) image data cube. We find excellent agreement in general, but with systematic effects that can be understood as due to the finite resolution in the folded images and the variation of parameters along the line of sight, which are ignored in the homogeneous source model. We discuss the use of such 2D parameter maps within a larger framework of 3D modeling, and the prospects for applying these methods to data from a new generation of multifrequency radio arrays now or soon to be available.

1. Introduction

The magnetic structure of the solar corona plays a key role in all of solar activity. For example, in a recent dedicated review, Aschwanden (2008) identified ten outstanding problems

Coronal Magnetometry
Guest Editors: S. Tomczyk, J. Zhang, and T.S. Bastian

D.E. Gary (✉) · G.D. Fleishman · G.M. Nita
Physics Dept., New Jersey Institute of Technology, Newark, NJ, USA
e-mail: dgary@njit.edu

G.D. Fleishman
e-mail: gfleishm@njit.edu

G.M. Nita
e-mail: gnita@njit.edu

in solar physics. Five of them – hydrodynamics of coronal loops, magnetohydrodynamical (MHD) oscillations and waves (coronal seismology), coronal heating, magnetic reconnection, and particle acceleration – require measurement of coronal parameters, especially the magnetic field, *in or near the flaring region* and on dynamical time scales.

However, direct measurements of the magnetic field in the tenuous atmosphere are extremely difficult to make. Instead, the field strength and direction are measured at non-flaring times at the photospheric (or possibly chromospheric) boundary; specifically, vector fields are measured from full-Stokes polarized intensity of Zeeman-sensitive spectral lines with circular polarization, which gives the line-of-sight field strength and the linear polarization that in turn provides the transverse field. Then, to assess the coronal magnetic field, these measured photospheric fields are extended into the corona through potential or force-free field extrapolations. However, even extrapolations with excellent data can yield incorrect results (De Rosa *et al.*, 2009) due to several limitations: i) the photosphere does not meet the force-free condition on which the extrapolations are generally based, ii) the curved boundary of the solar surface and resulting near-limb foreshortening complicates the geometry of the extrapolation, iii) the line profiles on which the measurements are based can be affected by non-local-thermodynamic-equilibrium (non-LTE) and Doppler effects, and iv) the measurements are affected by the 180-degree ambiguity (only the angle, not the direction of the transverse field is measured), scattered light, and evolution of the region during the measurements. Some of these limitations can be addressed. For example, measurements at the more force-free chromospheric boundary are possible (*e.g.* Socas-Navarro *et al.*, 2006), vector photospheric measurements can be preprocessed, *i.e.* modified to approximate the force-free boundary condition, with reference to other observations such as Hα fibrils, within observational errors of the transverse photospheric-field measurements (Wiegelmann, Inhester, and Sakurai, 2006; Wiegelmann *et al.*, 2008), and techniques exist to resolve the 180-degree ambiguity (*e.g.* Metcalf *et al.*, 2006). But even so, these methods give rise to modeled, not measured, pre-event coronal magnetic fields, which cannot follow the relevant dynamical changes that occur in flares.

More indirect observational clues to the *coronal magnetic field* can sometimes be exploited, such as morphological tests at the level of the chromosphere (Hα fibrils aligned with magnetic-field direction, *e.g.* Wiegelmann *et al.*, 2008) and corona (extreme-ultraviolet, EUV, and soft X-ray loops, although these provide only the shape of field lines, and even this has been called into question by the work of Mok *et al.* (2008), who showed through 3D modeling that apparent loops based on brightness do not necessarily reveal the underlying field-line shapes). Direct coronal magnetic-field measurements through Zeeman-splitting of infrared lines have been attempted (Lin, Penn, and Tomczyk, 2000; Lin, Kuhn, and Coulter, 2004; Liu and Lin, 2008), and more are planned (Tomczyk, 2012), but they require a long accumulation time and apply only along extended lines of sight above the solar limb where the extrapolations are most difficult, which frustrates attempts at directly comparing observations and models. To properly address the outstanding theoretical problems cited by Aschwanden (2008), it is essential to seek additional, independent techniques for directly measuring the coronal field, especially the dynamically changing fields in the flaring region.

Diagnostics of the *coronal thermal structure* are obtainable with a combination of EUV filtergram images and spectral-line measurements, although problems such as atomic and ionic species abundances, multithermal plasma along the line of sight, and non-LTE effects make an interpretation ambiguous and difficult. Moreover, the emission-measure- (density-squared-) weighted brightness makes some regions of tenuous plasma too faint for such

diagnostic information, while any flaring regions tend to saturate the detectors. Information on the high-energy component of the flaring plasma requires soft- and hard-X-ray observations, thus requiring the piecing-together of information from multiple spacecraft, pertaining to different regions of the corona and generally available for only a subset of events.

We outline a practical method of coronal diagnostics that in principle can achieve the required dynamical measurement of coronal magnetic field, thermal plasma, and particles: broadband microwave imaging spectropolarimetry, augmented by sophisticated modeling and forward-fitting. The feasibility of this approach has already been proven by numerical tests (Bastian, Benz, and Gary, 1998; Bastian, 2006; Fleishman, Nita, and Gary, 2009), assuming a hypothetical, ideal radio heliograph providing data with arbitrarily high spatial resolution. The forward-fitting of actual radio spectra has been attempted with some success for a limited number of events, whose spatially integrated microwave emission (recorded in the form of total power spectra) could be modeled by a relatively uniform source or a combination of two uniform sources (Bastian, Fleishman, and Gary, 2007; Altyntsev *et al.*, 2008; Fleishman *et al.*, 2011, 2013). However, in the more common case of an inhomogeneous flaring region, the quantitative diagnostics of flaring loops requires imaging spectroscopy and polarimetry data, which have not yet been routinely available. Fortunately, the recent advances in radio interferometric imaging instruments, such as the *Jansky Very Large Array* (JVLA), *Expanded Owens Valley Solar Array* (EOVSA), and others, will soon provide for the first time the level of microwave imaging spectropolarimetry and unprecedented data quality necessary to deduce the key thermal and nonthermal plasma parameters, including magnetic-field strength, needed for detailed coronal diagnostics. It is therefore timely to explore the potential for these soon-to-be-realized instruments to exploit microwave imaging spectropolarimetry for the practical measurement of dynamically changing coronal plasma parameters.

In Section 2 we describe the methodology that we used to create a realistic model flaring loop and its multifrequency polarized radio emission for further study, using the EOVSA instrument profile as a specific example for comparison purposes. In Section 3 we describe the method of forward-fitting theoretically determined microwave spectra to each resolution element of the model to obtain 2D parameter maps. In Section 4 we describe quantitative comparisons of the fitted parameters with the model, to show that even with the finite spatial resolution and image quality expected from EOVSA, it is possible to obtain both quantitative and qualitative information on the dynamically changing plasma parameters, including magnetic-field strength and direction along the flaring loop. We conclude in Section 5, and provide an outline of a more ambitious 3D modeling framework that could be developed in the future to overcome the unavoidable distortions caused by finite resolution.

2. Modeling Framework

We present in Figure 1 a block diagram showing the steps in the modeling framework that will be described in this section. There are three main steps: i) create a model (first three blocks on the left in Figure 1), ii) calculate the multifrequency radio emission from the model (yellow block on the left in Figure 1), and iii) fit the calculated radio spectra (bottom, pink block on the left in Figure 1). However, to include the effects of finite resolution and noise introduced by an actual instrument, we also include the steps in the right column of Figure 1. We now describe each of these steps in turn.

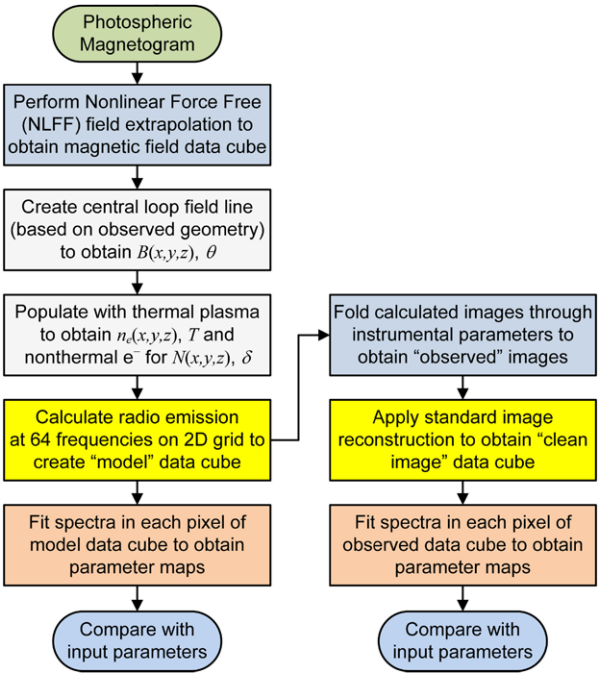

Figure 1 Block diagram showing the steps performed to create a flaring-loop model, which are used to calculate multifrequency radio emission from the model (the unfolded data cube), and to fold the images of the data cube through an actual instrument to obtain the folded data cube.

2.1. Generating the Flaring-Loop Model

To generate the spatial geometry of the flaring loop, we began with a tool that we developed, called the GX_simulator (a part of the Solarsoft (SSW) IDL distribution) (Nita *et al.*, 2011, 2012), which provides a graphical interface for creating and manipulating magnetic-field models including those generated from extrapolation of photospheric magnetograms. In the case used for illustration in this article, we began with a nonlinear force-free (NLFF) magnetic-field extrapolation of a *Hinode* vector magnetogram embedded in a wider-field *Michelson Doppler Imager* (MDI) magnetogram for Active Region 10956, taken on 18 May 2007, although we note that our results are not highly dependent on the choice of magnetic-field model. We seek only a loop with a realistic geometry, in this case one with a broad range of magnetic field up to reasonably high magnetic-field strength, a moderately high mirror ratio, and asymmetric magnetic footpoints. With this tool, we identified a suitable magnetic-field line to use as the central field line of the loop (footpoint fields $B_1 = 1090$ G, $B_2 = 664$ G; mirror ratio $B_1/B_{\rm min} = 9.1$), loop length $l = 6.478 \times 10^9$ cm, and then imposed the thermal plasma and an energetic electron distribution with parameterized spatial extent both along $[s]$ and across $[x, y]$ the loop, wider at the apex and tapering at the footpoints in accordance with the conservation of magnetic flux. We parameterized the thermal-electron distribution with a temperature $T = 2 \times 10^7$ K; a thermal density that is hydrostatic in height $[z]$

$$n_{\rm e} = n_0 \exp\left[-\left(\frac{x}{a}\right)^2 - \left(\frac{y}{b}\right)^2\right] \exp\left[-\frac{z/R}{6.76 \times 10^{-8} T}\right], \quad (1)$$

where $n_0 = 5 \times 10^9$ cm^{-3} is the on-axis base density and $a = b = 4.37$ Mm are the off-axis scale distances at the loop apex (point where $B = B_{\rm min}$), perpendicular to the loop, scaling

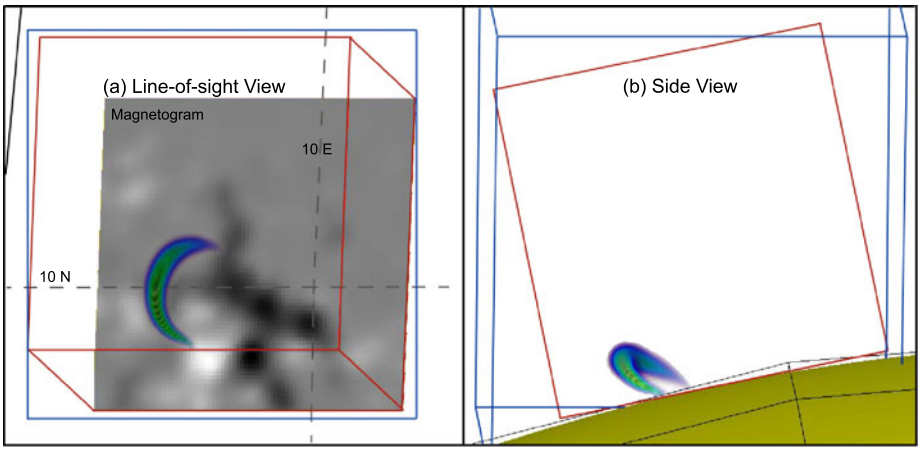

Figure 2 Left: (a) Line-of-sight view of the model loop, showing the base magnetogram ($162'' \times 162''$) as the gray-scale image and the distribution of nonthermal electrons. Right: (b) Same as in left panel (a), but shown as a side-view aligned with the line-of-sight. The solar surface is shown in yellow at the base of the loop.

at other points on the axis as $B_{\min}/B$; a number density of nonthermal electrons

$$N_{\rm e} = n_{\rm b} \exp\left[-\left(\frac{x}{a}\right)^2 - \left(\frac{y}{b}\right)^2\right] \exp\left[-2\left(\frac{s - s_0}{l}\right)^2\right], \tag{2}$$

where $n_{\rm b} = 3 \times 10^6$ cm^{-3}, a and b are as above, and $s_0 = -0.287l$ is the location of the peak of the nonthermal density relative to the loop apex, negative in the direction toward B_1; a power law in energy [$N_{\rm e} = (\delta - 1)(n_{\rm b}/E_0)(E/E_0)^{-\delta}$] with index $\delta = 5$; and high- and low-energy cutoffs $E_{\max} = 10$ MeV and $E_{\min} = 0.1$ MeV, respectively. For this model, we used an isotropic pitch-angle distribution, and the only electron parameters that vary spatially are $n_{\rm e}$ and $N_{\rm e}$.

We emphasize that for this model it is not essential that we have a physically consistent set of parameters; we seek only a model with sufficient complexity to be a good test of parameter recovery via spatially resolved microwave spectropolarimetry. The spatial complexity comes from the spatial variation of B, θ (angle between the line of sight and B), $n_{\rm e}$, and $N_{\rm e}$. In principle, we could have allowed the electron-energy parameters T, δ, $E_{\max}$, $E_{\min}$, and the pitch angle to vary spatially as well, but although this variation would be interesting to study (and indeed is planned for future work), it was not deemed essential to the point of this article.

Once the loop and electron geometries are set, the loop may be oriented for any line of sight prior to calculating the emission. For this test we oriented the loop near the center of the disk (heliographic coordinates E12, N11), but chose a central field line with a considerable angle to the line of sight, so that the variation of the magnetic-field direction along the loop ranges from $64^\circ < \theta < 123^\circ$. Figure 2 shows the final geometry of the loop.

2.2. Generating Microwave Emission from the Model

Once the parameters of the flaring loop were set and the line-of-sight orientation was chosen, we calculated the microwave emission using the hybrid fast codes of Fleishman and

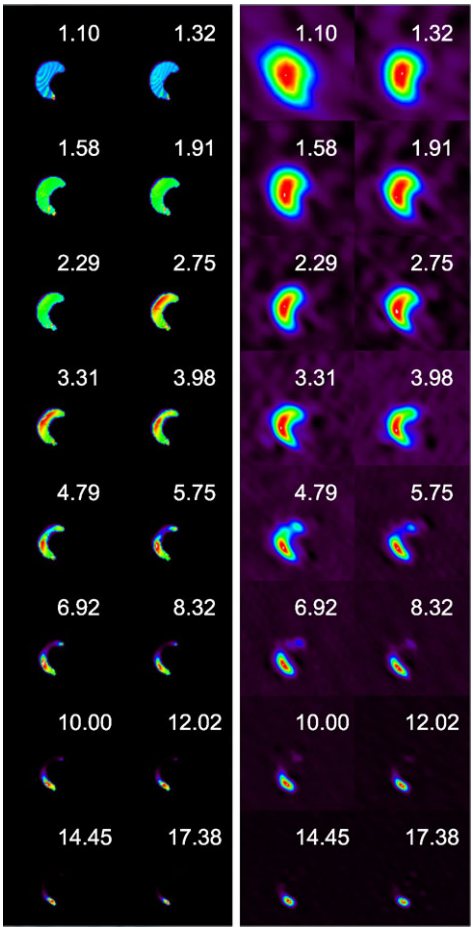

Figure 3 Left: LCP images from the model at 16 selected frequencies distributed logarithmically from 1 – 18 GHz. The number in each panel gives the frequency for that image [GHz]. The stripes in the lower-frequency images are predicted by the theory and are caused by brightness variations associated with the discrete, lower harmonics of the gyrofrequency. Right: Same as in left panel, but now folded through the EOVSA instrument and reconstructed using the CLEAN algorithm. The spatial extent of each image is $196'' \times 196''$.

Kuznetsov (2010). The emission from 1 – 18 GHz was calculated for each line-of-sight, with a spatial (3D voxel) resolution of $2''$ on a side, at 64 logarithmically spaced frequencies in two polarizations. The hybrid codes use exact calculations for the low harmonics of the gyrofrequency, and highly accurate but approximate calculations for the high harmonics, separately in the two magneto–ionic modes, from which the two senses of circular polarization can be derived. The calculation was performed considering each voxel as a homogeneous source using the parameters computed at the center of the voxel, but the resulting brightness of a 2D pixel takes into account the correct radiative transfer including frequency-dependent mode coupling (White, Thejappa, and Kundu, 1992; Bastian, 1995) through all voxels along the line-of-sight. These calculations were computed directly from within the GX_simulator tool, to generate the entire set of simulated multifrequency images (data cube) in just a few minutes. Figure 3 (left panel) shows a 16-image sampling of the 64-image data cube in left circular polarization (LCP), although the calculations were computed in both right circular and left circular polarizations (RCP and LCP, respectively).

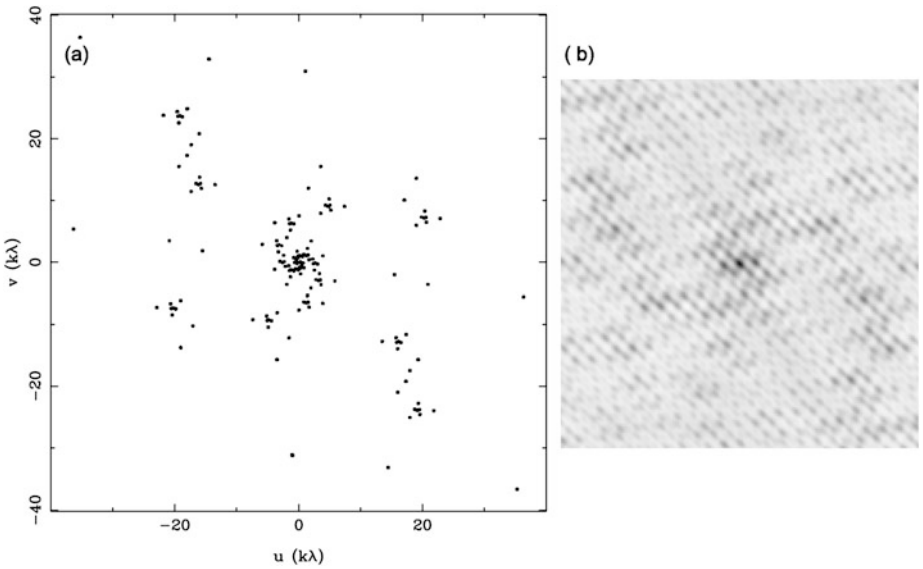

Figure 4 Left: Sampling in the Fourier $[u–v]$ plane used for the simulation. This represents the 78 baselines of EOVSA at a frequency of 10 GHz, for a time near local noon when the Sun is at $+15°$ declination. Right: The point-spread-function (synthesized beam) corresponding to the $u–v$ coverage in the left panel. The area shown is $256'' \times 256''$, and the gray-scale is inverted for clarity.

2.3. Folding Emission Through the EOVSA Instrument Profile

Since our goal is to assess the possibility of recovering flaring-loop parameters from real data, we must choose a specific instrument through which to fold the input data generated from the model. For this we selected EOVSA (Gary *et al.*, 2011), which is a 13-antenna array currently under construction for completion in 2013. Figure 4 shows the "snapshot" $u–v$ coverage and corresponding point-spread-function (synthesized beam) of EOVSA at a frequency of 10 GHz, near local noon on a date when the Sun was at a declination of $+15°$.

Using the Miriad radio-interferometric-imaging package (Sault, Teuben, and Wright, 2011), it is straightforward to use the individual images from the data cube as a brightness model, Fourier-transform the brightness model to obtain the visibilities in the $u–v$ plane, and then sample these visibilities with the $u–v$ coverage of Figure 4 to obtain a model-visibilities data set for each frequency and polarization. To these visibilities were added a realistic level of random noise representing the thermal noise of the system (4500 K), and the standard CLEAN algorithm was then used to generate reconstructed images representing the images that EOVSA would actually produce. Figure 3 (right) shows the reconstructed LCP images for the same 16 frequencies as in Figure 3 (left), where now the effect of the finite, frequency-dependent resolution is apparent. From the original (unfolded) 64-image data cube we thus constructed a parallel 64-image folded data cube representing the EOVSA reconstructed images in each circular polarization.

2.4. Comparing the Unfolded Model with the Folded Model

An alternative to viewing the datacube as a set of multifrequency images is to consider the third (spectral) dimension along various lines of sight, which provides spatially resolved, polarized brightness-temperature spectra. Figure 5 shows a comparison of polarized

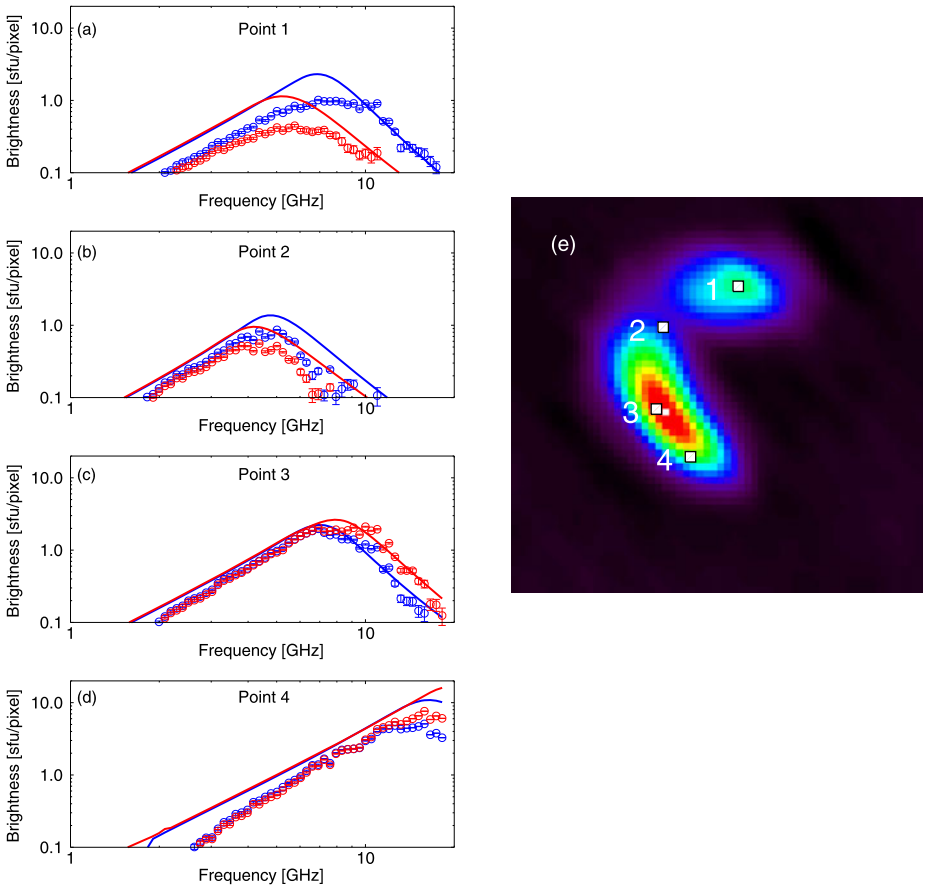

Figure 5 (a) – (d) Comparison of raw spectra for four selected pixels in both the unfolded (lines) and folded (symbols) data cubes. Red corresponds to RCP, while blue is LCP. (e) Folded RCP image at 6.3 GHz, 82″ on a side, showing the locations of the four points whose spectra are plotted in (a) – (d).

brightness-temperature spectra sampled at a few locations in the loop to show how the finite resolution and image reconstruction affect the spectra. In general, the folded spectra quite faithfully agree with the unfolded spectra, although there are systematic differences such as the lower flux density at low frequencies (due to the finite spatial resolution) and the corresponding steeper slope. This steeper slope also subtly shifts the peak of the spectrum of the folded data cube to slightly higher frequencies. In addition, the finite dynamic range causes the weaker emission at high frequencies (*i.e.* that near point 2, whose spectrum is shown in Figure 5(b)) to be poorly reconstructed if there is bright emission in the same image. The dynamic range of the images shown in Figure 3 (right) ranges from 100:1 to 200:1. Various strategies exist for improving the dynamic range of reconstructed images, such as the use of frequency synthesis (Conway, Cornwell, and Wilkinson, 1990; Sault and Wieringa, 1994; Rau and Cornwell, 2011), but they were not used in this study.

Figure 5(a) – (d) shows that the spectral differences from pixel to pixel in the images, especially shifts in the peak frequency, are greater than the differences between unfolded and folded spectra for a given pixel. This suggests that the spectral shape of the folded

spectra are dominated by changes in physical parameters rather than by the effects of finite spatial resolution, and hence spectral fits to the folded spectra promise to provide reasonable estimates of source parameters. We now proceed to demonstrate this by fitting both unfolded and folded spectra at each pixel in the two data cubes and comparing the fitted parameters.

3. Fitting Framework

Once the two parallel 2D data cubes (unfolded and folded) are available, we went through the 2D field-of-view pixel by pixel and forward-fitted a homogeneous source to the spectra via the downhill-simplex minimization algorithm (Press, Flannery, and Teukolsky, 1986), with some modifications detailed by Fleishman, Nita, and Gary (2009) to avoid local minima. The method is to choose a set of $N_{\rm par}$ parameters to fit, make an initial guess for parameter values, calculate the emission for that set of parameters using the fast codes, compare the fit with the data using a standard reduced-chi-squared [χ^2_ν] metric, adjust the parameters via the simplex method, and repeat this until some specified criterion for stopping has been met. As described by Fleishman, Nita, and Gary (2009), once a minimum is found, the solution is "shaken" by strongly perturbing the solution vector, and the algorithm is repeated to perhaps find the same or a different minimum solution. This is repeated until either the same minimum has been found several times or the number of shakes is $N_{\rm par}+6$. At the end of this procedure, the solution with the smallest χ^2_ν is taken. For the results in this article, the fitting was made using $N_{\rm par}=6$, *i.e.* B, θ, $n_{\rm e}$, $N_{\rm e}$, δ, and $E_{\rm min}$. The value of $E_{\rm max}$ is not well constrained for emission to 18 GHz, and was kept fixed at 5 MeV (a factor of two lower than the value actually used in the model).

For illustration, Figure 6(a)–(d) shows the same four "observed" dual-polarization spectra from the unfolded data cube as in Figure 5(a)–(d), with the minimum χ^2_ν fits overlaid, while Figure 7(a)–(d) shows the same for the folded data cube. Four of the parameters of each fit are shown in each panel: the magnetic-field strength [B], the angle of B to the line of sight [θ], the number density of nonthermal electrons [$N_{\rm e}$], and the electron powerlaw index [δ]. Because the fits were performed at every pixel in the 2D image cube, each parameter can be displayed as a 2D parameter map, as shown for the magnetic-field strength parameter B in Figures 6(e) and 7(e). Although the fits in Figure 6(a)–(d) look excellent, they are nevertheless an approximation since the spectral points are based on radiative transfer through an inhomogeneous 3D model while the fits were made assuming a homogeneous source, albeit an independent one, at each pixel.

The homogeneous source fits to the folded spectra in Figure 7(a)–(d) also adequately fit the points in each spectrum, but the fitted parameters listed in each panel differ from those of the unfolded data cube from which they are derived. Table 1 shows the comparison of parameters for the four points sampled in the figures, where $\Delta B_{\%} = (B_{\rm f} - B_{\rm unf})/B_{\rm unf}$ [percent], $\Delta\delta = \delta_{\rm f} - \delta_{\rm unf}$, and $N_{\rm e,rat} = N_{\rm e,f}/N_{\rm e,unf}$. The fitted parameters for Points 2–4 agree quite well; the magnetic-field strengths agree to within 15 %, the powerlaw indexes agree to within 0.5, and the densities agree to well within an order of magnitude; the latter is remarkable because in addition to differences in spectra themselves, variations of two other parameters, $E_{\rm min}$ and δ, recovered differently for the folded and unfolded models, also affect the value of $N_{\rm e}$. However, the agreement is poorer for Point 1 because of the finite resolution of the folded images for the compact source at the northern footpoint of the loop (Figure 3), which results in a considerable shift of the spectral peak in the folded compared with the unfolded spectra, apparent from Figure 5(a). We discuss these results in more detail below and compare them to the parameters actually used in the model.

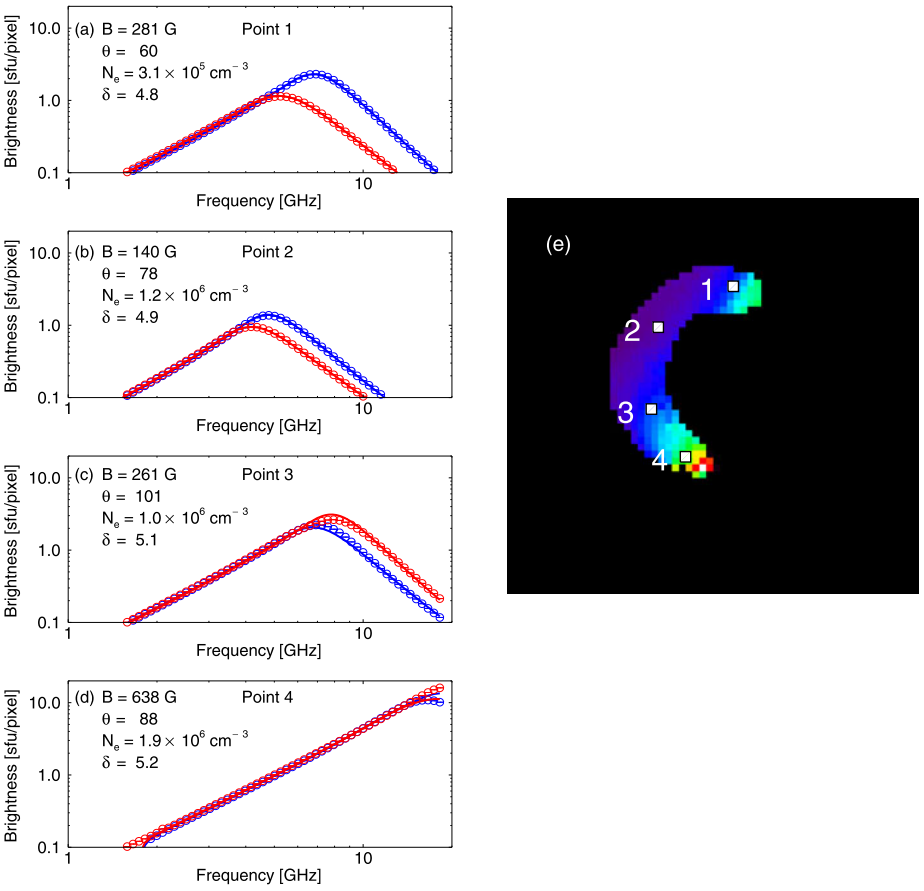

Figure 6 (a) – (d) Overlay of spectra (symbols) from the unfolded data cube and the fits (lines) for the same four selected pixels as in Figure 5. Red corresponds to RCP, while blue is LCP. (e) An example 2D parameter map [total B], $82''$ on a side, derived from the fits to the unfolded data cube, with the locations of the four points in (a) – (d) indicated by white squares.

4. Results

Comparing the B-parameter maps of Figures 6(e) and 7(e), it is clear that the best agreement is found along the central spine of the loop, with a poorer agreement at the edges, where the effects of the finite resolution of the folded images is most pronounced. To investigate the potential for obtaining spatially resolved parameters along a flaring loop, we show in Figure 8 the run of parameters along the spine of the loop, at the locations of the points shown in Figure 8(e). In agreement with the results of Fleishman, Nita, and Gary (2009), we find that the fit parameters from the unfolded data cube (green lines) in Figure 8(a) – (d), representing data from an "ideal" radio heliograph with infinite spatial resolution, agree very well with the model (gray lines) at nearly every point. New in this work, however, are the purple lines that represent the parameters derived from the folded data cube with its finite resolution. Even in this case, the magnetic-field strength (Figure 8(d)) qualitatively agrees well over the entire length of the loop, and even quantitatively over about 2/3 of the loop (the region from 6 – 47 Mm in the figure). Likewise, the other parameters also agree

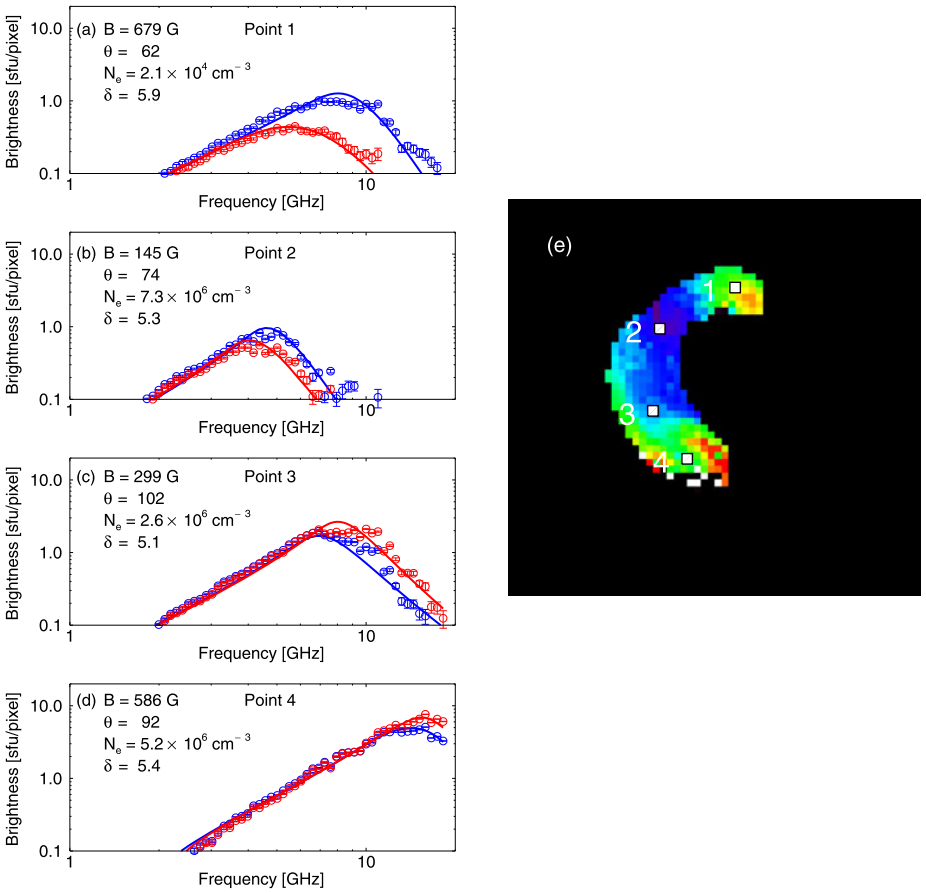

Figure 7 (a) – (d) Overlay of spectra (symbols) from the folded data cube and the fits (lines) for the same four selected pixels as in Figure 5. Red corresponds to RCP, while blue is LCP. (e) The 2D parameter map of total B, $82''$ on a side, derived from the fits to the folded data cube, with the locations of the four points in (a) – (d) indicated by white squares.

Table 1 Comparison of fit parameters for unfolded (Figure 6(a) – (d)) and folded (Figure 7(a) – (d)) spectra.

(1) Point	(2) $B_{\rm unf}$	(3) $B_{\rm f}$	(4) $\Delta B_{\%}$	(5) $\delta_{\rm unf}$	(6) $\delta_{\rm f}$	(7) $\Delta\delta$	(8) $N_{\rm e,unf}$	(9) $N_{\rm e,f}$	(10) $N_{\rm e,rat}$
1	281	679	141	4.8	5.9	+1.1	3.1×10^5	2.1×10^4	0.07
2	140	145	3.5	4.9	5.3	+0.4	1.2×10^6	7.3×10^6	6.1
3	261	299	14.6	5.1	5.1	0.0	1.0×10^6	2.6×10^6	2.6
4	638	586	−8.2	5.2	5.4	+0.2	1.9×10^6	5.2×10^6	2.7

tolerably well except at each end of the loop where distortions in the spectra caused by the finite resolution have the strongest effect. The error bars derived from the goodness of the spectral fits increase near the ends of the loop, and thus give a reasonable indication of where the parameters are less well determined.

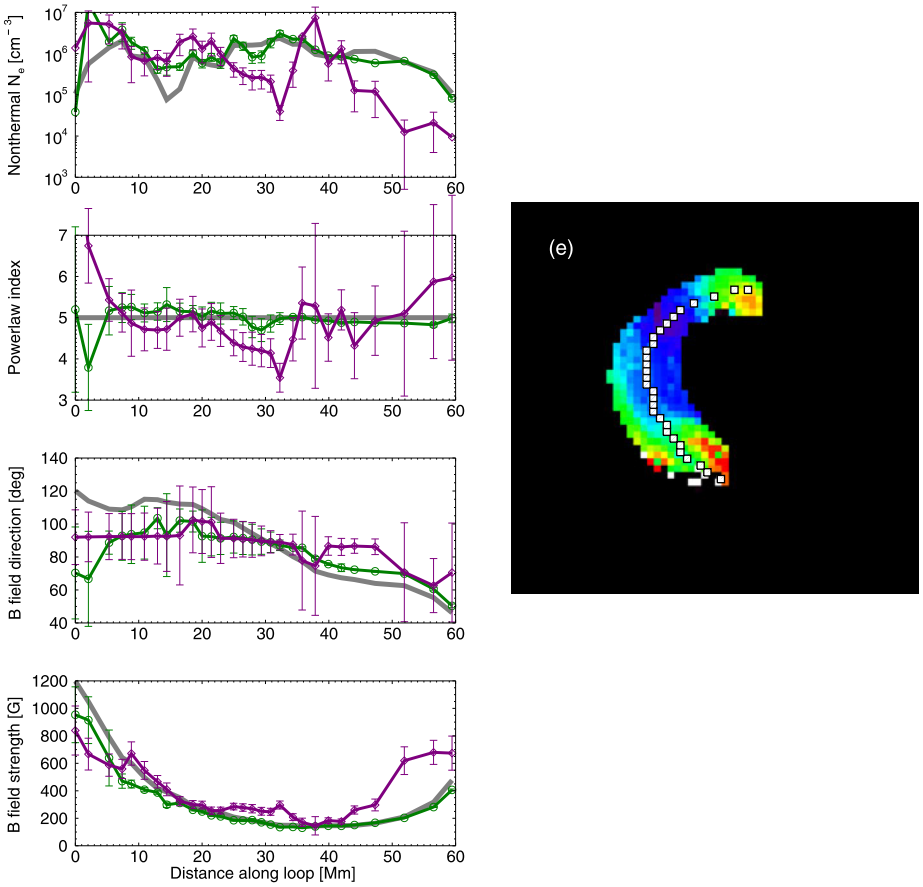

Figure 8 Comparison of parameters derived from the model (thick gray line), fits to the unfolded data (green line with open circles), and fits to the folded data (purple line with open diamonds) for positions [Mm] along the loop shown by the white squares in (e). The zero position corresponds to the southern footpoint of the model loop. The error bars shown are proportional to the formal errors of the corresponding spectral fits. (a) Model and fit parameters for energetic electron density [N_e]. (b) Model and fit parameters for powerlaw index [δ]. (c) Model and fit parameters for angle [θ] of B relative to the line of sight. (d) Model and fit parameters for magnetic field strength [B]. (e) Same 2D parameter map as in Figures 6(e) and 7(e), 82″ on a side, but now with 29 points along the spine of the loop, indicated by white squares, whose parameters are plotted in (a) – (d).

Another useful comparison is of the 2D parameter maps themselves, which are shown in pairs (unfolded on the left and folded on the right of each pair) in Figure 9. Below each pair is a color bar showing the range of the depicted parameter. Arguably the best-determined parameters, at least along the spine of the loop, are the magnetic parameters B and θ, because the key spectral features that determine these, the location of the peak frequency and the polarization, are robustly measured in the folded spectra. Although N_e and δ vary more erratically along the loop, their general values still compare well with those of the folded maps and the model, and represent a huge advance over what has been possible with existing radio instruments.

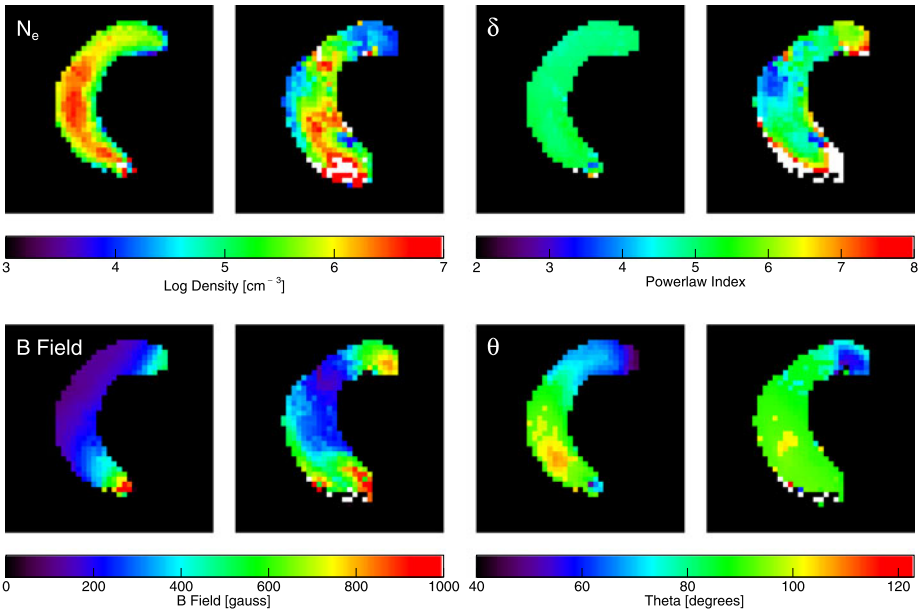

Figure 9 Comparison of 2D parameter map pairs, each 82″ on a side, for the unfolded (left) and folded (right) data cubes in each of the four parameters. The log density of nonthermal electrons [N_e] is shown at the upper left, the powerlaw index [δ] at the upper right, the B field at the lower left, and the angle [θ] of B to the line of sight at the lower right. Edge effects due to finite resolution are observed in the folded parameter maps, but are largely absent from the unfolded maps.

5. Discussion and Conclusions

The result shown in Figure 9 is derived for a single instant in time and can be repeated with EOVSA for independently measured spectra once per second to yield a powerful new tool for following the dynamically changing particle and field parameters in flaring loops. We conclude that with the advent of new, broadband, microwave-imaging instruments, the technique of microwave-imaging spectropolarimetry will soon become a viable and important means of obtaining dynamic, 2D parameter maps of flares. Figure 10 shows the procedure that one might use to obtain movies of such 2D parameter maps, which requires no 3D modeling and employs only measured radio data. One simply starts with the observed, multifrequency images, and fits the polarized spectra in each pixel of the images using a specified set of parameters, as we have shown above. If the χ^2_ν of the fits is generally not close to unity, it will suggest that some important physics is missing, and the addition of parameters such as pitch-angle non-isotropy and/or alteration of the electron-energy distribution is warranted, which can be added based on physically motivated trial-and-error. Once the fits are acceptable for a given time sample, the procedure is repeated for the next time step until the dynamic maps are obtained.

Although this procedure is possible and is a huge advance over what has been possible before, our results above have shown that finite resolution, finite dynamic range, and systematic effects from image reconstruction all play a role in distorting the measured microwave spectra. These effects can be reduced by improving the resolution and imaging capability of the instrument, which is an important motivation for constructing the high-performance *Frequency Agile Solar Radiotelescope* (FASR: Gary and Keller, 2004). Even with FASR,

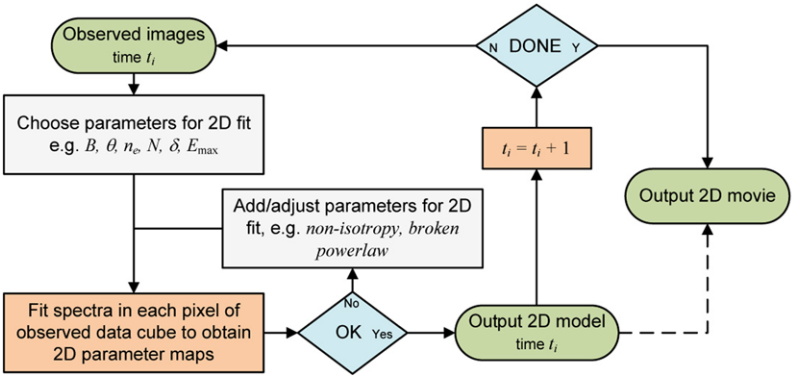

Figure 10 The steps performed to create 2D parameter-map movies from the data cube obtained from an actual instrument (the folded data cube).

however, the measured spectra would still represent emission from a range of parameters along the line of sight while the parameter fitting that we have described is achieved assuming a homogeneous source. Meanwhile, a great deal of useful information on magnetic field, thermal plasma, and energetic particles is available from spacecraft- and ground-based instruments, but was not used in the above scenario.

Figure 11 integrates the 2D information from Figure 10 with elements of the 3D modeling from Figure 1, and also incorporates all available data from other wavelengths. In this scheme, the 2D parameter maps merely provide a guide to 3D modeling. The 3D geometry starts from a model of the magnetic field, which is shown in Figure 11 as a magnetic-field extrapolation, but could be obtained by some other means such as MHD numerical modeling. Within this geometry one chooses the relevant field regions involved in flaring, using morphological information from radio, EUV, X-rays, or other data. One then populates the magnetic model with a suitable population of plasma and energetic particles, and it is here that the 2D parameter maps provide guidance, along with parameters obtained similarly from other wavelength regimes. The key step is to then use the populated 3D model to calculate emission (shown as radio emission in the figure, but EUV, X-ray, and other emissions can also be calculated from the model) and fold it through the relevant instrument(s) making the observations. The ultimate comparison then is made with the observed and the folded model images.

This approach completely side-steps problems of finite resolution, finite dynamic range, image reconstruction, and even homogeneous *vs* inhomogeneous sources. If the modeled images match the observed ones, one then accepts the entire 3D model. In the more likely case of a mismatch, however, one returns to adjust the choice of field regions or plasma and particle populations. This step will provide the key physical insights into the flaring process. Here particle-energy and pitch-angle distributions predicted from various levels of wave–particle interactions may be tried, or any of a large number of other adjustments. If this procedure does not converge, it may be that one must follow the dashed line on the right, and modify the magnetic model. Here key insights into the limitations and perhaps refinements of magnetic-field extrapolations, MHD simulations, or even new approaches to magnetic-field modeling will be stimulated. Here information from new magnetic-field measurement techniques can be incorporated, such as chromospheric magnetograms, Zeeman measurements of infrared coronal emission, measurements using the Hanlé effect, and others.

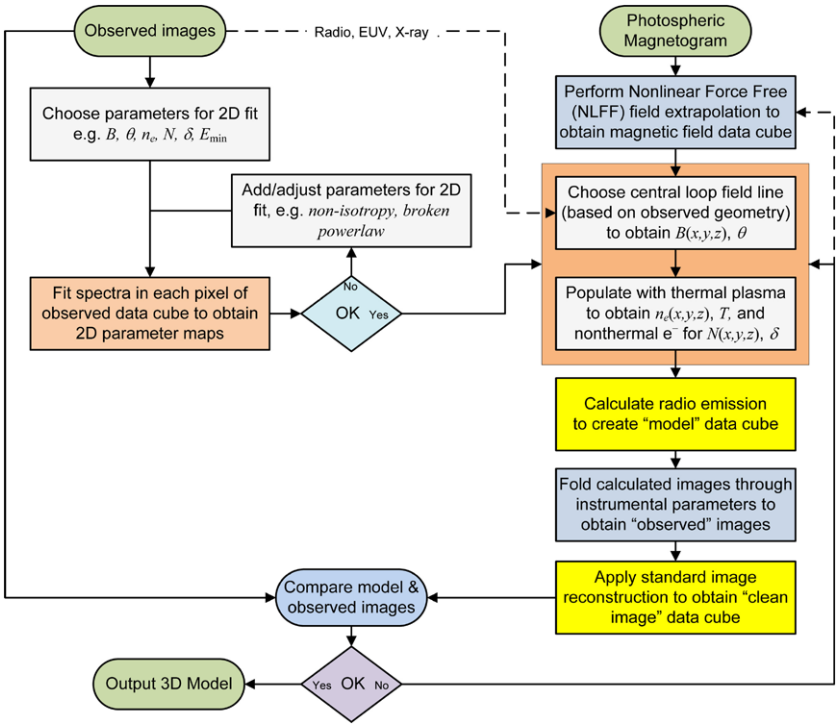

Figure 11 The 2D parameter maps obtained by the procedure of Figure 10 into a larger, integrated scheme of 3D modeling that also uses all available data from other wavelength regimes.

This forward-fitting approach is analogous to terrestrial weather modeling, and is a large and complex endeavor that will require the efforts of a broad segment of the solar community (Fleishman *et al.*, 2010). We anticipate that by working together, we can succeed in making true progress in understanding the physics of magnetic reconnection, particle acceleration, and the other areas of research noted in the Introduction. The ability of microwave imaging spectropolarimetry to make dynamic plasma, particle, and magnetic-field measurements, which we have demonstrated here, makes it an important tool in this endeavor.

Acknowledgements This work was supported in part by NSF grants AGS-0961867, AST-0908344, AGS-1250374 and NASA grants NNX10AF27G and NNX11AB49G to the New Jersey Institute of Technology. This work also benefited from workshop support from the International Space Science Institute (ISSI).

References

Altyntsev, A.T., Fleishman, G.D., Huang, G.-L., Melnikov, V.F.: 2008, A broadband microwave burst produced by electron beams. *Astrophys. J.* **677**, 1367 – 1377. doi:10.1086/528841.

Aschwanden, M.J.: 2008, Keynote address: outstanding problems in solar physics. *J. Astrophys. Astron.* **29**, 3 – 16. doi:10.1007/s12036-008-0002-5.

Bastian, T.S.: 1995, Angular scattering of radio waves: implications for mode coupling in the solar corona. *Astrophys. J.* **439**, 494 – 498. doi:10.1086/175190.

Bastian, T.S.: 2006, Magnetic field measurements in flare loops and CMEs. In: Casini, R., Lites, B.W. (eds.) *Solar Polarization 4* **CS-358**, Astron. Soc. Pac., San Francisco, 173.

Bastian, T.S., Benz, A.O., Gary, D.E.: 1998, Radio emission from solar flares. *Annu. Rev. Astron. Astrophys.* **36**, 131 – 188. doi:10.1146/annurev.astro.36.1.131.

Bastian, T.S., Fleishman, G.D., Gary, D.E.: 2007, Radio spectral evolution of an X-ray-poor impulsive solar flare: implications for plasma heating and electron acceleration. *Astrophys. J.* **666**, 1256 – 1267. doi:10.1086/520106.

Conway, J.E., Cornwell, T.J., Wilkinson, P.N.: 1990, Multi-frequency synthesis – a new technique in radio interferometric imaging. *Mon. Not. Roy. Astron. Soc.* **246**, 490.

De Rosa, M.L., Schrijver, C.J., Barnes, G., Leka, K.D., Lites, B.W., Aschwanden, M.J., Amari, T., Canou, A., McTiernan, J.M., Régnier, S., Thalmann, J.K., Valori, G., Wheatland, M.S., Wiegelmann, T., Cheung, M.C.M., Conlon, P.A., Fuhrmann, M., Inhester, B., Tadesse, T.: 2009, A critical assessment of nonlinear force-free field modeling of the solar corona for active region 10953. *Astrophys. J.* **696**, 1780 – 1791. doi:10.1088/0004-637X/696/2/1780.

Fleishman, G.D., Kuznetsov, A.A.: 2010, Fast gyrosynchrotron codes. *Astrophys. J.* **721**, 1127 – 1141. doi:10.1088/0004-637X/721/2/1127.

Fleishman, G.D., Nita, G.M., Gary, D.E.: 2009, Dynamic magnetography of solar flaring loops. *Astrophys. J. Lett.* **698**, L183 – L187. doi:10.1088/0004-637X/698/2/L183.

Fleishman, G., Gary, D., Nita, G., Alexander, D., Aschwanden, M., Bastian, T., Hudson, H., Hurford, G., Kontar, E., Longcope, D., Mikic, Z., DeRosa, M., Ryan, J., White, S.: 2010, Uncovering mechanisms of coronal magnetism via advanced 3D modeling of flares and active regions. arXiv:1011.2800.

Fleishman, G.D., Kontar, E.P., Nita, G.M., Gary, D.E.: 2011, A cold, tenuous solar flare: acceleration without heating. *Astrophys. J. Lett.* **731**, L19. doi:10.1088/2041-8205/731/1/L19.

Fleishman, G.D., Kontar, E.P., Nita, G.M., Gary, D.E.: 2013, Probing dynamics of electron acceleration with radio and X-ray spectroscopy, imaging, and timing in the 2002 April 11 solar flare. *Astrophys. J.* **768**, 1. doi:10.1088/0004-637X/768/1/1. arXiv:1303.4098.

Gary, D.E., Keller, C.U. (eds.): 2004, *Solar and Space Weather Radiophysics – Current Status and Future Developments*, *Astrophys. Space Science Lib.* **314**, Kluwer Academic. Dordrecht.

Gary, D.E., Hurford, G.J., Nita, G.M., White, S.M., Tun, S.D., Fleishman, G.D., McTiernan, J.M.: 2011, The expanded Owens Valley solar array. *Bull. Am. Astron. Soc.* **42**, 102.

Lin, H., Kuhn, J.R., Coulter, R.: 2004, Coronal magnetic field measurements. *Astrophys. J. Lett.* **613**, L177 – L180. doi:10.1086/425217.

Lin, H., Penn, M.J., Tomczyk, S.: 2000, A new precise measurement of the coronal magnetic field strength. *Astrophys. J. Lett.* **541**, L83 – L86. doi:10.1086/312900.

Liu, Y., Lin, H.: 2008, Observational test of coronal magnetic field models. I. Comparison with potential field model. *Astrophys. J.* **680**, 1496 – 1507. doi:10.1086/588645.

Metcalf, T.R., Leka, K.D., Barnes, G., Lites, B.W., Georgoulis, M.K., Pevtsov, A.A., Balasubramaniam, K.S., Gary, G.A., Jing, J., Li, J., Liu, Y., Wang, H.N., Abramenko, V., Yurchyshyn, V., Moon, Y.-J.: 2006, An overview of existing algorithms for resolving the 180° ambiguity in vector magnetic fields: quantitative tests with synthetic data. *Solar Phys.* **237**, 267 – 296. doi:10.1007/s11207-006-0170-x.

Mok, Y., Mikić, Z., Lionello, R., Linker, J.A.: 2008, The formation of coronal loops by thermal instability in three dimensions. *Astrophys. J. Lett.* **679**, L161 – L165. doi:10.1086/589440.

Nita, G.M., Fleishman, G.D., Gary, D.E., Kuznetsov, A., Kontar, E.P.: 2011, GX_Simulator: an interactive IDL widget tool for visualization and simulation of imaging spectroscopy. *Bull. Am. Astron. Soc.* **42**, 1811.

Nita, G.M., Fleishman, G.D., Gary, D.E., Kuznetsov, A., Kontar, E.P.: 2012, Integrated IDL tool for 3D modeling and imaging data analysis. *Bull. Am. Astron. Soc.* **220**, 51.

Press, W.H., Flannery, B.P., Teukolsky, S.A.: 1986, *Numerical Recipes. The Art of Scientific Computing*, Cambridge University Press, Cambridge.

Rau, U., Cornwell, T.J.: 2011, A multi-scale multi-frequency deconvolution algorithm for synthesis imaging in radio interferometry. *Astron. Astrophys.* **532**, A71. doi:10.1051/0004-6361/201117104.

Sault, R.J., Wieringa, M.H.: 1994, Multi-frequency synthesis techniques in radio interferometric imaging. *Astron. Astrophys. Suppl. Ser.* **108**, 585 – 594.

Sault, R.J., Teuben, P.J., Wright, M.C.H.: 2011, MIRIAD: multi-channel image reconstruction, image analysis, and display. In: *Astrophysics Source Code Library*, 6007, ascl.net/1106.007.

Socas-Navarro, H., Elmore, D., Pietarila, A., Darnell, A., Lites, B.W., Tomczyk, S., Hegwer, S.: 2006, Spinor: visible and infrared spectro-polarimetry at the National Solar Observatory. *Solar Phys.* **235**, 55 – 73. doi:10.1007/s11207-006-0020-x.

Tomczyk, S.: 2012, The Coronal Solar Magnetism Observatory (COSMO). *Am. Astron. Soc. Meet.* **220**, #202.11. ADS:2012AAS...22020211T.

White, S.M., Thejappa, G., Kundu, M.R.: 1992, Observations of mode coupling in the solar corona and bipolar noise storms. *Solar Phys.* **138**, 163 – 187. doi:10.1007/BF00146202.

Wiegelmann, T., Inhester, B., Sakurai, T.: 2006, Preprocessing of Vector Magnetograph data for a nonlinear force-free magnetic field reconstruction. *Solar Phys.* **233**, 215 – 232. doi:10.1007/s11207-006-2092-z.

Wiegelmann, T., Thalmann, J.K., Schrijver, C.J., De Rosa, M.L., Metcalf, T.R.: 2008, Can we improve the preprocessing of photospheric vector magnetograms by the inclusion of chromospheric observations? *Solar Phys.* **247**, 249 – 267. doi:10.1007/s11207-008-9130-y.

DOI 10.1007/978-1-4939-2038-9_7
Reprinted from *Solar Physics* Journal, DOI 10.1007/s11207-013-0331-7

Measuring the Magnetic-Field Strength of the Quiet Solar Corona Using "EIT Waves"

D.M. Long · D.R. Williams · S. Régnier · L.K. Harra

Received: 15 November 2012 / Accepted: 18 May 2013 / Published online: 10 July 2013

Abstract Variations in the propagation of globally propagating disturbances (commonly called "EIT waves") through the low solar corona offer a unique opportunity to probe the plasma parameters of the solar atmosphere. Here, high-cadence observations of two "EIT wave" events taken using the *Atmospheric Imaging Assembly* (AIA) instrument onboard the *Solar Dynamics Observatory* (SDO) are combined with spectroscopic measurements from the *Extreme ultraviolet Imaging Spectrometer* (EIS) onboard the *Hinode* spacecraft and used to examine the variability of the quiet coronal magnetic-field strength. The combination of pulse kinematics from SDO/AIA and plasma density from *Hinode*/EIS is used to show that the magnetic-field strength is in the range $\approx 2-6$ G in the quiet corona. The magnetic-field estimates are then used to determine the height of the pulse, allowing a direct comparison with theoretical values obtained from magnetic-field measurements from the *Helioseismic and Magnetic Imager* (HMI) onboard SDO using global-scale PFSS and local-scale extrapolations. While local-scale extrapolations predict heights inconsistent with prior measurements, the agreement between observations and the PFSS model indicates that "EIT waves" are a global phenomenon influenced by global-scale magnetic field.

Keywords Corona, quiet · Coronal seismology · Waves, propagation · Magnetic fields, corona

Coronal Magnetometry
Guest Editors: S. Tomczyk, J. Zhang, and T.S. Bastian

Electronic supplementary material The online version of this article (doi:10.1007/s11207-013-0331-7) contains supplementary material, which is available to authorized users.

D.M. Long (✉) · D.R. Williams · L.K. Harra
Mullard Space Science Laboratory, University College London, Holmbury St. Mary, Dorking, Surrey RH5 6NT, UK
e-mail: david.long@ucl.ac.uk

S. Régnier
Jeremiah Horrocks Institute, University of Central Lancashire, Preston, Lancashire PR1 2HE, UK

1. Introduction

Although the solar corona is dominated by the Sun's magnetic field, accurately determining its strength continues to be a difficult task. Estimates may be obtained in a small number of long-wavelength (forbidden) emission lines by measuring their Zeeman splitting (*cf.* Lin, Kuhn, and Coulter, 2004) or by using the Hanle effect (*cf.* Raouafi, Sahal-Bréchot, and Lemaire, 2002), but these are generally obtained near active regions where the magnetic-field strength is high and very strong lines in the near infrared may be used (such as, *e.g.*, Fe XIII λ10 747; Lin, Penn, and Tomczyk, 2000). The strength of the coronal magnetic field can also be derived from the gyro-resonance emission in radio wavelengths (*e.g.* White and Kundu, 1997). However, the optically thin emission lines and weak magnetic-field strength above quiet-Sun regions mean that these techniques are typically not suited to measuring magnetic-field strength there. An alternative approach is to infer the coronal magnetic-field strength and other plasma parameters by examining how the properties of waves change with propagation: a technique called *coronal seismology* (Uchida, 1970; Roberts, Edwin, and Benz, 1984).

From their initial discovery in images from the *Extreme ultraviolet Imaging Telescope* (EIT: Delaboudinière *et al.*, 1995) onboard the *SOlar and Heliospheric Observatory* (SOHO) spacecraft, large-scale coronal disturbances (commonly called "EIT waves": Dere *et al.*, 1997; Moses *et al.*, 1997; Thompson *et al.*, 1998) have been suggested as possible probes for studying the plasma parameters of the low corona (*e.g.* Ballai and Erdélyi, 2003, 2004). These pulses are quite fast, with typical velocities of $\approx 200-400$ km s^{-1} measured using data from SOHO/EIT (Thompson and Myers, 2009) and have been observed to exhibit deceleration (Long *et al.*, 2008; Warmuth *et al.*, 2004) and pulse broadening (Long, Deluca, and Gallagher, 2011; Muhr *et al.*, 2011) with propagation: features consistent with the propagation of a fast-mode magnetohydrodynamic (MHD) wave through a randomly structured medium (*e.g.* Murawski, Nakariakov, and Pelinovsky, 2001). The pulses appear to expand isotropically through quiet-Sun regions, although they do tend to avoid regions of lower and higher density such as coronal holes and active regions (Thompson *et al.*, 1999), a property that makes them ideal for determining the nature of the quiet corona.

However, the use of "EIT waves" to probe the quiet corona is predicated on the interpretation of these disturbances as MHD waves, which is not a simple issue. There are currently two competing physical interpretations for these disturbances. The first uses MHD wave theory to explain the phenomenon (*e.g.* Long *et al.*, 2008; Veronig *et al.*, 2010; Wang, 2000; Kienreich *et al.*, 2012; Patsourakos and Vourlidas, 2009) with observations of wave properties such as reflection and refraction at coronal-hole boundaries (Gopalswamy *et al.*, 2009) supporting this approach. An alternative interpretation visualises the pulse as a "pseudo-wave" resulting from the restructuring of the global magnetic field during the eruption of a coronal mass ejection (CME: *e.g.* Delannée *et al.*, 2008; Schrijver *et al.*, 2011; Attrill *et al.*, 2007). In this scenario, the bright feature observed as the "EIT wave" is due to Joule heating or small-scale magnetic reconnection as the erupting CME passes out of the low corona.

An alternative explanation for "EIT waves" combines both the wave and "pseudo-wave" theories to interpret this phenomenon as consisting of both a fast-mode wave initially driven by the erupting CME and a slower brightening due to reconfiguration of the magnetic field. This form was originally posited by Chen *et al.* (2002) and has been expanded in simulations performed by Chen, Fang, and Shibata (2005), Cohen *et al.* (2009), and Downs *et al.* (2011, 2012). There has also been some evidence of two distinct fronts in observations (*e.g.* Zhukov and Auchère, 2004; Chen *et al.*, 2011). Recent statistical analysis of a large

sample of "EIT waves" performed by Warmuth and Mann (2011) suggests that there may be three distinct classes of "EIT wave": Class 1 pulses are initially fast waves that exhibit pronounced deceleration, Class 2 pulses are waves with moderate and almost constant velocities, while Class 3 pulses exhibit erratic kinematic behaviour and are most likely explained as pseudo-waves.

"EIT waves" are traditionally identified and analysed using data from imagers such as SOHO/EIT (Thompson *et al.*, 1999), the *Transition Region And Coronal Explorer* (TRACE: *e.g.* Wills-Davey and Thompson, 1999), the *Extreme UltraViolet Imager* (EUVI) onboard the *Solar Terrestrial Relations Observatory* (STEREO: *e.g.* Long *et al.*, 2008) and the *Atmospheric Imaging Array* (AIA) onboard the *Solar Dynamics Observatory* (SDO: *e.g.* Liu *et al.*, 2010), as these instruments allow easy identification of the disturbance within a large field-of-view. However, a more detailed understanding of these disturbances requires the use of spectroscopic instruments as these allow their true physical nature to be investigated. This approach is hindered by the fact that these instruments generally have a restricted field-of-view, making observations of "EIT Waves" rare. Despite this, several events have been observed using the *Extreme ultraviolet Imaging Spectrometer* (EIS: Culhane *et al.*, 2007) onboard the *Hinode* spacecraft (Kosugi *et al.*, 2007).

As rare cases of "EIT waves" being observed by spectroscopic instruments, both of the events discussed here have previously been studied by other authors. The event from 12 June 2010 was analysed by Chen and Wu (2011), who found a significant change in the magnetic topology as the nearly circular pulse passed over an upflow region near a magnetic bipole. This led the authors to suggest that the event may be best explained using the magnetic-field-stretching model proposed by Chen, Fang, and Shibata (2005). The 16 February 2011 event was one of a series of eruptions from AR 11158 over the course of several days and the active region was the subject of a special *Hinode* Observing Plan (HOP) for studying "EIT waves". The eruption has been studied by both Harra *et al.* (2011) and Veronig *et al.* (2011) who found clear downward bulk motion towards the chromosphere at the pulse, followed by a later upward motion behind the pulse. The kinematics measured by *Hinode*/EIS also matched those using imagers, suggesting that "EIT waves" may be best interpreted as MHD waves propagating through the low corona.

In this article, we examine those two "EIT wave" events observed by both *Hinode*/EIS and SDO/AIA. The spectroscopic observations from *Hinode*/EIS are used to determine the density of the plasma through which the pulse is propagating, and this information is combined with the kinematics obtained from SDO/AIA, allowing the magnetic-field strength of the quiet corona to be estimated and compared with theoretical predictions from multiple extrapolated-field models. The observations of both events studied are outlined in Section 2, with the analysis of these observations from both SDO/AIA and *Hinode*/EIS discussed in Section 3. The results of this analysis are presented in Section 4 before being compared to extrapolated-field estimates in Section 5. Finally, some conclusions are outlined in Section 6.

2. Observations and Data Analysis

The events studied here were quite similar. The 12 June 2010 eruption from active region (AR) NOAA 11081 was associated with a GOES M2.0 flare, which began at 00:30 UT and peaked at 00:57 UT, while the eruption on 16 February 2011 from AR NOAA 11158 had an associated M1.6 flare (starting at 14:19 UT, peaking at 14:25 UT). Both events were also associated with Type II radio bursts, while CMEs were also identified using the Coordinated Data Analysis Workshops (CDAW) catalogue (cdaw.gsfc.nasa.gov/CME_list/)

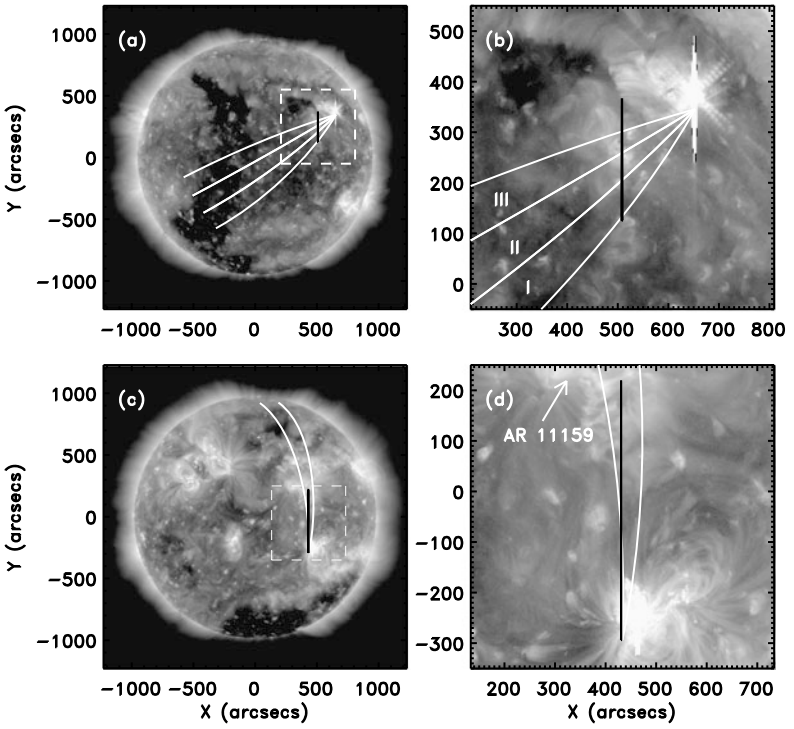

Figure 1 SDO/AIA 193 Å images showing the events from 12 June 2010 ($t = 00{:}58{:}30$ UT; full-disk in panel (a) and zoomed-in in panel (b)) and 16 February 2011 ($t = 14{:}25{:}31$ UT; full-disk in panel (c) and zoomed-in in panel (d)). The great-circle arc sectors used to determine the kinematics of the pulses are shown bounded in white, while the *Hinode*/EIS slit positions are in black in all panels. AR 11159, which lay to the North of the erupting AR 11158 for the 16 February 2011 event, is indicated in panel (d). The arcs in panel (b) are labelled I, II, and III for easier identification throughout the text. The variation of the zoomed-in regions with time is shown in the running-difference movies 1 and 2 in the electronic supplementary material.

for the 12 June 2010 event and by the instrument team for the Cor-1 coronagraph (cor1.gsfc.nasa.gov/catalog/), part of the *Sun Earth Connection Coronal and Heliospheric Investigation* (SECCHI) instrument package onboard the STEREO spacecraft for the 16 February 2011 event.

The *Hinode*/EIS data for these events were taken from two separate observation programmes, and consequently measured different sets of emission lines. The data for the 12 June 2010 event were taken using EIS study 387, which was designed to study the asymmetry of transition-region emission lines. This produced a set of 12 observations of $\approx$ five-minute duration taken in a region of the quiet Sun adjacent to the erupting active region (as shown in panels (a) and (b) of Figure 1). The data for the 16 February 2011 event were taken using HOP 180, which was a coordinated programme designed to study the plasma properties of "EIT waves". This data-set consists of a single sit-and-stare raster observing both the edge of the erupting active region and the adjacent quiet Sun (see panels (c) and (d) of Figure 1) and lasting $\approx$30 minutes.

Full-disk images ($0.6''$ pixel^{-1}) from the AIA instrument (Lemen *et al.*, 2012) onboard the SDO spacecraft (Pesnell, Thompson, and Chamberlin, 2012) were used to determine the kinematics and morphological evolution of both "EIT waves". The SDO/AIA data used

here were taken from the 193 Å passband (which is sensitive to coronal plasma at $\approx 1-2$ MK) as it provided the clearest observations of the pulse. The kinematic properties of both pulses were determined using the semi-automated intensity-profile technique utilised by Long, Deluca, and Gallagher (2011) and Long *et al.* (2011). This is outlined in more detail in Section 3.1.

3. Methods

Since our data are from two distinct instruments, each measuring different properties of the observed phenomenon, analysis of the observations from both *Hinode*/EIS and SDO/AIA was a two-step process. The full-disk images from SDO/AIA were primarily used to examine the kinematics of the disturbances, as well as to allow some comparison with the magnetic-field extrapolations obtained from the *Helioseismic and Magnetic Imager* (HMI: Scherrer *et al.*, 2012) onboard SDO. The spectra obtained from *Hinode*/EIS were used to determine the number density of the quiet-Sun region being examined using several density-sensitive line ratios.

3.1. SDO/AIA Analysis

The kinematics of the two pulses studied were determined using the semi-automated intensity-profile technique promulgated by Long, Deluca, and Gallagher (2011) and Long *et al.* (2011). This technique uses percentage base-difference intensity (PBD: Wills-Davey and Thompson, 1999) images to identify the disturbance, with each image derotated to the same pre-event time for each event. A series of 36 arcs of $\approx 10^\circ$ width radiating from a source point are used to create intensity profiles by averaging the PBD intensity across each arc sector in annuli of increasing radii and 1° width on the spherical surface. As this algorithm is designed to operate automatically with minimal user input, the source point from which to measure the distance of the pulse is taken as the position of the flare defined by the Heliophysics Event Knowledgebase (www.lmsal/hek/isolsearch/isolsearch.html; note that this is used to ensure consistency between events, but does not imply that the flare is the physical source of the wave). This creates a set of 36 intensity profiles for each image, with the mean and standard deviation of the PBD intensity values across the annulus taken as the intensity and associated error for that point on the profile.

Once the intensity profiles had been obtained, the intensity peak corresponding to the flare, the propagating pulse and any associated "stationary brightenings" were identified automatically by the algorithm for each arc, with a Gaussian model used to fit the position of the peak intensity of each feature individually. The pulse was then identified through its motion, with the pulse position, height, and width given by the centroid, peak, and full width at half maximum (FWHM), respectively (as "EIT waves" display a Gaussian cross-section, see Wills-Davey and Thompson, 1999). The errors associated with each parameter were obtained from the error on the fit to the intensity profile. This approach was used as it operates automatically, thus minimising user bias; there is no user input into the algorithm since the source of the arcs and start time of the analysis were both obtained from the identification of the flare defined by the HEK. In addition, the algorithm is designed to compare features between arc sectors, ensuring their accurate identification. The pulse position and width were therefore obtained with respect to time for each arc, allowing the kinematics and temporal behaviour of the pulse to be determined. The kinematics of the pulse were derived by fitting the pulse position with time using a quadratic equation of the form

$$r(t) = r_0 + v_0 t + \frac{1}{2} a t^2, \tag{1}$$

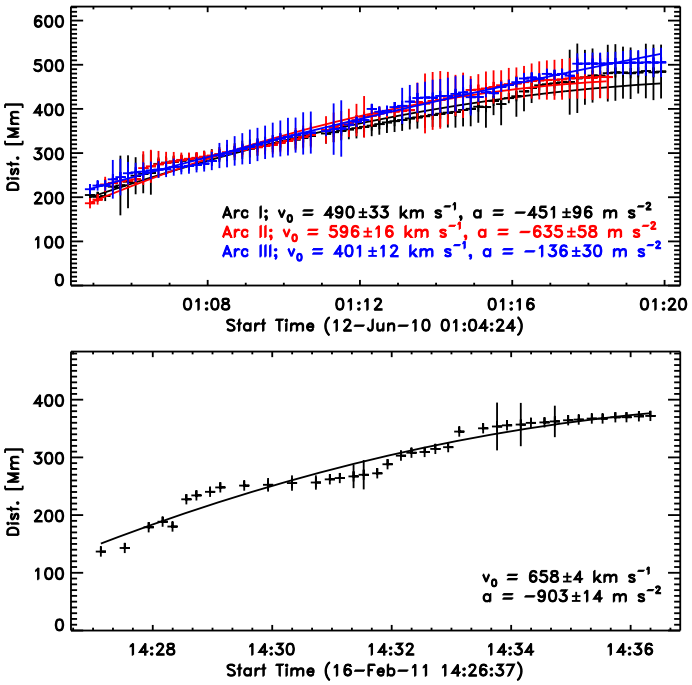

Figure 2 Time–distance plots for the events of 12 June 2010 (top) and 16 February 2011 (bottom). The kinematics derived for each of the arcs I, II, and III for the 12 June 2010 and 16 February 2011 "EIT waves" are given in the respective legends.

where r_0 is the initial pulse position, v_0 is the initial pulse velocity, and a is the acceleration of the pulse. Broadening of the pulse was identified by fitting the variation in pulse width with time using a linear function. Note that to compare the SDO/AIA kinematics for these events directly with the *Hinode*/EIS observations, only the three arcs that intersected the *Hinode*/EIS slit were used for the 12 June 2010 event, while just one arc was suitable for the 16 February 2011 event. This is shown in Figure 1.

The resulting distance-time plots produced by this analysis are shown in Figure 2. The kinematics derived for each arc were obtained using a residual resampling bootstrapping approach (see, *e.g.*, Long, Deluca, and Gallagher, 2011, for more details). This technique was chosen to determine the pulse kinematics as it provides a statistically significant estimate of the errors associated with the derived kinematic values by allowing each parameter to be characterised by a distribution.

The 12 June 2010 pulse was observed by *Hinode*/EIS with its slit positioned approximately perpendicularly to the direction of the pulse's propagation (see Figure 1). As a result, it was possible to measure the pulse kinematics where three different arc sectors cross the slit; these measurements are shown in the upper panel of Figure 2. It is clear that while the distance travelled by the pulse in each arc sector is comparable, the resulting pulse kinematics are different for each arc sector. This indicates that the pulse does not propagate isotropically, and it is therefore of interest to examine whether the differences in kinematics are driven by differences in the local or global plasma conditions, where *Hinode*/EIS may be used to study the local variations and SDO/AIA may be used to study the variations in global propagation.

The geometry of the 16 February 2011 event was slightly different, in that the pulse-propagation direction was almost parallel to the *Hinode*/EIS slit (see Figure 1). Only one arc sector was therefore required to determine the kinematics of the pulse. The resulting kinematics, shown in the bottom panel of Figure 2, indicate a slightly higher initial velocity and much stronger deceleration. This suggests that while the initial driver of the pulse may have been comparable to that of the 12 June 2010 event, the free propagation of the 16 February 2011 pulse was subject to more resistance.

3.2. *Hinode*/EIS Analysis

Analysis of the *Hinode*/EIS observations for the events studied was complicated by the fact that the data were taken from two distinct observing plans that were designed with different scientific goals in mind. Despite this, both sets of observations included density-sensitive line ratios that can be used to estimate the electron number-density variation of the low solar corona through which each pulse propagated.

Two density-sensitive line ratios were included in the 12 June 2010 observations: the Si X λ258.37/261.04 and Fe XIV λ264.78/274.20 ratios, which are sensitive to electron number-densities of $\log_{10}(n_e) \approx (8-10)$ and $\log_{10}(n_e) \approx (9-11)$ cm^{-3}, respectively (Young *et al.*, 2007). This combination meant that the coronal density could be determined over a temperature range of $\log_{10}(T) \approx (6.1-6.3)$ K (Mazzotta *et al.*, 1998), which covers the peak emission temperature of the 193 Å passband observed by SDO/AIA ($\log_{10}(T) \approx 6.1$ K). The 16 February 2011 event was observed using a more targeted EIS observing plan, and therefore the data include four density-sensitive line ratios. These were the Fe XII λ186.88/195.12, Fe XIII λ196.54/202.04, Fe XIII λ203.82/202.04, and Mg VII λ278.39/280.75 line ratios, corresponding to a range of densities of $\log_{10}(n_e) \approx (8-11)$ cm^{-3} and a temperature range of $\log_{10}(T) \approx (5.8-6.2)$ K.

For both events, the density-sensitive line ratios were obtained first by averaging the measured intensity in time to obtain a one-dimensional intensity profile along the *Hinode*/EIS slit. The number-densities were then calculated using the eis_density.pro routine contained within the SolarSoftWare (SSW) software package, producing a one-dimensional density profile along the slit for both events studied. Although multiple line ratios were available for each event, only the Si X λ258.37/261.04 and Fe XIII λ196.54/202.04 line ratios were used in this analysis for the 12 June 2010 and 16 February 2011 events, respectively, as they were most sensitive to variations in the range $\log_{10}(n_e) \approx 8-10$ cm^{-3}. The variation in density with time is shown in Figure 3 for both events studied. The resulting density profiles are shown in the upper panels of Figures 4 and 5 for each observed event.

4. Results

The derived kinematic parameters of the pulses studied here are shown in Figure 2 to be quite high (with initial velocities of $\approx$496 km s^{-1} and 658 km s^{-1}, respectively). These values are higher than the typically observed pulse velocities reported by Thompson and Myers (2009), but are consistent with other measurements using data from SDO/AIA reported by, *e.g.*, Zheng *et al.* (2012) and Olmedo *et al.* (2012). In addition, both events exhibited significant deceleration with values of $a = -136$ to -635 m s^{-2} and -903 m s^{-2} for the 12 June 2010 and 16 February 2012 events, respectively. The higher pulse velocity and significant deceleration observed here are consistent with the Class 1 "EIT wave" classification proposed by Warmuth and Mann (2011). According to this classification system, "EIT

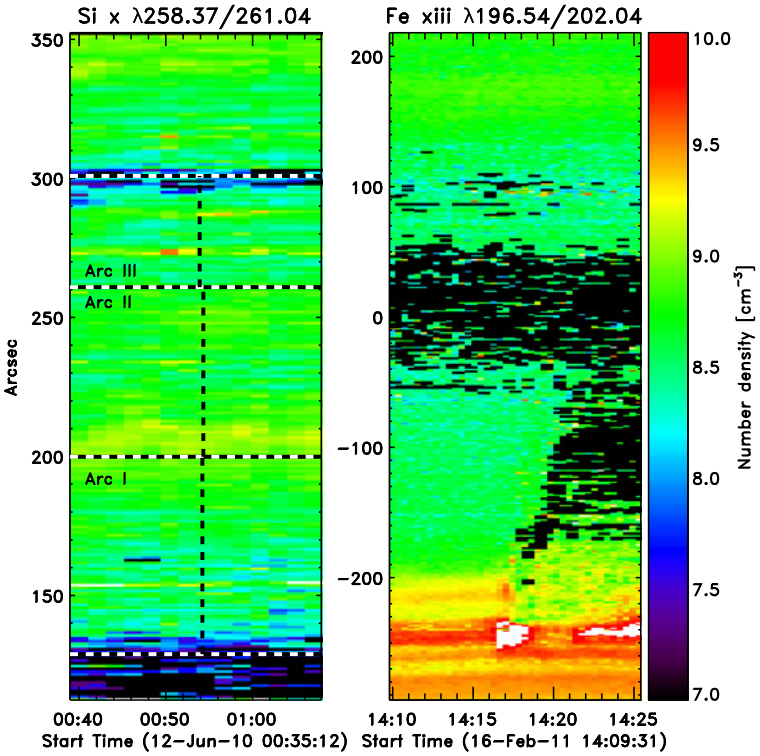

Figure 3 Variation in number density with time calculated for the 12 June 2010 event (Si X λ258.37/261.04 ratio; left panel) and 16 February 2011 event (Fe XIII λ196.54/202.04 ratio; right panel). The sections delineated by the horizontal lines in the left panel correspond to arc sectors (from bottom to top) I, II, and III respectively, with the vertical dashed lines indicating the time in each arc sector at which the pulse passed through the slit.

waves" exhibiting a high initial velocity (*i.e.*, > 325 km s^{-1}: Warmuth and Mann, 2011) and a resulting strong deceleration (such that the final pulse velocity is $\approx 200-300$ km s^{-1}) are thought to correspond to fast MHD wave modes, with the result that the events reported here are interpreted as such.

By interpreting these phenomena as fast-mode MHD waves (*e.g.* Priest, 1987), it is possible to examine their kinematics using the equation

$$v_{\rm fm} = \sqrt{v_{\rm A}^2 + c_{\rm s}^2}, \tag{2}$$

where the Alfvén speed and sound speed are defined as $v_{\rm A} = B/(4\pi nm)^{1/2}$ and $c_{\rm s} = (\gamma kT/m)^{1/2}$, respectively, and the propagation of the pulse is approximately perpendicular to the coronal magnetic field. The magnetic-field strength is defined by B, n is the particle number density, m is the proton mass, γ is the adiabatic index (typically 5/3), $k_{\rm B}$ is the Boltzmann constant, and T refers to the peak emission temperature of the density-sensitive lines used (see Section 3.2 and Mazzotta *et al.*, 1998). This equation can then be rewritten in terms of the magnetic-field strength [B] as,

$$B = \sqrt{4\pi n(mv_{\rm fm}^2 - \gamma k_{\rm B} T)}. \tag{3}$$

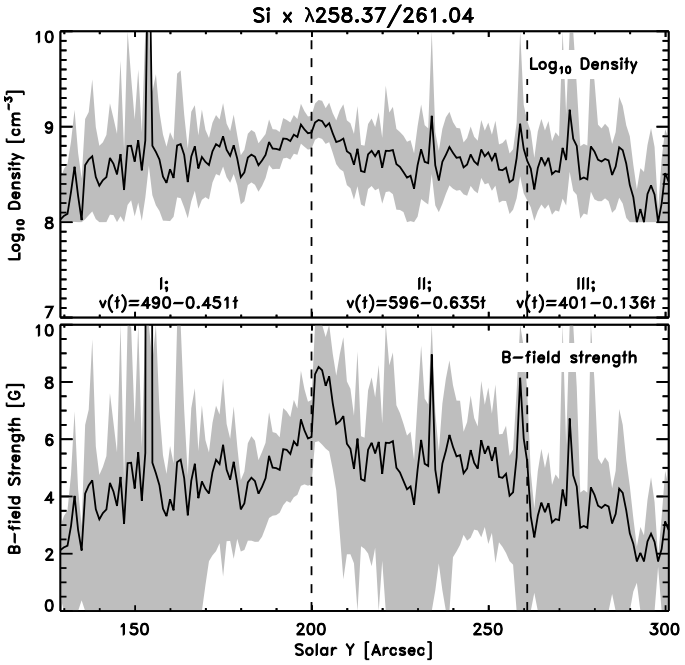

Figure 4 Variation in number density (top panel) and magnetic-field strength (bottom panel) with position for the 12 June 2010 event. The sections delineated by the vertical lines correspond to arc sectors (from left to right) I, II, and III, respectively, while the error associated with each parameter is indicated by the grey shaded region. The density variation was determined using the Si X λ258.37/261.04 density-sensitive line ratio.

This approach is discussed in more detail by Long *et al.* (2011) and West *et al.* (2011) and may be used to estimate the magnetic-field strength, given the plasma density and pulse velocity.

Equation (3) was used to estimate the quiet coronal magnetic-field strength for both of the events presented here. For the 12 June 2010 event, the distance of the *Hinode*/EIS slit from the pulse source was measured for each of the arc sectors studied, and the pulse kinematics were determined for this distance. Resulting velocities of ≈ 469 km s^{-1}, ≈ 558 km s^{-1}, and ≈ 400 km s^{-1} were estimated for arcs I, II, and III, respectively. These values were combined with the number-density profile shown in the upper panel of Figure 4 to produce the magnetic-field strength in the range 2 – 6 G, shown in the lower panel in the same figure. The sections delineated by the vertical black lines correspond to (from left to right) arc sectors I, II, and III, respectively.

The slightly different geometry of the 16 February 2011 event meant that the pulse propagated along the *Hinode*/EIS slit with a velocity shown in the bottom panel of Figure 2. Two kinematic models for the pulse were examined for this event: a pulse that propagated at a constant velocity of ≈ 472 km s^{-1}, obtained by taking the mean velocity of the pulse across the *Hinode*/EIS field-of-view, and a decelerating pulse with a velocity given by

$$v = 658 - 0.903t \text{ km s}^{-1}. \quad (4)$$

These velocity values were combined with the number-density profile obtained for this event (top panels of Figure 5) to produce the magnetic-field strength profiles shown in the bottom

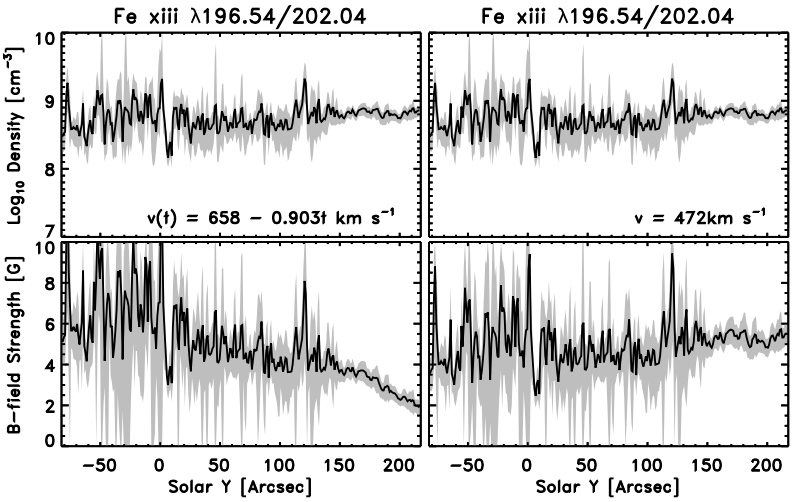

Figure 5 Variation in number density (top row). Note that both panels are the same in order to calculate magnetic-field strength (bottom row) with position for the 16 February 2011 event using a decelerating pulse velocity (left) and constant pulse velocity (right). The error associated with both the number density and magnetic-field strength is indicated by the grey shaded region. The density variation was determined using the Fe XIII λ196.54/202.04 density-sensitive line ratio.

panels of Figure 5, with the right panels showing the results for constant velocity and the left panels showing the results for variable velocity. It is clear that while both profiles are similar, the variation in pulse velocity does affect the derived magnetic-field strength. When a constant velocity is assumed, B is in the range 2 – 6 G; where deceleration is considered, the range of B increases to 1.5 – 10 G, and the difference in results is most easily seen in the upper part of the *Hinode*/EIS slit (100 – 220″).

These observations suggest that the magnetic-field strength of the quiet corona exhibits some variability with position, ranging here between $\approx 0 - 10$ G (within errors). Previous estimates of the quiet coronal magnetic-field strength using "EIT Waves" were constrained by the use of lower cadence images from STEREO/EUVI or by the use of general estimates of the coronal number density rather than precise measurements using *Hinode*/EIS. This was reflected in the resulting general estimates, with values of 0.7 ± 0.7 G and $\approx 1 - 2$ G returned by West *et al.* (2011) and Long *et al.* (2011), respectively. The higher values of magnetic-field strength here may reflect the use of measured rather than canonical values of density, in combination with higher-cadence data that better capture the kinematic properties of the pulse.

5. Magnetic-Field Extrapolation

These measurements of the coronal magnetic-field strength invite further investigation and comparison with theoretical models. A detailed examination of the magnetic-field configuration in the vicinity of the *Hinode*/EIS slit was therefore undertaken to try and understand them. Two different methods were used to examine the magnetic field: a potential-field source surface (PFSS) model giving a potential-field configuration for the full Sun (discussed in Section 5.1), and a potential-field extrapolation in a Cartesian box above the quiet

Sun (discussed in Section 5.2). Given the magnetic-field strength estimated using the propagation of the "EIT wave" and shown in Figures 4 and 5, the methods below are used to derive the height at which this field strength is most probable.

5.1. PFSS Model

The PFSS model developed by Altschuler and Newkirk (1969), Schatten, Wilcox, and Ness (1969), and Schrijver and De Rosa (2003) was used to investigate the magnetic-field strength associated with the observed "EIT waves". This model has the advantage of requiring only the distribution of the radial magnetic field on the photosphere as a boundary condition. Synoptic maps from SDO/HMI were used to determine the photospheric magnetic field for each event, using the maps at 00:04 UT for the 12 June 2010 event (Figure 6(a)) and at 12:04 UT for the 16 February 2011 event (Figure 6(c)). In both cases, the spatial resolution of the maps is 1°, while the source surface is located at 2.5 $R_\odot$ and assumes that the magnetic field is radial above this height. The PFSS model provides the magnetic field for each pixel of the domain.

A spherical-co-ordinate wedge ($\approx 23° \times 26°$ for the 12 June 2010 event and $\approx 19° \times 37°$ for the 16 February 2011 event) that included the *Hinode*/EIS slit was then extracted. This is shown by the white rectangle and the zoomed-in section of panels (a) and (c) of Figure 6.

Figure 6(b) shows the variation of the average B field with height for the 12 June 2010 event. The grey area defines the distribution of B delineated by the maximum of B at a given height. The vertical dashed lines indicate the heights at which B drops below 6 G and 2 G, respectively, implying that the height range of this event lies between 70 and 128 Mm. Similarly for the 16 February 2011 event, Figure 6(d) indicates that the heights at which B is lower than 6 G and 2 G are 72 Mm and 131 Mm, respectively.

The PFSS extrapolation allows an examination of the variation in the large-scale magnetic field of the Sun. The coarse spatial resolution removes the small-scale magnetic field, and thus the complexity of the quiet Sun as well as part of the complexity of active regions. In the following section, the influence of the quiet-Sun magnetic field on the determination of the height of the feature is investigated.

5.2. Quiet-Sun Model

The procedure described by Régnier, Priest, and Hood (2008) is adopted here to compute the potential field above quiet-Sun regions. SDO/HMI magnetograms are again employed, although in this case magnetograms closest in time to observations of the "EIT wave" are used rather than synoptic maps. The initial pixel size of 0.6″ for the SDO/HMI magnetograms is increased by a factor of two for the extrapolation. A small field-of-view encompassing the *Hinode*/EIS slit was extracted from the full-disk observations, with care taken to ensure that there is no contamination from the stronger magnetic field associated with nearby active regions. The field-of-view used for the potential-field extrapolation is shown in Figure 7(a) for the 12 June 2010 event (480″ × 360″) and Figure 7(c) for the 16 February 2011 event (330″ × 300″). The vertical extension of the computational domain is approximately 350″ (about 250 Mm) for both computations.

Similar to the approach followed for the PFSS model, the average magnetic-field strength was estimated at a given height, with the resulting variation with height then plotted (see Figure 7(b), (d)). It is determined that the height from which the magnetic-field strength is above 6 G or 2 G is 13 Mm or 36 Mm for the 12 June 2010 event (panel (b)) and 9 Mm or 17 Mm for the 16 February 2011 event (panel (d)).

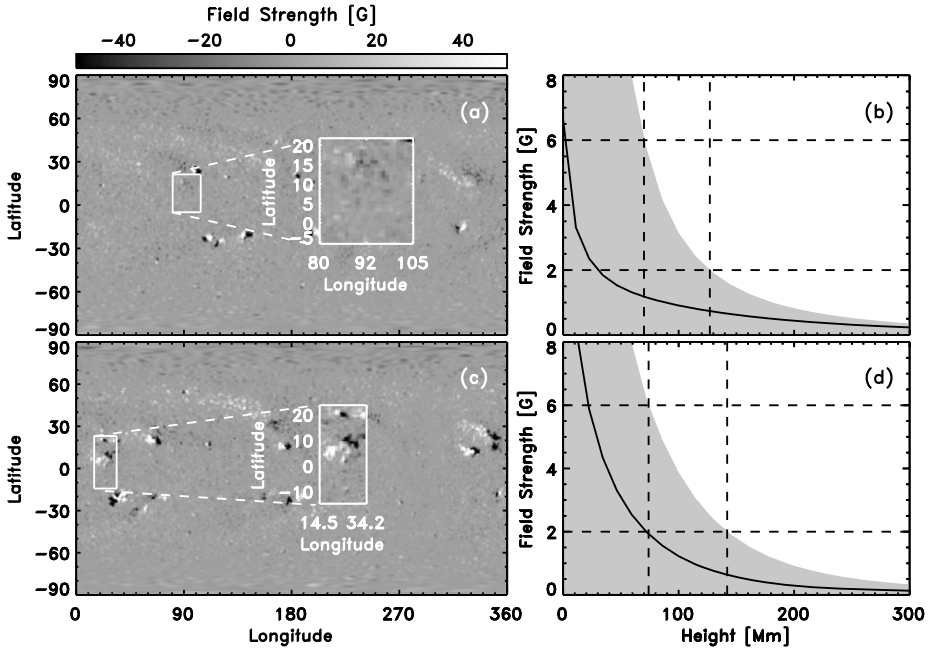

Figure 6 Synoptic maps from 12 June 2010 (panel (a)) and 16 February 2011 (panel (c)) used as a boundary condition for the PFSS model. The white box and enlarged section indicate the area in which the average magnetic-field strength is computed. The corresponding average field strength as a function of height in the corona is shown in panel (b) for the event of 12 June 2010 and panel (d) for the event of 16 February 2011. The grey area shows the spread of the magnetic-field strength. The vertical dashed lines indicate the height at which a maximum field strength of 6 G and 2 G is achieved (horizontal lines).

The values obtained for the characteristic height of the "EIT wave" pulse using the quiet-Sun field extrapolation are quite low, and not consistent with previous estimates or the heights estimated here using density and temperature scale heights. However, they may be explained by the fact that, even if the model includes the small-scale connectivity and complexity of the magnetic field, the intermediate scale of the active-region magnetic field has been removed.

Given the two different extrapolation techniques outlined above, it may be observed that the PFSS model provides more appropriate results for a large-scale event such as the eruption and propagation of an "EIT wave". The active-region scale extrapolation cannot be tackled without removing the small-scale field or the large-scale component with present limitations on the field-of-view and pixel size that are reasonably possible to use in extrapolation codes.

6. Discussion and Conclusions

The results presented here indicate that the magnetic-field strength of the quiet solar corona may be determined *in situ* using "EIT waves". High-cadence images from SDO/AIA have been analysed using a semi-automated technique for identifying and tracking "EIT waves", thus minimising user bias and allowing a more accurate estimation of the kinematic properties of the disturbance. This approach is complemented by high-resolution spectral obser-

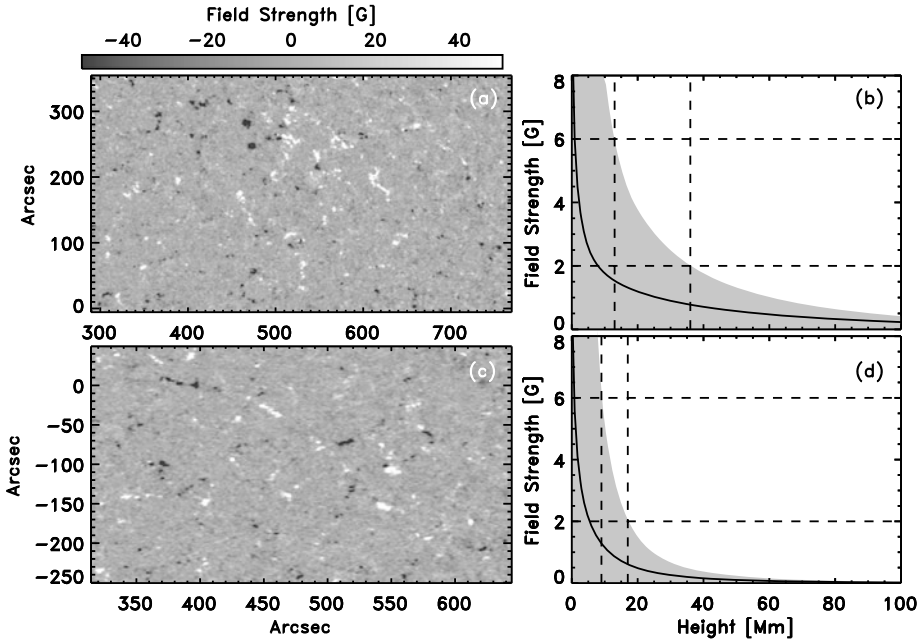

Figure 7 Quiet-Sun magnetograms from 12 June 2010 (panel (a); field-of-view of $480'' \times 360''$) and 16 February 2011 (panel (c); field-of-view of $330'' \times 300''$) used as a boundary condition for the local-domain model. The corresponding average field strength as a function of height in the corona is shown in panel (b) for the event of 12 June 2010 and panel (d) for the event of 16 February 2011. The grey area shows the spread of the magnetic-field strength. The vertical dashed lines indicate the height at which a maximum field strength of 6 G and 2 G is achieved (horizontal lines).

vations from *Hinode*/EIS, which allow the number density of the corona, through which the pulse was propagating, to be determined.

Two events from 12 June 2010 and 16 February 2011 are examined here using this rare combination of data: they were both observed at high cadence by SDO/AIA and *Hinode*/EIS. However, the magnetic structure of the local corona varies between these cases. The pulse on 12 June 2010 originated in a relatively isolated, simple-topology active region. The 16 February 2011 event instead erupted from a very complex active region and was tracked across a region of quiet Sun towards an extended active region of much simpler topology.

The combination of pulse kinematics and density measurements allows the coronal magnetic-field strength to be estimated for the region of the quiet corona through which the pulse propagated. Using this approach, some variability in number density and magnetic-field strength is observed for the region of the quiet corona studied, showing a range of 2 – 6 G. This variability may play a role in terms of the observed properties of the pulse, causing it to decelerate and broaden as it propagates through the randomly structured medium (see, *e.g.*, Murawski, Nakariakov, and Pelinovsky, 2001). These observations indicate that interpretation of the coronal magnetic-field strength, particularly in quiet coronal regions, is not trivial.

The estimates derived using this combination of data from SDO/AIA and *Hinode*/EIS are then compared to magnetic-field extrapolations of the coronal magnetic field. Data from SDO/HMI have been analysed using both a global-scale PFSS extrapolation and a

local-scale quiet-Sun magnetic-field extrapolation technique outlined by Régnier, Priest, and Hood (2008). Using each of these techniques it is possible to estimate the height range corresponding to the magnetic-field strength estimated using the propagating "EIT wave" pulse. It is found that the values obtained using the quiet-Sun approach are too low to be considered a realistic estimate of the height range. This indicates that the magnetic field at the height of the pulse is not dominated by the small-scale magnetic-field anchored in the photosphere below.

The PFSS extrapolation produces height estimates of $\approx 70-130$ Mm, which are most consistent with the height range estimated by Patsourakos *et al.* (2009) and Kienreich, Temmer, and Veronig (2009) using quadrature observations of an "EIT wave" made by STEREO/EUVI. This increasing number of observations made using a variety of instruments and techniques suggests that this is the true height range at which "EIT waves" propagate. Furthermore, this consistency strongly indicates that "EIT waves" are a global phenomenon influenced by global-scale features.

Direct measurements of the coronal magnetic-field are particularly difficult to make, with efforts generally focused on the variation of the magnetic-field strength in active regions rather than the quiet corona. These results indicate that it is possible to estimate the magnetic-field strength in the solar corona using "EIT waves" observed using a combination of broadband and spectroscopic imagers.

Acknowledgements The authors wish to thank the anonymous referee whose comments improved the article. *Hinode* is a Japanese mission developed and launched by ISAS/JAXA, collaborating with NAOJ as a domestic partner, NASA and STFC (UK) as international partners. Scientific operation of the *Hinode* mission is conducted by the *Hinode* science team organised at ISAS/JAXA. This team mainly consists of scientists from institutes in the partner countries. Support for the post-launch operation is provided by JAXA and NAOJ (Japan), STFC (UK), NASA, ESA and NSC (Norway). SDO/AIA data are courtesy of NASA/SDO and the AIA science team. The research leading to these results has received funding from the European Commission's Seventh Framework Programme under the grant agreement No. 284461 (eHEROES project).

References

Altschuler, M.D., Newkirk, G.: 1969, Magnetic fields and the structure of the solar corona. I: Methods of calculating coronal fields. *Solar Phys.* **9**(1), 131 – 149. ADS:1969SoPh....9..131A, doi:10.1007/BF00145734.

Attrill, G.D.R., Harra, L.K., van Driel-Gesztelyi, L., Démoulin, P., Wülser, J.P.: 2007, Coronal "wave": a signature of the mechanism making CMEs large-scale in the low corona? *Astron. Nachr.* **328**(8), 760. doi:10.1002/asna.200710794.

Ballai, I., Erdélyi, R.: 2003, In: Forgács-Dajka, E., Petrovay, K., Erdélyi, R. (eds.) *Challenges in Coronal Moreton Waves*, *Contributions to NATO Advanced Research Workshop Turbulence* **13**, Pub. Astron. Depart. Eötvös University, 121 – 126.

Ballai, I., Erdélyi, R.: 2004, Damping of coronal EIT waves as a tool for plasma diagnostics. In: Lacoste, H. (ed.) *Proc. SOHO 13 Waves, Oscillations and Small-Scale Transients Events in the Solar Atmosphere: A Joint View from SOHO and TRACE* **SP-547**, ESA, Noordwijk, 433.

Chen, P.F., Fang, C., Shibata, K.: 2005, A full view of EIT waves. *Astrophys. J.* **622**(2), 1202 – 1210. doi:10.1086/428084.

Chen, P.F., Wu, Y.: 2011, First evidence of coexisting EIT wave and coronal Moreton wave from SDO/AIA observations. *Astrophys. J. Lett.* **732**(2), L20. doi:10.1088/2041-8205/732/2/L20.

Chen, P.F., Wu, S.T., Shibata, K., Fang, C.: 2002, Evidence of EIT and Moreton waves in numerical simulations. *Astrophys. J. Lett.* **572**(1), L99 – L102. doi:10.1086/341486.

Chen, F., Ding, M.D., Chen, P.F., Harra, L.K.: 2011, Spectroscopic analysis of interaction between an Extreme-ultraviolet Imaging Telescope wave and a coronal upflow region. *Astrophys. J.* **740**(2), 116. doi:10.1088/0004-637X/740/2/116.

Cohen, O., Attrill, G.D.R., Manchester, W.B.I., Wills-Davey, M.J.: 2009, Numerical simulation of an EUV coronal wave based on the 2009 February 13 CME event observed by STEREO. *Astrophys. J.* **705**(1), 587 – 602. doi:10.1088/0004-637X/705/1/587.

Culhane, J.L., Harra, L.K., James, A.M., Al-Janabi, K., Bradley, L.J., Chaudry, R.A., Rees, K., Tandy, J.A., Thomas, P., Whillock, M.C.R., Winter, B., Doschek, G.A., Korendyke, C.M., Brown, C.M., Myers, S., Mariska, J., Seely, J., Lang, J., Kent, B.J., Shaughnessy, B.M., Young, P.R., Simnett, G.M., Castelli, C.M., Mahmoud, S., Mapson-Menard, H., Probyn, B.J., Thomas, R.J., Davila, J., Dere, K., Windt, D., Shea, J., Hagood, R., Moye, R., Hara, H., Watanabe, T., Matsuzaki, K., Kosugi, T., Hansteen, V., Wikstol, Ø.: 2007, The EUV imaging spectrometer for Hinode. *Solar Phys.* **243**(1), 19 – 61. ADS:2007SoPh..243...19C, doi:10.1007/s01007-007-0293-1.

Delaboudinière, J.P., Artzner, G.E., Brunaud, J., Gabriel, A.H., Hochedez, J.F., Millier, F., Song, X.Y., Au, B., Dere, K.P., Howard, R.A., Kreplin, R., Michels, D.J., Moses, J.D., Defise, J.M., Jamar, C., Rochus, P., Chauvineau, J.P., Marioge, J.P., Catura, R.C., Lemen, J.R., Shing, L., Stern, R.A., Gurman, J.B., Neupert, W.M., Maucherat, A., Clette, F., Cugnon, P., van Dessel, E.L.: 1995, EIT: Extreme-ultraviolet Imaging Telescope for the SOHO mission. *Solar Phys.* **162**(1), 291 – 312. ADS:1995SoPh..162..291D, doi:10.1007/BF00733432.

Delannée, C., Török, T., Aulanier, G., Hochedez, J.F.: 2008, A new model for propagating parts of EIT waves: a current shell in a CME. *Solar Phys.* **247**(1), 123 – 150. ADS:2008SoPh..247..123D, doi:10.1007/s11207-007-9085-4.

Dere, K.P., Brueckner, G.E., Howard, R.A., Koomen, M.J., Korendyke, C.M., Kreplin, R.W., Michels, D.J., Moses, J.D., Moulton, N.E., Socker, D.G., St Cyr, O.C., Delaboudinière, J.P., Artzner, G.E., Brunaud, J., Gabriel, A.H., Hochedez, J.F., Millier, F., Song, X.Y., Chauvineau, J.P., Marioge, J.P., Defise, J.M., Jamar, C., Rochus, P., Catura, R.C., Lemen, J.R., Gurman, J.B., Neupert, W., Clette, F., Cugnon, P., van Dessel, E.L., Lamy, P.L., Llebaria, A., Schwenn, R., Simnett, G.M.: 1997, EIT and LASCO observations of the initiation of a coronal mass ejection. *Solar Phys.* **175**(2), 601 – 612. ADS:1997SoPh..175..601D, doi:10.1023/A:1004907307376.

Downs, C., Roussev, I.I., van der Holst, B., Lugaz, N., Sokolov, I.V., Gombosi, T.I.: 2011, Studying extreme ultraviolet wave transients with a digital laboratory: direct comparison of extreme ultraviolet wave observations to global magnetohydrodynamic simulations. *Astrophys. J.* **728**(1), 2. doi:10.1088/0004-637X/728/1/2.

Downs, C., Roussev, I.I., van der Holst, B., Lugaz, N., Sokolov, I.V.: 2012, Understanding SDO/AIA observations of the 2010 June 13 EUV wave event: direct insight from a global thermodynamic MHD simulation. *Astrophys. J.* **750**(2), 134. doi:10.1088/0004-637X/750/2/134.

Gopalswamy, N., Yashiro, S., Temmer, M., Davila, J., Thompson, W.T., Jones, S., McAteer, R.T.J., Wuelser, J.P., Freeland, S., Howard, R.A.: 2009, EUV wave reflection from a coronal hole. *Astrophys. J. Lett.* **691**(2), L123 – L127. doi:10.1088/0004-637X/691/2/L123.

Harra, L.K., Sterling, A.C., Gömöry, P., Veronig, A.: 2011, Spectroscopic observations of a coronal Moreton wave. *Astrophys. J. Lett.* **737**(1), L4. doi:10.1088/2041-8205/737/1/L4.

Kienreich, I.W., Temmer, M., Veronig, A.M.: 2009, STEREO quadrature observations of the three-dimensional structure and driver of a global coronal wave. *Astrophys. J. Lett.* **703**(2), L118 – L122. doi:10.1088/0004-637X/703/2/L118.

Kienreich, I.W., Muhr, N., Veronig, A.M., Berghmans, D., De Groof, A., Temmer, M., Vršnak, B., Seaton, D.B.: 2012, Solar TErrestrial Relations Observatory-A (STEREO-A) and PRoject for On-Board Autonomy 2 (PROBA2) quadrature observations of reflections of three EUV waves from a coronal hole. *Solar Phys.* **286**(1), 201 – 291. doi:10.1007/s11207-012-0023-8.

Kosugi, T., Matsuzaki, K., Sakao, T., Shimizu, T., Sone, Y., Tachikawa, S., Hashimoto, T., Minesugi, K., Ohnishi, A., Yamada, T., Tsuneta, S., Hara, H., Ichimoto, K., Suematsu, Y., Shimojo, M., Watanabe, T., Shimada, S., Davis, J.M., Hill, L.D., Owens, J.K., Title, A.M., Culhane, J.L., Harra, L.K., Doschek, G.A., Golub, L.: 2007, The Hinode (Solar-B) mission: an overview. *Solar Phys.* **243**(1), 3 – 17. ADS:2007SoPh..243....3K, doi:10.1007/s11207-007-9014-6.

Lemen, J.R., Title, A.M., Akin, D.J., Boerner, P.F., Chou, C., Drake, J.F., Duncan, D.W., Edwards, C.G., Friedlaender, F.M., Heyman, G.F., Hurlburt, N.E., Katz, N.L., Kushner, G.D., Levay, M., Lindgren, R.W., Mathur, D.P., McFeaters, E.L., Mitchell, S., Rehse, R.A., Schrijver, C.J., Springer, L.A., Stern, R.A., Tarbell, T.D., Wuelser, J.-P., Wolfson, C.J., Yanari, C., Bookbinder, J.A., Cheimets, P.N., Caldwell, D., Deluca, E.E., Gates, R., Golub, L., Park, S., Podgorski, W.A., Bush, R.I., Scherrer, P.H., Gummin, M.A., Smith, P., Auker, G., Jerram, P., Pool, P., Soufli, R., Windt, D.L., Beardsley, S., Clapp, M., Lang, J., Waltham, N.: 2012, The Atmospheric Imaging Assembly (AIA) on the Solar Dynamics Observatory (SDO). *Solar Phys.* **275**(1), 17 – 40. ADS:2012SoPh..275...17L, doi:10.1007/s11207-011-9776-8.

Lin, H., Kuhn, J.R., Coulter, R.: 2004, Coronal magnetic field measurements. *Astrophys. J. Lett.* **613**(2), L177 – L180. doi:10.1086/425217.

Lin, H., Penn, M.J., Tomczyk, S.: 2000, A new precise measurement of the coronal magnetic field strength. *Astrophys. J. Lett.* **541**(2), L83 – L86. doi:10.1086/312900.

Liu, W., Nitta, N.V., Schrijver, C.J., Title, A.M., Tarbell, T.D.: 2010, First SDO AIA observations of a global coronal EUV "wave": multiple components and "ripples". *Astrophys. J. Lett.* **723**(1), L53 – L59. doi:10.1088/2041-8205/723/1/L53.

Long, D.M., Deluca, E.E., Gallagher, P.T.: 2011, The wave properties of coronal bright fronts observed using SDO/AIA. *Astrophys. J. Lett.* **741**(1), L21. doi:10.1088/2041-8205/741/1/L21.

Long, D.M., Gallagher, P.T., McAteer, R.T.J., Bloomfield, D.S.: 2008, The kinematics of a globally propagating disturbance in the solar corona. *Astrophys. J. Lett.* **680**(1), L81 – L84. doi:10.1086/589742.

Long, D.M., Gallagher, P.T., McAteer, R.T.J., Bloomfield, D.S.: 2011, Deceleration and dispersion of large-scale coronal bright fronts. *Astron. Astrophys.* **531**, 42. doi:10.1051/0004-6361/201015879.

Mazzotta, P., Mazzitelli, G., Colafrancesco, S., Vittorio, N.: 1998, Ionization balance for optically thin plasmas: rate coefficients for all atoms and ions of the elements H to NI. *Astron. Astrophys. Suppl.* **133**, 403 – 409. doi:10.1051/aas:1998330.

Moses, D., Clette, F., Delaboudinière, J.P., Artzner, G.E., Bougnet, M., Brunaud, J., Carabetian, C., Gabriel, A.H., Hochedez, J.F., Millier, F., Song, X.Y., Au, B., Dere, K.P., Howard, R.A., Kreplin, R., Michels, D.J., Defise, J.M., Jamar, C., Rochus, P., Chauvineau, J.P., Marioge, J.P., Catura, R.C., Lemen, J.R., Shing, L., Stern, R.A., Gurman, J.B., Neupert, W.M., Newmark, J., Thompson, B., Maucherat, A., Portier-Fozzani, F., Berghmans, D., Cugnon, P., van Dessel, E.L., Gabryl, J.R.: 1997, EIT observations of the extreme ultraviolet Sun. *Solar Phys.* **175**(2), 571 – 599. ADS:1997SoPh..175..571M, doi:10.1023/A:1004902913117.

Muhr, N., Veronig, A.M., Kienreich, I.W., Temmer, M., Vršnak, B.: 2011, Analysis of characteristic parameters of large-scale coronal waves observed by the Solar-Terrestrial Relations Observatory/Extreme Ultraviolet Imager. *Astrophys. J.* **739**(2), 89. doi:10.1088/0004-637X/739/2/89.

Murawski, K., Nakariakov, V.M., Pelinovsky, E.N.: 2001, Fast magnetoacoustic waves in a randomly structured solar corona. *Astron. Astrophys.* **366**, 306 – 310. doi:10.1051/0004-6361:20000027.

Olmedo, O., Vourlidas, A., Zhang, J., Cheng, X.: 2012, Secondary waves and/or the "reflection" from and "transmission" through a coronal hole of an extreme ultraviolet wave associated with the 2011 February 15 X2.2 flare observed with SDO/AIA and STEREO/EUVI. *Astrophys. J.* **756**(2), 143. doi:10.1088/0004-637X/756/2/143.

Patsourakos, S., Vourlidas, A.: 2009, "Extreme ultraviolet waves" are waves: first quadrature observations of an extreme ultraviolet wave from STEREO. *Astrophys. J. Lett.* **700**(2), L182 – L186. doi:10.1088/0004-637X/700/2/L182.

Patsourakos, S., Vourlidas, A., Wang, Y.M., Stenborg, G., Thernisien, A.: 2009, What is the nature of EUV waves? First STEREO 3D observations and comparison with theoretical models. *Solar Phys.* **259**(1), 49 – 71. ADS:2009SoPh..259...49P, doi:10.1007/s11207-009-9386-x.

Pesnell, W.D., Thompson, B.J., Chamberlin, P.C.: 2012, The Solar Dynamics Observatory (SDO). *Solar Phys.* **275**(1), 3 – 15. ADS:2012SoPh..275....3P, doi:10.1007/s11207-011-9841-3.

Priest, E.R.: 1987, *Solar Magneto-Hydrodynamics*, Reidel, Dordrecht.

Raouafi, N.E., Sahal-Bréchot, S., Lemaire, P.: 2002, Linear polarization of the O VI lambda 1031.92 coronal line. II. Constraints on the magnetic field and the solar wind velocity field vectors in the coronal polar holes. *Astron. Astrophys.* **396**, 1019 – 1028. doi:10.1051/0004-6361:20021418.

Régnier, S., Priest, E.R., Hood, A.W.: 2008, Coronal Alfvén speeds in an isothermal atmosphere. I. Global properties. *Astron. Astrophys.* **491**(1), 297 – 309. doi:10.1051/0004-6361:200810362.

Roberts, B., Edwin, P.M., Benz, A.O.: 1984, On coronal oscillations. *Astrophys. J.* **279**, 857 – 865. doi:10.1086/161956.

Schatten, K.H., Wilcox, J.M., Ness, N.F.: 1969, A model of interplanetary and coronal magnetic fields. *Solar Phys.* **6**(3), 442 – 455. ADS:1969SoPh....6..442S, doi:10.1007/BF00146478.

Scherrer, P.H., Schou, J., Bush, R.I., Kosovichev, A.G., Bogart, R.S., Hoeksema, J.T., Liu, Y., Duvall, T.L., Zhao, J., Title, A.M., Schrijver, C.J., Tarbell, T.D., Tomczyk, S.: 2012, The Helioseismic and Magnetic Imager (HMI) Investigation for the Solar Dynamics Observatory (SDO). *Solar Phys.* **275**(1), 207 – 227. ADS:2012SoPh..275..207S, doi:10.1007/s11207-011-9834-2.

Schrijver, C.J., De Rosa, M.L.: 2003, Photospheric and heliospheric magnetic fields. *Solar Phys.* **212**(1), 165 – 200. ADS:2003SoPh..212..165S, doi:10.1023/A:1022908504100.

Schrijver, C.J., Aulanier, G., Title, A.M., Pariat, E., Delannée, C.: 2011, The 2011 February 15 X2 flare, ribbons, coronal front, and mass ejection: interpreting the three-dimensional views from the Solar Dynamics Observatory and STEREO guided by magnetohydrodynamic flux-rope modeling. *Astrophys. J.* **738**(2), 167. doi:10.1088/0004-637X/738/2/167.

Thompson, B.J., Myers, D.C.: 2009, A catalog of coronal "EIT wave" transients. *Astrophys. J. Suppl.* **183**(2), 225 – 243. doi:10.1088/0067-0049/183/2/225.

Thompson, B.J., Plunkett, S.P., Gurman, J.B., Newmark, J.S., St Cyr, O.C., Michels, D.J.: 1998, SOHO/EIT observations of an Earth-directed coronal mass ejection on May 12, 1997. *Geophys. Res. Lett.* **25**(1), 2465 – 2468. doi:10.1029/98GL50429.

Thompson, B.J., Gurman, J.B., Neupert, W.M., Newmark, J.S., Delaboudinière, J.P., St Cyr, O.C., Stezelberger, S., Dere, K.P., Howard, R.A., Michels, D.J.: 1999, SOHO/EIT observations of the 1997 April 7 coronal transient: possible evidence of coronal Moreton waves. *Astrophys. J. Lett.* **517**(2), L151 – L154. doi:10.1086/312030.

Uchida, Y.: 1970, Diagnosis of coronal magnetic structure by flare-associated hydromagnetic disturbances. *Publ. Astron. Soc. Japan* **22**, 341.

Veronig, A.M., Muhr, N., Kienreich, I.W., Temmer, M., Vršnak, B.: 2010, First observations of a dome-shaped large-scale coronal extreme-ultraviolet wave. *Astrophys. J. Lett.* **716**(1), L57 – L62. doi:10.1088/2041-8205/716/1/L57.

Veronig, A.M., Gömöry, P., Kienreich, I.W., Muhr, N., Vršnak, B., Temmer, M., Warren, H.P.: 2011, Plasma diagnostics of an EIT wave observed by Hinode/EIS and SDO/AIA. *Astrophys. J. Lett.* **743**, L10. doi:10.1088/2041-8205/743/1/L10.

Wang, Y.M.: 2000, EIT waves and fast-mode propagation in the solar corona. *Astrophys. J. Lett.* **543**(1), L89 – L93. doi:10.1086/318178.

Warmuth, A., Mann, G.: 2011, Kinematical evidence for physically different classes of large-scale coronal EUV waves. *Astron. Astrophys.* **532**, 151. doi:10.1051/0004-6361/201116685.

Warmuth, A., Vršnak, B., Magdalenić, J., Hanslmeier, A., Otruba, W.: 2004, A multiwavelength study of solar flare waves. I. Observations and basic properties. *Astron. Astrophys.* **418**, 1101 – 1115. doi:10.1051/0004-6361:20034332.

West, M.J., Zhukov, A.N., Dolla, L., Rodriguez, L.: 2011, Coronal seismology using EIT waves: estimation of the coronal magnetic field strength in the quiet Sun. *Astrophys. J.* **730**(2), 122. doi:10.1088/0004-637X/730/2/122.

White, S.M., Kundu, M.R.: 1997, Radio observations of gyroresonance emission from coronal magnetic fields. *Solar Phys.* **174**(1), 31 – 52. ADS:1997SoPh..174...31W, doi:10.1023/A:1004975528106.

Wills-Davey, M.J., Thompson, B.J.: 1999, Observations of a propagating disturbance in TRACE. *Solar Phys.* **190**(1), 467 – 483. ADS:1999SoPh..190..467W, doi:10.1023/A:1005201500675.

Young, P.R., Del Zanna, G., Mason, H.E., Dere, K.P., Landi, E., Landini, M., Doschek, G.A., Brown, C.M., Culhane, L., Harra, L.K., Watanabe, T., Hara, H.: 2007, EUV emission lines and diagnostics observed with Hinode/EIS. *Publ. Astron. Soc. Japan* **59**, 857.

Zheng, R., Jiang, Y., Yang, J., Bi, Y., Hong, J., Yang, B., Yang, D.: 2012, Homologous extreme ultraviolet waves in the emerging flux region observed by the Solar Dynamics Observatory. *Astrophys. J.* **747**(1), 67. doi:10.1088/0004-637X/747/1/67.

Zhukov, A.N., Auchère, F.: 2004, On the nature of EIT waves, EUV dimmings and their link to CMEs. *Astron. Astrophys.* **427**, 705 – 716. doi:10.1051/0004-6361:20040351.

DOI 10.1007/978-1-4939-2038-9_8
Reprinted from *Solar Physics* Journal, DOI 10.1007/s11207-013-0395-4

CORONAL MAGNETOMETRY

Observations of a Quasi-periodic, Fast-Propagating Magnetosonic Wave in Multiple Wavelengths and Its Interaction with Other Magnetic Structures

Y.-D. Shen · Y. Liu · J.-T. Su · H. Li · X.-F. Zhang · Z.-J. Tian · R.-J. Zhao · A. Elmhamdi

Received: 12 December 2012 / Accepted: 13 August 2013 / Published online: 3 October 2013

Abstract We present observations of a quasi-periodic fast-propagating (QFP) magnetosonic wave on 23 April 2012, with high-resolution observations taken by the *Atmospheric Imaging Assembly* onboard the *Solar Dynamics Observatory*. Three minutes after the start of a C2.0 flare, wave trains were first observed along an open divergent loop system in 171 Å observations at a distance of 150 Mm from the footpoint of the guiding loop system and with a speed of 689 km s^{-1}, then they appeared in 193 Å observations after their interaction with a perpendicular, underlaying loop system on the path; in the meantime; their speed decelerated to 343 km s^{-1} within a short time. The sudden deceleration of the wave trains and their appearance in 193 Å observations are interpreted through a geometric effect and the density increase of the guiding loop system, respectively. We find that the wave trains have a common period of 80 seconds with the flare. In addition, a few low frequencies are also identified in the QFP wave. We propose that the generation of the period of 80 seconds was caused by the periodic releasing of energy bursts through some nonlinear processes in magnetic reconnection, while the low frequencies were possibly the leakage of pressure-driven

Coronal Magnetometry
Guest Editors: S. Tomczyk, J. Zhang, and T.S. Bastian

Electronic supplementary material The online version of this article (doi:10.1007/s11207-013-0395-4) contains supplementary material, which is available to authorized users.

Y.-D. Shen (✉) · Y. Liu · X.-F. Zhang · Z.-J. Tian · R.-J. Zhao · A. Elmhamdi
Yunnan Astronomical Observatory, CAS, Kunming 650011, China
e-mail: ydshen@ynao.ac.cn

Y.-D. Shen · Y. Liu · J.-T. Su
Key Laboratory of Solar Activity, National Astronomical Observatories, CAS, Beijing 100012, China

Y.-D. Shen · H. Li
Key Laboratory of Dark Matter and Space Astronomy, Purple Mountain Observatory, CAS, Nanjing 210008, China

A. Elmhamdi
Physics and Astronomy Department, College of Science, King Saud University, P.O. Box 2455, Riyadh 11451, Saudi Arabia

oscillations from the photosphere or chromosphere, which could be an important source for driving coronal QFP waves. Our results also indicate that the properties of the guiding magnetic structure, such as the distributions of magnetic field and density as well as geometry, are crucial for modulating the propagation behaviors of QFP waves.

Keywords Waves, magnetohydrodynamic · Coronal seismology · Magnetic fields, corona

1. Introduction

Investigations of magnetohydrodynamic (MHD) waves in the magnetically dominated solar atmosphere have a long history. However, due to the lack of actual observations in the past, the investigations were mainly limited to theoretical studies (*e.g.* Roberts, Edwin, and Benz, 1983, 1984; Edwin and Roberts, 1983, 1988; Appert *et al.*, 1986), besides a few observational studies based on ground-based radio or optical telescopes (*e.g.* Parks and Winckler, 1969; Koutchmy, Žugžda, and Locăns, 1983). In the last two decades, the launch of a series of space-borne solar telescopes such as SOHO, TRACE, STEREO, and *Hinode* has led to a revolutionary breakthrough in the observational study of MHD waves. However, these instruments have their own limitations for observing fast magnetosonic waves (see Nakariakov and Verwichte, 2005 for details). Thanks to the launch of the *Solar Dynamics Observatory* (SDO: Pesnell, Thompson, and Chamberlin, 2012) in 2010, many instrumental deficiencies are largely overcome due to the high temporal and spatial resolution and full-disk observation capability of this mission. Previous studies have indicated that MHD waves play an important role in the context of the enigmatic problems of coronal heating and acceleration of the fast solar wind, since they can carry magnetic energy over a large distance (*e.g.* Schatzman, 1949; Osterbrock, 1961; Walsh and Ireland, 2003; Tian, McIntosh, and De Pontieu, 2011; Morton *et al.*, 2012a). Furthermore, MHD waves can also be used to diagnose many physical parameters of the solar corona with the so-called coronal seismology technique (Uchida, 1970; Roberts, Edwin, and Benz, 1984). For example, with some measurable physical parameters, one can estimate the coronal magnetic-field strength (Nakariakov and Ofman, 2001; West *et al.*, 2011; Shen and Liu, 2012a, 2012b), coronal dissipative coefficients (Nakariakov *et al.*, 1999), and coronal sub-resolution structures (Robbrecht *et al.*, 2001; King *et al.*, 2003; Morton *et al.*, 2012b). These parameters are difficult to obtain with direct measurements, but they are crucial for understanding a number of complex physical processes in the solar corona.

It is generally known that there are three types of MHD waves in the solar corona, namely Alfvén and slow and fast magnetosonic waves. Except for the slow-mode waves, up to the present, reports on Alfvén and fast-mode waves are very rare. This is mainly due to the instrumental limitations such as low cadence. For observational investigations on quasi-periodic fast-mode waves, Williams *et al.* (2002) first reported a quasi-periodic fast wave that travels through the apex of an active-region coronal loop with a speed of 2100 $\mathrm{km\,s^{-1}}$ and a dominant period of six seconds. This event was observed during the total solar eclipse on 11 August 1999, with the *Solar Eclipse Corona Imaging System* (SECIS) instrument, which has a rapid cadence of 2.25×10^{-2} seconds and a pixel size of $4.07''$ (Williams *et al.*, 2001). This temporal resolution is sufficient to detect the short-period fast waves. In an open magnetic-field structure, Verwichte, Nakariakov, and Cooper (2005) found fast-propagating transverse waves that have phase speeds in the ranges of $200-700\ \mathrm{km\,s^{-1}}$ and periods in the range of 90 – 220 seconds. The authors interpreted them as propagating fast magnetosonic kink waves guided by a vertical, evolving, open structure. Solar decimetric radio emission

of fiber bursts are often interpreted as a signature of magnetosonic wave trains in the solar corona. They often have a period of minutes and show a "tadpole" structure in the wavelet spectra (*e.g.* Mészárosová *et al.*, 2009a, 2009b, 2013; Mészárosová, Karlický, and Rybák, 2011; Karlický, Jelínek, and Mészárosová, 2011), as predicted in theoretical studies (*e.g.* Nakariakov *et al.*, 2004; Jelínek, Karlický, and Murawski, 2012).

With the high temporal and spatial resolution observations of the *Atmospheric Imaging Assembly* (AIA: Lemen *et al.*, 2012; Boerner *et al.*, 2012) instrument onboard SDO, a new type of MHD wave dubbed quasi-periodic fast-propagating magnetosonic waves (QFP) has been detected recently. Such waves have multiple arc-shaped wave trains, and they are often observed in diffuse open coronal loops at 171 Å temperatures (Fe IX; $\log T = 5.8$). Initial observational results indicate that QFP waves have an intimate relationship with the accompanying flare. However, questions about their generation, propagation, and energy dissipation are still open questions. Liu *et al.* (2011) presented the first QFP wave study with observations taken by SDO/AIA, and they found that multiple arc-shaped wave trains successively emanate from near the flare kernel and propagate outward along a funnel-like structure of coronal loops with a phase speed of about 2200 $\mathrm{km\,s^{-1}}$. With Fourier analysis, they detected three dominant frequencies of 5.5, 14.5, and 25.1 mHz in the QFP wave, in which the frequency of 5.5 mHz temporally coincides with quasi-periodic pulsations of the accompanying flare, which suggests that the flare and the QFP wave were possibly excited by a common origin. Shen and Liu (2012a) investigated a similar case that occurred on 30 May 2011, and they compared the frequencies of the QFP wave and the accompanying flare. Their observational results indicate that all of the flare's frequencies can be found in the wave's frequency spectrum, but a few low frequencies of the QFP wave are not consistent with those of the flare. Thus they proposed that the leakage of pressure-driven oscillations from photosphere into the low corona could be another source for driving QFP waves. Recently, Yuan *et al.* (2013) reanalyzed the event on 30 May 2011 with AIA data and radio observations provided by the Nancay Radioheliograph. They found that the QFP wave could be divided into three distinct sub-QFP waves that have different amplitudes, speeds, and wavelengths. In addition, the radio emission show three radio bursts that are highly correlated in start time with the sub-QFP waves. This result suggests that the generation of QFP waves should be tightly related with the regimes of energy releasing in magnetic reconnections. QFP waves coupling with diffuse single broad pulse of extreme-ultraviolet (EUV) waves (so-called "EIT waves", *e.g.* Thompson *et al.*, 1998; Shen and Liu, 2012c) were observed recently by Liu *et al.* (2012). The authors found that multiple wave trains propagate ahead of and behind a coronal mass ejection (CME) simultaneously. However, the two components of the wave trains have different speeds and periods, in which only those running ahead of the CME have similar period to the flare. Modeling efforts have been made to understand the physics in QFP waves (Nakariakov, Melnikov, and Reznikova, 2003; Bogdan *et al.*, 2003; Heggland, De Pontieu, and Hansteen, 2009; Fedun, Shelyag, and Erdélyi, 2011; Ofman *et al.*, 2011). Especially, Ofman *et al.* (2011) performed a three-dimensional numerical simulation for the QFP wave presented by Liu *et al.* (2011). They successfully reproduced the multiple arc-shaped wave trains that have similar amplitude, wavelength, and propagation speeds as those obtained from observation.

In this article, we present an observational study of a QFP wave that occurred on 23 April 2012 and was accompanied by a *Geostationary Operational Environmental Satellite* (GOES) C2.0 flare in NOAA active region AR11461 (N12, W20). The wave trains were first observed in 171 Å observations; however, after their interaction with another loop system on the path, they appeared in the hotter 193 Å observations. In the meantime, the speed of the wave trains decelerated to about half of that before the interaction. With the Fourier and

wavelet analysis techniques, we study the periodicity, generation, and propagation of the QFP wave, then possible mechanisms for the quick deceleration of the wave trains during the interaction and their sudden appearance in 193 Å observations are discussed.

2. Observations

AIA onboard SDO is very suitable for detecting fast-propagating features such as fast magnetosonic waves with short periods. It captures images of the Sun's atmosphere out to 1.3 $R_{\odot}$ and has high temporal resolution of as short as 12 seconds. AIA produces imaging data with four 4096×4096 detectors with a pixel size of $0.6''$, corresponding to an effective spatial resolution of $1.2''$ in seven EUV and three UV–visible channels, which cover a wide temperature range from $\log T = 3.7$ to $\log T = 7.3$. All of these parameters are necessary ingredients for detecting fast-propagating waves. In the presented case, the wave trains were firstly captured in AIA 171 Å (Fe IX; $\log T = 5.8$) and then in 193 Å (Fe XII, XXIV; $\log T = 6.2, 7.3$) observations. We study the QFP wave using the running-difference, base, and running-ratio images, in which the running-difference images are constructed by subtracting from each image the previous one, the base-ratio images are obtained by dividing the time-sequence images by a pre-event image, and the running-ratio images are obtained by dividing each image by the previous one. In addition, the GOES soft X-ray fluxes are also used to analyze the periodicity of the accompanying C2.0 flare. The AIA images used in this article are calibrated with the standard procedure aia_prep.pro available in SolarSoftWare (SSW) and then differentially rotated to a reference time (17:30:00 UT), and solar North is up, West to the right.

3. Results

3.1. Overview of the QFP Wave on 23 April 2012

The QFP wave on 23 April 2012 was accompanied by a GOES C2.0 flare (N13, W17) in NOAA AR11461 (N12, W20), a global EUV wave, and a coronal mass ejection (CME). According to the GOES flare record, the start, peak, and end times of the flare are 17:37, 17:51, and 18:05 UT, respectively. The QFP wave could be observed about three minutes after the flare start, which indicates that the generation of the flare and the wave trains may have some internal physical relations. On the other hand, the relationship between the QFP wave and the preceding EUV wave is not obvious. Therefore, we will confine our attention to the QFP wave and the accompanying flare in the present article. Detailed analysis of the global EUV wave has been published very recently by Shen *et al.* (2013).

The wave trains were primarily observed in the 171 Å observations along an open loop system rooted in active region AR11461. Furthermore, the wave trains were also observed in the 193 Å observations after a few minutes. This phenomenon is different from the cases that have been documented in previous studies, where wave trains can only be identified at the 171 Å temperature (Liu *et al.*, 2011; Shen and Liu, 2012a). The pre-event magnetic condition of the source region and the morphology of the wave trains are displayed in Figure 1. It can be seen that the path of the wave trains was along the diverging coronal loop system, which can be identified in the 171 Å raw image as indicated by the white arrows (see Figure 1(a) and the animation available in the electronic supplementary material). On the path of the wave trains, there is another loop system that was nearly perpendicular to

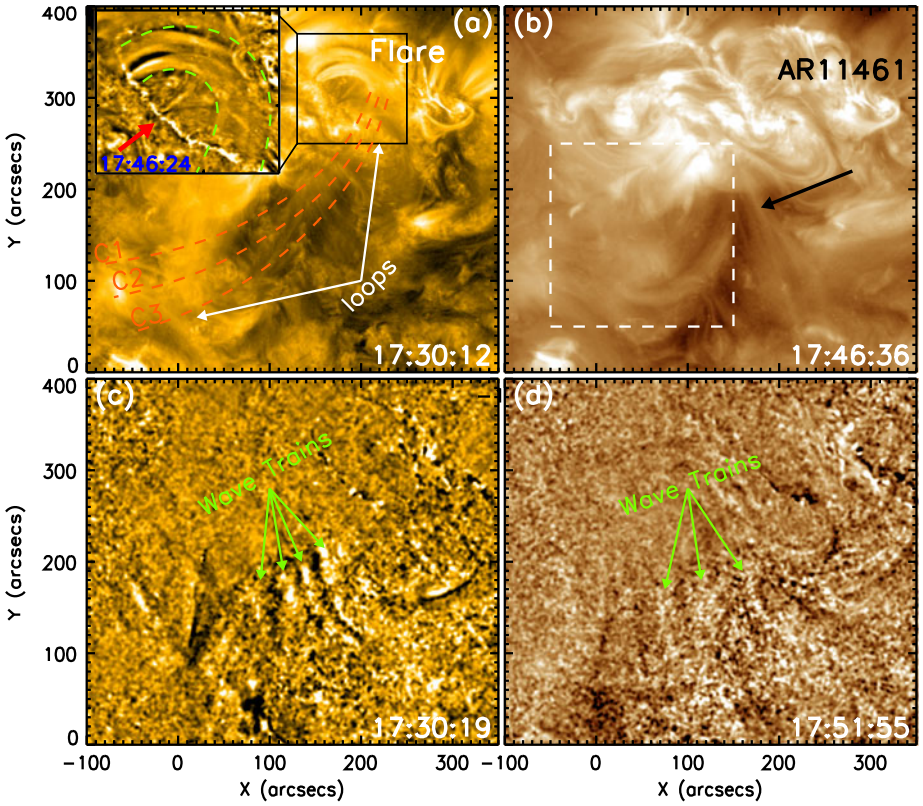

Figure 1 An overview of the QFP wave on 23 April 2012. (a) AIA 171 Å and (b) AIA 193 Å raw images show the pre-event magnetic environment, while (c) AIA 171 Å and (d) AIA 193 Å are base-ratio images displaying the multiple wave trains. The three orange-red dashed curves in panel (a) are used to obtain the time–distance diagrams shown in Figure 2, and the guiding loop is indicated by the two white arrows. The inset in panel (a) is a close-up view of the black box region at 17:46:24 UT. It is a filtered image obtained by subtracting a smoothed image with a boxcar average over 15 × 15 pixels. In the inset, the long flare ribbon is indicated by the red arrow, and the two green-dashed curves outline the loop system that guides the wave trains. In panel (b), the white-dashed box indicates the region where Fourier analysis is applied, while the black arrow points to the perpendicular loop system. The arrows in panels (c) and (d) point to the multiple wave trains. The field of view is $450'' \times 400''$ for each frame and an animation for this figure is available in the electronic supplementary materials.

the guiding field of the wave trains (see the black arrows in Figure 1(b) and the animation). The propagation of the wave trains was inevitably influenced by this perpendicular loop system, which will be analyzed in detail using time–distance diagrams obtained from the red dashed curves as shown in Figure 1(a). In Figure 1(c) and (d), we show the multiple arc-shaped wave trains in running-ratio 171 Å (Figure 1(c)) and 193 Å (Figure 1(d)) images. They emanated successively from the footpoint of the guiding loop and faded in sequence at a distance of about 300 Mm from the guiding loop's footpoint. The successive wave trains were manifested as alternating white–black–white fringes. The footpoint region of the guiding loop system is highlighted in the small inset in Figure 1(a), in which the loop system is outlined using two dashed-green curves. It is interesting that a long flare ribbon lay close to the footpoint of the guiding loop system. In consideration of the temporal relationship between the flare and the QFP wave, we conjecture that this flare rib-

bon might be a direct evidence for the generation of the wave trains. However, the wave trains did not show up immediately following the appearance of the flare ribbon, but rather appeared at a distance of about 150 Mm from the flare ribbon (also the footpoint of the guiding loop system) in the 171 Å images. Here the distance is measured along the curving coronal loop rather than a straight-line distance. As a comparison, the distance is about 260 Mm from the flare ribbon when the wave trains could be observed in the 193 Å images. From the time-sequence observations, we determine that the lifetimes of the wave trains are about 15 (17:40 – 17:55 UT) and 8 (17:47 – 17:55 UT) minutes at 171 Å and 193 Å wavelength bands, respectively. The start time of wave trains in the 171 (193) Å observations is delayed relative to that of the flare by about three (ten) minutes, while the appearance time in the 193 Å images is delayed relative to that from 171 Å by about seven minutes.

3.2. Kinematics Analysis of the Wave Trains

We study the kinematics of the wave trains using time–distance diagrams obtained along curves perpendicular to the propagation direction of the wave trains (see Figure 1(a)). To make a time–distance diagram, we first obtain the intensity profiles along a curve from time-sequence images by averaging ten pixels across the curve. Then, a time–distance diagram can be created by stacking the obtained profiles in time sequence. Figure 2 shows the time–distance diagrams made from base- and running-ratio 171 Å and 193 Å observations along cuts C1 and C2. The base-ratio time–distance diagrams show best the broad EUV wave stripe and dark dimming regions that are thought to be an effect of density decrease rather than temperature change (Jiang *et al.*, 2007; Shen *et al.*, 2010), while the running-ratio time–distance diagrams highlight the fast-propagating wave trains, which manifest themselves as narrow and steep stripes whose slopes represent the projection speeds of the wave trains on the plane of the sky. From these time–distance diagrams, one can see a long and broad stripe that represents the global EUV wave running ahead of the wave trains. The speed of the EUV wave along cut C1 is about 390 ± 10 km s^{-1}. It should be kept in mind that the propagation speed of the wave trains measured from time–distance diagrams are the lower limits of the true three-dimensional values due to projection effects. Although an obvious stationary brightening formed when the EUV wave reached a region of open magnetic fields, the EUV wave did not stop there but rather continued to propagate (see the black arrows in Figure 2(b)), which may manifest the true wave nature of the EUV wave. In addition, by comparing the base-ratio time–distance diagrams, we can find that the initial global EUV front was followed by dimming in 171 Å but emission enhancement in 193 Å; this may suggest that the coronal structures were heated by the EUV wave through adiabatic heating (Schrijver *et al.*, 2011; Downs *et al.*, 2012; Liu *et al.*, 2012), and may not be due to the dissipation of the wave trains.

The wave trains have different manifestations in 171 Å and 193 Å time–distance diagrams. We mainly compare the time–distance diagrams made from 171 and 193 Å running-ratio images along cut C2. In the 171 Å time–distance diagram, we can observe the stripes of the wave trains at a distance of about 30 Mm from the measurement origin (see Figure 2(e)), namely 150 Mm from the footpoint of the guiding loop system. Before the wave trains interacted with the perpendicular loop system as indicated by the blue dash–dotted line Figure 2(f), they propagated with an average speed (acceleration) of about 689 ± 23 km s^{-1} (-1043 m s^{-2}). However, this speed slowed down significantly to 343 ± 27 km s^{-1} after the interaction, about half of that before the interaction. This may indicate that the propagation of the wave trains was seriously influenced by the perpendicular loops due to the

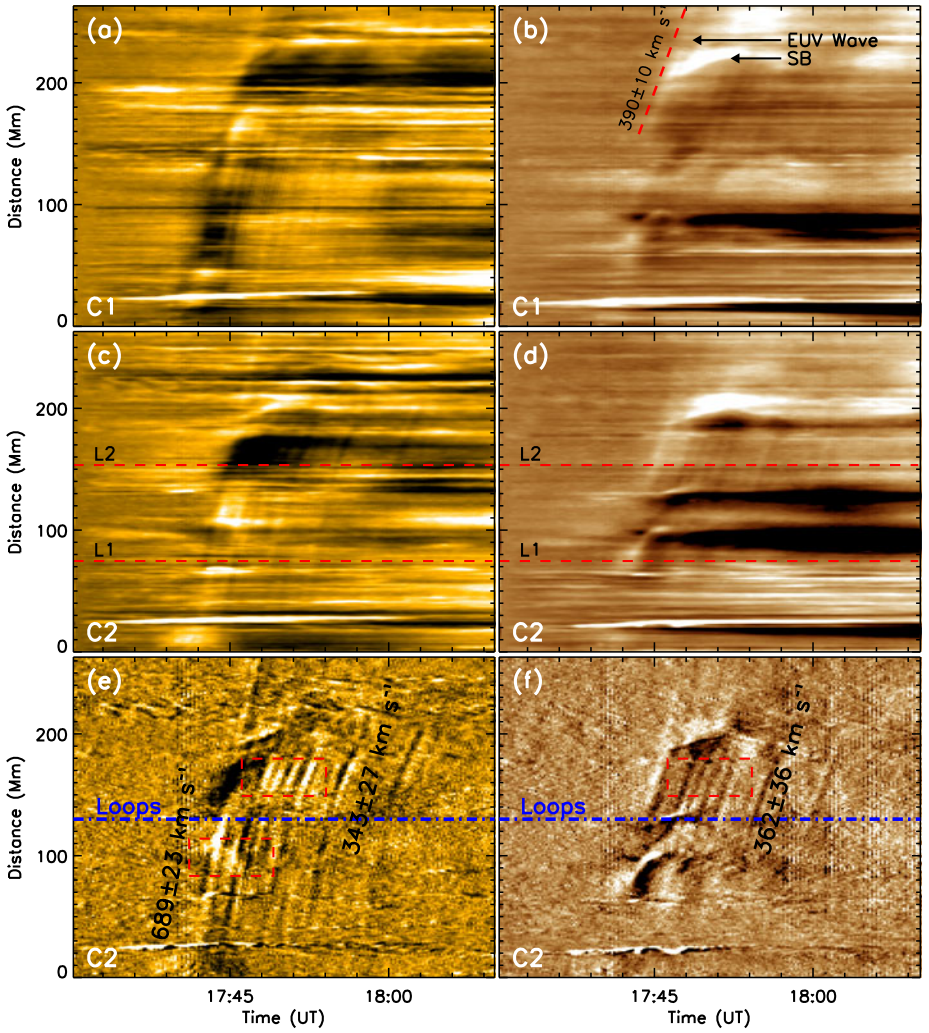

Figure 2 Time–distance diagrams show the kinematics of the wave trains. The top and middle rows are obtained from base-ratio images, while the bottom row are made from running-ratio images. The left and right columns are obtained from 171 and 193 Å images, respectively. The two black arrows in panel (b) point to the EUV wave stripe and the stationary brightening. The red-dashed lines in panels (c) and (d) mark the positions where we analyze the periodicity of the wave trains, while the blue-dash–dot line in panels (e) and (f) indicate the position of the perpendicular loop system. The average speeds of the EUV wave and the wave trains are also plotted in the figure. The three dashed-red boxes mark the regions shown in Figure 3, in which the top one in panel (e) and the one in panel (f) indicate the same region.

changing properties of the guiding loop system. In the 193 Å running-ratio time–distance along the same cut (Figure 2(f)), wave trains can only be identified after the interaction, and the stripes observed in 193 Å time–distance diagram are weaker than those observed in the 171 Å time–distance diagram. The average speed of the QFP wave trains measured from the 193 Å time–distance diagrams is about 362 ± 36 km s^{-1}, while the acceleration is about -364 m s^{-2}. This speed is slightly higher than that determined from the 171 Å time–

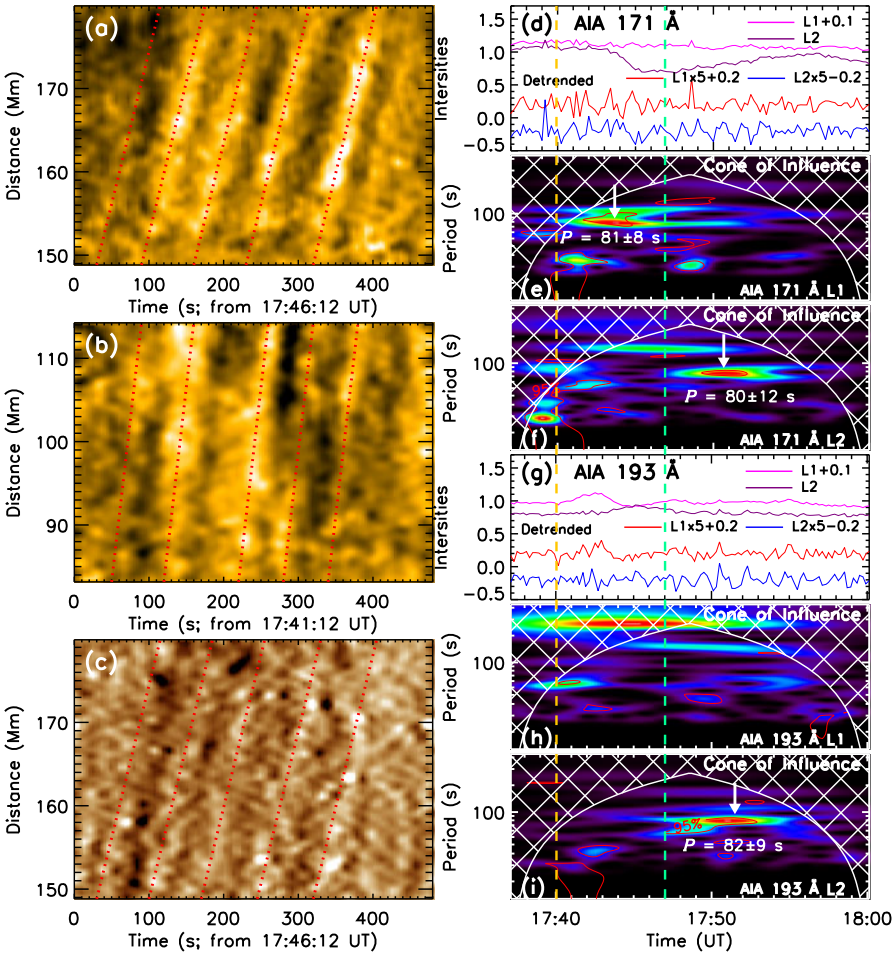

Figure 3 Periodicity analysis of the wave trains observed in 171 Å and 193 Å observations. Panels (a) and (b) display the close-up view of the top and bottom red-dashed box regions shown in Figure 2(e), while panel (c) is the region as shown in Figure 2(f). In these time–distance diagrams, the QFP wave stripes are highlighted using a series of parallel dotted lines. In panel (d), the pink (magenta) curve shows the intensity profile along L1 (L2) as shown in Figure 2(c), while the red (blue) curve displays the detrended intensity profile obtained by subtracting the smoothed flux using a 96-second boxcar. Panels (e) and (f) are the wavelet power spectra of the detrended intensity profiles along L1 and L2, respectively. Panels (g), (h), and (i) are to be compared with (d), (e), and (f), respectively, but they are for the 193 Å intensity profiles. The red contours in each wavelet power spectrum outline the region where the significance level is above 95 %, and the vertical yellow (green) line indicates the start time of the wave trains before (after) the interaction with the perpendicular loop system. In the power spectra, redder color corresponds to higher wavelet power, and those with high power regions are indicated by vertical white arrows, and the corresponding periods [P] are also plotted in the figure.

distance diagrams (343 km s^{-1}), which may reflect the temperature response to the wave trains at different temperatures (Kiddie *et al.*, 2012).

3.3. Periodic Analysis of the Wave Trains

The detailed analysis of the periodicity of the wave trains is displayed in Figure 3, in which panels (a) – (c) are the magnified sub-time–distance diagrams of the regions indicated by the

red boxes shown in Figure 2(e) and (f), while panels (d) – (i) are wavelet analyses of the base-ratio intensity profiles along dashed lines L1 and L2, as shown in Figure 2. In the sub-time–distance diagrams, the steep stripes of the wave trains are clear and parallel to each other. We highlight these wave stripes using a series of parallel red-dotted lines (see Figure 3(a) – (c)), and, therefore, the time intervals between neighboring lines represent the periods of the wave trains. The result indicates that the period of the QFP wave trains before their interaction with the perpendicular loop system ranges from 60 to 100 seconds (see Figure 3(b)), while that ranges from 70 to 90 seconds after the interaction (see Figure 3(a) and (c)). In addition, the QFP wave trains showed similar patterns and periods in the 171 Å and 193 Å time–distance diagrams after the interaction (see Figure 3(a) and (c)), which suggests an intimate relationship between the wave trains observed at the two different wavelength bands.

The base-ratio intensity profiles along L1 (pink) and L2 (magenta) of 171 Å are plotted in Figure 3(d), while those obtained from 193 Å are plotted in Figure 3(g). In the optically thin corona, it is usually true that the emission intensity is proportional to the square of the plasma density, *i.e.* $I \propto \rho^2$. Thus the base-ratio intensity perturbations appropriately represent the variations of the plasma density relative to the pre-event background. To better show the intensity variations and the periodic patterns of the base-ratio intensity profiles, we also plot the detrended intensity profiles in Figure 3(d) and (g) as shown by the red (L1) and blue curves (L2). The detrended intensity profiles are obtained by subtracting the smoothed intensities using a 96-second boxcar, and the results shown in the figure are fivefold magnifications of the original detrended profiles. To extract the periods of the wave trains, we apply a wavelet-analysis technique to the detrended intensity profiles along L1 and L2. The wavelet method is a common effective technique for analyzing localized variations of power within a time series, which allows us to investigate the temporal dependence periods within the observed data. The details of the procedure and the corresponding guidance can be found in Torrence and Compo (1998). In our analysis, we choose the "Morlet" function as the mother function, and a red-noise significance test is performed. Since both the time series and the wavelet function are finite, the wavelet can be altered by edge effects at the end of the time series. The significance of this edge effect is shown by a cone of influence (COI), defined as the region where the wavelet power drops by a factor of e^{-2}. Areas of the wavelet power spectrum outside the region bounded by the COI should not be included in the analysis.

The wavelet power spectra of 171 (193) Å detrended intensity profiles along L1 and L2 are shown in Figure 3(e) ((h)) and (f) ((i)), respectively. At the position L1, strong power with a period of 81 ± 8 seconds is identified. It starts from about 17:40 UT and lasts for about 12 minutes. However, no corresponding periodic signature could be detected at the same position in the 193 Å intensity profile (see Figure 3(h)). This is consistent with the imaging observations described above. At the position L2, we detect strong power with similar periods and durations both in the 171 and 193 Å power spectra. The duration of this strong power is about eight minutes (17:47 UT – 17:55 UT), and the periods are 80 ± 12 seconds and 82 ± 9 seconds in the 171 Å and 193 Å power spectra, respectively. In the two wavelength bands, the start times of the periodic signature are almost the same (see the vertical green line in Figure 3). The similar periods revealed by the power spectra indicate that the wave trains kept their period before and after their interaction with the perpendicular loop system, even though their speed slowed down significantly during the interaction. In our measurement, the periods are determined from the peak of the corresponding global power curve, and meanwhile the significance level should be higher than 95 %. The error of each period is determined by the full width at half maximum of each peak of the global power curve, which is obtained by fitting each peak with a Gaussian function.

To further analyze the periodicity of the wave trains observed in 171 Å and 193 Å observations, we generate k–ω diagrams from 171 Å and 193 Å running-difference observations,

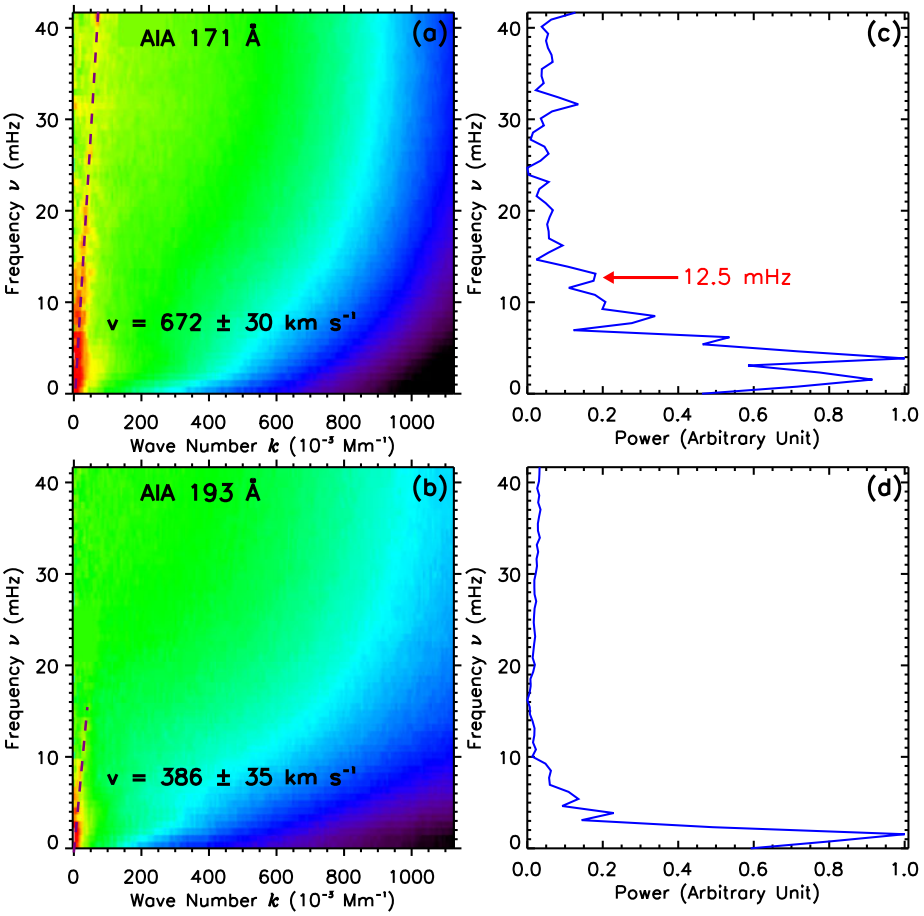

Figure 4 Fourier analysis of the QFP wave in the white-dashed box region shown in Figure 1(b). Panels (a) and (b) are Fourier power (k–ω diagram) of a three-dimensional data tube of 171 Å and 193 Å running-difference images during 17:40 – 17:58 UT, while (c) and (d) are the integrated power spectrum over the wave number of left panels (a) and (b), respectively. The dashed line in panels (a) and (b) is the linear fit to the wave ridge. The red arrow in panel (c) points to the frequency of 12.5 mHz (period: 80 seconds).

with the Fourier transform method, which can decompose the possible frequencies in the observed QFP wave. The principle and detailed operation steps have been documented in previous articles (DeForest, 2004; Liu *et al.*, 2011; Shen and Liu, 2012a). The analysis region is shown as the white-dashed box in Figure 1(b), and the analysis time is from 17:40 to 17:58 UT, close to the duration the QFP wave. The Fourier-analysis results are shown in Figure 4, in which panels (a) and (b) are the k–ω diagrams generated from 171 Å and 193 Å running-difference observations, respectively. Based on the selected field of view of the analysis region and the temporal interval of the observation, we can obtain the resolution of the k–ω diagrams, which is $\Delta k = 6.85 \times 10^{-3}$ Mm^{-1} in the x-axis direction and $\Delta \nu = 0.93$ mHz in the y-axis. In each k–ω diagram, one can find an obvious linear step ridge that represents the dispersion relation of the QFP wave, and it can be well fitted with a straight line passing through the origin (see the dashed lines in Figure 4(a) and (b)). The slope of each ridge gives the phase speed [$v_{\rm ph} = \nu/k$] of the QFP wave, which is about

672 ± 30 km s^{-1} obtained from the 171 Å k–ω diagram, while it is about 386 ± 35 km s^{-1} for the wave observed in 193 Å. The speed revealed by the 193 Å k–ω diagram is close to the average speed of the wave trains measured directly from the 193 Å time–distance diagrams, whereas the speed revealed by the 171 Å k–ω diagram is just consistent with the average speed measured from the 171 Å time–distance diagrams before the interaction with the perpendicular loop system. For each k–ω diagram, we plot the integrated power over the wave number in the right (see panels (c) and (d) in Figure 4), which shows a few peaks such as 1.3, 3.6, 8.2, and 12.5 mHz for the 171 Å Fourier power and 1.3, 3.5, and 5.1 for the 193 Å. Among these frequencies, the frequency (period) 12.5 mHz (80 seconds) coincides with the period revealed by wavelet analysis of the intensity variations at the positions of L1 and L2, as well as the direct estimation from the time–distance diagrams in Figure 3.

3.4. Periodic Analysis of the Flare Pulsation

For impulsively launched fast waves in the low corona, flares are thought to be an obvious source (Aschwanden, 2005). Recent high temporal and spatial resolution imaging results indicate that the associated flares have similar periods with the QFP waves (Liu *et al.*, 2011, 2012; Shen and Liu, 2012a). This may imply that the two phenomena are different manifestations of a single process such as magnetic reconnection. As expected, the QFP wave studied in this article shows an intimate relationship with the accompanying C2.0 flare. We use the light curves over the flare ribbon close to the guiding loop's footpoint to analyze the periodicity of the flare pulsation. The GOES soft X-ray fluxes of 1.0 – 8.0 Å and 0.5 – 4.0 Å bands, flare light curves of 171 Å, 193 Å, and 304 Å, and the wavelet power of the corresponding detrended fluxes are show in Figure 5. The two vertical dashed lines in Figure 5(a) indicate a temporal interval from 17:35 UT to 17:55 UT, and the light curves during this period are shown in panel (b). Panel (c) shows the detrended light curves whose wavelet power spectra are shown in panels (d) – (f). The detrended light curves of 171 Å, 193 Å, and 304 Å show coherent pulsations during the rising phase of the flare (see Figure 5(c)). As can be identified in the figure, the flare light curves have a strong period of 80 seconds, in agreement with the period of the wave trains obtained by direct estimation from imaging observations. The similar period for both the flare and the wave trains implies that they were probably excited by a common physical origin, consistent with previous results (Liu *et al.*, 2011; Shen and Liu, 2012a). In addition, the start time of the flare pulsation was the same as that of the flare, *i.e.* 17:37 UT, which is about three (tem) minutes earlier than the appearance time of the wave trains in the 171 (193) Å observations.

4. Discussions

4.1. The Generation of the QFP Wave

For impulsively generated fast magnetosonic waves in the solar corona, flares are thought to be an obvious source (Roberts, Edwin, and Benz, 1984; Aschwanden, 2005). However, up to the present, the detailed generation mechanisms of the periodicity of flares and thereby QFP waves remains unclear, although previous studies, as well as the present study, have indicated that QFP waves have similar periods to the accompanying flares (Liu *et al.*, 2011; Shen and Liu, 2012a). Based on these observational results, we propose that both QFP waves and the associated flares reflect the details of the energy releasing states in magnetic reconnections.

As summarized by Nakariakov, Pascoe, and Arber (2005), there are several physical mechanisms that can be responsible for flare periodicity, including

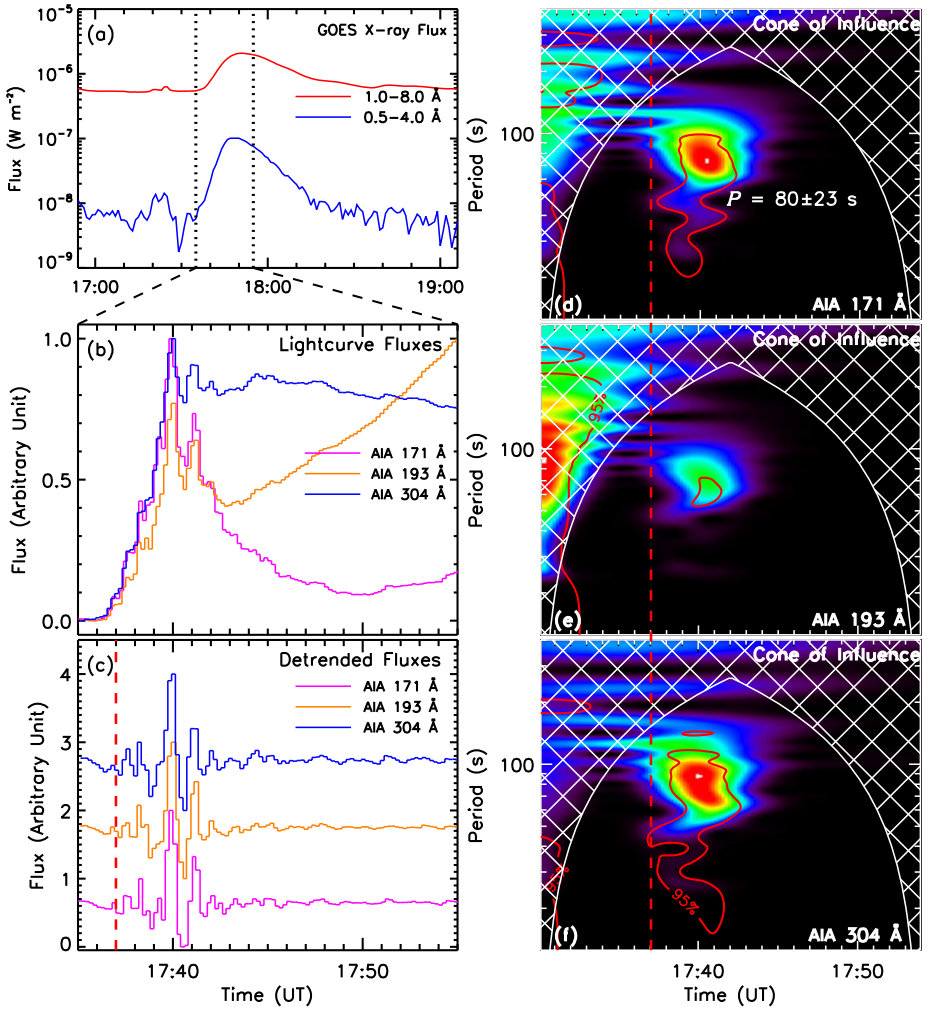

Figure 5 Periodicity analysis of the flare pulsations. Panel (a) is GOES soft X-ray fluxes, in which the red (blue) curve is the time profile of GOES 1 – 8 (0.5 – 4) Å flux. Panel (b) shows the light curves of 171 Å (pink), 193 Å (yellow), and 304 Å (blue) over the flare ribbon. The detrended 171 Å (pink), 193 Å (yellow), and 304 Å (blue) fluxes are plotted in panel (c). (e) – (f) are the wavelet power spectra of these detrended fluxes, in which the red contours indicate the region where the significance level is above 95 %. The vertical red-dashed lines in panels (c) – (f) indicate the start time of the flare (17:37 UT).

i) geometrical resonances,
ii) dispersive evolution of initially broadband signals,
iii) nonlinear processes in magnetic reconnections, and
iv) the leakage of oscillation modes from other layers of the solar atmosphere.

For the present study, the last two mechanisms can be used to interpret the generation of the periodicity of the QFP wave. Since the period of 80 seconds can be identified in both the flare pulsation and the QFP wave, we propose that this component should be excited by some nonlinear processes in the magnetic reconnection that produces the flare. For exam-

ple, recent numerical experiments indicate that repetitive generation of magnetic islands and their coalescence in current sheets are identified during magnetic reconnections, which can lead to an intermittent or impulsive bursty energy release (Kliem, Karlický, and Benz, 2000; Mei *et al.*, 2012; Ni *et al.*, 2012). The generation of a new island is suggested to be accompanied by a burst of magnetic energy. The repetition of such a process will form the periodicity of flares and QFP waves. In such a regime, the periods are determined by the properties of the current sheet such as the plasma concentration, temperature, and magnetic field outside the current sheet (Nakariakov and Melnikov, 2009). In addition, the so-called oscillatory reconnection could also be a possible mechanism for the generation of QFP waves (Murray, van Driel-Gesztelyi, and Baker, 2009; McLaughlin *et al.*, 2009, 2012). Oscillatory reconnection releases energy periodically and thereby produces the repetitive pulsations of the flare emission. Up to the present, various mechanisms have been proposed to explain the periodicity of flare pulsation. However, which one is the corresponding mechanism for QFP wave still needs to be proved.

Beside the common period of 80 seconds, a few low frequencies such as 1.3 ($P =$ 770 seconds) and 3.5 mHz ($P = 285$ seconds) are revealed by the k–ω diagrams of the QFP wave. These oscillation signatures are possibly the manifestations of the photospheric or chromospheric pressure-driven oscillations leaking into the solar corona. This mechanism has been identified in many observational and theoretical studies (*e.g.* De Moortel, Ireland, and Walsh, 2000; 2002; Marsh *et al.*, 2003; De Pontieu, Erdélyi, and James, 2004; De Pontieu, Erdélyi, and De Moortel, 2005; Didkovsky *et al.*, 2011; Zaqarashvili *et al.*, 2011). Hence we can propose that the leakage of oscillation modes from the layers below the corona is also an important driving mechanism for the generation of the observed QFP wave in the low corona, in line with our previous results (Shen and Liu, 2012a).

4.2. Propagation of the Wave Trains

According to the observational results based on the 171 Å observations, the propagation of the wave trains could be divided into three stages: the invisible stage (17:37 – 17:40 UT), the fast propagation stage (689 km s^{-1}), and the slow propagation stage (343 km s^{-1}). The wave trains underwent an invisible stage of about three minutes before their appearance at a distance of about 150 Mm from the footpoint of the guiding loop system; during this stage no significant intensity perturbation could be observed. This may caused by the strong magnetic-field strength or other properties of the footpoint section of the guiding loop system, which may result in insufficient plasma compression and thereby no wave trains could be detected in the imaging observations. We can estimate the average speed during this stage by dividing the distance (150 Mm) by the length of time (180 seconds), which yields a speed of about 833 km s^{-1}. This result indicates that the speed during the fast propagation stage has been slowed down to about 80 % of that during the invisible stage.

We can understand the deceleration of the wave trains from the basic equation of the fast magnetosonic wave when it propagates along a magnetic field, *i.e.* $v_f = \frac{B}{\sqrt{4\pi\rho}}(\theta = 0)$, B being the magnetic-field strength, ρ the plasma density, and θ the angle between the guiding magnetic field and the wave vector (Aschwanden, 2005). It can be seen that the propagation speed of the fast magnetosonic wave is determined by the magnetic-field strength and the density of the medium that supports the wave. Considering the guiding loop system that has a divergent geometry and the gravitational stratification of the density with altitude, the speed of the fast magnetosonic wave would decrease rapidly with height due to the decrease of the magnetic-field strength with height (Ofman *et al.*, 2011). In the meantime, if the total wave energy remains unchanged during the propagation, the decrease of density with

height will amplify the amplitudes of the wave trains which thereby become observable in the imaging observations. However, as the wave trains propagate outwards, the guiding loop become more and more diffuse. Therefore, the wave energy will spread to a broader extent, which will lead to the decrease of the amplitudes of the wave trains. The combined effects of the density stratification and the divergent geometry of the guiding loop can lead to the appearance of a maximum amplitude in the middle of the path as pointed out by Yuan *et al.* (2013). The quantitative relations among these parameters need to be investigate with numerical experiments.

After the wave trains interacted with the perpendicular loop system, the propagation entered a slow propagation stage with a speed of 343 $\mathrm{km\,s^{-1}}$ that is about half of that during the fast propagation stage. In the meantime, similar wave trains appeared in the 193 Å observations, which has the same period and speed of those observed in the 171 Å observations. The sudden decrease of the wave speed observed here could be interpreted from two aspects: the geometric effect and the density increase of the guiding loops. It is well known that the distribution of magnetic fields is very complex, but the basic configuration should be a funnel-like shape as proposed by Gabriel (1976). In the present case, the guiding loops carrying the wave trains may change their inclination angle significantly when approaching the perpendicular loop system, and thus the guiding loops become more curved upward over the underlaying perpendicular loops, *i.e.* a larger inclination angle relative to the solar surface. Therefore, due to the projection effect the observed wave speed can decrease to a small value within a short timescale. Since the 193 Å wavelength images higher layers of the solar corona than that of 171 Å, and the wave trains propagated from a lower height from the footpoint of the guiding loops, the projection effect can also account for the sudden appearance of the wave trains in the 193 Å observations. On the other hand, the sudden decrease of the wave speed can also be understood from the density increase of the guiding loop. When the wave-guiding loops interact with the underlying perpendicular loops, the wave trains will cause a strong compression of the guiding fields, which would increase the density of the guiding loops quickly and thereby decrease the speed of the wave trains within a short timescale. In addition, the compression can still cause a possible adiabatic heating that dissipates the wave energy and thus result in the wave trains in the 193 Å observations.

4.3. Estimation of Wave Energy and Magnetic Field

We can measure the intensity variation of the wave trains in amplitude above the background with equation $I_{\mathrm{A}} = \frac{I_{\mathrm{t}} - I_{t0}}{I_{\mathrm{t0}}}$. The amplitude is determined from the wave crests and troughs during the prominent period of the wave trains. In 171 Å observations, the amplitude variation along L1 is 2.3 % – 5.0 % of the background intensity, and the average value is 3.5 % ± 0.8 %. Along L2, the amplitude variations are 1.2 % – 4.0 % in 171 Å and 0.3 % – 3.7 % of the background intensity in 193 Å, and the average amplitudes are 2.6 % ± 1.1 % (171 Å) and 2.5 % ± 1.3 % (193 Å) of the background intensity. The error of the average amplitude is given by the standard deviation of the measured values. It can be seen that the average amplitude of the wave trains weakened significantly after their interaction with the perpendicular loop system.

The energy flux carried by the QFP wave can be estimated from the kinetic energy of the perturbed plasma that propagate with phase speed through a volume element. So that the energy of the perturbed plasma is $E = (\frac{1}{2}\rho v_1^2)v_{\mathrm{ph}}$, where v_1 is the disturbance speed of the locally perturbed plasma (Aschwanden, 2004), and v_{ph} is the phase speed. In the optically thin corona, it is usually true that $I \propto \rho^2$. Thus the density modulation of the background density $\frac{\mathrm{d}\rho}{\rho} = \frac{\mathrm{d}I}{2I}$. In addition, if we use the relation $\frac{v_1}{v_{\mathrm{ph}}} \geq \frac{\mathrm{d}\rho}{\rho}$, then the energy flux of the

perturbed plasma could be written as $E \geq \frac{1}{8}\rho v_{\rm ph}^3(\frac{dI}{I})^2$ (Liu *et al.*, 2011). For the present study, the average phase speeds during the fast and slow propagation stages are 689 and 343 km s^{-1}, while the average amplitudes are 3.5 % and 2.6 % of the background intensity during the two stages respectively. By assuming that the electron-number density of the wave-guiding loops is $n_{\rm e} = 1 \times 10^9$ cm^{-3}, we can calculate that the energy-flux density of the QFP wave before and after the interaction are $E \geq 1.7 \times 10^5$ erg cm^{-2} s^{-1} and $E \geq 0.1 \times 10^5$ erg cm^{-2} s^{-1}, respectively. As the typical energy-flux density requirement for heating coronal loops is about 10^5 erg cm^{-2} s^{-1} (Withbroe and Noyes, 1977; Aschwanden, 2005), so the energy flux carried by the QFP wave is sufficient for sustaining the coronal temperature of the guiding loops.

With the average speeds of the wave trains during the three distinct stages and the expression of the fast magnetosonic wave along magnetic fields [$v_f = \frac{B}{\sqrt{4\pi\rho}}$ ($\theta = 0$)], we can estimate the magnetic-field strength of the guiding loops at different sections of the guiding loop system with $B = v_f\sqrt{4\pi\rho}$. The calculation results indicate the magnetic-field strengths of the footpoint (invisible stage), middle (fast stage) and end (slow stage) sections of the guiding loop are 5.4, 4.5, and 2.2 gauss, respectively. Since these values are calculated from the projection speeds, they are just the lower limits of the real magnetic-field strength values. In addition, we use the same density [ρ] in our calculation. Therefore, it should be kept in mind that the energy fluxes obtained and magnetic-field strength may only roughly reflect the true situation. Even so, the values obtained still reflect the distribution of magnetic-field strength along the divergence guiding loop system.

5. Summary

With high temporal and spatial resolution observations taken by SDO/AIA, we present an observational study of a quasi-periodic fast-propagating magnetosonic wave along an open coronal loop rooted in active region AR11461. We study the generation, propagation, and the periodicity of the wave trains, as well as their relationship with the associated C2.0 flare. The wave trains first appeared in the 171 Å observations at a distance of about 150 Mm from the footpoint of the guiding loops, then they were observed in 193 Å after their interaction with an underlying perpendicular loop system on the path. To our knowledge, such a phenomenon as well as multi-wavelength observations of QFP waves have not been studied in the past. The main observational results of the present study can be summarized as follows.

i) The QFP wave trains and the associated flare have a common period of 80 seconds, which suggests that the generation of the wave trains and the flare pulsation originated from one common physical process. We propose that the periodic releasing of magnetic energy bursts through some regimes such as nonlinear processes in magnetic reconnections or the so-called oscillatory reconnections can account for the generation of the QFP wave trains. In addition, the component of the low frequencies revealed by the k–ω diagrams may be caused by the leakage of pressure-driven oscillations from the photosphere or chromosphere, which could be another important source for the generation of QFP waves in the low corona.
ii) The propagation of the wave trains can be divided into three stages: the invisible stage (833 km s^{-1}), the fast propagation stage (689 km s^{-1}), and the slow propagation stage (343 km s^{-1}). We conclude that the properties of the guiding loop have determined the manifestations of the wave trains during different stages, such as the distribution of

the density and magnetic-field strength along the guiding loop system, as well as the geometry morphology.

iii) The interaction of the wave trains with an underlaying perpendicular loop system is observed. This process caused two results: the sudden deceleration of the wave and the appearance of the wave trains in the 193 Å observations. These phenomena are new observational results for QFP waves, and they can be understood from the geometric effect and the density increase of the guiding loop system due to the interaction between the wave trains and the underlying perpendicular loop system. The interaction may also have caused the heating of the cool plasma to higher temperature through adiabatic heating.

iv) The amplitude of the wave trains is measured. In the 171 Å observations, the average value is about 3.5 % (2.6 %) of the background intensity before (after) the interaction with the perpendicular loop system, and about 2.5 % in the 193 Å observations. Based on these results, we estimate the energy-flux density of the QFP wave and the magnetic-field strength of the guiding loop system. The order of magnitude of the energy flux carried by the QFP wave is of 10^5 erg cm^{-2} s^{-1}, which is sufficient to sustaining the coronal temperature of the guiding loops. The magnetic-field strength estimated from the wave speeds indicates the distribution of the divergent geometry of the wave-guiding loops. From the footpoint of the guiding loops to the other end, the estimated mean magnetic-field strength decreases from 5.4 to 2.2 gauss.

In summary, these interesting QFP waves could be used for remote diagnostics of the local physical properties of the solar corona. However, details as regards the generation, propagation, and energy dissipation of QFP waves are still unclear. Further theoretical and statistical studies on QFP waves are required.

Acknowledgements The authors acknowledge the data support of GOES and SDO which is a mission for NASA's Living With a Star (LWS) program. We thank an anonymous referee for many helpful comments for improving the quality of this article. The wavelet software is provided by C. Torrence and G. Compo. It is available at atoc.colorado.edu/research/wavelets. This work is supported by the Natural Science Foundation of China under grants 10933003, 11078004, and 11073050, the National Key Research Science Foundation (2011CB811400), the Knowledge Innovation Program of the CAS (KJCX2-EW-T07), the Western Light Youth Project of CAS, the Open Research Program of the Key Laboratory of Solar Activity of CAS (KLSA201204, KLSA201219), and the Open Research Program of the Key Laboratory of Dark Matter and Space Astronomy of CAS (DMS2012KT008). A. Elmhamdi is supported by the CAS fellowships for young international scientists under grant number 2012Y1JA0002.

References

Appert, K., Collins, G.A., Hellsten, T., Vaclavik, J., Villard, L.: 1986, *Plasma Phys. Control. Fusion* **28**, 133.

Aschwanden, M.J.: 2004, In: Walsh, R.W., Ireland, J., Danesy, D., Fleck, B. (eds.) *Coronal Heating* **SP-575**, ESA, Noordwijk, 97.

Aschwanden, M.J.: 2005, *Physics of the Solar Corona. An Introduction with Problems and Solutions*, 2nd edn., Praxis Publishing Ltd., Chichester.

Boerner, P., Edwards, C., Lemen, J., Rausch, A., Schrijver, C., Shine, R., *et al.*: 2012, *Solar Phys.* **275**, 41. ADS:2012SoPh..275...41B. doi:10.1007/s11207-011-9804-8.

Bogdan, T.J., Carlsson, M., Hansteen, V., McMurry, A., Rosenthal, C.S., Johnson, M., *et al.*: 2003, *Astrophys. J.* **599**, 626.

DeForest, C.E.: 2004, *Astrophys. J. Lett.* **617**, L89.

De Moortel, I., Ireland, J., Walsh, R.W.: 2000, *Astron. Astrophys.* **355**, L23.

De Moortel, I., Ireland, J., Hood, A.W., Walsh, R.W.: 2002, *Astron. Astrophys.* **387**, L13.

De Pontieu, B., Erdélyi, R., De Moortel, I.: 2005, *Astrophys. J. Lett.* **624**, L61.

De Pontieu, B., Erdélyi, R., James, S.P.: 2004, *Nature* **430**, 536.

Didkovsky, L., Judge, D., Kosovichev, A.G., Wieman, S., Woods, T.: 2011, *Astrophys. J. Lett.* **738**, L7.
Downs, C., Roussev, I.I., van der Holst, B., Lugza, N., Sokolov, I.V.: 2012, *Astrophys. J.* **750**, 134.
Edwin, P.M., Roberts, B.: 1983, *Solar Phys.* **88**, 179. ADS:1983SoPh...88..179E. doi:10.1007/BF00196186.
Edwin, P.M., Roberts, B.: 1988, *Astron. Astrophys.* **192**, 343.
Fedun, V., Shelyag, S., Erdélyi, R.: 2011, *Astrophys. J.* **727**, 17.
Gabriel, A.H.: 1976, *Phil. Trans. Roy. Soc. Ser. A* **281**, 339.
Heggland, L., De Pontieu, B., Hansteen, V.H.: 2009, *Astrophys. J.* **702**, 1.
Jelínek, P., Karlický, M., Murawski, K.: 2012, *Astron. Astrophys.* **546**, A49.
Jiang, Y.C., Chen, H.D., Shen, Y.D., Yang, L.H., Li, K.J.: 2007, *Solar Phys.* **240**, 77. ADS:2007SoPh..240...77J. doi:10.1007/s11207-006-0257-4.
Karlický, M., Jelínek, P., Mészárosová, H.: 2011, *Astron. Astrophys.* **529**, A96.
Kiddie, G., De Moortel, I., Del Zanna, G., McIntosh, S.W., Whittaker, I.: 2012, *Solar Phys.* **279**, 427. ADS:2012SoPh..279..427K, doi:10.1007/s11207-012-0042-5.
King, D.B., Nakariakov, V.M., DeLuca, E.E., Golub, L., McClements, K.G.: 2003, *Astron. Astrophys.* **404**, L1.
Kliem, B., Karlický, M., Benz, A.O.: 2000, *Astron. Astrophys.* **360**, 715.
Koutchmy, S., Žugžda, Y.D., Locăns, V.: 1983, *Astron. Astrophys.* **120**, 185.
Lemen, J.R., Title, A.M., Akin, D.J., Boerner, P.F., Chou, C., Drake, J.F., *et al.*: 2012, *Solar Phys.* **275**, 17. ADS:2012SoPh..275...17L. doi:10.1007/s11207-011-9776-8.
Liu, W., Title, A.M., Zhao, J., Ofman, L., Schrijver, C.J., Aschwanden, M.J., *et al.*: 2011, *Astrophys. J. Lett.* **736**, L13.
Liu, W., Ofman, L., Nitta, N.V., Aschwanden, M.J., Schrijver, C.J., Title, A.M., *et al.*: 2012, *Astrophys. J.* **753**, 52.
Marsh, M.S., Walsh, R.W., De Moortel, I., Ireland, J.: 2003, *Astron. Astrophys.* **404**, L37.
McLaughlin, J.A., De Moortel, I., Hood, A.W., Brady, C.S.: 2009, *Astron. Astrophys.* **493**, 227.
McLaughlin, J.A., Verth, G., Fedun, V., Erdélyi, R.: 2012, *Astrophys. J.* **749**, 30.
Mei, Z., Shen, C., Wu, N., Lin, J., Murphy, N.A., Roussev, I.I.: 2012, *Mon. Not. Roy. Astron. Soc.* **425**, 2824.
Mészárosová, H., Karlický, M., Rybák, J.: 2011, *Solar Phys.* **273**, 393.
Mészárosová, H., Karlický, M., Rybák, J., Jiřička, K.: 2009a, *Astrophys. J. Lett.* **697**, L108.
Mészárosová, H., Karlický, M., Rybák, J., Jiřička, K.: 2009b, *Astron. Astrophys.* **502**, L13.
Mészárosová, H., Dudík, J., Karlický, M., Madsen, F.R.H., Sawant, H.S.: 2013, *Solar Phys.* **283**, 473.
Murray, M.J., van Driel-Gesztelyi, L., Baker, D.: 2009, *Astron. Astrophys.* **494**, 329.
Morton, R.J., Verth, G., Jess, D.B., Kuridze, D., Ruderman, M.S., Mathioudakis, M., *et al.*: 2012a, *Nat. Commun.* **3**, 1315.
Morton, R.J., Verth, G., McLaughlin, J.A., Erdélyi, R.: 2012b, *Astrophys. J.* **744**, 5.
Nakariakov, V.M., Melnikov, V.F.: 2009, *Space Sci. Rev.* **149**, 119.
Nakariakov, V.M., Melnikov, V.F., Reznikova, V.E.: 2003, *Astron. Astrophys.* **412**, L7.
Nakariakov, V.M., Pascoe, D.J., Arber, T.D.: 2005, *Space Sci. Rev.* **121**, 115.
Nakariakov, V.M., Ofman, L.: 2001, *Astron. Astrophys.* **372**, L53.
Nakariakov, V.M., Verwichte, E.: 2005, *Living Rev. Solar Phys.* **2**, 3. ADS:2005LRSP....2....3N. doi:10.12942/lrsp-2005-3.
Nakariakov, V.M., Ofman, L., Deluca, E.E., Roberts, B., Davila, J.M.: 1999, *Science* **285**, 862.
Nakariakov, V.M., Arber, T.D., Ault, C.E., Katsiyannis, A.C., Williams, D.R., Keenan, F.P.: 2004, *Mon. Not. Roy. Astron. Soc.* **349**, 705.
Ni, L., Roussev, I.I., Lin, J., Ziegler, U.: 2012, *Astrophys. J.* **758**, 20.
Ofman, L., Liu, W., Title, A., Aschwanden, M.: 2011, *Astrophys. J. Lett.* **740**, L33.
Osterbrock, D.: 1961, *Astrophys. J.* **134**, 347.
Parks, G.K., Winckler, J.R.: 1969, *Astrophys. J. Lett.* **155**, L117.
Pesnell, W.D., Thompson, B.J., Chamberlin, P.C.: 2012, *Solar Phys.* **275**, 3. ADS:2012SoPh..275....3P. doi:10.1007/s11207-011-9841-3.
Robbrecht, E., Verwichte, E., Berghmans, D., Hochedez, J.F., Poedts, S., Nakariakov, V.M.: 2001, *Astron. Astrophys.* **370**, 591.
Roberts, B., Edwin, P.M., Benz, A.Q.: 1983, *Nature* **305**, 688.
Roberts, B., Edwin, P.M., Benz, A.Q.: 1984, *Astrophys. J.* **279**, 857.
Schatzman, E.: 1949, *Ann. Astrophys.* **12**, 203.
Schrijver, C.J., Aulanier, G., Title, A.M., Pariat, E., Delannée, C.: 2011, *Astrophys. J.* **738**, 167.
Shen, Y.D., Liu, Y.: 2012a, *Astrophys. J.* **753**, 53.
Shen, Y.D., Liu, Y.: 2012b, *Astrophys. J.* **754**, 7.
Shen, Y.D., Liu, Y.: 2012c, *Astrophys. J. Lett.* **752**, L23.
Shen, Y.D., Li, K.J., Yang, L.H., Yang, J.Y., Jiang, Y.C.: 2010, *Acta Astron. Sin.* **51**, 151.
Shen, Y.D., Liu, Y., Su, J.T., Li, H., Zhao, R.J., Tian, Z.J., *et al.*: 2013, *Astrophys. J. Lett.* **773**, L33.

Thompson, B.J., Plunkett, S.P., Gurman, J.B., Newmark, J.S., St. Cyr, O.C., Michels, D.J.: 1998, *J. Geophys. Res.* **25**, 2465.
Tian, H., McIntosh, S.W., De Pontieu, B.: 2011, *Astrophys. J. Lett.* **727**, L37.
Torrence, C., Compo, G.P.: 1998, *Bull. Meteorol. Soc.* **79**, 61.
Uchida, Y.: 1970, *Publ. Astron. Soc. Japan* **22**, 341.
Verwichte, E., Nakariakov, V.M., Cooper, F.F.: 2005, *Astron. Astrophys.* **430**, L65.
Walsh, R.W., Ireland, J.: 2003, *Astron. Astrophys. Rev.* **12**, 1.
West, M.J., Zhukov, A.N., Dolla, L., Rodriguez, L.: 2011, *Astrophys. J.* **730**, 122.
Williams, D.R., Phillips, K.J.H., Rudawy, P., Mathioudakis, M., Gallagher, P.T., O'Shea, E., *et al.*: 2001, *Mon. Not. Roy. Astron. Soc.* **326**, 428.
Williams, D.R., Mathioudakis, M., Gallagher, P.T., Phillips, K.J.H., McAteer, R.T.J., Keenan, F.P., *et al.*: 2002, *Mon. Not. Roy. Astron. Soc.* **336**, 747.
Withbroe, G.L., Noyes, R.W.: 1977, *Annu. Rev. Astron. Astrophys.* **15**, 363.
Yuan, D., Shen, Y., Liu, Y., Nakariakov, V.M., Tan, B., Huang, J.: 2013, *Astron. Astrophys.* **554**, A144.
Zaqarashvili, T.V., Murawski, K., Khodachenko, M.L., Lee, D.: 2011, *Astron. Astrophys.* **529**, A85.

DOI 10.1007/978-1-4939-2038-9_9
Reprinted from *Solar Physics* Journal, DOI 10.1007/s11207-013-0361-1

Coronal Cavity Survey: Morphological Clues to Eruptive Magnetic Topologies

B.C. Forland · S.E. Gibson · J.B. Dove · L.A. Rachmeler · Y. Fan

Received: 15 January 2013 / Accepted: 11 July 2013 / Published online: 3 September 2013

Abstract We present a survey on coronal prominence cavities conducted using 19 months of data from the *Atmospheric Imaging Assembly* (AIA) instrument aboard the *Solar Dynamics Observatory* (SDO) satellite. Coronal cavities are elliptical regions of rarefied density lying above and around prominences. They can be long-lived (weeks to months) but are often observed to eventually erupt as part of a coronal mass ejection (CME). We determine morphological properties of the cavities both by qualitatively assessing their shape, and quantitatively fitting them with ellipses. We demonstrate consistency between these two approaches, and find that fitted ellipses are taller than they are wide for almost all cavities studied, in agreement with an earlier analysis of white-light cavities. We examine correlations between cavity shape, aspect ratio, and propensity for eruption. We find that cavities with a teardrop-shaped morphology are more likely to erupt, and we discuss the implications

Coronal Magnetometry
Guest Editors: S. Tomczyk, J. Zhang, and T.S. Bastian

Electronic supplementary material The online version of this article (doi:10.1007/s11207-013-0361-1) contains supplementary material, which is available to authorized users.

B.C. Forland · J.B. Dove
Physics Department, Metropolitan State University of Denver, Denver, CO 80217, USA

B.C. Forland
e-mail: bforland@msudenver.edu

B.C. Forland · S.E. Gibson (✉) · Y. Fan
High Altitude Observatory, NCAR, P.O. Box 3000, Boulder, CO 80307, USA
e-mail: sgibson@ucar.edu

B.C. Forland
e-mail: bforland@ucar.edu

Y. Fan
e-mail: yfan@ucar.edu

L.A. Rachmeler
University of St Andrews, St Andrews, Scotland, UK
e-mail: lar20@st-andrews.ac.uk

of this morphology for magnetic topologies associated with CME models. We provide the full details of the survey for broad scientific use as supplemental material.

Keywords Solar corona · Magnetic fields · Prominences · Cavities · Coronal mass ejections

1. Introduction

Coronal cavities, commonly observed in association with prominences (also known as filaments), possess clearly defined boundaries implying a self-contained organized magnetic system. Cavities are one component of a characteristic three-part magnetic field structure observed in the corona: a central prominence, an elliptical region of depleted material that is often referred to as the cavity itself, and a surrounding bright plasma structure (*e.g.*, arcade loops or a helmet streamer). Characterizing coronal magnetic structures is helpful for understanding the magnetic field of the corona as a whole; since cavities are often seen in association with coronal mass ejections (CMEs), a better understanding of their structure and evolution helps illuminate pre-CME magnetic field configurations (Engvold, 1989; Hudson *et al.*, 1999; Low and Hundhausen, 1995; Gibson *et al.*, 2006; Maričić, Vršnak, and Rosa, 2009; Régnier, Walsh, and Alexander, 2011).

Multiple approaches can be used to describe and infer information about the structure of the magnetic field of coronal cavities. One method is to make measurements sensitive to the coronal magnetic field. Using the *Coronal Multi-channel Polarimeter* (CoMP), it is possible to obtain information about the direction of the underlying magnetic fields (Tomczyk *et al.*, 2008). This is complicated by the fact that the corona is optically thin; however, forward modeling of specific magnetic field topologies has been demonstrated as an effective means of enabling interpretation of the CoMP observations of cavities (Dove *et al.*, 2011; Rachmeler, Casini, and Gibson, 2012; Rachmeler *et al.*, 2013; Bąk-Stęślicka *et al.*, 2013).

The approach utilized in this paper is to analyze observational data from the *Atmospheric Imaging Assembly* (AIA: Lemen *et al.*, 2012) on board the *Solar Dynamics Observatory* (SDO: Pesnell, Thompson, and Chamberlin, 2012), characterizing the morphology of cavities and determining any relationship they may have to eruptions. Our objective is to create a database of coronal cavities to identify morphologies indicative of pre-eruptive magnetic configuration and to also make the database available for future study. The high cadence of AIA and the fact that it has been operating for the rise of the solar cycle make the AIA dataset ideal for this type of analysis. Cavities are visible on a daily basis in this dataset and are clearly distinguishable from other structures in the corona – especially near the poles. We conduct a survey of 19 months of data and create a database that notes specific characteristics of the cavities, both qualitatively and quantitatively determined. We first establish a qualitative morphology of the observed cavities, classifying them as semicircular, elliptical, or teardrop-shaped. By fitting ellipses to each cavity, we are also able to quantify specific morphological properties such as cavity size, center position, and aspect ratio of ellipse width to height. We monitor the evolution of the cavity over several days, in order to identify a subset of cavities that erupt. In Section 2 we describe this methodology in detail. In Section 3, we present our analysis and results; in particular, our finding that both our qualitative assessment and quantitative measurements of cavity morphology indicate that a teardrop shape is an indicator of an increased propensity to erupt. In Section 4 we discuss these results in terms of theoretical models of magnetic precursors to CMEs, and in Section 5 we present our conclusions.

2. Methodology

In order to determine which line to use for a survey of cavities, we examined the visibility of cavities in each of the SDO/AIA lines. Both the 211 Å and 193 Å lines were potential candidates: of these two lines we deemed 193 Å more useful for our survey because it had a high contrast between the depleted region at the center of the cavity and the boundary between the cavity and the bright external plasma.

Although the 193 Å line is the most suitable line, standard online images are not optimal for isolating cavities due to the steep intensity drop-off above the solar limb. For this reason we developed a new image processing routine. We fit the theta-averaged data from the solar limb to the edge of the AIA viewing area to a function we defined as

$$I(r) = a \cdot \mathrm{e}^{-(r-1)/b}, \tag{1}$$

where a and b are fitting parameters and $I(r)$ is the intensity averaged over all polar angles for a given radius r. The intensity in each pixel above the limb is then multiplied by the inverse of $I(r)$. The result is an increase in the visibility and contrast of the cavities, making them more clear at higher heights (Figure 1).

We processed AIA data in this manner at a one-hour cadence to create movies covering the time interval 01 June 2010 through 31 December 2011. We then analyzed these movies in order to identify and characterize the cavities in our survey. Three-dimensional analyses of cavities indicate that they possess a tunnel-like morphology with an elliptical cross section (Gibson *et al.*, 2010). Solar rotation of such a structure extended along the line of sight manifests as a two-dimensional, often elliptical, cavity at the solar limb lasting for several days but varying somewhat in size and shape.

In order to make our survey as reproducible and consistent as possible, we developed criteria for defining cavities. One of the fundamental cavity characteristics that we documented is the shape of the cavity. We categorized cavities as having a teardrop, elliptical, or semicircular shape (Figure 2).

Since the cavity is three dimensional, its two-dimensional projection could be described as one or more of these three shapes during its rotation past the limb. If a cavity was first observed as a semicircle but was later observed as an ellipse, it was recorded as an ellipse. If at any time a teardrop shape was observed, we classified that cavity as a teardrop.

We also determined criteria for labeling cavities in order to ensure that each observed structure was a unique cavity. Cavities often came into and out of visibility over the course of minutes or several hours. If a cavity reoccurred at the same latitude within 12 hours of a previously well-defined cavity, it was considered part of that same three-dimensional cavity structure. If more than 12 hours passed without a clear cavity, any cavity appearing at that latitude was classified as a separate structure. This meant that cavities were defined as distinct, although they may have been associated with the same extended filament channel. In addition, no attempts were made to connect cavities that existed on opposite limbs at the same latitude. Along with the beginning and end times and qualitative assessment of cavity morphology, many other characteristics of the cavities were documented. The full survey is available as supplemental online material. The entry for a single cavity is shown in Table 1 as an example of the information contained in the survey.

Of particular interest was that, for those cavities that were observed to erupt, we recorded information about the eruption such as the time of eruption, the point at which it was most clear that the cavity was unstable and that equilibrium had been lost, and the state of the cavity post-eruption. In associating a cavity with an eruption, in order to ensure that the

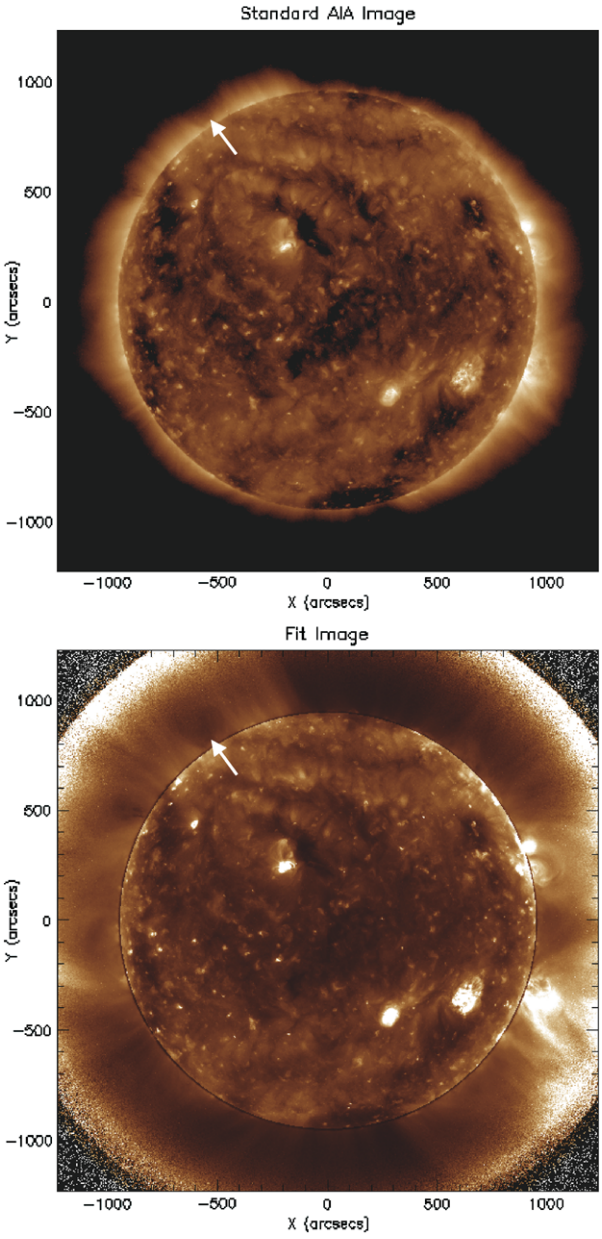

Figure 1 Comparison of pre- and post-processed AIA 193 Å images. (Top) Unprocessed image, (bottom) image processed with radial filter to highlight cavities above the limb. Note the increased visibility and detail of the cavity in the North-East associated with the extended northern polar-crown filament.

cavity existed before the eruption, we required the cavity to be clearly visible at the limb and stable (possessing nearly constant center height) for more than six hours prior to an eruption. In some cases an eruption occurred in the filament channel associated with a portion of the cavity that had rotated onto the disk. In such cases we required that some part of the cavity still be visible at the limb and that this limb portion be visibly perturbed by the eruption occurring in the filament channel. We noted cases in which there was an associated

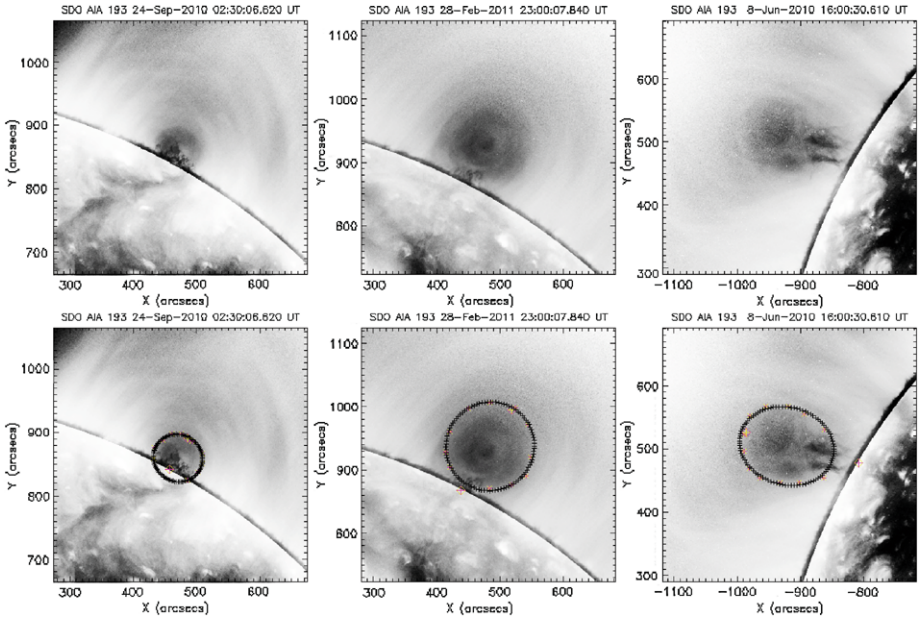

Figure 2 Examples of the three different morphologies used to characterize cavities for this survey. Semi-circular (left) cavities did not show evidence of elliptical or oval cross section at any time while visible. Elliptical (middle) cavities possessed symmetry about both width and height axes. A teardrop shape (right) was assigned to cavities that departed from an elliptical shape (*i.e.*, possessing a narrower bottom than top). Ellipses shown overlaid on bottom row are best fits to data – fit to semicircle extrapolates ellipse below the solar limb, and fit to teardrop is necessarily overwide at its base.

Table 1 Example survey entry for a coronal cavity. Quadrant of the cavity; Start and end times (when cavity was visible); Best time (when cavity was most visible – this is the time the cavity was fit with an ellipse); Shape (as described in text); Eruption time, type, and post-eruption status (as described in text); Axis height, colatitude (coordinates of center of ellipse fit); Aspect ratio (ratio of ellipse fit width to height, where height is axis closest to radial); Non-radial tilt (tilt of height axis from radial); Cavity bottom (radial height from photosphere of bottom of the ellipse, in tilted coordinate frame). The online supplemental table includes this information for all of the cavities and also the quantitative data from the ellipse fits that define the cavity size, position, and shape.

Location	Start time	End time	Best time	Shape	Eruption (time)
NW	2010-06-11 10:30:08	2010-06-13 12:30:08	2010-06-12 19:30:08	Teardrop	2010-06-13 09:30:08
Eruption type	Post- eruption status	Axis height R_{Sun}	Axis colatitude Degrees	Aspect ratio	Non-radial tilt Degrees
Complete cavity	No clear cavity visible	1.20 ± 0.011	42 ± 0.37 (north)	0.71 ± 0.05	-1.1 ± 4.2
Ellipse bottom R_{Sun}					
1.02 ± 0.01					

prominence eruption, and/or the cavity was observed to bodily erupt (Gibson *et al.*, 2006; Maričić, Vršnak, and Rosa, 2009; Maričić *et al.*, 2004).

In order to quantitatively analyze our cavities, we fitted them with ellipses (Figure 2, bottom row) and recorded information about their size, center position, and aspect ratio. This was done through a semi-interactive SolarSoft IDL program, in which users selected the border between the cavity region and the surrounding bright plasma to trace out the ellipse that best fit this boundary (Gibson *et al.*, 2010). The program interpolated regions of ambiguity, such as those where the boundary could not be confidently traced, or where the boundary departed from an ellipse as in the case of teardrop-shaped cavities. The bottom of the ellipse could be either above or below the solar limb: semicircles were fit with ellipses that extended below the solar limb. Ellipse fitting of all the observed cavities was independently completed by three of the authors in order to gauge measurement error.

3. Results

We located 129 unique cavities in the 19 months of AIA data that we surveyed, classifying 39 teardrop-shaped cavities, 66 elliptical cavities, and 24 semicircular cavities. Of these 129 cavities, 28 % erupted. 13 % of semicircular and 17 % of elliptical cavities, compared to 56 % of teardrop-shaped cavities erupted. Teardrop-shaped cavities accounted for 61 % of all eruptions observed (Figure 3, top).

We further considered observational biases associated with observing cavities at the east *vs.* the west limbs. Eruptions are as likely to occur on the back of the Sun as the front. As mentioned above, we examined the filament channel associated with the cavity for evidence of eruption. In several cases we identified front-side, east-limb eruptions where the cavity had almost completely rotated onto the disk and eruption would have been difficult to detect based solely on the remaining portion of the cavity at the limb. Equivalent cases where an eruption occurred after a west-limb cavity had largely rotated behind the west limb, were likely to go unnoticed. Such cases would therefore be "false negatives." (Similar east-limb, back-side and west-limb, front-side filament eruptions would not affect our survey since the eruptions would tend to remove the cavities before they could be identified.) Indeed, as indicated in Figure 3 (middle and bottom), we found 33 % of east-limb cavities to be eruptive as opposed to 22 % of west-limb cavities, indicative of our observational bias.

The associations with eruptions for the east limb are therefore more accurate, and Figure 3 (middle and bottom) shows that they strengthen the result that teardrop-shaped cavities are more likely to erupt: 68 % of teardrop-shaped east-limb cavities erupted, as compared to 23 % of elliptical and 10 % of semicircular east-limb cavities. Teardrop-shaped cavities were thus nearly three times more likely to erupt than elliptical cavities, and seven times more likely to erupt than semicircular cavities.

The assignment of cavity shape as teardrop, elliptical, or semicircular was necessarily a qualitative assessment. We therefore turned to fits of the cavities to investigate the relationship between shape and eruption more quantitatively. We first considered the width-to-height aspect ratio of the ellipses that were fit to each cavity. Figure 4 shows that most cavities had aspect ratios less than one, implying a norm of "narrow" elliptical cavities. This is in agreement with an earlier survey of cavities observed in white light (Gibson *et al.*, 2006), which found that cavities with heights less than 1.4 solar radii were taller than they were wide.

Figure 4 also demonstrates that cavities classified as teardrop-shaped had the smallest aspect ratios on average, followed by ellipses and then semicircles. Table 2 shows that this was true for all populations of cavities, including erupting and non-erupting. This indicates that

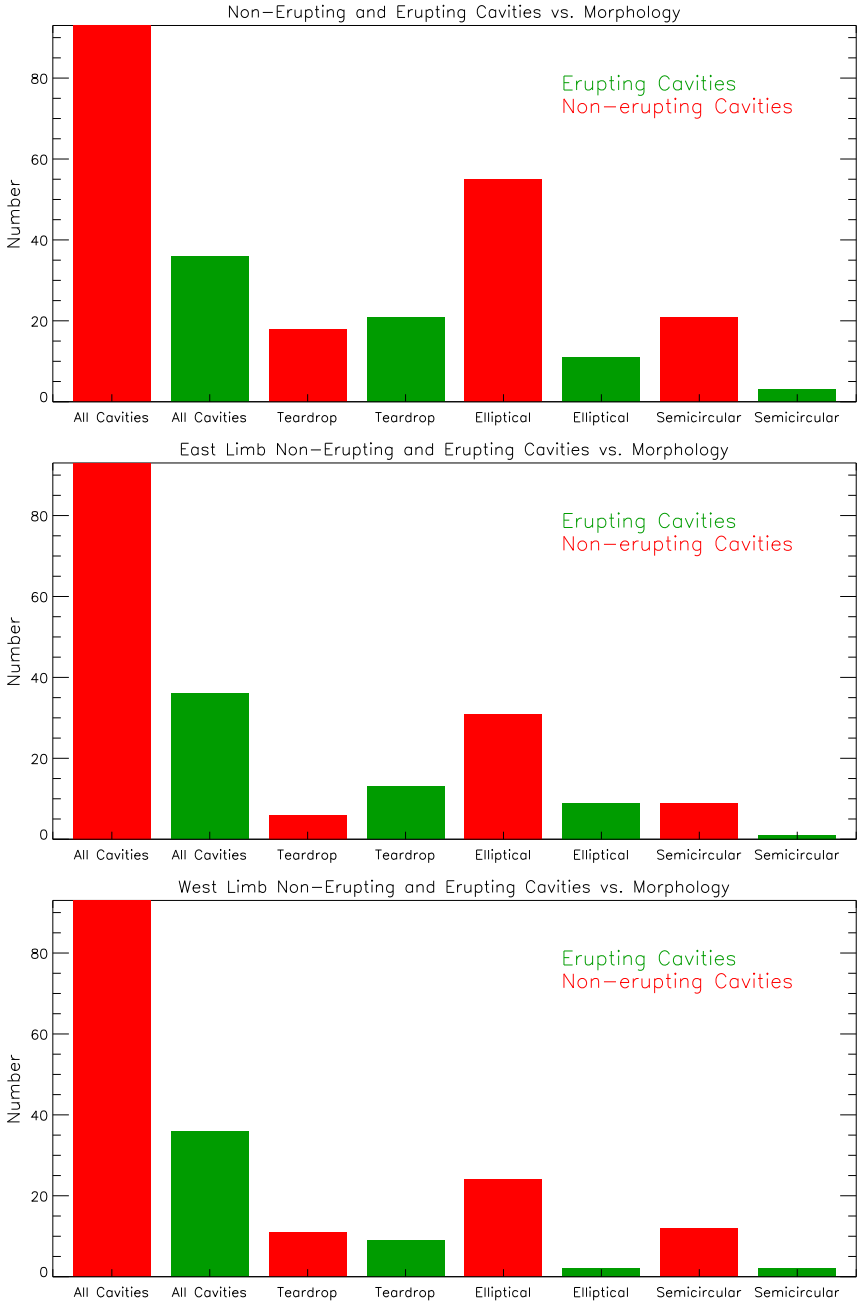

Figure 3 Comparison of the number of eruptive and non-eruptive cavities *vs.* morphology, with three samples: the full dataset, only east-limb cavities, and only west-limb cavities. Notice that not only do teardrop-shaped cavities have more eruptions than any other morphology, they are also the only morphology with more eruptive cases than non-eruptive cases. For reasons stated in the text, the east-limb results are most trustworthy for identification of eruptions; the predominance of erupting teardrop-shaped cavities is particularly clear for this subset.

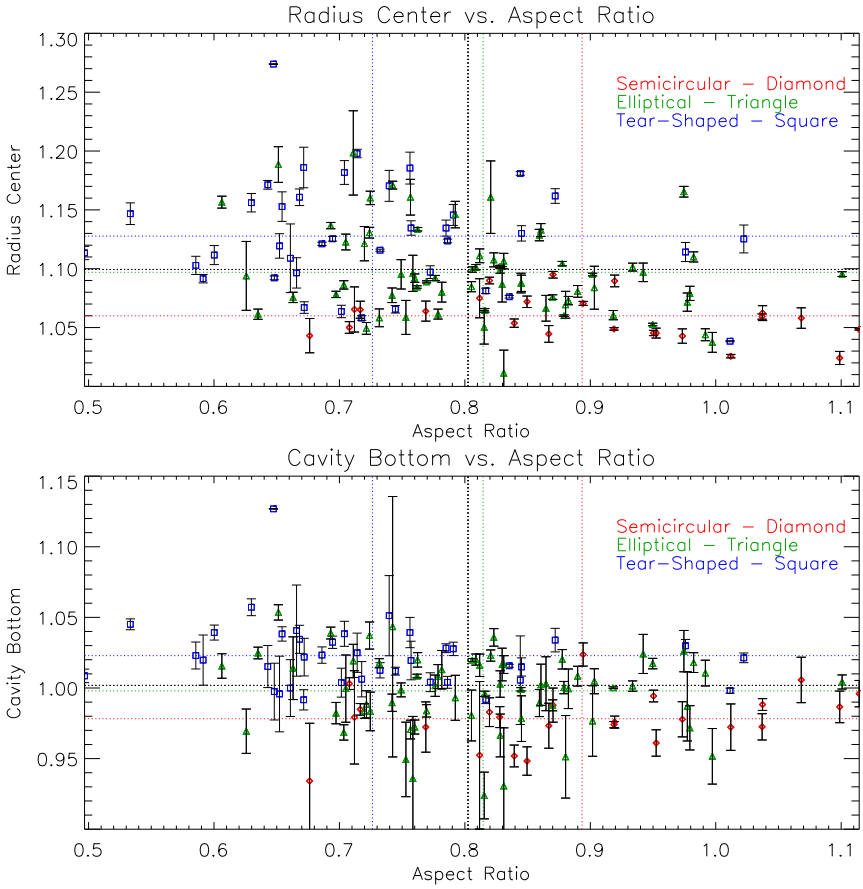

Figure 4 Cavity morphology plotted against ellipse parameters. (Top) Cavity center height (solar radii) *vs.* aspect ratio (width to height) shows a trend for teardrop-shaped cavities to possess smaller (narrower) aspect ratios and lie at higher heights. (Bottom) Height of cavity bottom (solar radii) *vs.* aspect ratio shows a related trend of teardrop-shaped cavities to be fit by ellipses lying completely above the limb. By definition, semicircular cavities were fit with ellipses with bottoms lying below the limb. Horizontal and vertical lines indicate averages for each of the populations, color-coded by morphology (black is the entire population). See also Table 2.

our qualitative assessment of shapes is directly related to the quantitatively measured aspect ratio. However, the characterization of "teardrop-shaped" was not completely captured by the aspect ratio of our ellipses. Figure 4 (top) shows that the central height of the cavity is also correlated with its morphology; in particular, teardrop-shaped cavities on average had higher centers, followed by elliptical and then semicircular cavities. Figure 4 (bottom) demonstrates that teardrop-shaped cavities also tended to be fit to ellipses whose bottoms lay above the limb (by definition semicircular cavities were fit to ellipses with bottoms lying below the limb). As seen in Table 2, all three of these quantitatively measured properties – aspect ratio, center height, and (to a lesser extent) bottom height – may be correlated to a teardrop-shaped morphology.

Figure 5 and Table 2 show that, consistent with our conclusion regarding teardrop-shaped cavities, on average eruptive cavities are narrow, high-centered, and high-bottomed. If we

Table 2 Mean and standard deviation of properties of the cavity ellipse fits as described in Table 1 for various populations of cavities. East-limb cavities only are used for the non-erupting cases, because of the possibility of false negatives in west-limb analysis (see text).

	Mean aspect ratio	Mean axis height $R_\odot$	Mean ellipse bottom $R_\odot$
All tear-shaped	0.73 ± 0.12	1.13 ± 0.047	1.02 ± 0.024
All elliptical	0.81 ± 0.10	1.10 ± 0.037	1.00 ± 0.027
All semicircular	0.89 ± 0.13	1.06 ± 0.020	0.98 ± 0.020
All erupting	0.73 ± 0.13	1.12 ± 0.050	1.01 ± 0.036
Erupting tear-shaped	0.70 ± 0.11	1.15 ± 0.051	1.03 ± 0.028
Erupting elliptical	0.78 ± 0.12	1.09 ± 0.049	0.99 ± 0.039
Erupting semicircular	0.86 ± 0.16	1.06 ± 0.038	0.98 ± 0.020
All non-erupting	0.83 ± 0.12	1.09 ± 0.038	1.00 ± 0.025
Non-erupting tear-shaped	0.76 ± 0.12	1.11 ± 0.028	1.02 ± 0.017
Non-erupting elliptical	0.82 ± 0.10	1.10 ± 0.050	1.00 ± 0.023
Non-erupting semicircular	0.90 ± 0.13	1.06 ± 0.037	0.98 ± 0.021

take as a dividing line an aspect ratio of 0.8, which is the average aspect ratio for the total population of cavities, we find that 40 % of cavities with aspect ratios smaller than this (narrow cavities) erupt, as compared to 16 % for the cavities with aspect ratios greater than this average. If we consider just east-limb cavities, we find the following: narrow cavities erupt 50 % of the time; cavities with heights greater than average (1.1 solar radius) erupt 47 % of the time (as opposed to 22 % for cavities with heights below average); cavities with bottoms higher than average (1.0 solar radius) erupt 39 % of the time (compared to 27 % for cavities with bottoms below average). East-limb cavities possessing all three properties together – narrow aspect ratio, high center, and high bottom – erupt 77 % of the time, as opposed to 20 % for cavities with below-average values for these three qualities.

It is important to note that there is a significant spread in the ellipse properties of eruptive and non-eruptive cavities, as seen in the large standard deviations in the distributions (*e.g.*, uncertainties). Figure 6 illustrates this for aspect ratio.

The cavities have been separated into eruptive (green) and non-eruptive (red) populations, and plotted as normal distributions for aspect ratio, with shading indicating one standard deviation on either side of average (see also Table 2). These standard deviations are approximately equivalent to the difference between the peaks in the normal distributions. This large spread is partly due to uncertainties in the fitting process, but may also be affected by both false positives and false negatives in identifying eruptive cavities in relation to aspect ratio. False negatives have been discussed above, and we have addressed them to some extent by plotting only east-limb cases in our baseline non-eruptive (red) distribution. False positives occur if a CME is associated with a cavity that has a relatively large aspect ratio, but the true aspect ratio has been misidentified because the cavity has not rotated fully into view before the eruption. It is also possible that some CMEs are triggered by a global redistribution of coronal magnetic fields which perturbs the cavity (Schrijver and Title, 2011), resulting in the loss of equilibrium of a large aspect-ratio cavity that otherwise would not have erupted. Despite these caveats, the consistency of our results, both qualitative and quantitative, leads us to believe that a teardrop-shaped morphology is a significant indicator of impending eruption.

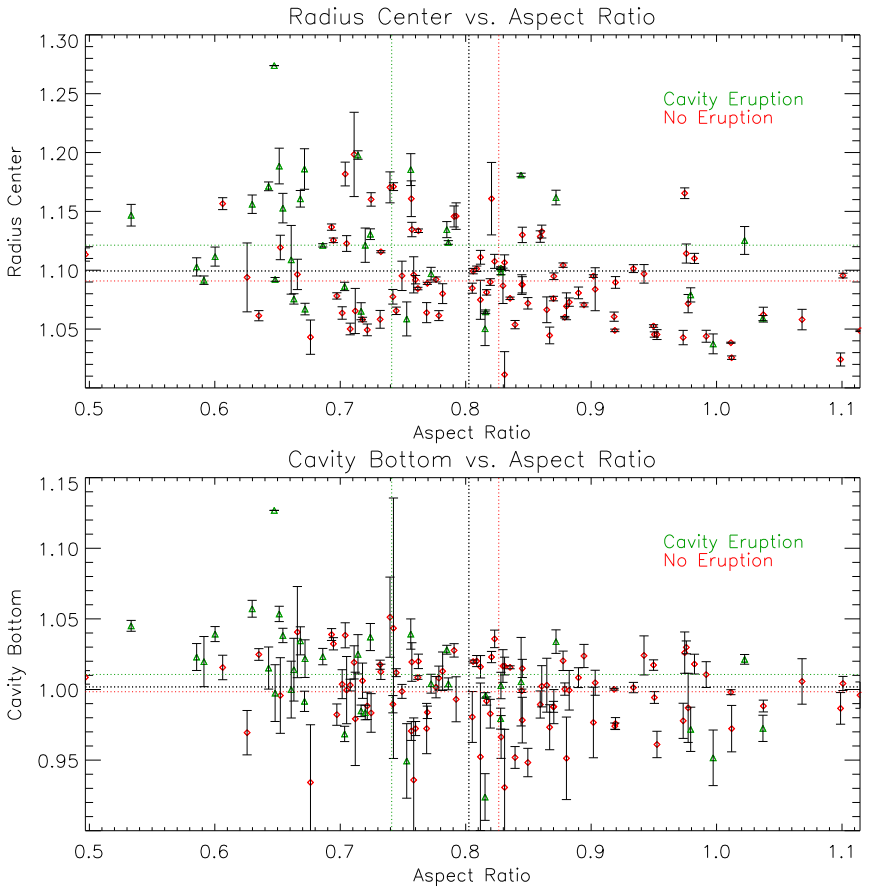

Figure 5 Eruptivity plotted against ellipse parameters. (Top) Cavity center height (solar radii) *vs.* aspect ratio (width to height) shows a trend for narrower, higher cavities to erupt. (Bottom) Height of cavity bottom (solar radii) *vs.* aspect ratio shows a related trend for those with higher bottom heights to erupt. Horizontal and vertical lines indicate averages for each of the populations, color-coded by eruptivity (black is the entire population). See also Table 2.

4. Discussion

The long life of the cavity before eruption indicates that it exists in a quasi-stable magneto-hydrodynamic (MHD) equilibrium. The elliptical cross section of most cavities coupled with coronal magnetic observations of a sheared field at the heart of the cavity (Bąk-Stęślicka *et al.*, 2013) suggest a magnetic flux rope topology. Loss of equilibrium of flux ropes has been simulated for cases where an ideal "torus instability" occurs due to the flux rope axis height lying above a critical point relative to the radial drop-off of the overlying field (Bateman, 1978; Török and Kliem, 2005; Fan, 2005). Recent simulations (Aulanier *et al.*, 2010; Fan, 2010) find a slow evolution of the flux rope via reconnections that increase its magnetic helicity and its axis height to a point where it is unstable to the torus instability. The mechanisms leading up to the loss equilibrium may involve multiple processes (see Forbes and Isenberg, 1991; Vršnak, 1990; Török and Kliem, 2005). This hypothesis is supported by three-dimensional nonlinear force-free extrapolations of vector magnetic field observa-

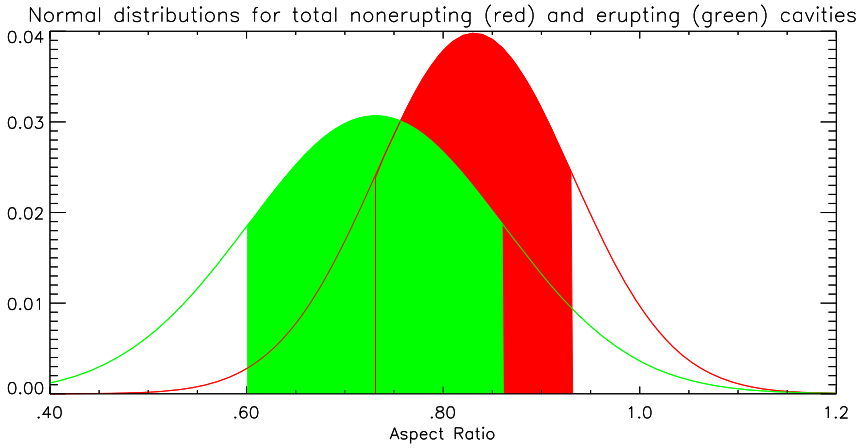

Figure 6 A normal distribution of the aspect ratio for total eruptive and east-limb non-eruptive cavities. The shaded region is an indication of one standard deviation up and down from the mean aspect ratio.

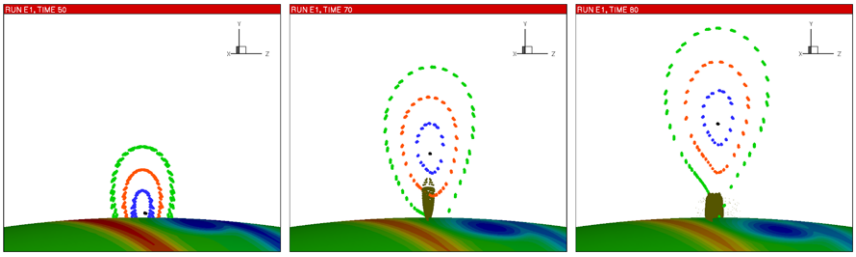

Figure 7 Magnetic flux surfaces (blue, orange, green) within a flux rope at three stages of evolution. Flux surfaces are shown in a plane perpendicular to the underlying polarity inversion line. The possible location of prominence mass accumulation is indicated by brown dots, which fill dips in magnetic field lines up to a prominence scale height (0.01 $R_{\odot}$). (Left) The flux rope axis (black) is very low lying, and the flux surfaces are largely semicircular; (middle) flux surfaces are now elliptical, and dipped fields are now present; (right) the flux surfaces are now teardrop-shaped, and a current sheet is beginning to form aligned with the dipped magnetic field at the flux rope base. Compare to the three types of cavities in Figure 2.

tions, indicating the gradual formation of magnetic flux ropes and their eventual eruption (Savcheva *et al.*, 2012). In that analysis, the flux ropes are initially confined to lower heights, but just before eruption they develop a teardrop-shaped cross section with vertical current sheets beneath the rising flux ropes.

Figure 7 illustrates a similar sequence of quasi-stable equilibrium from the flux rope simulation of Fan (2010). Initially, the amount of magnetic twist is minor, lying within semicircular flux surfaces of sheared field (Figure 7, left). After the flux rope axis emerges, the flux surfaces are ellipses. These ellipses are narrow, due to the upward expansion of the flux rope into the corona and lateral confinement by a surrounding arcade field. When helicity is further increased, a current sheet begins to form at the base of the flux rope aligned with the dipped field region identified with the filament, and the flux surfaces are teardrop-shaped (Figure 7, right).

If cavities are indeed signatures of magnetic flux ropes, we can explain the two main observational findings of this paper: the narrow elliptical cross section of cavities in general,

and the association of a teardrop shape with impending eruption. The increased height of near-eruptive cavities is also consistent with the torus instability as a driver of eruption, and in general with theories of critical heights for eruption onset (Vršnak, Ruždjak, and Rompolt, 1991; Chen *et al.*, 2006; Filippov and Koutchmy, 2008). This is related to prominence observations that indicate an upper limit for prominence height (Liu and Schuck, 2012), although we note that, as seen in Figure 7 (right), because of the curvature of the rope, the location of the prominence may lie well below its axis. It is possible that the center of the cavity is a better indicator of the axis than the prominence height. This height could be monitored to establish thresholds for the torus instability by comparisons to the coronal field (de Toma, private communication).

5. Conclusions

We have undertaken the first large survey of extreme ultraviolet coronal prominence cavities and have made the survey open and available for future research. Our analysis demonstrated connections between cavity morphology and eruptivity. Our two major findings are that cavities are nearly always narrow (with a larger height than width) and that teardrop-shaped cavities have an increased propensity for eruption. We have found by fitting ellipses to cavities that this teardrop-shaped morphology is correlated to some extent to aspect ratio (narrow), center height (high), and bottom height of ellipse (above limb), and that all of these quantities are associated with cavities that erupt from hours to days later. However, we believe that the fundamental quantity is the teardrop shape, and that it is indicative of topological changes associated with the formation of a current sheet beneath a flux rope. This acts as a slow-burning fuse, pushing the flux rope ever higher until ultimately it crosses a threshold height for the torus instability, and the cavity and some or all of its entrained prominence erupt as a coronal mass ejection.

Acknowledgements We would like to thank Giuliana De Toma, Don Schmit, Erin Wood, and the University of Colorado's Laboratory for Atmospheric and Space Physics (LASP) Research Experience for Undergraduates (REU) program. The National Center for Atmospheric Research (NCAR) is sponsored by the National Science Foundation. The AIA data was provided by the Joint Science Operations Center (JSOC) HMI-AIA Science Data Processing (SDP) home at Stanford University. This work is supported in part by the NASA LWS Grant NNX09AJ89G.

References

Aulanier, G., Török, T., Démoulin, P., DeLuca, E.E.: 2010, Formation of torus-unstable flux ropes and electric currents in erupting sigmoids. *Astrophys. J.* **708**, 314.

Bąk-Stęślicka, U., Gibson, S.E., Fan, Y., Bethge, C., Forland, B., Rachmeler, L.A.: 2013, Twisted magnetic structure of solar prominence cavities: new observational signature revealed by coronal magnetometry. *Astrophys. J. Lett.* **770**, L28. doi:10.1088/2041-8205/770/2/L28.

Bateman, G.: 1978, *MHD Instabilities*, MIT Press, Cambridge, 84 – 85.

Chen, J., Marqué, C., Vourlidas, A. Krall, J., Schuck, P.W.: 2006, The flux-rope scaling of the acceleration of CMEs and eruptive prominences. *Astrophys. J.* **649**, 452.

Dove, J.B., Gibson, S.E., Rachmeler, L.A., Tomczyk, S., Judge, P.: 2011, A ring of polarized light: evidence for twisted coronal magnetism in cavities. *Astrophys. J.* **731**, 1.

Engvold, O.: 1989, In: Priest, E.R. (ed.) *Dynamics and Structures of Quiescent Prominences*, Reidel, Dordrecht, 47.

Fan, Y.: 2005, Coronal mass ejections as loss of confinement of kinked magnetic flux ropes. *Astrophys. J.* **630**, 543.

Fan, Y.: 2010, On the eruption of coronal flux ropes. *Astrophys. J.* **719**, 728.

Filippov, B., Koutchmy, S.: 2008, Causal relationships between eruptive prominences and coronal mass ejections. *Ann. Geophys.* **26**, 3025 – 3031. doi:10.5194/angeo-26-3025-2008.

Forbes, T.G., Isenberg, P.A.: 1991, A catastrophe mechanism for coronal mass ejections. *Astrophys. J.* **373**, 294. doi:10.1086/170051.

Gibson, S.E., Foster, D., Burkepile, J., de Toma, G., Stanger, A.: 2006, The calm before the storm: the link between quiescent cavities and CMEs. *Astrophys. J.* **641**, 590.

Gibson, S.E., Kucera, T.A., Rastawicki, D., Dove, J., de Toma, G., Hao, J., Hill, S., Hudson, H.S., Marque, C., McIntosh, P.S., Rachmeler, L., Reeves, K.K., Schmieder, B., Schmit, D.J., Seaton, D.B., Sterling, A.C., Tripathi, D., Williams, D.R., Zhang, M.: 2010, Three-dimensional morphology of a coronal prominence cavity. *Astrophys. J.* **723**, 1133.

Hudson, H.S., Acton, L.W., Harvey, K.A., McKenzie, D.M.: 1999, A stable filament cavity with a hot core. *Astrophys. J.* **513**, 83.

Lemen, J.R., Title, A.M., Akin, D.J., Boerner, P.F., Chou, C., Drake, J.F., *et al.*: 2012, The Atmospheric Imaging Assembly (AIA) on the Solar Dynamics Observatory (SDO). *Solar Phys.* **275**, 17. doi:10.1007/s11207-011-9776-8.

Liu, Y., Schuck, P.W.: 2012, Magnetic energy and helicity in two emerging active regions in the Sun. *Astrophys. J.* **761**, 105. doi:10.1088/0004-637X/761/2/105.

Low, B.C., Hundhausen, J.R.: 1995, Magnetostatic structures of the solar corona. II. The magnetic topology of quiescent prominences. *Astrophys. J.* **443**, 818.

Maričić, D., Vršnak, B., Rosa, D.: 2009, Relative kinematics of the leading edge and the prominence in coronal mass ejections. *Solar Phys.* **260**, 177.

Maričić, D., Vršnak, B., Stanger, A.L., Veronig, A.: 2004, Coronal mass ejection of 15 May 2001: I. Evolution of morphological features of the eruption. *Solar Phys.* **225**, 337.

Pesnell, W.D., Thompson, B.J., Chamberlin, P.C.: 2012, The Solar Dynamics Observatory (SDO). *Solar Phys.* **275**, 3 – 15. doi:10.1007/s11207-011-9841-3.

Rachmeler, L.A., Casini, R., Gibson, S.E.: 2012, Interpreting coronal polarization observations. In: Rimmele, T.R., Tritschler, A., Wöger, F., Collados Vera, M., Socas-Navarro, H., Schlichenmaier, R., Carlsson, M., Berger, T., Cadavid, A., Gilbert, P.R., Goode, P.R., Knölker, M. (eds.) *Astron. Soc. Pac.* **CS-463**, 227.

Rachmeler, L.A., Gibson, S.E., Dove, J.B., DeVore, C.R., Fan, Y.: 2013, Polarimetric properties of flux ropes and sheared arcades in coronal prominence cavities. *Solar Phys.*, in this issue. doi:10.1007/s11207-013-0325-5.

Régnier, S., Walsh, R.W., Alexander, C.E.: 2011, A new look at a polar crown cavity as observed by SDO/AIA. Structure and dynamics. *Astron. Astrophys.* **533**, L1. doi:10.1051/0004-6361/201117381.

Savcheva, A., Pariat, E., van Ballegooijen, A., Aulanier, G., DeLuca, E.: 2012, Sigmoidal active region on the sun: comparison of a magnetohydrodynamical simulation and a nonlinear force-free field model. *Astrophys. J.* **750**, 15. doi:10.1088/0004-637X/750/1/15.

Schrijver, C.J., Title, A.M.: 2011, Long-range magnetic couplings between solar flares and coronal mass ejections observed by SDO and STEREO. *J. Geophys. Res.* **116**(15), 4108. doi:10.1029/2010JA016224.

Tomczyk, S., Card, G.L., Darnell, T., Elmore, D.F., Lull, R., Nelson, P.G., Streander, K.V., Burkepile, J., Casini, R., Judge, P.G.: 2008, An instrument to measure coronal emission line polarization. *Solar Phys.* **247**, 411.

Török, T., Kliem, B.: 2005, Confined and ejective eruptions of kink-unstable flux ropes. *Astrophys. J. Lett.* **630**, L97.

Vršnak, B.: 1990, Eruptive instability of cylindrical prominences. *Solar Phys.* **129**, 295. doi:10.1007/BF00159042.

Vršnak, B., Ruždjak, V., Rompolt, B.: 1991, Stability of prominences exposing helical-like patterns. *Solar Phys.* **136**, 151. doi:10.1007/BF00151701.

DOI 10.1007/978-1-4939-2038-9_10
Reprinted from *Solar Physics* Journal, DOI 10.1007/s11207-013-0325-5

Polarimetric Properties of Flux Ropes and Sheared Arcades in Coronal Prominence Cavities

L.A. Rachmeler · S.E. Gibson · J.B. Dove · C.R. DeVore · Y. Fan

Received: 12 December 2012 / Accepted: 8 May 2013 / Published online: 14 June 2013

Abstract The coronal magnetic field is the primary driver of solar dynamic events. Linear and circular polarization signals of certain infrared coronal emission lines contain information about the magnetic field, and to access this information either a forward or an inversion method must be used. We study three coronal magnetic configurations that are applicable to polar-crown filament cavities by doing forward calculations to produce synthetic polarization data. We analyze these forward data to determine the distinguishing characteristics of each model. We conclude that it is possible to distinguish between cylindrical flux ropes, spheromak flux ropes, and sheared arcades using coronal polarization measurements. If one of these models is found to be consistent with observational measurements, it will mean pos-

Coronal Magnetometry
Guest Editors: S. Tomczyk, J. Zhang, and T.S. Bastian

Electronic supplementary material The online version of this article (doi:10.1007/s11207-013-0325-5) contains supplementary material, which is available to authorized users.

L.A. Rachmeler
School of Mathematics and Statistics, University of St. Andrews, North Haugh, St. Andrews, Fife KY16 9SS, UK

L.A. Rachmeler
Royal Observatory of Belgium, Avenue Circulaire 3, 1180 Brussels, Belgium
e-mail: rachmeler@oma.be

S.E. Gibson (✉) · Y. Fan
High Altitude Observatory, NCAR, P.O. Box 3000, Boulder, CO 80307-3000, USA
e-mail: sgibson@ucar.edu

J.B. Dove
Physics Department, Metropolitan State University of Denver, P.O. Box 173362, Denver, CO 80217-3362, USA

C.R. DeVore
Laboratory for Computational Physics and Fluid Dynamics, Naval Research Laboratory, Washington, DC 20375, USA

itive identification of the magnetic morphology that surrounds certain quiescent filaments, which will lead to a better understanding of how they form and why they erupt.

Keywords Corona, quiet · Magnetic fields, corona · Polarization · Prominences, models

1. Introduction

To understand coronal evolution and predict dynamic events such as coronal mass ejections (CMEs) and solar flares, we need to measure the coronal magnetic field. However, this is no trivial task. Much of the difficulty is due to the optically thin nature of the coronal plasma and the relatively weak intensities of coronal emission lines. Measuring the field will resolve many long-standing debates about the corona, including the magnetic-field morphology surrounding prominences.

Prominences can be extremely stable on the solar surface; some polar-crown filaments survive for many rotations (Gibson *et al.*, 2006), but they are also known to erupt suddenly. When prominences are seen on the limb and are aligned with an observer's line-of-sight (LOS), they are often seen to be embedded in coronal cavities. These cavities are typically depleted in density by a factor of about two relative to the surrounding streamer (Fuller and Gibson, 2009; Schmit and Gibson, 2011). Cavities are the coronal manifestation of the magnetic system that also includes the filament channel and the prominence (Hudson *et al.*, 1999; Gibson *et al.*, 2006; Heinzel *et al.*, 2008; Gibson *et al.*, 2010). Because the cavity comprises the bulk of the system volume, the magnetic structure of the system can be determined from measurements of the cavity. The cavity–prominence structure is known to erupt bodily as a CME (Maričić *et al.*, 2004; Régnier, Walsh, and Alexander, 2011). The initiation of these eruptions depends critically on the magnetic field threading through, and around, the prominence.

Flux-rope models with magnetic field wrapped around a distinct axis, and sheared-arcade models without such an axis, have both been posited as possible morphologies of prominences and their surrounding magnetic field (see Mackay *et al.*, 2010 and references therein). Flux-rope systems have also been explicitly compared with cavities (Low and Hundhausen, 1995; Gibson *et al.*, 2006; Dove *et al.*, 2011). Both morphological models contain dipped field lines where mass can cool and condense into prominence material. Coronal polarization measurements could provide a means of distinguishing between these structures, which would lead to a better understanding of not only the quiescent nature of prominences and cavities, but would also help in understanding how they are formed, and how they destabilize and erupt. Our objective in this article is to determine the characteristic polarization signatures of these different models of prominence cavities.

In Section 2 we discuss the difficulties of measuring the coronal magnetic field and the specifics of the Stokes vector in the Fe XIII 1074.7 nm coronal emission line. Section 3 describes the forward calculations, followed by details of the three individual coronal models in Section 4. We analyze these synthetic forward-modeled observations and look for distinguishing features, which can be compared to solar observations of prominence–cavity systems to identify magnetic morphologies. We present these features in Section 5 and conclude with a discussion of our results in Section 6.

2. Measuring the Coronal Magnetic Field

There are several methods currently employed to determine the magnetic field in the corona. Given that the thermal conductivity along the field is higher than across the field, the *bright*

loops seen in extreme ultra-violet (EUV) and X-ray images of the corona trace out magnetic field lines. Using EUV images, it is possible to follow these lines subject to projection effects (Aschwanden *et al.*, 1999). However, this method does not produce a measure of the magnitude of the field, and full three-dimensional (3D) traces require tomographic inversions and/or stereoscopic methods, which can be tricky in the optically thin coronal plasma. Moreover, this technique only provides magnetic morphology information on specific bright loops, and not the full volume containing the magnetic field.

Measuring *Faraday rotation* along an LOS to a known radio source supplies information about the LOS magnetic field, if the plasma density is known. This technique has been used to study the corona (Patzold *et al.*, 1987; Jensen, 2007), but a limited number of sight lines exist along which this technique is valid. *Gyroresonant emission* in radio wavelengths is related to the total magnetic-field strength in the emitting region, but is limited to areas of strong magnetic field (>200 Gauss) such as active regions (White and Kundu, 1997), although instrumentation with a broader spectral range, such as the *Frequency Agile Solar Radiotelescope* (FASR: Bastian, 2005) would allow for more extensive application. Observation of modified *bremsstrahlung emission* in radio and microwave frequencies provides information on the LOS magnetic field in the corona on the disk. These measurements sample a thin layer in the lower corona/upper chromosphere, not in the full coronal volume (Gelfreikh, 1994; Grebinskij *et al.*, 2000). In some coronal emission lines, particularly in forbidden magnetic-dipole emission lines in the infrared, *resonant scattering* of anisotropic light in a magnetized plasma can produce polarized emission subject to the Hanle and the Zeeman effects. We now discuss the use of coronal emission-line polarization in more detail and further proceed to forward-modeling of this emission.

2.1. Coronal Stokes Vector

Charvin (1965) was one of the first to show that linear-polarization signals from forbidden coronal emission-line transitions could be used to determine the plane-of-sky (POS) magnetic-field direction. Harvey (1969) was the first to attempt to use circular polarization to measure the LOS magnetic-field strength. Compared with modern technology, early detectors of the coronal Stokes vector had significantly lower signal-to-noise ratios, coarser resolution, and required longer integration times, which in turn limited temporal resolution. One such early detector was the *Coronal Emission Line Polarimeter* (Querfeld, 1977), which was a scanning photodiode polarimeter. A full-Sun measurement with this instrument would typically take about two hours and contain 1408 data points from $1.01\mathrm{R}_{\odot}$ to $1.65\mathrm{R}_{\odot}$ (Querfeld, 1977; Arnaud and Newkirk, 1987).

In the intervening 40 years, there has been steady progress in the field of coronal polarization. Today, there are two main coronal polarimeters currently in use: The first is the *Optical Fiber-bundle Imaging Spectropolarimeter* (OFIS) on the *Solar Observatory for Limb Active Regions and Coronae* (SOLARC) at Mt. Haleakala (Lin, Kuhn, and Coulter, 2004). It generates 128 spectra from a 16×8 fiber optic array that subtends 5×2.5 arcminutes. It is capable of measuring full Stokes profiles at each of the 128 positions. This instrument has been used to successfully measure the linear-polarization strength and direction in the Fe XIII 1074.7 nm line, and to determine an LOS field strength from circular-polarization signals above an active region (Lin, Kuhn, and Coulter, 2004; Liu and Lin, 2008). The second instrument is the *Coronal Multi-channel Polarimeter* (CoMP: Tomczyk *et al.*, 2008), which is installed at the Mauna Loa Solar Observatory, and began taking full-corona measurements in October 2010. CoMP is an imaging coronagraph polarimeter with a tunable birefringent filter capable of detecting the Fe XIII 1074.7 nm and

1079.8 nm lines as well as the He I 1083 nm line. The new CoMP observations provide, for the first time, daily full-Sun observations of the magnetic field in the corona. The primary observables of CoMP are the four Stokes parameters (I, Q, U, V).

These observations are taken above the solar limb in the corona, which is optically thin in these wavelengths, and thus the measurements contain information from an extended LOS source. The polarization signal strength is weaker than the line intensity (linear polarization/intensity $\approx 10^{-2}$ and circular polarization/intensity $\approx 10^{-4}$ for a one-Gauss field: Arnaud and Newkirk, 1987; Lin, Penn, and Tomczyk, 2000). It takes on the order of a few minutes to obtain a useable full-Sun linear-polarization measurement with CoMP, and circular-polarization measurements of sufficient signal-to-noise are made by averaging over an hour of data (Tomczyk *et al.*, 2008). The polarization is the result of resonant scattering of anisotropic incident radiation by highly ionized coronal plasma in the presence of an external magnetic field. However, different aspects of this unified process dominate the linear- and circular-polarization signals of the coronal emission lines (*e.g.* Casini and Judge, 1999; Casini, 2002; Judge, 2007; Rachmeler, Casini, and Gibson, 2012, and references therein). We restrict the rest of this discussion to the Fe XIII 1074.7 nm coronal emission line. This is also the line used in the forward calculations.

The linear-polarization signal is completely dominated by the Hanle effect: a depolarization of scattered light associated with a radiation-induced population imbalance of the atomic levels (Trujillo Bueno, 2001). The *atomic alignment* [σ] describes this population imbalance. The transverse Zeeman effect, which is due to the energy splitting of the magnetic sublevels by the coronal field, is a secondary source of linear polarization, because the splitting is smaller than the thermal width of these coronal lines (the transverse Zeeman effect is quadratic in the field strength). The Larmor frequency is higher than the inverse lifetime of the excited state, so the linear polarization signal occurs in the strong-field regime, also known as the *saturated* Hanle effect. In this regime, the linear-polarization strength and direction is dependent on the angle of the magnetic field, but no information about the magnitude is contained in the signal.

The strength of the *total linear polarization* [$L = \sqrt{Q^2 + U^2}$] (same as P in Dove *et al.*, 2011; Rachmeler, Casini, and Gibson, 2012) is dependent on the angle [Θ] between the LOS and the local magnetic-field vector. Specifically, $L \propto \sin^2\Theta$ such that L is strong when the magnetic field is in the POS, and weak when the magnetic field is along the LOS. The relative strengths of Q and U are used to determine the *azimuth angle* [Ψ; $U/Q = \tan 2\Psi$], the POS angle of the LOS integrated magnetic field. There is a 90° ambiguity known as the Van Vleck effect (van Vleck, 1925; House, 1977) such that the magnetic-field direction could be parallel or perpendicular to the measured Ψ. When the local magnetic field is at the Van Vleck angle of roughly 54.7° with respect to solar radial, the light becomes unpolarized, and the strength of L goes to zero. When the magnetic field is less than 54.7° from radial, Ψ is parallel to the direction of the POS component of $\mathbf{B}$, but switches to perpendicular when that angle is surpassed (see, *e.g.*, Figure 5(c)). The Van Vleck effect results in linear polarization directions in the corona that are mostly radial (Arnaud and Newkirk, 1987). If the location of the Van Vleck inversion can be identified, the 90° ambiguity can be removed, although a 180° ambiguity remains.

A measure of the magnetic-field strength is not possible with linear polarization in this regime, but the *circular polarization* does contain information about its magnitude along the LOS. The Stokes-V profile is proportional to $B\cos\Theta$. The longitudinal Zeeman effect (which is linear in the field strength) is the main contributor to the circular-polarization signal. However, the atomic alignment can yield a significant correction to this signal, changing the amplitude of the anti-symmetric V profile, and therefore affecting the diagnostics of the magnetic-field strength (Casini and Judge, 1999).

Stokes I, Q, U, and V are all dependent on the plasma parameters in the emitting region. They are weakly dependent on the temperature as long as the emission line is excited. All Stokes components are directly weighted by the density. At a given location along the LOS, the density dependence cancels when analyzing the *relative* polarizations [L/I and V/I], but this is not the case in a signal that is integrated along the LOS. For an integrated measurement, the signal will be dominated by the areas along the LOS that have the highest density. Since collisions tend to equalize the sublevel populations, a density dependence also enters into the Stokes vector through σ.

There are two general methods for interpreting the coronal-polarization measurements. The first is by inverting the signals into physical properties of the magnetic field. This is the approach taken with photospheric polarization data. However, because the plasma is optically thin in the corona, the signal is coming from an elongated source along an LOS. Inversions generally solve for a single point of emission, so not all calculations will converge to a solution. Inversions of these polarization signals require numerous initial assumptions about the emitting plasma, and are quite difficult due to multiple integrals that must be inverted. These calculations are known to be ill-posed (Judge, 2007). Information about atomic level-populations, and hence the plasma parameters, at each point along the LOS is required to solve the POS magnetic-field direction. To determine the field strength and direction everywhere, tomographic inversions are needed. The tomographic inversion process requires multiple viewpoints of the field, and if only one is available, as is currently the case, solar rotation must be used to generate these viewpoints (Kramar, Inhester, and Solanki, 2006; Kramar and Inhester, 2007). This adds the additional assumption that the coronal field does not change appreciably over rotational timescales. An alternate approach to extracting information from coronal-polarization data is forward-modeling.

Our forward technique involves creating simulated polarimetric observables from models of the corona (Judge and Casini, 2001; Judge, Low, and Casini, 2006). In the work presented here, we use this technique to study the differences between several pre-CME magnetic morphologies, and expand upon the work begun by Judge, Low, and Casini (2006). The ultimate goal of this research is to determine if it is possible to use coronal polarization to positively identify flux ropes, or other magnetic morphologies, in the cavities that surround pre-CME filaments.

3. Description of the Forward Calculations

The basic procedure of our forward technique is to calculate the Stokes vector produced along a given LOS in a magnetic model and build an image from a grid of sight lines. To do this, the magnetic field, temperature, density, and velocity at every location along each LOS are used. Given this information, we calculate the level populations and the emitted polarization profiles for the Fe XIII 1074.7 nm transition at each location using the publicly available Fortran code (FORCOMP) discussed by Judge and Casini (2001). The forward model has an IDL user interface and is publicly available for download and use (people.hao.ucar.edu/sgibson/FORWARD/).

FORCOMP first calculates the statistical-equilibrium equations based on the location and the local plasma parameters from the model: height above the solar surface [h], density [ρ], temperature [T], magnetic field [**B**], and velocity [**v**]. Using standard atomic data, the statistical-equilibrium equations determine the relevant level populations of the atomic system for the transition in question. The code treats inelastic and superelastic collisional processes, but neglects elastic collisions. This omission affects the magnitude, but not the

direction, of L and leads to a small uncertainty in V. The LOS field strength and the POS field direction are not strongly affected by the elastic collisions. Once the level populations are determined, FORCOMP solves the radiative-transfer equations to calculate the polarization of the reemitted radiation in the direction of the observer (Judge and Casini, 2001). The signals are then integrated over wavelength into a single number for each pixel (or LOS), and are assembled into an image.

The benefit of the forward technique is that we can easily calculate the simulated polarization signals from a theoretical model of a magnetic system and then compare these images with observations. It allows us to test the theories against an observable that is directly sensitive to the magnetic field in the corona. Additionally, it allows for comparison between the models themselves.

The forward-model outputs Stokes I, Q, U, V and combinations thereof. We use mainly intensity $[I]$, relative linear polarization $[L/I]$, azimuth $[\Psi]$, and relative circular polarization $[V/I]$.

4. MHD Models

For our study of magnetic flux rope and sheared-arcade signatures in the corona, we used three models, each having a distinct magnetic morphology: The first model is a 3D analytic spheromak flux rope in exact equilibrium (Gibson and Low, 1998, 2000). The second is an azimuthally symmetric (2.5D) cylindrical flux rope taken from an MHD simulation created to study current-sheet formation during CME initiation (Fan and Gibson, 2006). The last is a 2.5D sheared arcade taken from MHD simulations of CME initiation by the multipolar breakout mechanism (Antiochos, DeVore, and Klimchuk, 1999; Karpen, Antiochos, and DeVore, 2012, and references therein). All models are in, or near, equilibrium and have been argued as models for prominence magnetic structure. The two flux-rope models contain a region of concave-up magnetic dips that can support prominence plasma against gravity, and they also capture many observed properties of coronal cavities (Hudson *et al.*, 1999; Gibson and Low, 2000; Mackay *et al.*, 2010; Reeves *et al.*, 2012). Sheared arcades in 2.5D typically contain only concave-down regions that can support time-dependent prominence condensations if the field is sufficiently flat (Karpen *et al.*, 2001). In three dimensions, sheared arcades can develop regions of concave-up field lines like those in flux ropes, and they then can support the plasma statically against gravity (Antiochos, Dahlburg, and Klimchuk, 1994; Luna, Karpen, and DeVore, 2012, and references therein).

We used a single snapshot from the two time-dependent MHD models. Because we are studying the steady-state pre-CME magnetic structure, all velocities were set to zero. The times used are those where the field is near equilibrium, and thus have close to zero velocity everywhere.

Two of our models are 2.5D. Azimuthal symmetry creates structures that are elongated along the LOS. When structures are highly 3D, the magnetic information can become smeared along the LOS, making magnetic signatures more difficult to identify. We used 2.5D models because the observational signatures of the magnetic field we are studying are clear coronal cavities. When a coronal filament channel and associated neutral line are along the LOS – nearly parallel with the solar Equator – a cavity commonly becomes visible, which implies that cavities are elongated along the LOS (Gibson *et al.*, 2010). The 2.5D assumption is thus justified by cavity observations.

For the spheromak model, we used the density and temperature provided by the analytic model. The parameters were chosen such that the density and temperature vary only

slightly in the calculation domain (Dove *et al.*, 2011). For the two MHD models, a range of plasma parameters was explored. The goal of this work is to study the impact of the magnetic morphology on the polarization signatures. We looked at our models both with the original plasma distributions from the MHD simulations and with simple spherically symmetric plasma profiles. These new plasma distributions are not strictly in equilibrium with the magnetic fields. However, they serve the useful purpose of providing a means of distinguishing the features in the polarization data that are caused by the magnetic morphology from those that are heavily influenced by the plasma parameters. In addition, any effects of changing the plasma distributions on the magnetic-field structures would be very weak, since the prominence and cavity are in the low-β regime and are nearly in force-free equilibrium in both MHD examples.

Coronal Stokes vectors were calculated for each theoretical system using the forward code described in Section 3. We compared these polarization signatures with each other to determine their similarities and differences and to identify their distinguishing features.

4.1. Model Descriptions

The first magnetic system we explored is that of an analytic spheromak flux rope. A more detailed study of forward-model results from this particular flux rope can be found in Dove *et al.* (2011). The spheromak model (Figure 1) is an exact solution to the MHD equations in full magnetostatic equilibrium (Gibson and Low, 1998). The magnetic field of the flux rope is a closed, twisted-flux system attached to the photosphere, which has been shown to reproduce observational features of a three-part CME including the cavity and the bright prominence (Gibson and Low, 2000). The external field has a split bipolar configuration with a hydrostatic density background. We used an orientation such that the flux-rope axis, and hence the prominence material, is oriented along the LOS, and the axial magnetic field is directed toward the observer (Figure 1(b)). As stated by Dove *et al.* (2011), we chose a parameter set such that the density is close to spherically symmetric. The background-density profile was taken from Schmit and Gibson (2011). The density decreases from around 5×10^8 cm^{-3} at photosphere to about 3×10^7 cm^{-3} near the top of the spheromak at 1.3R$_\odot$. The temperature is between 7×10^5 and 1×10^6 K. The magnetic-field strength is strongest at the axis, where it is around 1 G, and the external field strength near the flux rope is about 0.1 G. Thus, the plasma β is high outside the spheromak, above 100, and between 1 and 10 in most of the flux rope.

The second model is a 2.5D axisymmetric cylindrical flux rope (Figure 2) and is described in Fan and Gibson (2006). This numerical model comprises a 2×10^6 K isothermal atmosphere occupied by a potential arcade field under which a twisted toroidal flux tube kinematically emerges. With continual emergence, the system is quasi-static until time $t = 114\mathrm{R}_\odot/v_{\mathrm{A0}}$, where v_{A0} is the characteristic Alfvén speed, after which the flux rope erupts. If the emergence is stopped before that, the system remains stable. We analyzed a time step at $t = 114$ where the emergence was stopped at $t = 112$. The model extended from 1R$_\odot$ to 14.4R$_\odot$ radially and from $\pi/3$ to $2\pi/3$ in latitude. For the forward analysis, the system was oriented such that the flux rope was in the equatorial plane and the axial field pointed away from the observer. The magnetic-field strength at the axis was about 10 G. The electron density in the flux rope was on the order of 10^{6-7} cm^{-3}. The plasma β was below 0.1 except near the footprint of the arcade immediately surrounding the flux rope.

The third model (Figure 3) is a 2.5D axisymmetric numerical datacube of a breakout quadrupolar system (Karpen, Antiochos, and DeVore, 2012). The computational domain extended from 1 to 125R$_\odot$ radially and over π radians in latitude. The system was energized by shearing the innermost polarities near the neutral line. The shearing resulted in a

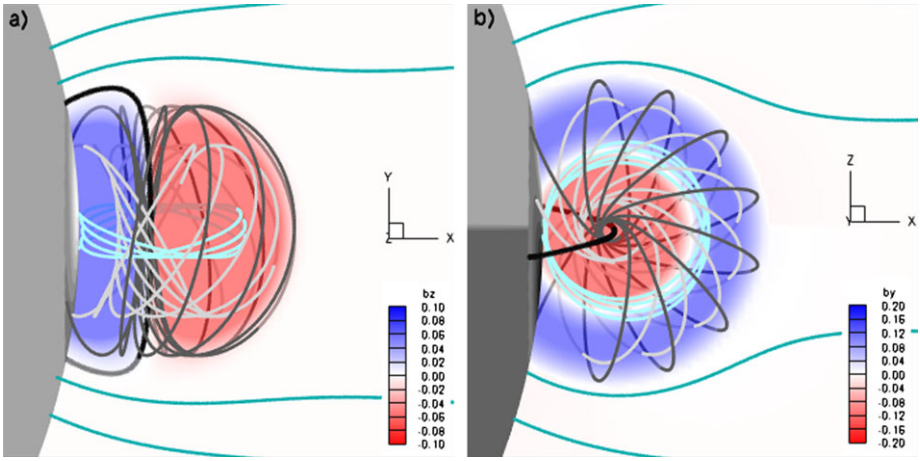

Figure 1 Field-line traces in the analytic spheromak flux-rope model seen from two different view points. Prominence material would theoretically sit below the thick black line, which traces the flux-rope axis, in the dips of the magnetic field. We used the orientation in b) in the forward calculations, with the magnetic field along the axis pointed toward the observer. An animated version of this figure is available in the electronic supplementary material.

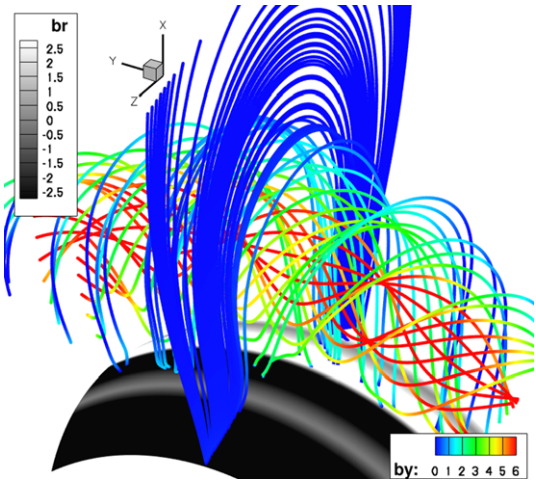

Figure 2 Field lines traced from the 2.5D axisymmetric cylindrical flux rope. Colors on the field lines represent the strength of the y-, or axial, component of the field. An animated version of this figure is available in the electronic supplementary material.

field that is pointed away from the observer in our orientation. The field that connects these two polarities sheared and expanded both radially and laterally. Because a simple adiabatic energy equation and a closed lower-boundary condition were used, the plasma entrained in the sheared field rarefied and adiabatically cooled relative to the background. This configuration did not form a flux rope with a central axis until flare reconnection set in after the eruption. The time shown in Figure 3 is $t = 60\,000$ seconds; stopping the shearing motions at this time resulted in a stable equilibrium state, while continuing the motions led inexorably to an eruption. In and around the sheared arcade, the magnetic-field strength was about 1 G. In this same area, the plasma densities were 10^{6-7} cm^{-3}. The temperature reached a local minimum around 3×10^5 K within the sheared field, while it was about 10^6 in the surrounding, unsheared field. The plasma β was below 0.01 in the sheared region and of order unity

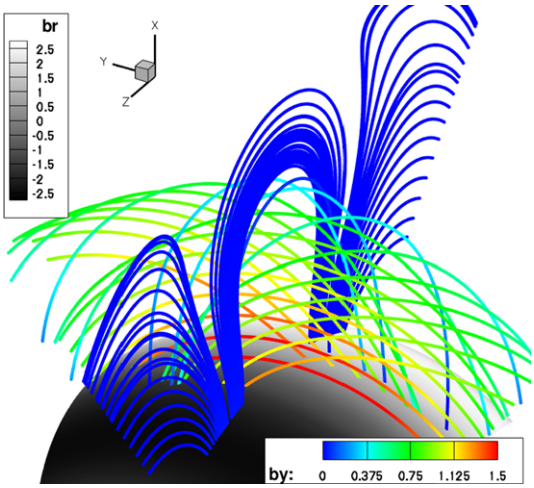

Figure 3 Field lines traced from the 2.5D sheared arcade model. Colors on the field lines represent the strength of the y-, or axial, component of the field. An animated version of this figure is available in the electronic supplementary material.

in the unsheared region (except, of course, in the immediate vicinity of the null point, where β becomes very high).

5. Results

Interpreting a polarization image is not necessarily straightforward (see Judge, 2007; Rachmeler, Casini, and Gibson, 2012 for detailed descriptions of the signal interpretation). For L/I images (*i.e.* Figure 4(b)), the magnitude of the signal is always positive, and the images are usually plotted on a logarithmic scale. Bright areas indicate magnetic field that is primarily in the POS. Dark areas generally indicate magnetic field that is along the LOS. Sharp, elongated dark structures are usually indicative of Van Vleck inversions, marking where the magnetic field is at an angle of $\approx 54°$ from radial. The L/I images may have the magnetic-field direction overlaid as arrows or lines. In the images presented in this article, the red arrows indicate the true POS direction of the magnetic field in a thin POS slice that bisects the Sun. The blue lines indicate the azimuth direction of the linear polarization, which is subject to the 90° Van Vleck ambiguity (Section 2.1). They are generally parallel when the magnetic field is close to radial, and perpendicular when it is not. V/I images are plotted on a linear scale with blue as negative and red as positive; white is zero. In our coordinate system, positive Stokes V (blue) indicates magnetic field toward the observer.

5.1. Spheromak Flux Rope

We used the parameter set from Dove *et al.* (2011) to demonstrate the main features for the spheromak flux rope. In the LOS-integrated images, the following features are identifiable and are robust signatures of this magnetic morphology: Figure 4 shows the forward-model results, as presented also in Dove *et al.* (2011). We summarize the conclusions from that analysis as follows:

i) *Dark L/I central core.* A dark core is clearly visible at the location of the flux-rope axis in the L/I image (Figure 4(b); $Z = 0$, $Y = 1.1$). This is due to the LOS field associated with the axis. The axis of this type of flux rope is particularly clear because it is straight

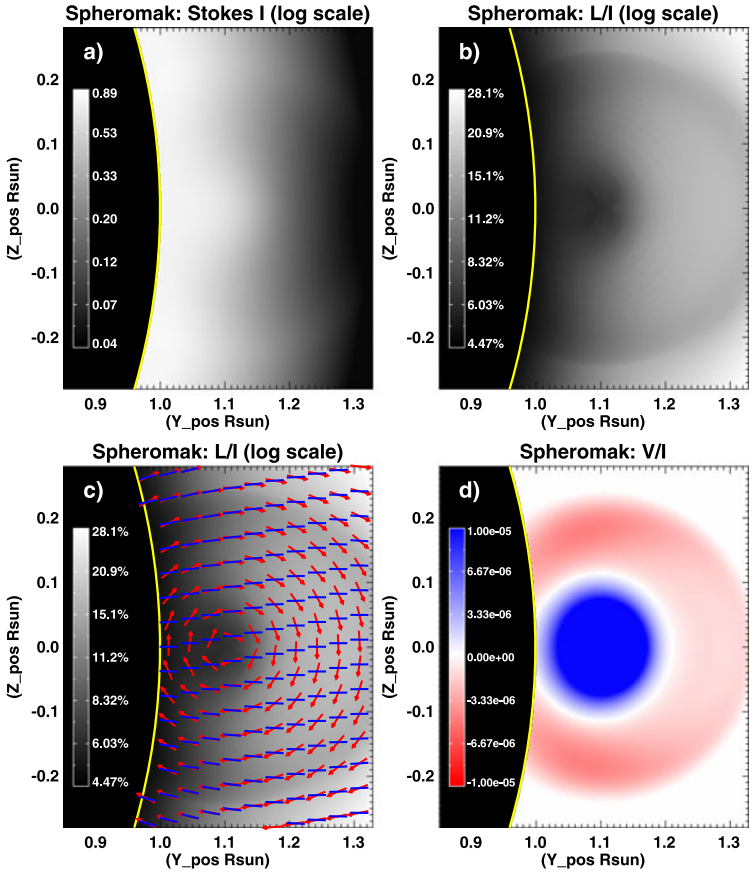

Figure 4 Forward-model results of the spheromak flux rope. a) Stokes intensity, b) relative linear polarization, c) relative linear polarization with magnetic-field direction plotted as red arrows and integrated polarization azimuth direction plotted as blue lines, d) relative circular polarization.

along the LOS, and not curved like the axis of the cylindrical flux rope. The dark central core is visible if the axis is oriented within about 30° of the LOS.

ii) *Dark L/I outer ring*. A ring of darker L/I is visible at the edge of the spheromak bubble (Figure 4(b)), and it is also associated with LOS field. This ring is much fainter than the axis field because **B** on the outer edge of the bubble is only aligned with the LOS in a relatively narrow volume of space.

iii) *Bright L/I ring*. Between i) and ii) is a bright ring in L/I (Figure 4(b)), which is due to the POS field in the flux rope.

iv) *Radial azimuth.* The linear polarization direction shows no clear Van Vleck inversion locations (blue lines in Figure 4(c)). Although there are Van Vleck inversions within the spheromak, the rotation of the field along the LOS smears these out such that they are not visible in the integration.

v) *Bi-directional circular polarization* (V/I). The circular polarization comprises a clear circular positive signal around the axis surrounded by a weaker rung of negative signal (Figure 4(d)). The presence of both positive and negative Stokes-V is not found in either of the other models studied here.

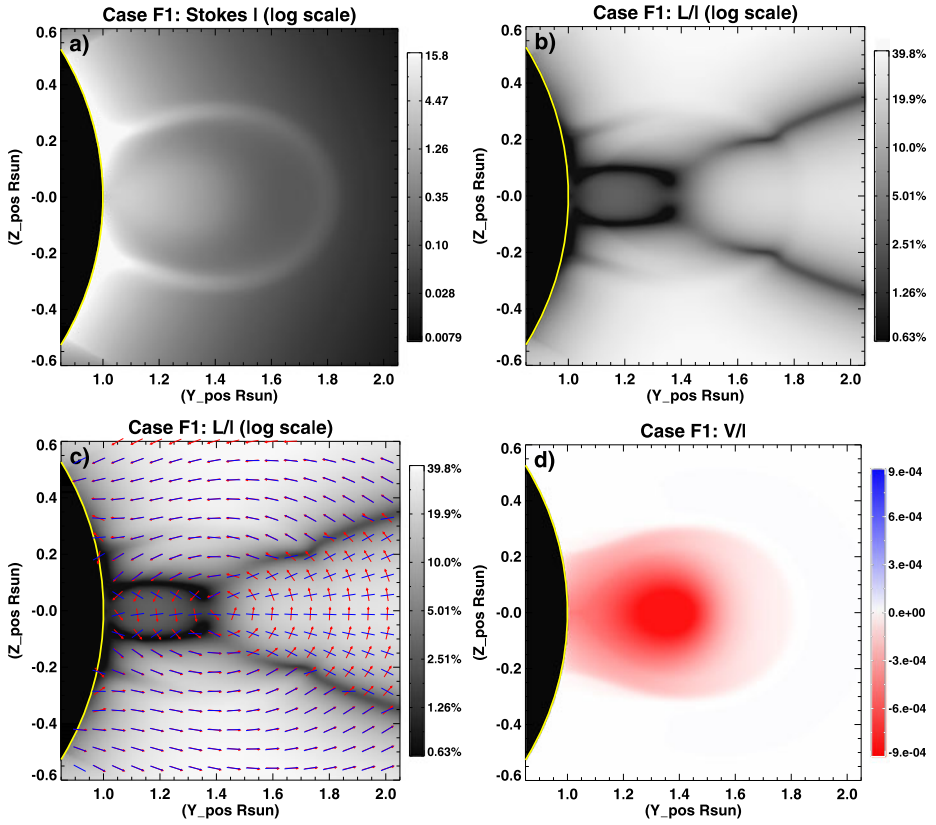

Figure 5 Forward-model results from the flux-rope model case F1 with the density of the original MHD data cube and a temperature of 2×10^6 K. a) Stokes intensity, b) relative linear polarization, c) relative linear polarization with magnetic-field direction plotted as red arrows and integrated polarization azimuth direction plotted as blue lines, d) relative circular polarization.

5.2. Cylindrical Flux Rope

Figure 5 shows the forward-model results for the cylindrical flux-rope configuration. To test the robustness of the magnetic signatures in the polarization signals, we ran the forward calculations on three cases. Case F1 used the original density and isothermal temperature of $T = 2 \times 10^6$ K from the MHD model (Figure 5). Case F2 used an isothermal hydrostatic density fall-off with a scale height of $(2R_\odot k_b T)/(GM_\odot m_p) \approx 0.13R_\odot$ [$R_\odot$ and $M_\odot$ are the solar radius and mass, k_b is the Boltzmann constant, G is the universal gravity constant, m_p is the mass of a proton, and $T = 1.5 \times 10^6$ K is the temperature] and a density at the coronal base of 5.8×10^8 electrons cm^{-3}. Case F3 used a hydrostatic power-law density and temperature function derived from fits to coronal-streamer densities (Gibson *et al.*, 1999). The magnetic field in this model was in nearly force-free equilibrium. The imposed plasma was also low-β. If re-relaxed to true equilibrium, the scale-height of the plasma along field lines would be altered, but the field topology would remain nearly unchanged.

Stokes-I changed noticeably when a spherically symmetric density was used. Almost none of the structure seen in F1 (Figure 5(a)) is present in F2 or F3 (not shown). This is not surprising because the intensity of emitted radiation is strongly dependent on the

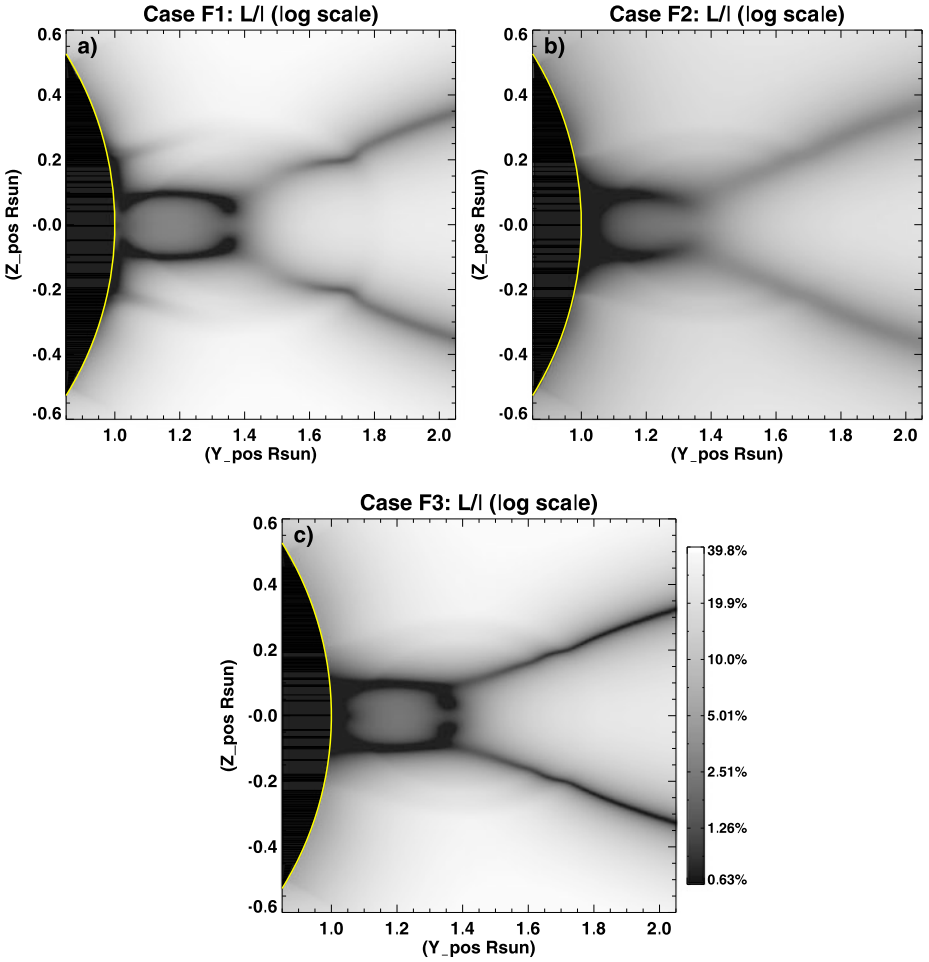

Figure 6 Comparison of the relative linear polarization for the three cases of the cylindrical flux rope. All three images use the same scale.

local plasma density, so a spherically symmetric density results in a virtually spherically symmetric Stokes-I. The relative linear polarization signals varied little between the three cases (Figure 6); these differences are discussed at the end of this section. We first analyze the signatures of F1.

i) *Dark* $\vee$*-shaped Van Vleck inversions in the arcade*. These are the Van Vleck inversions in the external arcade field (Figure 5(b); $Y = 1.4$ to 2). The field outside of the $\vee$ is less than 54° from radial, and the field inside the $\vee$ is greater than that. This is clearly visible (Figure 5(c)) in the shift of the linear-polarization direction (blue lines) from parallel to perpendicular to the POS magnetic-field direction (red arrows). These two Van Vleck inversions extend downward into the flux rope.

ii) *Darker central region in* L/I. In general, the region near the flux-rope axis ($Z = 0$, $Y = 1.35$) is slightly darker (Figure 5(b)). This is because there is more LOS field in this region, so the linear-polarization signal is lower. However, because of the LOS

integration and the curvature of the central flux-rope axis, the location of the axis is unclear. See also iii) below.

iii) *Dark beads in L/I near the axis*. These are visible in F1 and F3, but not in F2 (Figure 6). These locations are dark because they are signatures of the LOS field in the flux-rope axis. This flux rope is axisymmetric, so it curves around the limb of the Sun. The curvature results in a perspective effect such that the location of the LOS field is only co-spatial with the location of the flux-rope axis in the central POS slice. The true location of the flux-rope axis is not readily apparent in the integrated data because the volume of space where they are co-located is a small. The location of the LOS field follows a $\supset$-shaped arc whose legs coincide with iv).

iv) *Two dark horizontal lines in L/I intersecting the photosphere*. These are a combination of a Van Vleck inversion in the lower part of the flux rope and the LOS field from the legs of the $\supset$-shape described in iii) and are thus the darkest features in the image.

v) *Slightly spoked azimuth direction*. The azimuth directions are mostly radial, but there is a slight spoke-like signature around the flux-rope axis (Figure 5(c)). Since the Van Vleck inversion locations are obvious (in this model), the 90° ambiguity can be removed, and the flux-rope nature of the field becomes evident. Even without removing the ambiguity, the slight spoke may be a feature that can help to identify this type of magnetic morphology. Note that the linear-polarization azimuth direction (blue lines) everywhere is close to radial.

vi) *Bulb of circular polarization*. The circular polarization has the same sign throughout (Figure 5(d)). The strongest signal comes from above the limb and surrounds the location of the flux-rope axis.

Although almost all these listed features are present in each case, some are more pronounced in certain cases. For instance, the dark beads in iii) are distinctly visible in F3, but not at all in F2. The density differences in each case change the weighting of the signal along the LOS. Thus, certain features are more or less clear depending on whether the signal is concentrated at the central POS, or spread out along the LOS. Case F2 has the most gradual density drop with height, and thus the dark beads from iii) are overcome by brighter signal in the foreground and background.

5.3. Sheared Arcade

Much like the cylindrical flux-rope model, we ran the forward calculations on the sheared-arcade model with several different density and temperature profiles. The cases presented here are as follows: S0 – the density and temperature provided by the MHD model; S2 – the density provided by the MHD model and isothermal temperature of 1.5×10^6 K; S3 – hydrostatic streamer density and temperature fit from Gibson *et al.* (1999). We did not relax the configuration to equilibrium with the imposed plasma parameters. In all cases, the plasma was low-β except in the region of the null-line. We do not discuss the results from S0 because the temperature of the plasma falls below the minimum temperature threshold for the forward-calculations (around 5×10^5 K). Most of the sheared-field plasma is at or below this temperature, due to the assumption of adiabatic energy transport, so any calculations on the original data only produce signal from the unsheared field, which is not useful for this work.

Figure 7(g), (h) shows the comparison of the integrated L/I for the S2 and S3 cases in the sheared region. We have looked at the polarization signals from thin POS slices along the LOS, and found that for any given slice, the L/I is qualitatively similar between the two cases. The differences seen in Figure 7 arise from the relative contributions to the integrated

signal from the sheared field versus the background unsheared field. Stokes I, Q, and U are weighted by density. Hence, higher-density regions contribute more to the integrated signal than lower-density regions. The original density was used in S2 and a spherically symmetric density was used in S3. These densities are plotted in Figure 7(a), (b). Note that in S2, the density in the unsheared field is about an order of magnitude more dense than the sheared field because of the large volumetric expansion of the sheared field and the closed lower boundary condition imposed in the simulation. From a broad range of observations, it is known that streamers tend to be about a factor of two more dense than the embedded cavity (Fuller and Gibson, 2009; Schmit and Gibson, 2011). Thus, the S3 results emphasize the sheared field too much, and the S2 results emphasize this region to little compared with observations.

The following list describes the features that are present in the data. After the list we analyze in more detail features that are found to a lesser degree or not at all in one of the cases.

i) *Quadrupolar Van Vleck signal*. A clear Van Vleck signature is associated with the quadrupolar field (Figure 7(c), (d)). Even in the absence of any sheared field, there would be three pairs of Van Vleck inversions associated with the inner three loop systems. These pairs are the top two, the middle two, and the lower two elongated Van Vleck nulls.

ii) $\vee$*-shaped Van Vleck inversion.* At the top of the central loop system, there are Van Vleck lines in a $\vee$-shape (Figure 7(e), (f); at a height of $1.6-2\mathrm{R}_{\odot}$), which is analogous to property i) in the cylindrical flux-rope model. The sheared field is confined to the central part of this system (*i.e.*, the areas of negative V/I in Figure 7(i), (j)) and the $\vee$-shaped Van Vleck lines are associated with the unsheared portion of this central magnetic-loop system (dark-blue loops above the sheared field in Figure 3).

iii) *Parallel Van Vleck inversions.* In the sheared field, there are two dark parallel Van Vleck inversion lines (Figure 7(e), (f); at a height of $1-1.6\mathrm{R}_{\odot}$) that emanate from the photosphere and connect to the $\vee$-shape listed in ii). The parallel Van Vleck inversion lines are associated with the legs of the sheared region. This field is inclined toward/away from the observer at $\approx 54^{\circ}$ from radial. These inversions are more pronounced in S3 than in S2.

iv) *Dark LOS core in* L/I. The central sheared area generally has a lower linear polarization magnitude due to the presence of fields that are more LOS than the surrounding field. This effect is stronger in S3 than in S2.

v) *Anomalous LOS signal in* L/I. A dark spot in L/I is visible in the sheared-field region in case S3 (Figure 7(f); $Z = 0$, $Y = 1.35$). This is not due to an axis of LOS field. This anomalous LOS signal (Rachmeler, Casini, and Gibson, 2012) arises from cancellation in the LOS-integrated Stokes Q and U due to the symmetry in the system and is dependent on the relative density in the sheared and unsheared regions. This feature is not present in S2 (Figure 7(e)).

vi) *Non-radial azimuth direction.* In the sheared-field region, the linear-polarization azimuth direction is parallel to the limb in the S3 case (blue lines in Figure 7(h)), which creates an illusion of a cylindrical flux rope. In this area the magnetic-field angle exceeds the Van Vleck angle, so the true field is perpendicular to the observed azimuth direction. Note that at this location, the field is actually predominantly in the LOS, and the POS component is weak. This feature is not present in S2 (Figure 7(g)).

vii) *Strongest circular polarization near limb* (V/I). The relative circular polarization is shown in Figure 7(i), (j). The shear is not concentrated above the limb, as in the flux-

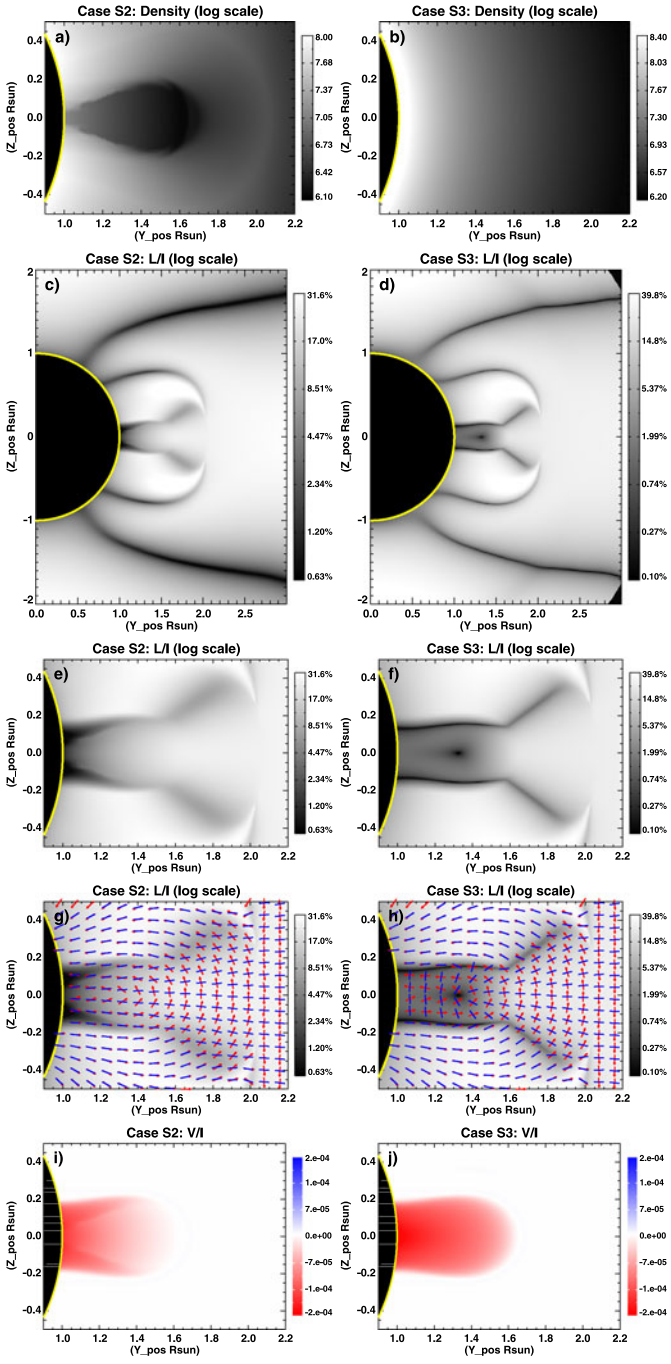

Figure 7 Forward-model results from the sheared arcade system. The left column shows case S2 and the right column shows case S3. a) and b) Density in the central region, the electron number density is given by 10^X cm^{-3}, where X is the value indicated by the color bar; c) and d) relative linear polarization of the entire system; e) and f) relative linear polarization of the central region; g) and h) same as above overlaid with red field vectors and blue azimuth directions; i) and j) relative circular polarization of the inner region.

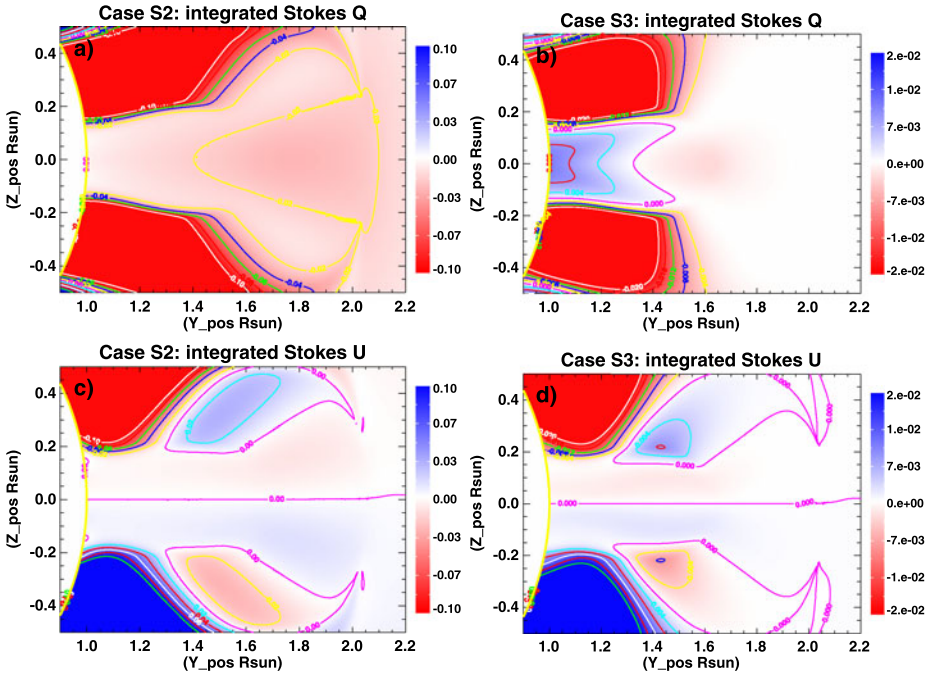

Figure 8 Integrated Stokes Q and U signals from cases S2 and S3 of the sheared-arcade model. Lines of zero Q or U are shown in magenta.

rope case, but at the limb. The features within the negative V/I in S2 are due to density variations (Figure 7(a)). The V/I in the S3 case shows a smooth profile.

Most of these features are present in both cases, but they are not always obvious in the integrated S2 data. The locations of the Van Vleck inversion and the LOS field i) – iii) are the same in both cases. Figure 8 shows the LOS integrated values of Stokes Q and U $[L = \sqrt{Q^2 + U^2}]$ for cases S2 and S3. The locations of lowest Q and U are the same for both cases, but there are no true nulls in Q inside the sheared-field region in S2. Thus, the integrated L/I for S2 (Figure 7(e)) does not show true Van Vleck nulls. The inversions are there, but the signal from the unsheared portion of the LOS obscures them.

There is clearly no anomalous LOS signal iv) in S2 (Figure 7(e)). This is because the background dominates the integrated signal at all heights in this case. Investigation of the polarization generated in thin POS slices shows that the unsheared field in all cases produces a negative Stokes-Q signal, and the sheared field produces a signal that is predominantly positive. The relative density in the sheared and background field determines where the sheared field dominates in the integrated Stokes profiles. The integrated Stokes-Q signal for S3 (Figure 8(b)) is positive in the central region, showing that the sheared field dominates the LOS signal there. Where a zero-line in Stokes Q crosses a zero-line in Stokes U (Figure 8(b), (d)) there is an anomalous LOS signal (Figure 7(f)) (Rachmeler, Casini, and Gibson, 2012). Since the sheared field in S2 has a lower density, the integrated Stokes Q is always dominated by the background field (Figure 8(a)) and is never negative. Thus there is no anomalous LOS signal in S2.

The relative weighting of the sheared *versus* the unsheared field also causes the difference in the azimuth direction for cases S2 and S3. The volume of space that contains a sheared field lies inside a Van Vleck inversion – such that the azimuth is perpendicular to the POS magnetic-field direction – and inspections of a thin POS slice reveals azimuth directions that are consistent with Figure 7(h). The integrated L/I in case S2 shows radial azimuths because the background field dominates, so the non-radial azimuth signal is overwhelmed.

6. Discussion

We have presented three coronal models and their synthetic polarization signatures. We found that each of these models is distinct and distinguishable, even when using linear polarization alone. The spheromak flux rope is the most recognizably different, while the cylindrical flux rope and the sheared-arcade models are somewhat similar.

This work highlights the importance of using a forward approach on coronal emission-line polarization. It can teach us what to look for in observations, such as Van Vleck inversions and LOS field. It also calls attention to the fact that we cannot trust our intuition to pick out magnetic morphologies. The sheared-arcade model is a good example of this. On initial inspection, the polarization signatures of the S3 sheared arcade resemble a flux rope; the azimuth direction is parallel to the limb between the inner Van Vleck inversions, and a false axial signature may be present. Both of these signatures can be logically explained when analyzing the forward results, but this example underlines the need for forward or inverse analysis before magnetic-structure identification can be made. Another important strength of the forward approach is that it fully takes into account the LOS integration of the polarization signal. The optically thin plasma is a significant challenge for the inverse technique and so is often seen as a limitation for coronal polarization data as a whole, but the forward approach incorporates the lack of opacity. By looking at a given magnetic configuration with multiple plasma profiles, we can also learn about how the signatures change due to the plasma parameters alone. We have shown that for cavities that are about half as dense as the surrounding streamer, the polarization signature from the streamer can obscure some of the features that are present in the cavity. For future observations, it is clear that knowledge of the LOS density structures is important for analysis and interpretation. Density diagnostics that determine a 3D density distribution could be used in conjunction with polarization observations and forward calculations.

Our work is not the first to use this forward approach to understand hypothetical or actual observations. Judge, Low, and Casini (2006) applied the same forward code to study prominence-supporting magnetic fields and current sheets. Liu and Lin (2008) compared observations of an active region on the limb with potential-field extrapolations to study how the LOS affects the fit of the forward calculation to the observations. Dove *et al.* (2011) compared the spheromak model presented here with an early CoMP observation of a large cavity. The next important step is to take the knowledge gained with these forward studies and apply it directly to observations, looking for the specific morphologies; this work is already underway. Bąk-Stęślicka *et al.* (2013) have found that cavities observed in CoMP in 2011 and 2012 usually have a characteristic "rabbit-head" signature in L/I. This signature consists of two Van Vleck inversions, with or without a dark central region indicating an LOS field. They have shown that this observation is consistent with a 3D flux-rope topology where the height of the dark central "head" is approximately co-spatial with the center of the cavity.

Observations carry their own challenges because of noise and small-scale density structures in the corona. CoMP is an occulted coronagraph and the occulter is at approximately $1.05R_{\odot}$, which means that especially for small cavities, the distinguishing characteristics such as azimuth direction would most likely be obscured by the occulter. We used extremely simplified density structures to isolate the magnetic features, but in reality, the Stokes-I observations are highly structured. By analyzing *relative* linear and circular polarization, we removed some of the density component, but the signal is still density dependent, and we showed that the relative importance of the structures along the LOS is highly dependent on their density. Our current approach is more applicable in coronal cavities, which are, in general, fairly smooth in intensity compared with active regions with clear bright loops. In future forward-modeling research, more realistic density models are needed. The observational noise, the occulter, and the highly structured coronal density make it difficult to uniquely characterize observed cavities, as they may be consistent with more than one model.

We are just beginning to scratch the surface of what the polarization data can teach us about the solar corona. Here we have studied idealized equilibrium structures. Not only is there a wide range of magnetic morphologies left to study, there is also the important aspect of time-dependence that is still open for exploration. The forward approach is only one of the methods available for analyzing these data, and there is still much to do with comparisons with observations, true forward-fitting for given observations, and looking at the Sun as a whole as opposed to specific magnetic structures. We look forward to witnessing the advances that come out of these data in conjunction with both forward and inverse techniques.

Acknowledgements The authors would like to thank R. Casini, P. Judge, and S. Tomczyk for many helpful conversations on coronal polarization and CoMP in general, and this article in specific. We would also like to thank all those who have contributed to the continued expansion of the FORWARD model. LAR acknowledges the HAO visitors' fund, STFC (UK), and PRODEX grant C90193 managed by the European Space Agency in collaboration with the Belgian Federal Science Policy Office for financial support. This work was also supported in part by NASA grant NNX08AU30G. CRD acknowledges support from NASA for his participation. NCAR is sponsored by the National Science Foundation.

References

Antiochos, S.K., Dahlburg, R.B., Klimchuk, J.A.: 1994, The magnetic field of solar prominences. *Astrophys. J. Lett.* **420**, L41 – L44. doi:10.1086/187158.

Antiochos, S.K., DeVore, C.R., Klimchuk, J.A.: 1999, A model for solar coronal mass ejections. *Astrophys. J.* **510**, 485 – 493. doi:10.1086/306563.

Arnaud, J., Newkirk, G. Jr.: 1987, Mean properties of the polarization of the Fe XIII 10747 Å coronal emission line. *Astron. Astrophys.* **178**, 263 – 268.

Aschwanden, M.J., Newmark, J.S., Delaboudinière, J.-P., Neupert, W.M., Klimchuk, J.A., Gary, G.A., Portier-Fozzani, F., Zucker, A.: 1999, Three-dimensional stereoscopic analysis of solar active region loops. I. SOHO/EIT observations at temperatures of (1.0–1.5) $\times$ 10^6 K. *Astrophys. J.* **515**, 842 – 867. doi:10.1086/307036.

Bąk-Stęślicka, U., Gibson, S.E., Fan, Y.E., Bethge, C.W., Forland, B., Rachmeler, L.A.: 2013, The magnetic structure of solar prominence cavities: new observable. *Astrophys. J. Lett.* **770**, L28. doi:10.1088/2041-8205/770/2/L28.

Bastian, T.S.: 2005, The frequency agile solar radiotelescope. In: Gary, D.E., Keller, C.U. (eds.) *Solar and Space Weather Radiophysics*, *Astrophys Space Sci. Lib.* **314**, 47 – 69. doi:10.1007/1-4020-2814-8_3.

Casini, R.: 2002, The Hanle effect of the two-level atom in the weak-field approximation. *Astrophys. J.* **568**, 1056 – 1065. doi:10.1086/338986.

Casini, R., Judge, P.G.: 1999, Spectral lines for polarization measurements of the coronal magnetic field. II. Consistent treatment of the Stokes vector for magnetic-dipole transitions. *Astrophys. J.* **522**, 524 – 539. doi:10.1086/307629.

Charvin, P.: 1965, Étude de la polarisation des raies interdites de la couronne solaire. Application au cas de la raie verte λ 5303. *Ann. Astrophys.* **28**, 877.

Dove, J.B., Gibson, S.E., Rachmeler, L.A., Tomczyk, S., Judge, P.: 2011, A ring of polarized light: evidence for twisted coronal magnetism in cavities. *Astrophys. J. Lett.* **731**, L1. doi:10.1088/2041-8205/731/1/L1.

Fan, Y., Gibson, S.E.: 2006, On the nature of the X-ray bright core in a stable filament channel. *Astrophys. J. Lett.* **641**, L149 – L152. doi:10.1086/504107.

Fuller, J., Gibson, S.E.: 2009, A survey of coronal cavity density profiles. *Astrophys. J.* **700**, 1205 – 1215. doi:10.1088/0004-637X/700/2/1205.

Gelfreikh, G.B.: 1994, Radio measurements of coronal magnetic fields. In: Rusin, V., Heinzel, P., Vial, J.-C. (eds.) *Solar Coronal Structures, IAU Coll.* **144**, VEDA Slovak Acad. Sciences, 21 – 28.

Gibson, S.E., Fludra, A., Bagenal, F., Biesecker, D., del Zanna, G., Bromage, B.: 1999, Solar minimum streamer densities and temperatures using whole sun month coordinated data sets. *J. Geophys. Res.* **104**, 9691 – 9700. doi:10.1029/98JA02681.

Gibson, S.E., Foster, D., Burkepile, J., de Toma, G., Stanger, A.: 2006, The calm before the storm: the link between quiescent cavities and coronal mass ejections. *Astrophys. J.* **641**, 590 – 605. doi:10.1086/500446.

Gibson, S.E., Kucera, T.A., Rastawicki, D., Dove, J., de Toma, G., Hao, J., Hill, S., Hudson, H.S., Marqué, C., McIntosh, P.S., Rachmeler, L., Reeves, K.K., Schmieder, B., Schmit, D.J., Seaton, D.B., Sterling, A.C., Tripathi, D., Williams, D.R., Zhang, M.: 2010, Three-dimensional morphology of a coronal prominence cavity. *Astrophys. J.* **724**, 1133 – 1146. doi:10.1088/0004-637X/724/2/1133.

Gibson, S.E., Low, B.C.: 1998, A time-dependent three-dimensional magnetohydrodynamic model of the coronal mass ejection. *Astrophys. J.* **493**, 460. doi:10.1086/305107.

Gibson, S.E., Low, B.C.: 2000, Three-dimensional and twisted: an MHD interpretation of on-disk observational characteristics of coronal mass ejections. *J. Geophys. Res.* **105**, 18187 – 18202. doi:10.1029/1999JA000317.

Grebinskij, A., Bogod, V., Gelfreikh, G., Urpo, S., Pohjolainen, S., Shibasaki, K.: 2000, Microwave tomography of solar magnetic fields. *Astron. Astrophys. Suppl.* **144**, 169 – 180. doi:10.1051/aas:2000202.

Harvey, J.W.: 1969, Magnetic fields associated with solar active-region prominences. PhD thesis, University of Colorado at Boulder.

Heinzel, P., Schmieder, B., Fárník, F., Schwartz, P., Labrosse, N., Kotrč, P., Anzer, U., Molodij, G., Berlicki, A., DeLuca, E.E., Golub, L., Watanabe, T., Berger, T.: 2008, Hinode, TRACE, SOHO, and ground-based observations of a quiescent prominence. *Astrophys. J.* **686**, 1383 – 1396. doi:10.1086/591018.

House, L.L.: 1977, Coronal emission-line polarization from the statistical equilibrium of magnetic sublevels. I – Fe XIII. *Astrophys. J.* **214**, 632 – 652. doi:10.1086/155289.

Hudson, H.S., Acton, L.W., Harvey, K.L., McKenzie, D.E.: 1999, A stable filament cavity with a hot core. *Astrophys. J. Lett.* **513**, L83 – L86. doi:10.1086/311892.

Jensen, E.A.: 2007, High frequency Faraday rotation observations of the solar corona. PhD thesis, University of California, Los Angeles.

Judge, P.G.: 2007, Spectral lines for polarization measurements of the coronal magnetic field. V. Information content of magnetic dipole lines. *Astrophys. J.* **662**, 677 – 690. doi:10.1086/515433.

Judge, P.G., Casini, R.: 2001, A synthesis code for forbidden coronal lines. In: Sigwarth, M. (ed.) *Advanced Solar Polarimetry – Theory, Observation, and Instrumentation* **CS-236**, Astron. Soc. Pacific, 503.

Judge, P.G., Low, B.C., Casini, R.: 2006, Spectral lines for polarization measurements of the coronal magnetic field. IV. Stokes signals in current-carrying fields. *Astrophys. J.* **651**, 1229 – 1237. doi:10.1086/507982.

Karpen, J.T., Antiochos, S.K., DeVore, C.R.: 2012, The mechanisms for the onset and explosive eruption of coronal mass ejections and eruptive flares. *Astrophys. J.* **760**, 81. doi:10.1088/0004-637X/760/1/81.

Karpen, J.T., Antiochos, S.K., Hohensee, M., Klimchuk, J.A., MacNeice, P.J.: 2001, Are magnetic dips necessary for prominence formation? *Astrophys. J. Lett.* **553**, L85 – L88. doi:10.1086/320497.

Kramar, M., Inhester, B.: 2007, Inversion of coronal Zeeman and Hanle observations to reconstruct the coronal magnetic field. *Mem. Soc. Astron. Ital.* **78**, 120.

Kramar, M., Inhester, B., Solanki, S.K.: 2006, Vector tomography for the coronal magnetic field. I. Longitudinal Zeeman effect measurements. *Astron. Astrophys.* **456**, 665 – 673. doi:10.1051/0004-6361:20064865.

Lin, H., Kuhn, J.R., Coulter, R.: 2004, Coronal magnetic field measurements. *Astrophys. J. Lett.* **613**, L177 – L180. doi:10.1086/425217.

Lin, H., Penn, M.J., Tomczyk, S.: 2000, A new precise measurement of the coronal magnetic field strength. *Astrophys. J. Lett.* **541**, L83 – L86. doi:10.1086/312900.

Liu, Y., Lin, H.: 2008, Observational test of coronal magnetic field models. I. Comparison with potential field model. *Astrophys. J.* **680**, 1496 – 1507. doi:10.1086/588645.

Low, B.C., Hundhausen, J.R.: 1995, Magnetostatic structures of the solar corona. 2: The magnetic topology of quiescent prominences. *Astrophys. J.* **443**, 818 – 836. doi:10.1086/175572.

Luna, M., Karpen, J.T., DeVore, C.R.: 2012, Formation and evolution of a multi-threaded solar prominence. *Astrophys. J.* **746**, 30. doi:10.1088/0004-637X/746/1/30.

Mackay, D.H., Karpen, J.T., Ballester, J.L., Schmieder, B., Aulanier, G.: 2010, Physics of solar prominences: II – Magnetic structure and dynamics. *Space Sci. Rev.* **151**, 333 – 399. doi:10.1007/s11214-010-9628-0.

Maričić, D., Vršnak, B., Stanger, A.L., Veronig, A.: 2004, Coronal mass ejection of 15 May 2001: I. Evolution of morphological features of the eruption. *Solar Phys.* **225**, 337 – 353. doi:10.1007/s11207-004-3748-1.

Patzold, M., Bird, M.K., Volland, H., Levy, G.S., Seidel, B.L., Stelzried, C.T.: 1987, The mean coronal magnetic field determined from HELIOS Faraday rotation measurements. *Solar Phys.* **109**, 91 – 105. doi:10.1007/BF00167401.

Querfeld, C.W.: 1977, A near-infrared coronal emission-line polarimeter. In: Azzam, R.M.A., Coffeen, D.L. (eds.) *Optical Polarimetry: Instrumentation and Applications*, *Proc. SPIE* **112**, 200 – 208.

Rachmeler, L.A., Casini, R., Gibson, S.E.: 2012, Interpreting coronal polarization observations. In: Rimmele, T.R., Tritschler, A., Wöger, F., Collados Vera, M., Socas-Navarro, H., Schlichenmaier, R., Carlsson, M., Berger, T., Cadavid, A., Gilbert, P.R., Goode, P.R., Knölker, M. (eds.) *Second ATST-EAST Meeting: Magnetic Fields from the Photosphere to the Corona.* **CS-463**, Astron. Soc. Pac., 227.

Reeves, K.K., Gibson, S.E., Kucera, T.A., Hudson, H.S., Kano, R.: 2012, Thermal properties of a solar coronal cavity observed with the X-ray telescope on Hinode. *Astrophys. J.* **746**, 146. doi:10.1088/0004-637X/746/2/146.

Régnier, S., Walsh, R.W., Alexander, C.E.: 2011, A new look at a polar crown cavity as observed by SDO/AIA. Structure and dynamics. *Astron. Astrophys.* **533**, L1. doi:10.1051/0004-6361/201117381.

Schmit, D.J., Gibson, S.E.: 2011, Forward modeling cavity density: a multi-instrument diagnostic. *Astrophys. J.* **733**, 1. doi:10.1088/0004-637X/733/1/1.

Tomczyk, S., Card, G.L., Darnell, T., Elmore, D.F., Lull, R., Nelson, P.G., Streander, K.V., Burkepile, J., Casini, R., Judge, P.G.: 2008, An instrument to measure coronal emission line polarization. *Solar Phys.* **247**, 411 – 428. doi:10.1007/s11207-007-9103-6.

Trujillo Bueno, J.: 2001, Atomic polarization and the Hanle effect. In: Sigwarth, M. (ed.) *Advanced Solar Polarimetry – Theory, Observation, and Instrumentation* **CS-236**, Astron. Soc. Pac., 161.

van Vleck, J.H.: 1925, On the quantum theory of the polarization of resonance radiation in magnetic fields. *Proc. Natl. Acad. Sci. USA* **11**, 612 – 618. doi:10.1073/pnas.11.10.612.

White, S.M., Kundu, M.R.: 1997, Radio observations of gyroresonance emission from coronal magnetic fields. *Solar Phys.* **174**, 31 – 52. doi:10.1023/A:1004975528106.

DOI 10.1007/978-1-4939-2038-9_11
Reprinted from *Solar Physics* Journal, DOI 10.1007/s11207-013-0317-5

Observations of Coronal Mass Ejections with the Coronal Multichannel Polarimeter

H. Tian · S. Tomczyk · S.W. McIntosh · C. Bethge · G. de Toma · S. Gibson

Received: 31 December 2012 / Accepted: 2 May 2013 / Published online: 5 June 2013

Abstract The *Coronal Multichannel Polarimeter* (CoMP) measures not only the polarization of coronal emission, but also the full radiance profiles of coronal emission lines. For the first time, CoMP observations provide high-cadence image sequences of the coronal line intensity, Doppler shift, and line width simultaneously over a large field of view. By studying the Doppler shift and line width we may explore more of the physical processes of the initiation and propagation of coronal mass ejections (CMEs). Here we identify a list of CMEs observed by CoMP and present the first results of these observations. Our preliminary analysis shows that CMEs are usually associated with greatly increased Doppler shift and enhanced line width. These new observations provide not only valuable information to constrain CME models and probe various processes during the initial propagation of CMEs in the low corona, but also offer a possible cost-effective and low-risk means of space-weather monitoring.

Keywords Active regions · Coronal mass ejections · Flares · Magnetic fields · Waves

1. Introduction

Coronal mass ejections (CMEs) are probably the most important sources of adverse space-weather effects (*e.g.* Gosling *et al.*, 1991; Gopalswamy *et al.*, 2001; Wang *et al.*, 2002;

Coronal Magnetometry
Guest Editors: S. Tomczyk, J. Zhang, and T.S. Bastian

Electronic supplementary material The online version of this article (doi:10.1007/s11207-013-0317-5) contains supplementary material, which is available to authorized users.

H. Tian
Harvard-Smithsonian Center for Astrophysics, Cambridge, MA, USA
e-mail: hui.tian@cfa.harvard.edu

S. Tomczyk (✉) · S.W. McIntosh · C. Bethge · G. de Toma · S. Gibson
High Altitude Observatory, National Center for Atmospheric Research, Boulder, CO, USA
e-mail: tomczyk@ucar.edu

Howard *et al.*, 2006; Zhang *et al.*, 2007; Temmer *et al.*, 2010), and they are often associated with dramatic changes of coronal magnetic fields (*e.g.* Zhang and Low, 2005; Liu *et al.*, 2009; Su and van Ballegooijen, 2012). Using mainly white-light coronagraphs, observations of CMEs are now made routinely both on the ground and in space. These instruments measure the polarized or total brightness of the corona, and CMEs are usually identified as large-scale disturbances in the coronal intensity-image sequences. White-light coronagraphs such as MK4 (Elmore *et al.*, 2003; Reiner *et al.*, 2003; Gibson *et al.*, 2006) at the Mauna Loa Solar Observatory (MLSO) and the *Large Angle Spectrometric Coronagraph* (LASCO: Brueckner *et al.*, 1995) onboard the *Solar and Heliospheric Observatory* (SOHO) have made great contributions to our understanding of the initiation and propagation of CMEs.

Spectroscopic observations of emission lines could provide valuable information on the plasma properties and dynamics in CMEs near the Sun (*e.g.* Harrison *et al.*, 2003; Harra and Sterling, 2003; Ko *et al.*, 2003; Lin *et al.*, 2005; McIntosh, de Pontieu, and Leamon, 2010; Landi *et al.*, 2010; Tian *et al.*, 2012a; Giordano *et al.*, 2013). However, conventional slit spectrographs such as the *Extreme-Ultraviolet Imaging Spectrometer* (EIS: Culhane *et al.*, 2007) onboard *Hinode* and the *Ultraviolet Coronagraph Spectrometer* (UVCS: Kohl *et al.*, 1995) onboard SOHO can only observe a small region. In addition, repeated raster scans of the same region can only be done at a low cadence (*e.g.* about five minutes for *Hinode*/EIS; see Tian *et al.*, 2012a) because it takes minutes or even hours to scan the region. A filter instrument, on the other hand, can provide high-cadence observations of a large field of view in the solar corona, thus offering significant advantages over a spectrograph when observing large-scale solar eruptions such as CMEs. The LASCO-C1 instrument, which has revealed some important characteristics of CMEs' propagation in the low corona (*e.g.* Plunkett *et al.*, 1997; Schwenn *et al.*, 1997; Zhang *et al.*, 2001), might be considered as one of such instruments. However, it took minutes to record a complete line profile (Mierla *et al.*, 2005) so that the cadence could not be high. Moreover, this instrument only lasted for less than two years during solar minimum, making it not very useful for CME studies.

The *Coronal Multichannel Polarimeter* (CoMP: Tomczyk *et al.*, 2008) is also such an instrument. It uses a narrow-band tunable filter to take high-cadence observations of the polarization state at a few spectral locations across the profiles of three infrared lines (Fe XIII 1074.7 nm and 1079.8 nm, He I 1083.0 nm). Images taken by CoMP have a field of view (FOV) of 1.05 – 1.40 solar radii, a spatial resolution of 4.46″ pixel^{-1}, and a typical cadence of 30 seconds. The instrument was initially deployed at the National Solar Observatory/Sacramento Peak in 2004. Several successful observations of coronal Alfvén waves (Tomczyk *et al.*, 2007; Tomczyk and McIntosh, 2009) and coronal cavities (Schmit *et al.*, 2009; Dove *et al.*, 2011) have been performed since then. The instrument was recently moved to the Mauna Loa Solar Observatory (MLSO) and started to obtain almost daily routine observations since October 2010.

Since CoMP can provide simultaneous measurements of the coronal line intensity, Doppler shift, line width, linear/circular polarization, and coronal density, it opens a completely new window for observations of the solar corona and CMEs. Here we report the first results of CoMP observations of CMEs. These observations might bring new insights into the initiation process of CMEs.

2. Data Reduction and Correction

Here we mainly use the three-point (sampled at three spectral locations 1074.50 nm, 1074.62 nm, 1074.74 nm) data of the Fe XIII 1074.7 nm line taken after December 2011. In

these observations, sequences of the polarization (Stokes-I, -Q, and -U only) images were obtained at each of these three spectral locations at a cadence of approximately 30 seconds. In this paper we mainly focus on the intensity (Stokes-I) data.

Although there are measurements at only three spectral locations, the intensity profile is in principle the same as the spectral line profile obtained by spectrographs. Thus, we can simply apply a least-squares single Gaussian fit to each intensity profile and obtain the line-center intensity, central wavelength, and line width (Tomczyk *et al.*, 2007; Tomczyk and McIntosh, 2009). However, it takes too much time to apply the Gaussian fit to all intensity profiles in the full FOV for hundreds of frames. Fortunately, we found that a simple analytical solution can be derived from the three-point measurement. It is far more efficient to derive the line parameters by using the analytical solution.

If I_1, I_2, and I_3 are the measured intensities at known wavelengths (spectral locations) λ_1, λ_2, and λ_3, we have the following set of three equations:

$$I_1 = i\mathrm{e}^{\frac{-(\lambda_1-\lambda_0)^2}{w^2}}, \tag{1}$$

$$I_2 = i\mathrm{e}^{\frac{-(\lambda_2-\lambda_0)^2}{w^2}}, \tag{2}$$

$$I_3 = i\mathrm{e}^{\frac{-(\lambda_3-\lambda_0)^2}{w^2}}. \tag{3}$$

It is clear that there are only three unknowns: the line center intensity $[i]$, center wavelength $[\lambda_0]$, and line width $[w]$. Therefore, we should be able to directly derive these three unknowns from the three equations. If we take the natural logarithm of the ratios I_3/I_2 and I_1/I_2 and denote them as a and b, we have

$$a = \ln\left(\frac{I_3}{I_2}\right) = \frac{-(\lambda_3-\lambda_0)^2}{w^2} + \frac{(\lambda_2-\lambda_0)^2}{w^2}, \tag{4}$$

$$b = \ln\left(\frac{I_1}{I_2}\right) = \frac{-(\lambda_1-\lambda_0)^2}{w^2} + \frac{(\lambda_2-\lambda_0)^2}{w^2}. \tag{5}$$

If we take the sum $a+b$ and define δ as the spectral pixel size ($\lambda_2-\lambda_1$ or $\lambda_3-\lambda_2$), the line width can be derived and expressed as

$$w = \sqrt{\frac{-2\delta}{a+b}}. \tag{6}$$

The Doppler shift relative to λ_2 can be derived by taking the difference $a-b$:

$$v = \lambda_0 - \lambda_2 = \frac{w^2}{4\delta}(a-b). \tag{7}$$

Finally, the line-center intensity can be computed as

$$i = I_2\mathrm{e}^{\frac{v^2}{w^2}}. \tag{8}$$

We show in Figure 1 three examples of observed intensity profiles and the line parameters derived by using the analytical solution. The solid line in each panel is the Gaussian function constructed by using the derived line parameters. Here positive and negative values of the Doppler shift mean red shift (away from the Earth) and blue shift (towards the Earth),

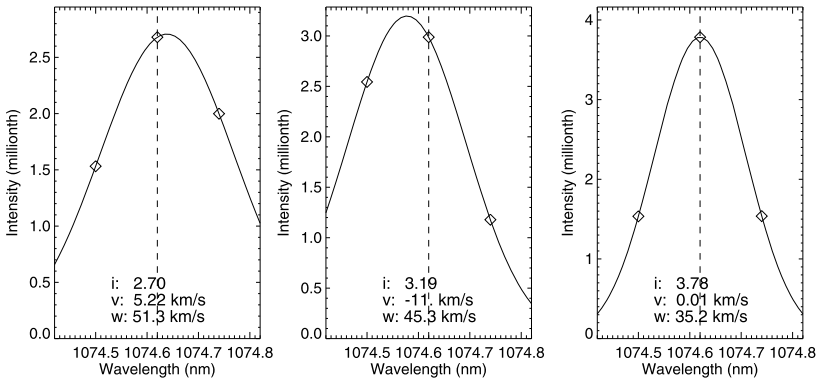

Figure 1 Three examples of observed emission line profiles (diamonds) and the analytical solution (solid line). The dashed line indicates the rest wavelength of the line. The line center intensity [i], Doppler shift [v], and line width [w] are marked in each panel.

respectively. We do not remove the instrument filter width from the measured line width since the filter width has a fixed value, and we are only interested in changes of the line width.

Once we derive the line parameters for each intensity profile in the FOV, we can produce maps of intensity, Doppler shift, and line width. Maps generated from observations at different times can then be used to make movies of intensity, Doppler shift, and line width.

The Doppler-shift maps usually show predominant blue shift at the east limb and red shift at the west limb, which suggests an East–West trend in the line of sight (LOS) Doppler shift. This trend is at least partly caused by the rotation of the solar corona. We calculate the median value of Doppler shift at each solar-x location to produce the East–West trend (Doppler shift as a function of solar-x). A median filter is then applied to this trend to eliminate possible abnormal values. Then we apply a fifth-order polynomial fit to the filtered trend. The resulting smooth trend is then subtracted from the map of Doppler shift.

Since there is no calibration lamp or cold lines, we could not perform an absolute wavelength calibration. We simply assume that the median value of Doppler shift is zero in each image. This assumption is usually valid since non-radial flows should on average cancel each other out (*e.g.* Hassler *et al.*, 1999; Peter and Judge, 1999; Tian *et al.*, 2010) at the limb and CoMP has such a large FOV. In addition, we are only interested in large Doppler shift perturbation which is unlikely to be affected by the accuracy of the absolute wavelength scale.

3. First Results of CME Observations

As we mentioned previously, CoMP provides simultaneous high-cadence (30 seconds) observations of coronal line intensity, Doppler shift, and line width in a large FOV for the first time. Such completely new types of observations may provide new insights into the processes of CME initiation and propagation. We have checked the CoMP data archive as well as the *Atmospheric Imaging Assembly* (AIA: Lemen *et al.*, 2012) onboard the *Solar Dynamics Observatory* (SDO) and SOHO/LASCO data, and found 27 clear cases where CMEs or CME-related signatures were observed by CoMP between December 2011 and February 2013. Table 1 lists some information (observation date, approximate time when CoMP

Table 1 CMEs observed by CoMP between December 2011 and February 2013.

ID	Date	Time	Flare class	Limb	White light signature	Remarks
1	07 December 2011	20:10	C2.7	East	No	Loop oscillation
2	30 December 2011	20:18	C4.4	West	MK4 & LASCO	Flux rope, Type-II burst
3	09 January 2012	20:13	C2.6	East	LASCO	
4	14 January 2012	21:12	No	West	No	
5	15 March 2012	01:33	C1.1	West	MK4 & LASCO	Prominence eruption
6	17 March 2012	23:55	B8.1	West	MK4 & LASCO	
7	27 March 2012	21:40	No	West	MK4 & LASCO	
8	11 April 2012	20:40	No	West	MK4 & LASCO	
9	27 April 2012	17:20	No	East	MK4 & LASCO	
10	15 May 2012	17:20	No	West	MK4 & LASCO	Null reconnection
11	26 May 2012	20:38	No	West	Partial halo in MK4 & LASCO	Originates from back side of the Sun
12	01 June 2012	22:16	C3.3	West	MK4 & LASCO	Type-II burst
13	08 June 2012	23:24	No	West	MK4 & LASCO	Prominence eruption
14	06 July 2012	23:05	X1.1	West	MK4 & LASCO	Type-II burst
15	08 July 2012	19:00	No	West	MK4 & LASCO	Slowly rising loops
16	13 July 2012	19:45	C1.3	West	No	
17	07 August 2012	19:02	C3.0	East	No	Prominence eruption
18	16 August 2012	00:30	No	East	MK4 & LASCO	Prominence eruption
19	24 August 2012	19:30	No	East	LASCO	Narrow eruption
20	15 September 2012	22:57	B9.6	West	Faint in LASCO	Type-II burst
21	22 September 2012	19:30	B9.2	East	MK4 & LASCO	
22	01 November 2012	21:56	No	West	No	
23	12 November 2012	18:55	C2.0	East	LASCO	
24	08 January 2013	19:11	C4.0	West	No	Prominence eruption
25	01 February 2013	19:23	No	West	LASCO	
26	04 February 2013	20:43	C1.9	East	LASCO	
27	15 February 2013	20:00	No	East	LASCO	

observes the CME, associated flare class, east/west limb, white-light signatures, and other characteristics) of these CMEs. The data of flare class are taken from the *Hinode* Flare Catalogue (st4a.stelab.nagoya-u.ac.jp/hinode_flare/) and NOAA/SWPC Solar Region Summary (www.swpc.noaa.gov/ftpmenu/warehouse.html).

Inspection of the movies shows that the typical characteristics of CMEs in the CoMP data are the dramatic changes of Doppler shift and the obviously enhanced line width. Although all CMEs do show some perturbation in the image sequences of the intensity, the perturbation is much more obvious in the image sequences of the Doppler shift and line width. This is not difficult to understand since higher-order moments are usually more sensitive to changes. The significant changes of Doppler shift are probably largely associated with the coronal response to the mass eruptions and lateral expansion of CMEs. The increased line width might be caused by the enhanced flow inhomogeneity and turbulence in various substructures of CMEs in the LOS direction.

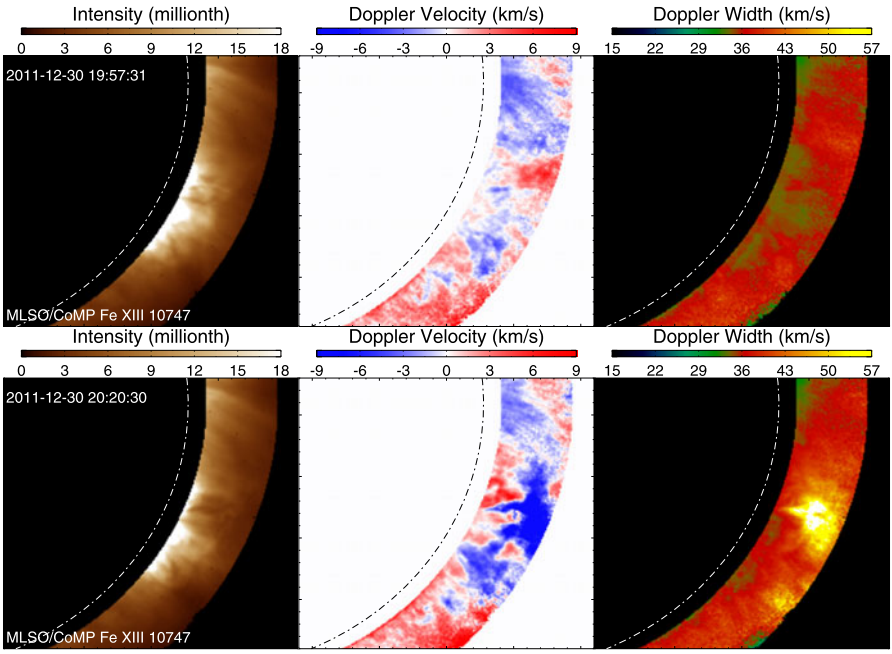

Figure 2 An eruption observed by CoMP on 30 December 2011. The first and second rows show images of the line center intensity, Doppler shift, and line width at 19:57:31 (before eruption) and 20:20:30 UT (during eruption), respectively. The dot–dashed line in each panel marks the limb of the solar disk. Two ESM movies (m2a.mov, m2b.mov) are associated with this figure.

We have to mention that the values of Doppler shift during CME eruption should not be interpreted as the line-of-sight component of the CME propagation speed in these observations. The reason is that the line wings are poorly sampled in our three-point measurements. However, the red and blue patterns in the Dopplergram do suggest that the plasma motions averaged along the line-of-sight direction are directed away and towards the observer, respectively. These motions include not only the outward movement of the CME, but also its lateral expansion and the dynamic response of the surrounding coronal plasma along the line-of-sight direction. This explains the complex Doppler-shift patterns in some CME eruption events. Nevertheless, the Doppler shift should experience a dramatic change in all CME eruption events and the largely perturbed (usually enhanced) Doppler shift should have an outward motion as the CME moves outward. Thus, the outward motion of largely enhanced Doppler shift is a good marker of CME eruption. In the future we plan to perform measurements of the line profile at more spectral locations. A better spectral sampling may help to separate these different types of motions due to their different speeds.

Figure 2 shows the three line parameters before and during the 30 December 2011 CME. The CME-caused changes of all line parameters can be clearly identified through a comparison between the first and second rows. Continuous evolution of different line parameters can be seen from the Electronic Supplementary Material (ESM) movies m2a.mov (full FOV) and m2b.mov (partial FOV). The outward propagating ejecta causes a dimming of ≈ 50 % in the intensity, shifts the line center by about 20 km s^{-1} blueward, and enhances the line width by ≈ 20 km s^{-1}. The spatial pattern of the intensity change roughly coincides with those of the Doppler-shift and line-width enhancement.

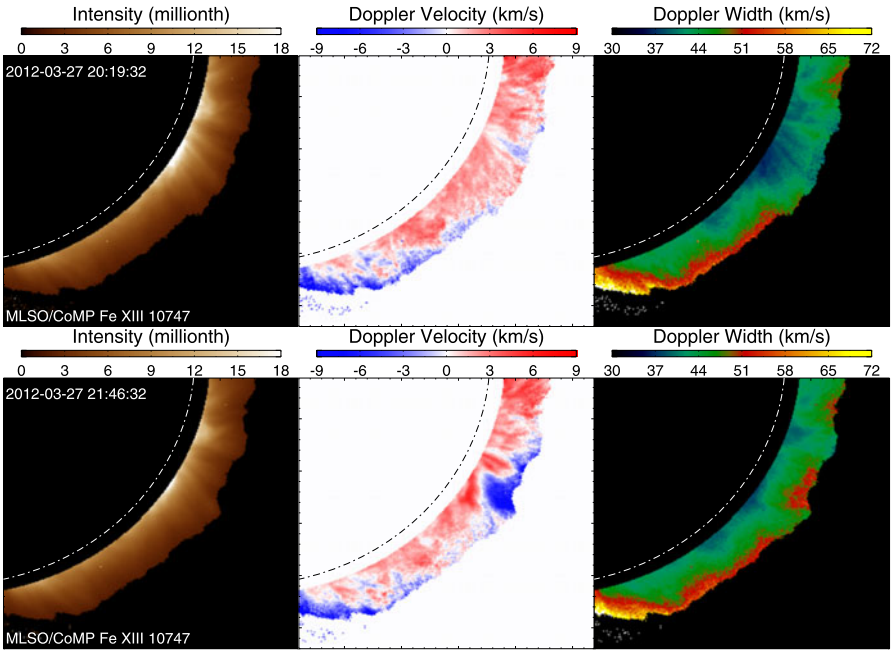

Figure 3 An eruption observed by CoMP on 27 March 2012. The first and second rows show images of the line-center intensity, Doppler shift, and line width at 20:19:32 (before eruption) and 21:46:32 UT (during eruption), respectively. The dot–dash line in each panel marks the limb of the solar disk. An ESM movie (m3.mov) is associated with this figure.

From LASCO movies (lasco-www.nrl.navy.mil/daily_mpg/), we can see that this CME developed into a ring-shaped propagating feature in the FOV of LASCO-C2 and -C3. Such a feature is likely to be a signature of flux rope or magnetic cloud (*e.g.*, DeForest, Howard, and Tappin, 2011). From Figure 2 we can see that this CME erupts from an active region (AR). It is not clear whether the flux rope existed prior to eruption (*e.g.* Gibson *et al.*, 2006) or formed during the eruption (*e.g.* Cheng *et al.*, 2011).

A possible flux rope is also identified from the LASCO-C2 and -C3 movies on 13 October 2011. From AIA images, we can see that this flux-rope-type CME seems to originate from a coronal cavity at the northwest limb. Such a connection favors the flux-rope interpretation of coronal cavities (Low and Hundhausen, 1995; Gibson *et al.*, 2006). Unfortunately, on that day CoMP data were only available prior to the CME eruption and the observation of the cavity is limited by an obstruction in the instrument. We also checked the list of cavities of Forland *et al.* (2011) but none of the erupting cavities were caught by CoMP. We hope that future observations may catch the complete process of flux-rope ejection and thus better our understanding of the role played by flux ropes in CME initiation and eruption.

The intensity perturbation of the 27 March 2012 CME is very small, which might be due to the fact that the CME propagates largely off the plane of sky (POS). Despite the weak signal in the intensity, we see an obvious change of the Doppler shift and line width. From Figure 3 and the ESM movie m3.mov we can clearly see the significant perturbation of Doppler shift and line width as the CME propagates into the FOV of CoMP.

The 7 December 2011 eruption revealed only very weak perturbation in the daily LASCO-C2 and -C3 movies. However, as we can see from Figures 4 and 5, this eruption was

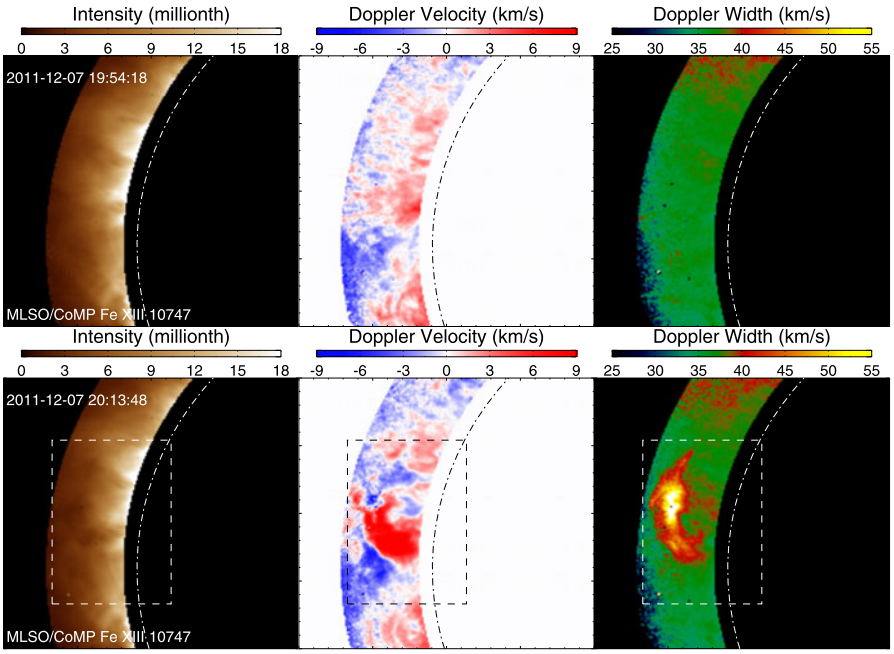

Figure 4 An eruption observed by CoMP on 7 December 2011. The first and second rows show images of the line-center intensity, Doppler shift, and line width at 19:54:18 and 20:13:48 UT, respectively. The dot–dashed line in each panel marks the limb of the solar disk. The rectangular region indicates the field of view shown in Figure 5. An ESM movie (m4.mov) is associated with this figure.

clearly recorded by both CoMP and SDO/AIA. The dominant ions in the 304 Å, 171 Å, and 193 Å passbands are He II, Fe IX, and Fe XII, respectively (O'Dwyer *et al.*, 2010). The eruption appears as a dark propagating feature in the CoMP intensity data, as can be seen from Figure 4 and the ESM movie m4.mov. The eruption also shifts the line center by about 20 km s^{-1} redward and enhances the line width by more than 20 km s^{-1}. The dark feature roughly coincides with the enhanced line width and largely perturbed Doppler shift.

In Figure 5 we present the high-resolution AIA images in three passbands. These images were taken around 20:13:48 UT, the time when the images in the lower panel of Figure 5 were taken. The most enhanced line width (larger than 42 km s^{-1}) region, which is also approximately the region where the most significant perturbation of the line center intensity and Doppler shift occurs, is outlined by the white contours in each panel. It seems that this region is immediately ahead of the ejecta. A comparison between Figures 4 and 5 suggests that the ejecta are also associated with large changes of Doppler shift and enhancement of the line width. However, these changes are clearly not as prominent as those ahead of the ejecta. The large perturbation ahead of the ejecta is likely largely caused by the large disturbance of the plasma and magnetic environment around the leading edge of the fast ejection.

Interestingly, we do not see any obvious dark propagating feature ahead of this ejecta in the AIA movies (not shown here). It is known that all of these three passbands of AIA have significant contribution from emission of cooler materials, whereas the CoMP emission is almost purely from the hot Fe XIII ion. But it is still not clear how the perturbation ahead of

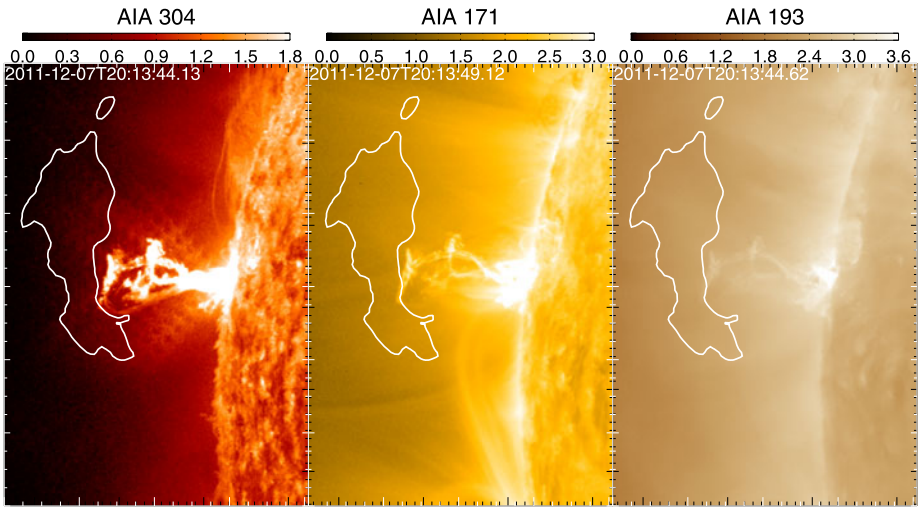

Figure 5 AIA observations of the 7 December 2011 event. Images of the AIA 304 Å, 171 Å, and 193 Å passbands around 20:13:48 are presented from left to right. The contours mark locations where the line width of Fe XIII 1074.7 nm is larger than 42 km s^{-1}.

the ejecta causes a reduction in the intensity of Fe XIII 1074.7 nm but no reduction in the AIA intensities.

Another interesting aspect of the 7 December 2011 eruption is the transverse oscillation of a loop system excited by the ejecta. The loop oscillation is best seen in the AIA 171 Å movie (not shown here). The oscillating loop is clearly present in Figure 5 and is about 432 Mm in length. The oscillation has a period of about 15 minutes and lasts for four cycles before damping out. The kink speed (twice the loop length divided by the period) at the apex of this oscillating loop can thus be calculated as 960 km s^{-1}. The Alfvén speed inside the oscillating loop can be constrained to the range of $960/\sqrt{2}$ km s^{-1} – 960 km s^{-1} (*e.g.* Edwin and Roberts, 1983; Aschwanden *et al.*, 1999; Nakariakov and Ofman, 2001; Wang and Solanki, 2004; Van Doorsselaere, Nakariakov, and Verwichte, 2008; Chen *et al.*, 2011; Feng *et al.*, 2011; Tian *et al.*, 2012b; White and Verwichte, 2012). The two Fe XIII lines used by CoMP (1074.7 nm and 1079.8 nm) can in principle be used to diagnose the coronal electron density. Combining information of the Alfvén speed and electron density, we can directly calculate the coronal magnetic-field strength. Unfortunately, this oscillating loop is barely resolved by CoMP. In addition, the density diagnostics of CoMP are still not finalized. We are planning to do joint observations of *Hinode*/EIS and CoMP, trying to use the density diagnostics of EIS to calibrate those of CoMP.

Figure 6 shows snapshots of CoMP observations of a partial-halo CME. A complete halo is seen at the viewpoint of STEREO-A. This eruption seems to originate from the backside of the Sun and propagates away from the Sun. The quickly developed large-scale disturbance can be clearly identified from movies of the Doppler shift and line width (available on mlso.hao.ucar.edu/mlso_datasum_comp.php?2012&5&26&COMP, mainly at the west limb). Figure 6 clearly shows that the perturbation in the intensity data is not as significant as in the Doppler shift and line width, probably because of the strong foreground and background coronal emission. The quickly developed perturbation might be associated with the propagation of "EUV waves". Chen, Ding, and Chen (2010) suggests that spectroscopic observations may be used to identify the nature of "EUV waves", namely fast waves (*e.g.* Patsourakos and

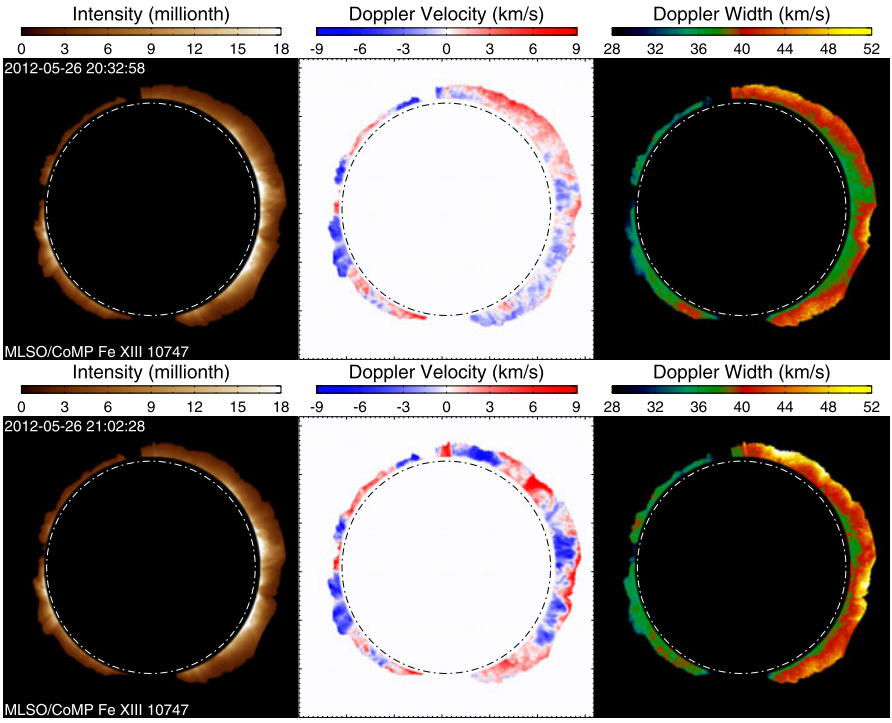

Figure 6 A partial halo-CME observed by CoMP on 26 May 2012. The first and second rows show images of the line-center intensity, Doppler shift and line width at 20:32:58 and 21:02:28 UT, respectively. The dot–dashed line in each panel marks the limb of the solar disk.

Vourlidas, 2009; Shen and Liu, 2012) or non-wave phenomenon such as successive stretching of magnetic field lines (*e.g.* Chen *et al.*, 2002). Thus, combining numerical simulations and the spectroscopic-like large-FOV CoMP observations might reveal more insights into the process of "EUV waves".

CoMP observations of the 26 May 2012 CME suggest the importance of monitoring space weather on the ground. The 26 May 2012 CME first appears as a partial halo in the FOV of LASCO-C2 at 20:57, which is about 20 minutes later than the time (20:38 UT) when CoMP observes the larger-scale perturbation in the coronal line width and Doppler shift. So it is clear that CoMP observations can be very important for the prediction of Earth-directed halo CMEs. In this sense, observations of halo-CMEs by ground-based instruments such as CoMP provide a cost-effective and low-risk means of space weather monitoring.

4. Summary and Future Perspectives

CoMP provides high-cadence, large-FOV, spectroscopic-like observations of CMEs for the first time. We have presented first results of CME observations by CoMP in this article. Our results show that the primary characteristics of CMEs are the dramatic change of the Doppler shift and obviously enhanced line width. The information provided by these CoMP observations might be important for our better understanding of various CME processes such as the formation of flux ropes and propagation of "EUV waves". CoMP observations

clearly demonstrate that space-weather monitoring is possible with inexpensive and low-risk observations from the ground. So far we have identified 27 obvious CMEs in the CoMP data. With the increase of the solar activity, we expect to observe more CMEs in the future.

CoMP observations of CMEs are not restricted to the images of line-center intensity, Doppler shift, and line width. In fact CoMP measures the complete polarization state of three emission lines. The linear (Stokes-Q and -U) and circular (Stokes-V) polarization data are not used in our analysis because our preliminarily processed polarization data shows no significant change of the linear polarization during CME eruptions and the circular-polarization signal is weak. We plan in the future to examine these data more thoroughly in order to establish whether changes may be evident if the data are averaged over longer time intervals, or whether a more optimal observation program might be established for analyzing CMEs with linear/circular polarization. Linear polarization is a promising diagnostic of coronal magnetic structures (*e.g.* Rachmeler *et al.*, 2013) and it may be possible to demonstrate changes in magnetic topology by examining data before, during and after CME eruptions.

As we mentioned above, density diagnostics using the two Fe XIII lines is under way. Once this is finalized, we should be able to study density changes during CMEs, which could be used to estimate the CME mass (Harrison *et al.*, 2003; Jin *et al.*, 2009; Tian *et al.*, 2012a). In addition, combining the density diagnostics and the Alfvén wave (Doppler shift oscillation) analysis (Tomczyk *et al.*, 2007; Tomczyk and McIntosh, 2009; McIntosh, de Pontieu, and Tomczyk, 2008), we can produce maps of the electron density, Alfvén speed, and magnetic-field strength before and after CMEs. Such information can be used to constrain background coronal parameters prescribed in models of CMEs.

CoMP is a prototype of the *Large-aperture Coronagraph* component of the proposed *COronal Solar Magnetism Observatory* (COSMO). With a FOV of 1.05 – 2.0 solar radii, COSMO can greatly expand the ability of CME observations by CoMP. In addition, the *Chromosphere and Prominence Magnetometer* (ChroMag) component of COSMO can monitor solar activity on the disk. Thus, a combination of both components is likely to monitor the complete process of (halo) CME initiation and early phase propagation.

Acknowledgements SDO is the first mission of NASA's Living With a Star (LWS) Program. SDO data a courtesy of NASA/SDO and the AIA science team. H. Tian's work at CfA is supported under contract 8100002705 from Lockheed-Martin to SAO. Part of this work was done at NCAR, where H. Tian was supported under the ASP Postdoctoral Fellowship Program. The National Center for Atmospheric Research is sponsored by the National Science Foundation. We thank L. Sitongia for processing the CoMP level-0 data. We also thank P. Judge, B.C. Low, and H. Peter for helpful discussions.

References

Aschwanden, M.J., Fletcher, L., Schrijver, C.J., Alexander, D.: 1999, Coronal loop oscillations observed with the Transition Region and Coronal Explorer. *Astrophys. J.* **520**, 880 – 894. doi:10.1086/307502.

Brueckner, G.E., Howard, R.A., Koomen, M.J., Korendyke, C.M., Michels, D.J., Moses, J.D., Socker, D.G., Dere, K.P., Lamy, P.L., Llebaria, A., Bout, M.V., Schwenn, R., Simnett, G.M., Bedford, D.K., Eyles, C.J.: 1995, The Large Angle Spectroscopic Coronagraph (LASCO). *Solar Phys.* **162**, 357 – 402. doi:10.1007/BF00733434.

Chen, F., Ding, M.D., Chen, P.F.: 2010, Spectroscopic analysis of an EIT wave/dimming observed by Hinode/EIS. *Astrophys. J.* **720**, 1254 – 1261. doi:10.1088/0004-637X/720/2/1254.

Chen, P.F., Wu, S.T., Shibata, K., Fang, C.: 2002, Evidence of EIT and Moreton waves in numerical simulations. *Astrophys. J. Lett.* **572**, L99 – L102. doi:10.1086/341486.

Chen, Y., Feng, S.W., Li, B., Song, H.Q., Xia, L.D., Kong, X.L., Li, X.: 2011, A coronal seismological study with streamer waves. *Astrophys. J.* **728**, 147. doi:10.1088/0004-637X/728/2/147.

Cheng, X., Zhang, J., Liu, Y., Ding, M.D.: 2011, Observing flux rope formation during the impulsive phase of a solar eruption. *Astrophys. J. Lett.* **732**, L25. doi:10.1088/2041-8205/732/2/L25.

Culhane, J.L., Harra, L.K., James, A.M., Al-Janabi, K., Bradley, L.J., Chaudry, R.A., Rees, K., Tandy, J.A., Thomas, P., Whillock, M.C.R., Winter, B., Doschek, G.A., Korendyke, C.M., Brown, C.M., Myers, S., Mariska, J., Seely, J., Lang, J., Kent, B.J., Shaughnessy, B.M., Young, P.R., Simnett, G.M., Castelli, C.M., Mahmoud, S., Mapson-Menard, H., Probyn, B.J., Thomas, R.J., Davila, J., Dere, K., Windt, D., Shea, J., Hagood, R., Moye, R., Hara, H., Watanabe, T., Matsuzaki, K., Kosugi, T., Hansteen, V., Wikstol, Ø.: 2007, The EUV Imaging Spectrometer for Hinode. *Solar Phys.* **243**, 19 – 61. doi:10.1007/s01007-007-0293-1.

DeForest, C.E., Howard, T.A., Tappin, S.J.: 2011, Observations of detailed structure in the solar wind at 1 AU with STEREO/HI-2. *Astrophys. J.* **738**, 103. doi:10.1088/0004-637X/738/1/103.

Dove, J.B., Gibson, S.E., Rachmeler, L.A., Tomczyk, S., Judge, P.: 2011, A ring of polarized light: evidence for twisted coronal magnetism in cavities. *Astrophys. J. Lett.* **731**, L1. doi:10.1088/2041-8205/731/1/L1.

Edwin, P.M., Roberts, B.: 1983, Wave propagation in a magnetic cylinder. *Solar Phys.* **88**, 179 – 191. doi:10.1007/BF00196186.

Elmore, D.F., Burkepile, J.T., Darnell, J.A., Lecinski, A.R., Stanger, A.L.: 2003, Calibration of a ground-based solar coronal polarimeter. In: Fineschi, S. (ed.) *Soc. Photo-Optical Instrument. Eng. (SPIE)* **CS-4843**, 66 – 75. doi:10.1117/12.459279.

Feng, S.W., Chen, Y., Li, B., Song, H.Q., Kong, X.L., Xia, L.D., Feng, X.S.: 2011, Streamer wave events observed in solar cycle 23. *Solar Phys.* **272**, 119 – 136. doi:10.1007/s11207-011-9814-6.

Forland, B., Rachmeler, L.A., Gibson, S.E., Dove, J.: 2011, Cavity magnetic observations: a survey using AIA and CoMP data. *AGU Fall Meeting Abstracts*, B1951.

Gibson, S.E., Foster, D., Burkepile, J., de Toma, G., Stanger, A.: 2006, The calm before the storm: the link between quiescent cavities and coronal mass ejections. *Astrophys. J.* **641**, 590 – 605. doi:10.1086/500446.

Giordano, S., Ciaravella, A., Raymond, J., Ko, Y.K., Suleiman, R.: 2013, UVCS/SoHO catalog of coronal mass ejections from 1996 to 2005: spectroscopic proprieties. *J. Geophys. Res.* **118**, 967 – 981. doi:10.1002/jgra.50166.

Gopalswamy, N., Lara, A., Yashiro, S., Kaiser, M.L., Howard, R.A.: 2001, Predicting the 1-AU arrival times of coronal mass ejections. *J. Geophys. Res.* **106**, 29207 – 29218. doi:10.1029/2001JA000177.

Gosling, J.T., McComas, D.J., Phillips, J.L., Bame, S.J.: 1991, Geomagnetic activity associated with Earth passage of interplanetary shock disturbances and coronal mass ejections. *J. Geophys. Res.* **96**, 7831 – 7839. doi:10.1029/91JA00316.

Harra, L.K., Sterling, A.C.: 2003, Imaging and spectroscopic investigations of a solar coronal wave: properties of the wave front and associated erupting material. *Astrophys. J.* **587**, 429 – 438. doi:10.1086/368079.

Harrison, R.A., Bryans, P., Simnett, G.M., Lyons, M.: 2003, Coronal dimming and the coronal mass ejection onset. *Astron. Astrophys.* **400**, 1071 – 1083. doi:10.1051/0004-6361:20030088.

Hassler, D.M., Dammasch, I.E., Lemaire, P., Brekke, P., Curdt, W., Mason, H.E., Vial, J.C., Wilhelm, K.: 1999, Solar wind outflow and the chromospheric magnetic network. *Science* **283**, 810. doi:10.1126/science.283.5403.810.

Howard, T.A., Webb, D.F., Tappin, S.J., Mizuno, D.R., Johnston, J.C.: 2006, Tracking halo coronal mass ejections from 0 – 1 AU and space weather forecasting using the Solar Mass Ejection Imager (SMEI). *J. Geophys. Res.* **111**, 4105. doi:10.1029/2005JA011349.

Jin, M., Ding, M.D., Chen, P.F., Fang, C., Imada, S.: 2009, Coronal mass ejection induced outflows observed with Hinode/EIS. *Astrophys. J.* **702**, 27 – 38. doi:10.1088/0004-637X/702/1/27.

Ko, Y.K., Raymond, J.C., Lin, J., Lawrence, G., Li, J., Fludra, A.: 2003, Dynamical and physical properties of a post-coronal mass ejection current sheet. *Astrophys. J.* **594**, 1068 – 1084. doi:10.1086/376982.

Kohl, J.L., Esser, R., Gardner, L.D., Habbal, S., Daigneau, P.S., Dennis, E.F., Nystrom, G.U., Panasyuk, A., Raymond, J.C., Smith, P.L., Strachan, L., van Ballegooijen, A.A., Noci, G., Fineschi, S., Romoli, M., Ciaravella, A., Modigliani, A., Huber, M.C.E., Antonucci, E., Benna, C., Giordano, S., Tondello, G., Nicolosi, P., Naletto, G., Pernechele, C., Spadaro, D., Poletto, G., Livi, S., von der Lühe, O., Geiss, J., Timothy, J.G., Gloeckler, G., Allegra, A., Basile, G., Brusa, R., Wood, B., Siegmund, O.H.W., Fowler, W., Fisher, R., Jhabvala, M.: 1995, The Ultraviolet Coronagraph Spectrometer for the Solar and Heliospheric Observatory. *Solar Phys.* **162**, 313 – 356. doi:10.1007/BF00733433.

Landi, E., Raymond, J.C., Miralles, M.P., Hara, H.: 2010, Physical conditions in a coronal mass ejection from Hinode, Stereo, and SOHO observations. *Astrophys. J.* **711**, 75 – 98. doi:10.1088/0004-637X/711/1/75.

Lemen, J.R., Title, A.M., Akin, D.J., Boerner, P.F., Chou, C., Drake, J.F., Duncan, D.W., Edwards, C.G., Friedlaender, F.M., Heyman, G.F., Hurlburt, N.E., Katz, N.L., Kushner, G.D., Levay, M., Lindgren, R.W., Mathur, D.P., McFeaters, E.L., Mitchell, S., Rehse, R.A., Schrijver, C.J., Springer, L.A., Stern, R.A., Tarbell, T.D., Wuelser, J.P., Wolfson, C.J., Yanari, C., Bookbinder, J.A., Cheimets, P.N., Caldwell, D., Deluca, E.E., Gates, R., Golub, L., Park, S., Podgorski, W.A., Bush, R.I., Scherrer, P.H., Gummin, M.A., Smith, P., Auker, G., Jerram, P., Pool, P., Soufli, R., Windt, D.L., Beardsley, S., Clapp, M., Lang, J., Waltham, N.: 2012, The Atmospheric Imaging Assembly (AIA) on the Solar Dynamics Observatory (SDO). *Solar Phys.* **275**, 17 – 40. doi:10.1007/s11207-011-9776-8.

Lin, J., Ko, Y.K., Sui, L., Raymond, J.C., Stenborg, G.A., Jiang, Y., Zhao, S., Mancuso, S.: 2005, Direct observations of the magnetic reconnection site of an eruption on 2003 November 18. *Astrophys. J.* **622**, 1251 – 1264. doi:10.1086/428110.

Liu, Y., Luhmann, J.G., Lin, R.P., Bale, S.D., Vourlidas, A., Petrie, G.J.D.: 2009, Coronal mass ejections and global coronal magnetic field reconfiguration. *Astrophys. J. Lett.* **698**, L51 – L55. doi:10.1088/0004-637X/698/1/L51.

Low, B.C., Hundhausen, J.R.: 1995, Magnetostatic structures of the solar corona. 2: The magnetic topology of quiescent prominences. *Astrophys. J.* **443**, 818 – 836. doi:10.1086/175572.

McIntosh, S.W., de Pontieu, B., Tomczyk, S.: 2008, A coherence-based approach for tracking waves in the solar corona. *Solar Phys.* **252**, 321 – 348. doi:10.1007/s11207-008-9257-x.

McIntosh, S.W., de Pontieu, B., Leamon, R.J.: 2010, The impact of new EUV diagnostics on CME-related kinematics. *Solar Phys.* **265**, 5 – 17. doi:10.1007/s11207-010-9538-z.

Mierla, M., Schwenn, R., Teriaca, L., Stenborg, G., Podlipnik, B.: 2005, Using LASCO-C1 spectroscopy for coronal diagnostics. *Adv. Space Res.* **35**, 2199 – 2203. doi:10.1016/j.asr.2005.04.031.

Nakariakov, V.M., Ofman, L.: 2001, Determination of the coronal magnetic field by coronal loop oscillations. *Astron. Astrophys.* **372**, L53 – L56. doi:10.1051/0004-6361:20010607.

O'Dwyer, B., Del Zanna, G., Mason, H.E., Weber, M.A., Tripathi, D.: 2010, SDO/AIA response to coronal hole, quiet Sun, active region, and flare plasma. *Astron. Astrophys.* **521**, A21. doi:10.1051/0004-6361/201014872.

Patsourakos, S., Vourlidas, A.: 2009, "Extreme ultraviolet waves" are waves: first quadrature observations of an extreme ultraviolet wave from STEREO. *Astrophys. J. Lett.* **700**, L182 – L186. doi:10.1088/0004-637X/700/2/L182.

Peter, H., Judge, P.G.: 1999, On the Doppler shifts of solar ultraviolet emission lines. *Astrophys. J.* **522**, 1148 – 1166. doi:10.1086/307672.

Plunkett, S.P., Brueckner, G.E., Dere, K.P., Howard, R.A., Koomen, M.J., Korendyke, C.M., Michels, D.J., Moses, J.D., Moulton, N.E., Paswaters, S.E., St. Cyr, O.C., Socker, D.G., Wang, D., Simnett, G.M., Bedford, D.K., Biesecker, D.A., Eyles, C.J., Tappin, S.J., Schwenn, R., Lamy, P.L., Llebaria, A.: 1997, The relationship of green-line transients to white-light coronal mass ejections. *Solar Phys.* **175**, 699 – 718. doi:10.1023/A:1004981125702.

Rachmeler, L.A., Gibson, S.E., Dove, J.B., DeVore, C.R., Fan, Y.: 2013, Polarimetric properties of flux ropes and sheared arcades in coronal prominence cavities. *Solar Phys.* accepted.

Reiner, M.J., Vourlidas, A., Cyr, O.C.S., Burkepile, J.T., Howard, R.A., Kaiser, M.L., Prestage, N.P., Bougeret, J.L.: 2003, Constraints on coronal mass ejection dynamics from simultaneous radio and white-light observations. *Astrophys. J.* **590**, 533 – 546. doi:10.1086/374917.

Schmit, D.J., Gibson, S.E., Tomczyk, S., Reeves, K.K., Sterling, A.C., Brooks, D.H., Williams, D.R., Tripathi, D.: 2009, Large-scale flows in prominence cavities. *Astrophys. J. Lett.* **700**, L96 – L98. doi:10.1088/0004-637X/700/2/L96.

Schwenn, R., Inhester, B., Plunkett, S.P., Epple, A., Podlipnik, B., Bedford, D.K., Eyles, C.J., Simnett, G.M., Tappin, S.J., Bout, M.V., Lamy, P.L., Llebaria, A., Brueckner, G.E., Dere, K.P., Howard, R.A., Koomen, M.J., Korendyke, C.M., Michels, D.J., Moses, J.D., Moulton, N.E., Paswaters, S.E., Socker, D.G., St. Cyr, O.C., Wang, D.: 1997, First view of the extended green-line emission corona at solar activity minimum using the LASCO-C1 coronagraph on SOHO. *Solar Phys.* **175**, 667 – 684. doi:10.1023/A:1004948913883.

Shen, Y., Liu, Y.: 2012, Evidence for the wave nature of an extreme ultraviolet wave observed by the Atmospheric Imaging Assembly on board the Solar Dynamics Observatory. *Astrophys. J.* **754**, 7. doi:10.1088/0004-637X/754/1/7.

Su, Y., van Ballegooijen, A.: 2012, Observations and magnetic field modeling of a solar polar crown prominence. *Astrophys. J.* **757**, 168. doi:10.1088/0004-637X/757/2/168.

Temmer, M., Veronig, A.M., Kontar, E.P., Krucker, S., Vršnak, B.: 2010, Combined STEREO/RHESSI study of coronal mass ejection acceleration and particle acceleration in solar flares. *Astrophys. J.* **712**, 1410 – 1420. doi:10.1088/0004-637X/712/2/1410.

Tian, H., Tu, C., Marsch, E., He, J., Kamio, S.: 2010, The nascent fast solar wind observed by the EUV imaging spectrometer on board Hinode. *Astrophys. J. Lett.* **709**, L88 – L93. doi:10.1088/2041-8205/709/1/L88.

Tian, H., McIntosh, S.W., Xia, L., He, J., Wang, X.: 2012a, What can we learn about solar coronal mass ejections, coronal dimmings, and extreme-ultraviolet jets through spectroscopic observations? *Astrophys. J.* **748**, 106. doi:10.1088/0004-637X/748/2/106.

Tian, H., McIntosh, S.W., Wang, T., Ofman, L., De Pontieu, B., Innes, D.E., Peter, H.: 2012b, Persistent Doppler shift oscillations observed with Hinode/EIS in the solar corona: spectroscopic signatures of Alfvénic waves and recurring upflows. *Astrophys. J.* **759**, 144. doi:10.1088/0004-637X/759/2/144.

Tomczyk, S., McIntosh, S.W.: 2009, Time–distance seismology of the solar corona with CoMP. *Astrophys. J.* **697**, 1384 – 1391. doi:10.1088/0004-637X/697/2/1384.

Tomczyk, S., McIntosh, S.W., Keil, S.L., Judge, P.G., Schad, T., Seeley, D.H., Edmondson, J.: 2007, Alfvén waves in the solar corona. *Science* **317**, 1192. doi:10.1126/science.1143304.

Tomczyk, S., Card, G.L., Darnell, T., Elmore, D.F., Lull, R., Nelson, P.G., Streander, K.V., Burkepile, J., Casini, R., Judge, P.G.: 2008, An instrument to measure coronal emission line polarization. *Solar Phys.* **247**, 411 – 428. doi:10.1007/s11207-007-9103-6.

Van Doorsselaere, T., Nakariakov, V.M., Verwichte, E.: 2008, Detection of waves in the solar corona: kink or Alfvén? *Astrophys. J. Lett.* **676**, L73 – L75. doi:10.1086/587029.

Wang, T.J., Solanki, S.K.: 2004, Vertical oscillations of a coronal loop observed by TRACE. *Astron. Astrophys.* **421**, L33 – L36. doi:10.1051/0004-6361:20040186.

Wang, Y.M., Ye, P.Z., Wang, S., Zhou, G.P., Wang, J.X.: 2002, A statistical study on the geoeffectiveness of Earth-directed coronal mass ejections from March 1997 to December 2000. *J. Geophys. Res.* **107**, 1340. doi:10.1029/2002JA009244.

White, R.S., Verwichte, E.: 2012, Transverse coronal loop oscillations seen in unprecedented detail by AIA/SDO. *Astron. Astrophys.* **537**, A49. doi:10.1051/0004-6361/201118093.

Zhang, M., Low, B.C.: 2005, The hydromagnetic nature of solar coronal mass ejections. *Annu. Rev. Astron. Astrophys.* **43**, 103 – 137. doi:10.1146/annurev.astro.43.072103.150602.

Zhang, J., Dere, K.P., Howard, R.A., Kundu, M.R., White, S.M.: 2001, On the temporal relationship between coronal mass ejections and flares. *Astrophys. J.* **559**, 452 – 462. doi:10.1086/322405.

Zhang, J., Richardson, I.G., Webb, D.F., Gopalswamy, N., Huttunen, E., Kasper, J.C., Nitta, N.V., Poomvises, W., Thompson, B.J., Wu, C.C., Yashiro, S., Zhukov, A.N.: 2007, Solar and interplanetary sources of major geomagnetic storms (Dst $= -100$ nT) during 1996 – 2005. *J. Geophys. Res.* **112**(11), 10102. doi:10.1029/2007JA012321.

DOI 10.1007/978-1-4939-2038-9_12
Reprinted from *Solar Physics* Journal, DOI 10.1007/s11207-013-0419-0

Near-Limb Zeeman and Hanle Diagnostics

I.S. Kim · I.V. Alexeeva · O.I. Bugaenko · V.V. Popov · E.Z. Suyunova

Received: 8 December 2012 / Accepted: 19 September 2013 / Published online: 1 November 2013

Abstract "Weak" magnetic-field diagnostics in faint objects near the bright solar disk are discussed in terms of the level of non-object signatures, in particular, of the stray light in telescopes. Calculated dependencies of the stray light caused by diffraction at the 0.5-, 1.6-, and 4-meter entrance aperture are presented. The requirements for micro-roughness of refractive and reflective primary optics are compared. Several methods for reducing the stray light (the Lyot coronagraphic technique, multiple stages of apodizing in the focal and exit pupil planes, apodizing in the entrance aperture plane with a special mask), and reducing the random and systematic errors are noted. An acceptable level of stray light in telescopes is estimated for the V-profile recording with a signal-to-noise ratio greater than three. Prospects for the limb chromosphere magnetic measurements are indicated.

Keywords Magnetic field measurements · Prominences · Chromosphere · Corona · Coronagraphs · Stray light

1. Introduction

Near-limb Zeeman and Hanle diagnostics are connected with weak magnetic-field measurements in the upper solar atmosphere: prominences, the chromosphere, and the corona. Key items of magnetic measurements in the upper solar atmosphere are low-scattered-light feed optics (telescopes), an advanced analyzing equipment (polarimeters), and advanced recording equipment. So far, such measurements have not become routine in spite of available advanced coronagraphs, polarimeters, and recording systems (Lin, Kuhn, and Coulter, 2004; Tomczyk *et al.*, 2008). This is a task for forthcoming exciting ground- and space-based projects (Keil, Rimmele, and Keller, 2003; Rimmele *et al.*, 2010; Wagner *et al.*, 2010; Tomczyk, 2011; Peter *et al.*, 2012). Non-solar object signatures in the final focal plane, in

Coronal Magnetometry
Guest Editors: S. Tomczyk, J. Zhang, and T.S. Bastian

I.S. Kim (✉) · I.V. Alexeeva · O.I. Bugaenko · V.V. Popov · E.Z. Suyunova
Sternberg Astronomical Institute, Moscow M.V. Lomonosov State University, Moscow, Russia
e-mail: kim@sai.msu.ru

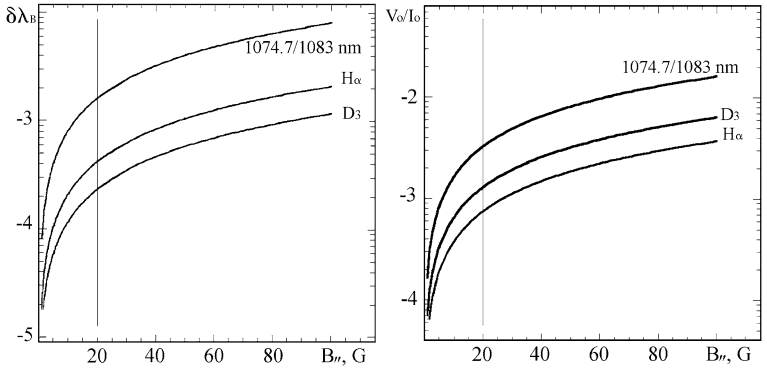

Figure 1 The Zeeman splitting [$\delta\lambda_{B_{//}}$] (left) and k-factor [V_0/I_0] (right) *versus* longitudinal magnetic-field strength [$B_{//}$] for H I Hα, He I D_3 and 1083.0 nm, and Fe XIII 1074.7 nm lines.

particular, the stray light [$I_{\rm stray}$], the sky brightness [$I_{\rm sky}$], and the continuum corona [$I_{\rm cont}$] complicate both linear and circular non-eclipse coronagraphic and eclipse polarimetry.

In this article we consider general expressions applicable in the upper solar atmosphere and several previous long-term magnetic measurements in prominences with the emphasis on $I_{\rm stray}$ of feeding optics (Section 1), dependencies of $I_{\rm stray}$ on distance caused by diffraction at the edge of an entrance aperture of 0.5, 1.6, and 4.0 meters and several ways of reducing $I_{\rm stray}$ (Section 2), reducing random and systematic errors (Section 3) and acceptable levels of $I_{\rm stray}$ for the V-profile recording with a signal-to-noise ratio greater than three (Section 4). Finally, prospects for magnetic measurements in the upper solar atmosphere are noted.

1.1. General Expressions

The term "weak magnetic field" is used when the Zeeman splitting [$\delta\lambda_B$] is three to four orders of magnitude less than the line width [$\Delta\lambda$: the full width at half maximum]. $\delta\lambda_B = 4.67 \times 10^{-11} g \lambda_0^2 B_{//}$, where λ_0 is the wavelength in nm, $B_{//}$ denotes the strength of longitudinal magnetic field in gauss, and g is the Landé factor. Hereinafter the Zeeman splitting is given in units of 0.1 nm both in the Figure 1 and in the text. As a rule, the effective Landé factor [$g_{\rm e}$] is used to take into account the different contributions to the magnetic splitting caused by different components of the line. The left part of Figure 1 shows $\delta\lambda_B$ *versus* $B_{//}$ for the chromospheric He I D_3 ($g_{\rm e} = 1.12$) and 1083.0 nm ($g_{\rm e} = 1.46$), H I Hα ($g_{\rm e} = 1.05$), and coronal Fe XIII 1074.7 nm ($g_{\rm e} = 1.46$) lines. The $g_{\rm e}$ used for the He I lines does not take into account the low-intensity component, which is valid when $\Delta\lambda_{D_3} \geq 0.04$ nm and $\Delta\lambda_{1083} \geq 0.1$ nm. $\delta\lambda_B$ of the IR lines differ by a factor of 0.99 and are presented by the same curve. The $\delta\lambda_B$ range is $2 \times (10^{-4} - 10^{-3})$ for $B_{//} = 10 - 20$ G.

In prominences, the chromosphere, and the corona $\Delta\lambda = 0.04 - 0.1$ nm, and in the first approximation the upper part of I-profiles is well fitted by a Gaussian. In "weak" fields the V-profile is proportional to the first derivative of the I profile.

$$V(\lambda) \approx {\rm d}I = -I_0 \frac{2(\lambda - \lambda_0) \times {\rm d}\lambda}{\Delta\lambda_{\rm D}^2} \exp^{-(\frac{\lambda-\lambda_0}{\Delta\lambda_{\rm D}})^2}, \quad (1)$$

where I_0 is the peak of the line intensity, λ_0 denotes the wavelength of the emission line, λ is measured from λ_0, and $\Delta\lambda_{\rm D}$ is the Doppler width. Equating the first derivative of V to

zero, we find the value of the V peak [V_0] and the wavelength corresponding to V_0 [λ_B] as follows:

$$V_0 \approx I_0 \frac{\Delta\lambda_{\rm D} \exp^{-(\frac{\Delta\lambda}{\sqrt{2}\Delta\lambda_{\rm D}})^2}}{\sqrt{2}\Delta\lambda_{\rm D}^2} \delta\lambda_B \approx 1.4 \times I_0 \frac{\delta\lambda_B}{\Delta\lambda}; \quad \lambda_B = \lambda_0 \pm \frac{\Delta\lambda_{\rm D}}{\sqrt{2}} \approx \pm 0.71 \Delta\lambda_{\rm D}. \quad (2)$$

Let us introduce a k-factor that is defined as the ratio of V_0 to I_0 and is needed for further estimates. In other words, k indicates the amplification factor in the V channel to record I and V on the same scale:

$$k = \frac{V_0}{I_0} \approx 1.4 \times \frac{\delta\lambda_B}{\Delta\lambda}. \quad (3)$$

$k(B_{\prime\prime})$ is shown in Figure 1 (right). Sophisticated polarimeters were needed to record the V-profile which is $7 \times 10^{-4} I$ when using Hα line and $B_{\prime\prime} = 20$ G.

1.2. Feeding Optics of Previous Long-Term Prominence Magnetic-Field Measurements

The direct magnetic-field determination in the upper solar atmosphere is based on the circular and linear-polarization analysis. The Zeeman analysis does not need any assumption on the mechanism of radiation and allows an approach close to the limb. The main steps of several long-term magnetic studies in prominences are outlined in the recent memoir by Tandberg-Hanssen (2011). The feeding optics used (telescopes with the entrance aperture < 0.5 meter) are briefly noted below. Hereinafter, only references concerning the aspects of $I_{\rm stray}$ are cited.

i) The first magnetic measurements in active prominences were made by Zirin and Severny (1961) and Ioshpa (1962): Babcock-type magnetographs, 30-cm solar tower telescopes, $B_{\prime\prime} \approx 100$ G.

ii) Next successes were based on magnetographs developed specifically for Zeeman analysis in prominences (Lee, Rust, and Zirin, 1965; Lee, Harvey, and Tandberg-Hanssen, 1969) and Climax 40-cm coronagraph: the magnetograph slit of $14'' - 25''$; an integration time up to ten minutes. Rust (1966) carried out magnetic research in quiescent prominences (QP): $B_{\prime\prime}$ ranges from a few G to 10 G, sometimes 20 – 30 G. Harvey and Tandberg-Hanssen (1968), Malville (1968), and Harvey (1969) carried out measurements in active prominences (AP): $B_{\prime\prime} = 40 - 200$ G, possible dependence on the phase of solar cycle, the angle between the field vector and the long axis of prominences $[\alpha] < 20°$ (Tandberg-Hanssen and Anzer, 1970).
Determinations of the magnetic-field vector in prominences have been made by Athay *et al.* (1983) with the *Advanced Stokes Polarimeter* and the 40-cm coronagraph of the National Solar Observatory/Sacramento Peak: the polarimeter slit of $7'' \times 10''$, an integration time of two minutes.

iii) Contradictory results were reported by Smol'kov and Bashkirtsev (1971) and Bashkirtsev, Smolkov, and Shmulevsky (1971) for the first stage of their measurements with the 50-cm horizontal solar telescope and the magnetograph scanning across the line profile: the magnetograph slit of $7''$, $B_{\prime\prime}$ up to 100 G in QP, and up to 1000 G in AP.

iv) The next long-term Zeeman analysis was made with Nikolsky's magnetograph developed in cooperation with Institute d'Astrophysique de Paris (En den, Kim, and Nikolskii, 1977; Nikolskii, Kim, and Koutchmy, 1982; Stepanov, 1989) and the 50-cm domeless refractive coronagraph: the magnetograph pinhole of $8''$, an integration time of 30 seconds.

- A piezo-scanning Fabry–Pérot interferometer with a pre-filter.
- A $LiNbO_3$ crystal as an analyzer.
- Measurements in the vicinity of the optical axis ($< 30''$).
- The use of the magnetic-field etalon (Kim, 2000).
- Compensation of the instrumental polarization (Klepikov, 1999).

Results of the statistical analysis were as follows (Kim, 1990): $B_{//}$ in QP of several G, sometimes reaching 30 – 40 G; in AP $B_{//} = 40 - 150$ G; $\alpha \leq 25°$; both the inverse and the normal polarities may exist in the same prominence. To summarize, only coronagraphs as feeding optics provided long-term "weak" magnetic-field measurements [10 – 20 G] in prominences.

1.3. Non-object Signatures

On average, V_0 depends on I_0, λ, g, and $B_{//}$. Nevertheless, the Zeeman diagnostics in spicules are technically more complicated despite the fact that their intensities are greater than the intensity of bright prominences. Significant noise appears when approaching the limb.

Non-object signatures complicate the direct near-limb Zeeman diagnostics. Let S/N be the signal-to-noise ratio. In our case $S = V_0$ and N is the noise in the V channel caused mainly by input of non-object signatures: $I_{\rm stray}$, $I_{\rm cont}$, and $I_{\rm sky}$ that are one to three orders of magnitude lower than I. Photon noise is assumed. In the first approximation, $N \approx k \times [\sqrt{I_{\rm stray}} + \sqrt{I_{\rm sky}} + \sqrt{I_{\rm cont}}]$. Let $S/N = V_0/N$ be ≥ 3. Using the expressions (2) and (3) we obtain

$$N \leq 0.47 \times I_0 \frac{\delta\lambda_B}{\Delta\lambda} \quad \Longrightarrow \quad \left[\sqrt{I_{\rm stray}} + \sqrt{I_{\rm sky}} + \sqrt{I_{\rm cont}}\right] \leq 0.47 \frac{I_0 \times \delta\lambda_B}{k \times \Delta\lambda}. \tag{4}$$

Note that for reasonable non-object signatures (the total $< 10^{-5}$), $B_{//} = 20$ G, $\delta\lambda_B$ and k derived from Figure 1, the above expression is satisfied for $I_0 > 7 \times 10^{-3}$ in Hα and $> 10^{-2}$ in IR lines that correspond to prominences. The intensity of coronal lines is much lower. An increase of the integration time and the entrance aperture is required to effectively increase the incoming flux.

2. Reducing the Stray Light in Telescopes

The existence of large-spread-angle stray light may significantly affect polarization measurements. According to Chae *et al.* (1998), the observed polarization degrees are always underestimated. The main sources of "parasitic" background in the final focal plane of any telescope are the following:

i) A ghost solar image produced by multiple reflections in the primary lens.
ii) Random inhomogeneities in the glass of the primary lens.
iii) Departures of the surface of the primary optics from a uniform shape.
iv) Diffraction of the solar-disk light at the entrance aperture [$I_{\rm dif}$].
v) Scattering at micro-roughness of the primary optics [$I_{\rm sc}$].
vi) The sky brightness [$I_{\rm sky}$].
vii) The continuum corona [$I_{\rm cont}$].
viii) The dust on the primary optics [$I_{\rm dust}$].

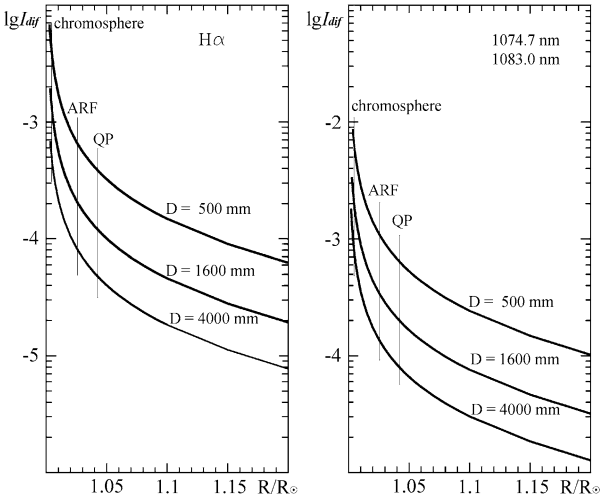

Figure 2 Stray light caused by diffraction of the solar-disk light at the entrance aperture. Left: Hα line. Right: the He I 1083.0 nm and Fe XIII 1074.7 nm lines.

Reducing items i) – iv) was partly discussed by Newkirk and Bohlin (1963). Items iv) – vi) are negligible during total solar eclipses (TSE), and they dominate for high-altitude coronagraphic observations. Reducing item viii) for 53-cm refractive primary optics (our experience) was done by cleaning the lens before each set of observations. But this item becomes very important for large-aperture reflective primary optics. Below, the role of the stray light for magnetic-field measurements will be discussed. Hereinafter we denote $I_{\rm stray}$ as $I_{\rm dif} + I_{\rm sc}$.

2.1. Reducing the Stray Light Caused by Diffraction of the Bright Round Source at the Round Aperture

The diffraction of the bright round source at the round aperture was treated by Nagaoka (1920). For estimations of $I_{\rm dif}$, we used the simplified expression suggested by Sazanov (1968), which is valid in the range $R < 1.3\ \mathrm{R}_\odot$. Deviations not more than 20 % are expected as compared with values based on Nagaoka's equations.

$$\log I_{\rm dif}(\rho) = \log \frac{2\lambda}{\pi^3 D\gamma_0} + \log\left(\frac{\sqrt{1+(\nu-1)^2}}{\nu-1} - \frac{\sqrt{1+(\nu+1)^2}}{\nu+1}\right) - 0.27(\nu-1) - 0.017, \quad (5)$$

where ρ is the distance from the solar-disk center in the units of $\mathrm{R}_\odot$, $\nu = \frac{\rho}{a}$, $a = \frac{\pi D}{\lambda}\gamma_0$ is the radius of the round source in arbitrary units, D is the diameter of the primary lens, γ_0 is the angular radius of the source. $I_{\rm dif}(R)$ is shown in Figure 2 for Hα (left) and near IR (right) lines for 0.5-, 1.6-, and 4-meter apertures. Vertical lines indicate typical maximum altitudes observed [*h*] of QP ($40'' \approx 0.042\ \mathrm{R}_\odot$), active-region filaments (ARF) ($25'' \approx 0.026\ \mathrm{R}_\odot$), and the upper chromosphere ($4'' \approx 0.004\ \mathrm{R}_\odot$). Hereinafter intensities, brightness, and equivalent width are given in units of 0.1 nm in nearby solar-disk continuum.

It is seen that the stray light in Hα caused by diffraction at the 0.5-m aperture of a conventional (non-coronagraphic) telescope can reach 10^{-3} at prominence heights and is $> 5 \times 10^{-3}$ at the chromosphere level.

2.1.1. Coronagraphic Technique (the Lyot Method)

The coronagraphic technique suggested by Lyot (1931) is based on masking in the primary focal plane and in the plane of the exit pupil to eliminate i) and ii), and to minimize the input of iv). The optical sketch of the Lyot-type coronagraph has the primary single lens, the primary focal plane, the mask in the primary focal plane (an artificial Moon), the field lens, the mask in the plane of the exit pupil (the Lyot stop), the relay optics, and the final focal plane. Multiple Fresnel reflections at the surfaces of the primary lens create a system of the solar-disk images, decreasing in brightness. For a single primary lens with the refraction index $n = 1.5$, the brightness ratio of the first, most bright reflection to the solar-disk one is $(n-1)^4/(n+1)^4 = 1/625$, and the ratio of the primary focal length to the space between the image and the lens is $[2/(n-1)] + 3 = 7$. A round screen in the center of the Lyot stop results in removal of the reflection. The procedure is not applicable for multi-lens primary optics, as the brightest reflection is near the primary focal plane. The correct use of the Lyot method results in $I_{\rm dif}$ reducing by one to two orders of magnitude depending on the size of the mask in the primary focal plane and in the plane of the Lyot stop. In practice, reducing $I_{\rm stray}$ by $\approx 50-100$ (the coronagraphic efficiency $[K]$) for prominences and $10-25$ for the chromosphere can be achieved depending on the height observed.

2.1.2. Multiple Cascade Coronagraphic Technique

To our knowledge, the multiple-cascade coronagraphic technique has not been used practically. Terrile (1989) found that an additional factor of more than ten can be achieved through multiple stages of apodizing both in the focal plane and in the Lyot-stop plane. The calculated point spread function (PSF) showed that in such a hybrid coronagraph $I_{\rm dif}$ can be reduced by more than three orders of magnitude.

We used the two-stage coronagraphic approach for the last version of Nikolsky's magnetograph (Stepanov, 1989). The main goal was to match the focal ratio of the coronagraph with the spectral resolution of the Fabry–Pérot interferometer through the inclusion of an additional focal and the Lyot-stop planes. This complicated the optical adjustment of the "coronagraph + magnetograph" assembly. Depending on the brightness of prominences, the magnetic-field strength, and the height observed, the signal-to-noise ratio became two to three times better.

2.1.3. Apodizing with a Special Mask in the Plane of an Entrance Aperture

The diffraction pattern in the focal plane is the result of discontinuity of the transmission function $[G]$ (or its derivatives) of the entrance aperture. The characteristic frequency of the damping intensity oscillations depends on the distance between the points of discontinuity, the asymptotic damping rate depends on the order of the derivative in which the continuity of G (G^2 in intensity) is broken. For a round aperture, there is a discontinuity in the transmission function: $G(\rho) = 1$ in the range $\rho < 1$ and $G = 0$ in the range $\rho \geq 1$, where ρ is the distance from the center of aperture. In the case of a point source, it creates the Airy diffraction pattern $I \propto [J_1(r)/r]^2$ with intensity damping as r^{-3}, where $J_1(x)$ is the Bessel function of the first kind. A mask with variable transmission $[G(\rho) = 1 - \rho^2]$ has discontinuities only in the first derivative. The use of such a mask in the plane of the entrance aperture results in the diffraction image $I \propto \{[J_1(r) + J_3(r)]/r\}^2$ with the more effective damping as r^{-5}.

We considered an extended object, *e.g.* the Sun (Kim *et al.*, 1995) using Nagaoka's equations (Nagaoka, 1920). The stray light in the center of the solar-disk image caused by diffraction at the entrance aperture is given by

$$I_{\rm dif}(0) = 1 - J_0^2(a) - J_1^2(a), \tag{6}$$

where $a = (\pi D \sin\gamma_0)/\lambda$, λ is the wavelength, γ_0 is the angular radius of solar disk, and D is the diameter of aperture. If $a \gg 1$, then $I_{\rm dif}(0) \approx (1-2)/(\pi a)$. For $\gamma_0 = 960''$, $\lambda = 600$ nm, $D = 200$ mm, we obtain $a = 4874$ and $I_{\rm dif}(0) = (1-1.3) \times 10^{-4}$.

In the case when the entrance aperture is apodized by the mask $G = (1-\rho^2)$, we found the relation between the apodized $[I^a_{\rm dif}]$ and non-apodized $[I_{\rm dif}]$ for points at the angular distance $\gamma = (1+\epsilon)\gamma_0$ from the disk center:

$$I^a_{\rm dif}(\epsilon) \approx 2/3\pi^4 \left[I_{\rm dif}(\epsilon)\right]^3. \tag{7}$$

Let us estimate the efficiency of the mask for chromospheric and prominence heights and $a \approx 5000$.

- The upper-chromosphere heights: $h = 4''$, $\epsilon = 0.004$ ($\epsilon\gamma_0 = 4''$). Then $I\,(0.004) = 10^{-2}$ and $I^a\,(0.004) = 0.7 \times 10^{-4}$. A calculated efficiency up to 10^2 can be achieved.
- Quiescent-prominence heights: $h = 40''$, $\epsilon = 0.04$ ($\epsilon\gamma_0 = 40''$). Then $I_{\rm dif}(0.04) = 10^{-3}$ and $I^{(a)}_{\rm dif}\,(0.04) = 0.7 \times 10^{-7}$. A calculated efficiency up to 10^4 can be achieved.

No classical Lyot-type coronagraphs are needed. Note that the mask $(1-\rho^2)$ reduces transmittance by a factor of three.

2.2. Comments on Scattering by Micro-Roughness of the Primary Optics

In this subsection, we do not analyze scattering by micro-roughness of the primary optics. This is a topic requiring detailed studies. In the case of the statistical nature of the micro-roughness, $I_{\rm sc}$ is proportional to the square of the average height of the inhomogeneity (RMS). The fabrication of super-smooth primary optics is the key technology for creating a low-scattered-light coronagraph. Reflecting optics are achromatic and do not depend on bulk inhomogeneities of the material compared to a refractor. Let n be the index of refraction. At the same value of RMS, the energy scattered by a reflecting surface $(n^* = -1)$ $[I_{\rm sc}]$ is greater by a factor of $[(n^*-1)/(n-1)]^2 = 16$ compared to the refractive case. Possible ways to reduce the scattered light include the following:

- The use of a super-smooth primary optics with RMS = 0.3 – 1 nm. Pioneering studies performed by Socker and Korendyke (1988) showed that the $I_{\rm stray}$ of a 9.8-cm diameter super-smooth silicon mirror is comparable with the stray light of a single lens.
- The use of moderately smooth primary optics with a given profile of the micro-relief can significantly reduce the scattered light in the range of interest. According to numerical calculations by Romanov *et al.* (1991) made for Earth-environment monitoring, RMS of 2.5 nm and the spatial period of the micro-relief (the correlation length of inhomogeneities) of 0.76 – 0.78 μ can provide scattered light of $\approx 10^{-5}$ in the range < 1.1 $R_\oplus$ where $R_\oplus$ is the radius of the Earth.

3. Acceptable Level of the Stray Light in Telescopes for Zeeman Diagnostics

Using Equation (4), Figures 1 and 2, let us estimate the acceptable level of the stray light in telescopes for Zeeman diagnostics with the signal-to-noise ratio ≥ three. Several conditions exist.

– The stray light is caused by diffraction at the entrance aperture (super-smooth primary optics).
– The noise of the recording assembly is negligible.
– W is the equivalent width of the emission line.
– The instrumental width is $0.7\Delta\lambda_D \approx 0.5\Delta\lambda$ to achieve the maximum signal-to-noise ratio (Nikolskij *et al.*, 1985).
– In the case of scattering by aerosols ($\sim\lambda^{-2}$), $I_{sky} = 10^{-5}$ in Hα and $I_{sky} \approx 2 \times 10^{-6}$ in the IR lines.
– I_{cont} passed through the instrumental profile is $< 10^{-6}$.

Hα *bright prominences*, $B_{//} = 100$ G: W $= 10^{-1}$, $\Delta\lambda \approx 0.06$ nm. $I_0 = 5 \times 10^{-2}$, $\delta\lambda_B = 2 \times 10^{-3}$ and $k = 4 \times 10^{-3}$ (Figure 1). The required I_{stray} should be $\leq 5 \times 10^{-4}$. Referring to Figure 2 (left), we see that the aperture of 0.5 meters provides this level of scattered light at $h > 35''$. The first magnetic measurements in prominences with 30-cm solar tower telescopes as feeding optics confirm this (Zirin and Severny, 1961; Ioshpa, 1962).

A non-coronagraphic 4-meter telescope with a super-smooth primary optics can provide Zeeman diagnostics of 100 G field strengths in bright prominences from $h \geq 10''$ as well.

Hα *moderate-brightness prominences*, $B_{//} = 20$ G: $W = 2 \times 10^{-2}$, $\Delta\lambda \approx 0.06$ nm. $I_0 = 10^{-2}$, $\delta\lambda_B = 4 \times 10^{-4}$, and $k = 7 \times 10^{-4}$ (Figure 1). The required I_{stray} should be $\leq 2 \times 10^{-5}$. Only coronagraphs (at the limit of 0.5 meters, and reliably with 4-meter apertures) provide the required I_{stray} from heights $> 20''$. Note the crucial role of the sky brightness, the polarimeter performance, and the integration time.

Limb chromosphere, He I 1083.0 nm, $B_{//} = 20$ G: $W \approx 3 \times 10^{-2}$, $\Delta\lambda \approx 0.08$ nm. $h = 4''$, $I_0 = 1.5 \times 10^{-2}$, $\delta\lambda_B = 1.3 \times 10^{-3}$, and $k = 3 \times 10^{-3}$ (Figure 1). Then the required $I_{stray} \leq 1.6 \times 10^{-5}$ will be provided with the 4-meter coronagraph in which the scattered light is reduced by a factor of 30 – 40.

Corona, Fe XIII 1074.7 nm, $B_{//} = 20$ G: $W = 2 \times 10^{-4}$, $\Delta\lambda \approx 0.08$ nm. The expected total of all non-coronal signatures is $\approx 10^{-5}$. $\delta\lambda_B = 1.5 \times 10^{-3}$, and $k = 3.3 \times 10^{-3}$ (Figure 1). $I_0 = 10^{-4}$, that is increasing I_0 up to 10^2 (see above), is required. A 4-meter aperture allows an increase in the flux by 64 times as compared to a 0.5-meter one. In this case, the conditions will be similar to magnetic-field measurements in moderate brightness prominences when using a 0.5-meter coronagraph. I_{sky}, the performance of the polarimeter, and the integration time become important factors.

4. Reduction of Random and Systematic Errors

We have developed an approach for high-precision linear polarimetry with actual accuracy of 2 % for the linear-polarization degree [p] and 2° for the polarization angle [χ] that allow us to obtain "polarization images" of an object: 2D distributions of p, χ, and the sign of χ. The description of the last version was presented recently (Kim *et al.*, 2011). The key components are the following:

i) Low level of the sky brightness [I_{sky}].
ii) A low level of the stray light in telescopes [I_{stray}].
iii) Uniformity of the polarizer performance for any "point" of the image.
iv) Reduction of random errors based on "statistics": the use of 24 orientations of a polarizer instead of traditional three.
v) Reduction of systematic errors based on Stokes-vector presentation of the light and the solution of the over-determined system of 24 equations (the number of equations is greater than the number of unknowns) by least squares.

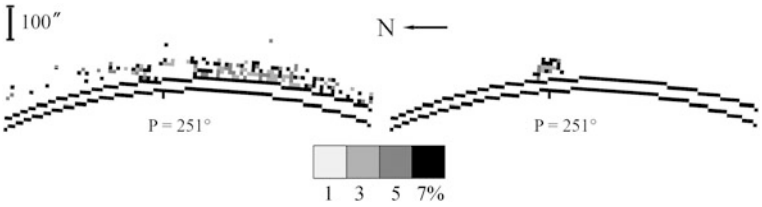

Figure 3 The 2D distribution of p in the red spectral interval including Hα line based on three orientations of a polarizer (left) and on 24 orientations (right). The right p-image reveals the polarized feature at $P = 251°$, which is identified with the low-brightness Hα prominence.

The role of the last two points is shown below. We use the total solar eclipse of 29 March 2006 observations, as $I_{\rm sky}$ and $I_{\rm stray}$ were negligible during totality. The approach was applied to the red polarization movie of the continuum corona to check the potential of our method, the reliability of the predicted accuracy, and the importance of items iv) and v) for the near-limb polarimetry. The red series of 24 sequential frames centered at 25 seconds before the third contact [T_3] was treated in two ways to search for evidence for Hα prominences in polarization as our red filter transmitted the Hα line. Until now, measurements of linear polarization in low-brightness prominences [$I < 10^{-2}$] were rarely carried out in spite of available advanced polarimeters. Figure 3 shows the 2D distribution of p in the range 0 – 8 % for distances $< 1.1\ R_\odot$ above the SW limb. The left distribution is based on three orientations of a polarizer spaced by 120° and exhibits a noise of 3 – 7 %. The right one is based on 24 orientations of the same series for the same position angle range and clearly reveals the polarized feature at position angle $P = 251°$ with p = 3 – 7 %. Position angles are measured counter-clockwise from the North Pole of the Sun. The solar and lunar limbs, the scales of heights and p, and the North are shown. The step of the p-scale is 2 %. Synoptic data from the Pulkovo Observatory identify this p-feature with a low brightness Hα prominence ($10^{-3} – 10^{-2}$) at the same $P = 251°$. It is known that in the absence of longitudinal magnetic fields, the polarization degree in prominences increases from 3 to 8 % with an increase in height from 10″ to 96″. The distribution agrees with the expected p-values and indirectly confirms the accuracy to be < 2 %. We note that these "raw" 2D distributions were obtained only to test the ability of our method to distinguish the near-limb several-percent linear polarization and to verify the accuracy < 2 %. Actual values of p are expected to be 1 – 2 % lower as the transfer to intensities was based on a polynomial approximation of degree four over the wide range of densities from the background to prominences and no corrections for the red coronal continuum input was made. The corrected eclipse linear polarimetry in prominences as well as p, χ, and the sign of χ images will be discussed in a separate article.

5. Summary

The stray light [$I_{\rm stray}$] seems to be a crucial factor determining the reliable near-limb V-profile recording in the range $< 1.2\ R_\odot$. Our estimates of non-object signatures quantitatively show that the most advanced polarimeter will be powerless if $I_{\rm stray}$ in a feeding optics exceeds the acceptable level. A brief comparison of several ways of $I_{\rm stray}$ reduction results in the following.

– The well-known coronagraphic technique (the Lyot method) provides the coronagraphic efficiency $[K]$ of 10 – 100 depending on the size of mask in the primary focal plane and in the plane of the Lyot stop (depending on the object under study).
– According to our experience, multiple stages of apodizing both in the focal plane and in the Lyot-stop plane provides $K = 2-3$ and complicates the optical adjustment of the "coronagraph + magnetograph" assembly.
– Apodizing with a mask with variable transmission placed in the plane of an entrance aperture $[G(\rho) = 1 - \rho^2]$, where ρ is the distance from the center of aperture. For a 200-mm aperture, calculated efficiency factors up to 10^2 at the upper chromosphere level [4″] and up to 10^4 at the QP heights [40″] can be achieved. Recent technology advances allow the consideration of manufacturing such a mask. Synoptic chromospheric and prominence magnetic research seem to be reliable.
– The use of a super-smooth primary optic with RMS = 0.3 – 1 nm or a moderately smooth primary optic (RMS of 2.5 nm) with a given profile of the micro-relief can significantly reduce the scattered light in the range of interest.
– The important role of reduction of random and systematic errors is shown by the example of eclipse linear polarimetry of prominences.

Estimation of the acceptable level of the stray light in a 0.5-, 1.6-, and 4-meter aperture telescope for Zeeman diagnostics with the signal-to-noise ratio > three show that the 4-meter-aperture ATST with $I_{\text{stray}} < 10^{-5}$ will provide V-profile recording of "weak" fields $[B_{//} = 10-20$ G] in prominences in visual and IR lines, the limb chromosphere and corona in IR lines with the finest magnetic "resolution" comparable with the characteristic size of the structures.

Acknowledgements This work was partially supported by research project No 11-02-00631 of the Russian Foundation for Basic Research. We are very indebted to the referee for corrections and important comments concerning the sources of stray light.

References

Athay, R.G., Querfeld, C.W., Smartt, R.N., Landi Degl'Innocenti, E., Bommier, V.: 1983, Vector magnetic fields in prominences. III – He I D_3 Stokes profile analysis for quiescent and eruptive prominences. *Solar Phys.* **89**, 3 – 30. ADS:1983SoPh...89....3A, doi:10.1007/BF00211948.

Bashkirtsev, V.S., Smolkov, G.Y., Shmulevsky, V.N.: 1971, *Issled. Geomagn. Aèron. Fiz. Solnca* **20**, 212.

Chae, J., Yun, H.S., Sakurai, T., Ichimoto, K.: 1998, Stray-light effect on magnetograph observations. *Solar Phys.* **183**, 229 – 244. ADS:1998SoPh..183..229C, doi:10.1023/A:1005012509071.

En den, O., Kim, I.S., Nikolskii, G.M.: 1977, Measurement of the prominences magnetic field. *Solar Phys.* **52**, 35 – 36. ADS:1977SoPh...52...35D, doi:10.1007/BF00935786.

Harvey, J.W.: 1969, Magnetic fields associated with solar active-region prominences. Ph.D. thesis, University of Colorado at Boulder.

Harvey, J.W., Tandberg-Hanssen, E.: 1968, The magnetic field in some prominences measured with the He I, 5876 Å line. *Solar Phys.* **3**, 316 – 320. ADS:1968SoPh....3..316H, doi:10.1007/BF00155165.

Ioshpa, B.A.: 1962, *Geomagn. Aeron.* **2**, 149.

Keil, S., Rimmele, T., Keller, C. (The ATST Team): 2003, Design and development of the advanced technology solar telescope. *Astron. Nachr.* **324**, 303 – 304.

Kim, I.S.: 1990, Prominence magnetic field observations. In: Ruzdjak, V., Tandberg-Hanssen, E. (eds.) *IAU Colloq. 117: Dynamics of Quiescent Prominences*, *Lecture Notes in Physics* **363**, Springer, Berlin, 49 – 69.

Kim, I.S.: 2000, Observing the solar magnetic field. In: Zahn, J.P., Stavinschi, M. (eds.) *NATO ASIC, Adv. Solar Res. Eclipses from Ground and from Space* **558**, Kluwer, Dordrecht, 67 – 83.

Kim, I., Bugaenko, O., Bruevich, V., Evseev, O.: 1995, Problems of reflecting coronagraphs. *Bull. Russ. Acad. Sci., Phys.* **59**, 153.

Kim, I.S., Lisin, D.V., Popov, V.V., Popova, E.V.: 2011, Eclipse high-precision linear polarimetry of the inner white-light corona: polarization degree. In: Kuhn, J.R., Harrington, D.M., Lin, H., Berdyugina, S.V., Trujillo-Bueno, J., Keil, S.L., Rimmele, T. (eds.) *Solar Polarization 6* **CS-437**, Astron. Soc. Pac., San Francisco, 181 – 188.

Klepikov, V.Y.: 1999, Magnitnye polya spokoinykh protuberantsev (Magnetic fields of quiscent prominences). Ph.D. thesis, IZMIRAN, Moscow.

Lee, R.H., Harvey, J.W., Tandberg-Hanssen, E.: 1969, The improved solar magnetograph of the high altitude observatory. *Appl. Opt.* **8**, 2370.

Lee, R.H., Rust, D.M., Zirin, H.: 1965, The solar magnetograph of the high altitude observatory. *Appl. Opt.* **4**, 1081.

Lin, H., Kuhn, J.R., Coulter, R.: 2004, Coronal magnetic field measurements. *Astrophys. J. Lett.* **613**, L177 – L180.

Lyot, B.: 1931, Photographie de la couronne solaire en dehors des eclipses. *C. R. Acad. Sci.* **193**, 1169.

Malville, J.M.: 1968, Magnetic fields in two active prominences. *Solar Phys.* **5**, 236 – 239. ADS:1968SoPh....5..236M, doi:10.1007/BF00147967.

Nagaoka, H.: 1920, Diffraction of a telescopic objective in the case of a circular source of light. *Astrophys. J.* **51**, 73.

Newkirk, G. Jr., Bohlin, D.: 1963, Reduction of scattered light in the coronagraph. *Appl. Opt.* **2**, 131.

Nikolskii, G.M., Kim, I.S., Koutchmy, S.: 1982, Measurements of the magnetic field in solar prominences with a spectrally scanning magnetograph. *Solar Phys.* **81**, 81 – 89. ADS:1982SoPh...81...81N, doi:10.1007/BF00151982.

Nikolskij, G.M., Kim, I.S., Koutchmy, S., Stepanov, A.I.: 1985, Measurement of magnetic fields in solar prominences. *Astron. Zh.* **62**, 1147 – 1153.

Peter, H., Abbo, L., Andretta, V., Auchère, F., Bemporad, A., Berrilli, F., Bommier, V., Braukhane, A., Casini, R., Curdt, W., Davila, J., Dittus, H., Fineschi, S., Fludra, A., Gandorfer, A., Griffin, D., Inhester, B., Lagg, A., Degl'Innocenti, E.L., Maiwald, V., Sainz, R.M., Pillet, V.M., Matthews, S., Moses, D., Parenti, S., Pietarila, A., Quantius, D., Raouafi, N.E., Raymond, J., Rochus, P., Romberg, O., Schlotterer, M., Schühle, U., Solanki, S., Spadaro, D., Teriaca, L., Tomczyk, S., Bueno, J.T., Vial, J.C.: 2012, Solar magnetism eXplorer (SolmeX). Exploring the magnetic field in the upper atmosphere of our closest star. *Exp. Astron.* **33**, 271 – 303.

Rimmele, T.R., Wagner, J., Keil, S., Elmore, D., Hubbard, R., Hansen, E., Warner, M., Jeffers, P., Phelps, L., Marshall, H., Goodrich, B., Richards, K., Hegwer, S., Kneale, R., Ditsler, J.: 2010, The Advanced Technology Solar Telescope: beginning construction of the world's largest solar telescope. In: *SPIE CS* **7733**, 77330G – 77330G17.

Romanov, A.D., Starichenkova, V.D., Fes'kov, A.I., Folomkin, I.P.: 1991, *J. Opt. Technol.* **6**, 11 – 14 (OMP in Russian).

Rust, D.M.: 1966, Measurements of the magnetic fields in quiescent solar prominences. Ph.D. thesis, University of Colorado at Boulder.

Sazanov, A.A.: 1968, Bol'shoi vnezatmenny koronagraph IZMIR-GAO an SSSR i ego issledovanie (The large non-eclipse coronagraph IZMIR-GAO as of the USSR and its research). PhD thesis, IZMIRAN, Moscow.

Smol'kov, G.Y., Bashkirtsev, V.S.: 1971, On the precision of records of the magnetic field in quiet prominences using a magnetograph. *Soln. Dannye Bull. Akad. Nauk SSSR* **1971**, 99 – 105.

Socker, D., Korendyke, C.: 1988, Stray light measurements of reflecting coronagraph mirrors at lambda = 6328 Å. *Bull. Am. Astron. Soc.* **20**, 990.

Stepanov, A.A.: 1989, Magnitograficheskie issledovaniya protuberanzev (Magnetographic research of prominences). Ph.D. thesis, IZMIRAN, Moscow.

Tandberg-Hanssen, E.: 2011, Solar prominences – an intriguing phenomenon. *Solar Phys.* **269**, 237 – 251. ADS:2011SoPh..269..237T, doi:10.1007/s11207-010-9704-3.

Tandberg-Hanssen, E., Anzer, U.: 1970, The orientation of magnetic fields in quiescent prominences. *Solar Phys.* **15**, 158 – 166. ADS:1970SoPh...15..158T, doi:10.1007/BF00149482.

Terrile, R.J.: 1989, Direct imaging of extra-solar planetary systems with the Circumstellar Imaging Telescope (CIT). In: Weaver, H.A., Danly, L. (eds.) *The Formation and Evolution of Planetary Systems*, *Space Telescope Science Institute Symp. Ser.* **3**, Cambridge University Press, Cambridge, 333 – 334.

Tomczyk, S.: 2011, The Coronal Solar Magnetism Observatory (COSMO). *AGU Fall Meeting Abs.*, B1952.

Tomczyk, S., Card, G.L., Darnell, T., Elmore, D.F., Lull, R., Nelson, P.G., Streander, K.V., Burkepile, J., Casini, R., Judge, P.G.: 2008, An instrument to measure coronal emission line polarization. *Solar Phys.* **247**, 411 – 428. ADS:2008SoPh..247..411T, 10.1007/s11207-007-9103-6.

Wagner, J., Hansen, E., Hubbard, R., Rimmele, T.R., Keil, S.: 2010, Advanced technology solar telescope project management. In: *Soc. Photo-Opt. Instr. Eng. (SPIE)* **CS-7738**, 77380Q – 77380Q24.

Zirin, H., Severny, A.: 1961, Measurement of magnetic fields in solar prominences. *Observatory* **81**, 155 – 156.

DOI 10.1007/978-1-4939-2038-9_13
Reprinted from *Solar Physics* Journal, DOI 10.1007/s11207-014-0525-7

3D Coronal Density Reconstruction and Retrieving the Magnetic Field Structure during Solar Minimum

M. Kramar · V. Airapetian · Z. Mikić · J. Davila

Received: 25 October 2013 / Accepted: 27 March 2014 / Published online: 11 April 2014

Abstract Measurement of the coronal magnetic field is a crucial ingredient in understanding the nature of solar coronal phenomena at all scales. We employed STEREO/COR1 data obtained during a deep minimum of solar activity in February 2008 (Carrington Rotation CR 2066) to retrieve and analyze the three-dimensional (3D) coronal electron density in the range of heights from 1.5 to 4 $R_\odot$ using a tomography method. With this, we qualitatively deduced structures of the coronal magnetic field. The 3D electron-density analysis is complemented by the 3D STEREO/EUVI emissivity in the 195 Å band obtained by tomography for the same CR. A global 3D MHD model of the solar corona was used to relate the reconstructed 3D density and emissivity to open/closed magnetic-field structures. We show that the density-maximum locations can serve as an indicator of current-sheet position, while the locations of the density-gradient maximum can be a reliable indicator of coronal-hole boundaries. We find that the magnetic-field configuration during CR 2066 has a tendency to become radially open at heliocentric distances greater than 2.5 $R_\odot$. We also find that the potential-field model with a fixed source surface is inconsistent with the boundaries between the regions with open and closed magnetic-field structures. This indicates that the assumption of the potential nature of the coronal global magnetic field is not satisfied even during the deep solar minimum. Results of our 3D density reconstruction will help to constrain

Coronal Magnetometry
Guest Editors: S. Tomczyk, J. Zhang, and T.S. Bastian

Electronic supplementary material The online version of this article (doi:10.1007/s11207-014-0525-7) contains supplementary material, which is available to authorized users.

M. Kramar (✉)
Physics Department, The Catholic University of America, 620 Michigan Ave NE, Washington, DC 20064, USA
e-mail: kramar@cua.edu

M. Kramar · V. Airapetian · J. Davila
NASA-GSFC, Code 671, Greenbelt, MD 20771, USA

Z. Mikić
Predictive Science, Inc., 9990 Mesa Rim Rd., Ste. 170, San Diego, CA 92121, USA

solar coronal-field models and test the accuracy of the magnetic-field approximations for coronal modeling.

Keywords Corona, quiet, structures · Magnetic fields, corona

1. Introduction

Solar coronal magnetic fields play a key role in the energetics and dynamics of coronal heating, solar flares, coronal mass ejections, and filament eruptions. They also determine space-weather processes. Therefore, one of the central problems of solar physics is to measure the magnetic fields in the solar corona. However, currently available routine extrapolation methods do not provide direct ways for characterizing global magnetic fields in the solar corona.

The main techniques that are currently used to deduce the global magnetic structure of the solar corona include potential-field source-surface (PFSS) models, nonlinear force-free field (NLFFF) models, and multidimensional magnetohydrodynamic (MHD) models of the global solar corona. These methods are based on boundary conditions of the solar photospheric magnetic field that are derived directly from photospheric magnetograms. The PFSS model is a relatively simple model, which is routinely used to extrapolate the photospheric magnetic field into the global solar corona (Altschuler and Newkirk, 1969; Schatten, Wilcox, and Ness, 1969; Wang and Sheeley, 1992; Luhmann *et al.*, 2002; Schrijver and DeRosa, 2003). It assumes that the magnetic field is current-free between the photosphere (the inner boundary) and the source surface (outer boundary). Its inner boundary is based on synoptic maps of photospheric magnetograms. The outer boundary represents a spherical source surface with constant radius, typically ranging from 1.5 to 3.5 $R_{\odot}$ (Lee *et al.*, 2011). Since the potential magnetic field is the field with the lowest energy for a given photospheric radial boundary condition (Sakurai, 1989), it cannot account for dynamical processes such as eruptions, flares, and magnetic reconnection, during which magnetic energy is converted into plasma kinetic energy, without significantly changing the magnetic boundary flux. Indeed, soft X-ray observations of active regions often show a nonpotential structure of the magnetic field (Jiao, McClymont, and Mikic, 1997).

The NLFFF model is a more advanced step in extrapolating the surface magnetic field into the corona. It is suitable for use with recently available data from the *Helioseismic and Magnetic Imager* (HMI) onboard the *Solar Dynamic Observatory* (SDO) and *Vector SpectroMagnetograph* (VSM) at the National Solar Observatory (NSO). Unlike the PFSS model, it assumes that the current is parallel to the magnetic field. This approach uses the photospheric vector magnetograms, such as those from the HMI and VSM instruments to extrapolate the surface data into the solar corona (Wiegelmann *et al.*, 2005; Wiegelmann, 2008; Tadesse *et al.*, 2014), and therefore provides a better description of the coronal magnetic field. However, the NLFFF method is not suitable for determining the magnetic field if the force-free assumption is not satisfied everywhere in the volume of the extrapolation (Demoulin, Cuperman, and Semel, 1992; Gary, 2001). In addition, this model does not provide information about the plasma density or temperature of coronal structures, and therefore cannot be used to predict emission measure, so the results cannot be compared with extreme ultraviolet (EUV) observations.

Complementary to the PFSS and NLFFF extrapolation methods, a number of self-consistent magnetohydrodynamic (MHD) models of the solar corona have been developed (Mikić *et al.*, 1999, 2007; Riley, Linker, and Mikić, 2001; Lionello, Linker, and Mikić, 2009;

Airapetian *et al.*, 2011; Tóth *et al.*, 2012; van der Holst *et al.*, 2014). Unlike the PFSS or NLFFF techniques, this approach includes a self-consistent time-dependent treatment of the plasma pressure, gravitational and magnetic forces that are required to describe the dynamics of helmet streamers, coronal mass ejections, and the solar wind. However, the application of these models is limited by approximations used for describing the coronal heating, and the uncertainties in the boundary conditions that are deduced from synoptic data. Therefore, these complex models need to be validated by direct observations of the coronal magnetic field.

All of these methods are essentially extrapolation methods based on inner boundary conditions taken at the photosphere. However, the magnetic field at the photosphere and the lower chromosphere is far from potential or force-free, because of the dominance of the plasma pressure there. It has been suggested that chromospheric magnetograms are better suited as boundary conditions for extrapolation methods (Judge, 2010). Sophisticated multi-dimensional MHD–RHD (radiation hydrodynamics) models of the solar chromosphere are currently under development.

Direct measurements of the coronal magnetic field are among the most challenging problems in observational solar astronomy. Significant progress has recently been achieved here with the deployment of the *Coronal Multichannel Polarimeter* (CoMP) of the High Altitude Observatory (HAO). The instrument provides polarization measurements of the Fe XIII 10 747 Å forbidden-line emission (Tomczyk *et al.*, 2007; Tomczyk and McIntosh, 2009). The observed polarization depends on the magnetic field through the coronal Hanle and Zeeman effects (Charvin, 1965; Sahal-Brechot, 1977; House, 1977; Casini and Judge, 1999; Lin and Casini, 2000). To use this type of data, the vector-tomography method has been developed for 3D reconstruction of the coronal magnetic field (Kramar, Inhester, and Solanki, 2006; Kramar *et al.*, 2013). However, because of the small field of view (FOV) of the CoMP instrument, it is problematic to reliably reconstruct the coronal magnetic field above $\approx 1.2\ R_\odot$ based on these CoMP observations (Kramar *et al.*, 2013). In this respect, the *Solar Terrestrial Relations Observatory* (STEREO) COR1 coronal observations provide a unique opportunity to characterize global coronal conditions at heights greater than $\approx 1.4\ R_\odot$.

In this article, we study the 3D structure of coronal streamers to determine the height at which the coronal magnetic field becomes radial. Specifically, we use data from the STEREO/COR1 coronagraph for half a solar rotation period during CR 2066 to reconstruct the 3D coronal electron density with the tomography method. Our results are complemented by the 3D emissivity obtained by tomography for the STEREO/*Extreme Ultraviolet Imager* (EUVI) data in the 195 Å band. We tested the tomography method for systematic errors with simulated pB-data produced by integrating the results of a 3D thermodynamic MHD model over the line of sight (LOS). Finally, we compare the reconstructed 3D coronal structures with the PFSS model.

2. Tomography

For wavelengths for which the corona is optically thin, the radiation coming from the corona is a LOS integral of the emissivity in the observed direction. Therefore, it is impossible to reconstruct the spatial distribution of the emissivity from a single (in a geometric sense) measurement or projection. The solution space is reduced if we have measurements from many different viewpoints. The reconstruction based on the observations of an object from different view angles is essential for tomography. The possibility of reconstructing a function from its projections was first studied by Radon (1917). Several decades later, this purely

mathematical research formed the basis for the tomography method, which was developed to reconstruct the X-ray absorption coefficient in human bodies. The first experimental X-ray tomographic scanner was made by Hounsfield (1972), and Cormack (1963, 1964) independently discovered some of the algorithms for the reconstruction. These two authors received the Nobel prize for their investigations in 1979. Today, tomography is used in many fields: medicine, material structure testing, geophysics, astrophysics (Boffin, Steeghs, and Cuypers, 2001). In solar coronal physics, the use of tomography was first proposed by Wilson (1976) and later by Davila (1994). In astrophysical applications the input data can suffer from noise and data incompleteness. However, the regularization method allows solar coronal tomography to produce more reliable reconstructions (Tikhonov, 1963; Frazin and Janzen, 2002; Kramar, Inhester, and Solanki, 2006; Kramar *et al.*, 2009) (see also Section 4 of this article).

2.1. Tomography Based on White-Light STEREO/COR1 Data

To reconstruct extended coronal structures, the reconstruction algorithm requires observations from more than two directions. This is the key requirement of tomography. Tomography applications for coronal studies typically assume a rigid rotation of the coronal density structures. The algorithm requires coronagraph data for half a solar rotation as input if observed from a single spacecraft, and, generally, coronal structures that are stable over their observation periods can reliably be reconstructed (Davila, 1994; Zidowitz, 1999; Frazin and Kamalabadi, 2005; Kramar *et al.*, 2009). However, depending on the positions of a coronal structure relative to the spacecraft during the observation period, the stationarity assumption for that structure can be reduced to about a week (Kramar *et al.*, 2011).

For our density reconstructions we used the polarized brightness (pB) intensity images from the COR1 instrument onboard the STEREO-B spacecraft taken 28 images per half a solar rotation as input for the tomographic inversion. We limited here the data input for the tomography based on COR1 data to the STEREO-B spacecraft because COR1-B had lower levels of stray light during CR 2066 than COR1-A.

In the STEREO/COR1-B field of view (below $\approx 4\,\mathrm{R}_\odot$), the white-light pB coronal emission is dominated by scattering sunlight on the free electron in the corona (Blackwell and Petford, 1966a,b; Moran *et al.*, 2006; Frazin *et al.*, 2007). The intensity of the pB-signal as a fraction of the mean solar brightness is given as

$$I_{\mathrm{pB}}(\hat{\boldsymbol{e}}_{\mathrm{LOS}}, \boldsymbol{\rho}) = \int_{\mathrm{LOS}} K(\boldsymbol{r}) N_{\mathrm{e}}(\boldsymbol{r})\, \mathrm{d}\ell, \tag{1}$$

where N_{e} is the electron density, $\boldsymbol{\rho}$ is a vector in the plane-of-sky (POS) from the Sun center to the LOS and perpendicular to LOS, ℓ is length along the LOS, and $\hat{\boldsymbol{e}}_{\mathrm{LOS}}$ is the unit vector along the LOS. The kernel function $[K]$ is defined by the Thompson-scattering effect (van de Hulst, 1950; Billings, 1966; Quémerais and Lamy, 2002):

$$K = \frac{\pi\sigma}{2(1-\frac{u}{3})}\left[(1-u)A(r) + uB(r)\right]\frac{\rho^2}{r^2}, \tag{2}$$

where the expressions for $A(r)$ and $B(r)$ are the same as those given by Quémerais and Lamy (2002), $\sigma = 7.95 \times 10^{-26}$ cm^2 is the Thompson-scattering cross-section for a single electron, $\mathrm{R}_\odot$ is the solar radius, and the linear limb-darkening coefficient $[u]$ is set to 0.6 in the present calculations.

Because COR1 views the corona close to the limb, the instrument has a significant amount of scattered light, which must be subtracted from the image prior to be applied in the reconstruction method. Proper removal of instrumental scattered light is essential

for coronal reconstruction. One way is to subtract a monthly minimum (MM) background. The monthly minimum approximates the instrumental scatter by finding the lowest value of each pixel in all images during a period of about one month. However, this method tends to overestimate the scattered light in the streamer belt (equatorial region). The lowest value of these pixels during a month will contain both the scattered light and the steady-intensity value from the corona. Hence, if we were to use such pixels as input for our electron-density reconstruction, we would obtain an electron density that is lower than the actual density.

Another way to account for the scattered light is to subtract a roll-minimum (RM) background. The roll-minimum background is the lowest value of each pixel obtained during a roll maneuver of the spacecraft (instrument) around its optical axis. Because the coronal polar regions are much darker than the equatorial ones, the lowest pixel values in the equatorial region during the roll maneuver are nearer to the value of the scattered-light intensity than the MM.

The sensitivity of the COR1-B instrument decreases at a rate of about 0.25 % per month (Thompson and Reginald, 2008). Moreover, variations in the spacecraft's distance from the Sun cause changes of the amount of scattered light in the coronagraph images. But the roll maneuvers occur rather rarely. Therefore it is impossible to use an RM background obtained in one month for data from another month when the highest possible photometric accuracy is needed. One way to obtain a background image for the period between the roll maneuvers is to interpolate RM backgrounds over time in such a way that this temporal dependence follows the temporal dependence of the MM backgrounds, because the MM background images are available for every month. This approach is realized by W. Thompson in the SolarSoft IDL routine secchi_prep with the keyword parameter calroll. We used backgrounds obtained in this way. The photometric calibration is based on Jupiter's passage through the COR1 FOV (Thompson and Reginald, 2008).

After subtracting the scattered light, a median filter with a width of three pixels was applied to reduce anomalously bright pixels caused by cosmic rays. Then, every third image pixel was taken (resulting in a 340×340 pixel image) to reduce the computer memory size. The reconstruction domain is a spherical grid with a size of $50 \times 180 \times 360$ covering heliocentric distances from 1.5 to 4 $R_\odot$, Carrington latitudes from -90 to 90°, and Carrington longitudes from 0 to 360°, respectively.

The inversion was performed for the function

$$F = |\mathbf{A} \cdot \mathbf{X} - \mathbf{Y}|^2 + \mu |\mathbf{R} \cdot \mathbf{X}|^2. \tag{3}$$

Here, the elements x_j of the column matrix $\mathbf{X}$ contain the values of electron density $[N_e]$ in the grid cells with index $j = 1, \ldots, n$, and y_i is the data value for the i-th ray, where index $i = 1, \ldots, m$ accounts for both the viewing direction and pixel position in the image. The element a_{ij} of the matrix $\mathbf{A}$ represents the intersection of volume element j with the LOS related to pixel i, multiplied by the kernel function that is defined by the Thompson-scattering effect for the pB-intensity signal (see Equation (1)). The second term on the right-hand side of Equation (3) is the regularization term that minimizes the effects of noise and data gaps (Tikhonov, 1963). The matrix $\mathbf{R}$ is a diagonal-like matrix such that the regularization is the first-order smoothing term, *i.e.* operation $|\mathbf{R} \cdot \mathbf{X}|^2$ produces the square difference in value between two neighboring grid cells, summed over all cells. The regularization parameter $[\mu]$ regulates balance between the smoothness of the solution on one hand and the noise and reconstruction artifacts on the other. The result of the inversion depends on a number of factors, including the number of iterations and the value of μ. The value of μ was chosen using the cross-validation method (Frazin and Janzen, 2002). We iterated until the first term in Equation (3) became slightly lower than the data noise level, which is essentially the Poisson noise in the data.

The coronal electron density drops very rapidly with distance from the Sun, introducing a wide dynamic range in the data, which causes linear artifacts in the reconstruction. To increase the contribution of signals from those LOS that pass through the low-density regions and to reduce the artifacts in the numerical reconstruction at larger distances from the Sun, we applied a set of weighting coefficients (or preconditioning)

$$w_i = \frac{1}{(y_i^{(\mathrm{FT1})})^2} \tag{4}$$

for the first term in Equation (3) in such way that $\sum_j (w_i a_{i,j} x_j) = w_i y_i$. Here, $y_i^{(\mathrm{FT1})}$ is the inverse Fourier transform of the function $y_i(r_p, \phi_p)$ on ϕ_p with harmonics taken up to first order, where $y_i(r_p, \phi_p)$ is the data value at the position (r_p, ϕ_p) in the polar coordinate system for some particular image. The value of r_p was fixed for a given pixel and set equal to the radial distance from the center of the Sun's disk to the pixel. A more detailed description of the used tomography method is given in Kramar *et al.* (2009). We describe the error estimation of the tomographic method in Section 4. The reconstruction results are discussed in Section 5.

2.2. Tomography for Emissivity from STEREO/EUVI Data

The STEREO/EUVI instrument observes the corona up to about 1.7 $\mathrm{R}_\odot$ in four spectral channels (171, 195, 284, and 304 Å) that span the 0.1 to 20 MK temperature range (Wuelser *et al.*, 2004; Howard *et al.*, 2008). The measured coronal emission in the 171, 195, and 284 Å channels can be represented as the result of emission integrated over the LOS as

$$I(\hat{\boldsymbol{e}}_{\mathrm{LOS}}, \boldsymbol{\rho}) = k \int_{\mathrm{LOS}} \varepsilon(\boldsymbol{r})\, \mathrm{d}\ell, \tag{5}$$

where $\varepsilon(\boldsymbol{r})$ is the emissivity at the position $\boldsymbol{r}$ in the selected channel, *i.e.* light intensity (in photons per second for example) emitted per unit volume, per unit solid angle. The coefficient k accounts for pixel size, aperture, and distance to the Sun.

As input, we used EUVI 195 Å images calibrated by applying IDL SolarSoft routines. to reduce anomalously bright pixels caused by cosmic rays, the IDL SolarSoft routine despike_gen was applied. Three images taken with about two hours' difference were averaged into one. Three averaged images per day were taken during a period of half a solar rotation. Then, every fourth pixel was taken, resulting in 512×512 input image.

We inverted $\varepsilon(\boldsymbol{r})$ in the same manner as for the electron density in the white-light tomography with K and N_e in Equation (1) substituted by k and ε, respectively, according to Equation (5). The inversion result is the 3D emissivity distribution for the EUVI 195 Å channel in the coronal range from 1.05 to 1.5 $\mathrm{R}_\odot$. Figure 7 shows a spherical cross-section of the reconstructed EUVI 195 Å emissivity at a heliocentric distance of 1.1 $\mathrm{R}_\odot$ for CR 2066. The reconstruction result is discussed in Section 5.

3. Implicit Reconstruction of Some Coronal Magnetic Field Structures

3.1. Relationship Between the Coronal Electron Density and Coronal Magnetic Field Structures

To establish the relationship between the coronal electron density and the corresponding magnetic-field structures, we used the results from 3D MHD simulations based on synoptic

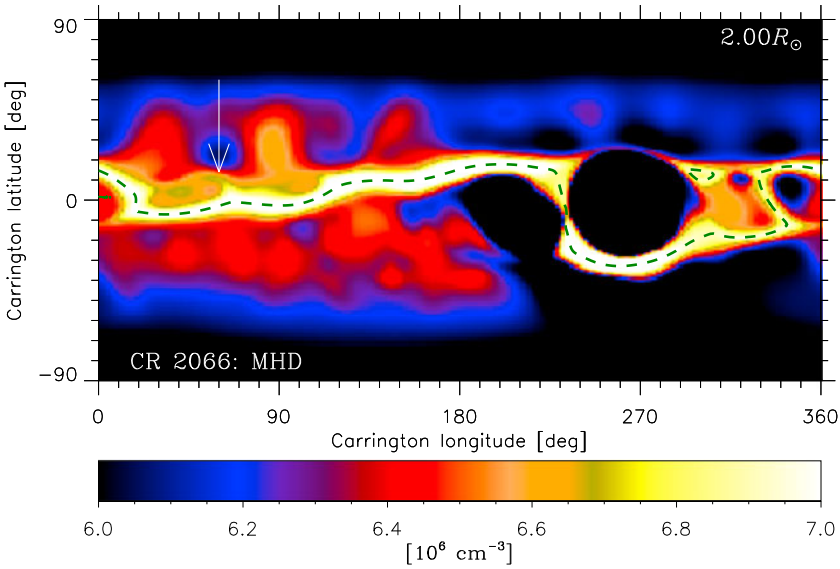

Figure 1 MHD simulation for CR 2066. Spherical cross-section of the electron density at heliocentric distance of 2 $R_\odot$. The dashed line marks the position of the magnetic neutral line.

magnetograms for the specified time period. We first investigate the results from a simpler polytropic MHD model (Riley, Linker, and Mikić, 2001) for CR 2066. In this model, the energy equation is simplified by assuming a polytropic equation of state, with a reduced polytropic index $\gamma = 1.05$, in the spirit of the original model for the solar wind of Parker (1963). The description of the energy transport in the solar corona provided by the simplified polytropic model is less accurate than the full thermodynamic model (see below). However, because the polytropic model is computationally more efficient, its solutions can be obtained more routinely. It is known that the polytropic model does not estimate the coronal plasma density and temperature accurately, a result that we confirm and discuss below in more detail. The group at Predictive Science, Inc., has produced a set of polytropic MHD solutions for all of the Carrington rotations in the STEREO era, which are available online at www.predsci.com/stereo/. We selected the specific solution for CR 2066, which was based on the SOHO/MDI synoptic magnetic-field data measured during the period 15 January – 21 February 2008. The radial component of the magnetic field inferred from the MDI data is used as a boundary condition for the model at the lower radial boundary.

Figures 1 and 2 represent result of the polytropic MHD model for CR 2066. Figure 1 shows the spherical cross-section of the electron density at a heliocentric distance of 2 $R_\odot$. The dashed line marks the magnetic neutral line (where $B_r = 0$). The density distribution is characterized by two main structures: the most dense central structure associated with the magnetic neutral line–streamer belt, and smaller less dense structures connecting neighboring peaks in latitude direction of the streamer belt. The latter, called pseudo-streamers, do not coincide with the magnetic neutral line. One of the pseudo-streamers located at Carrington longitude 60° is marked by a white arrow in the figure.

Figure 2 shows meridional cross-sections of the electron density for $\phi = 60°$. In this meridional cross-section, the image for density values was processed through a radial filter and re-scaled with a scaling factor depending on the height to magnify low-density structures. This makes it impossible to show the color-bar scale for the density in this figure.

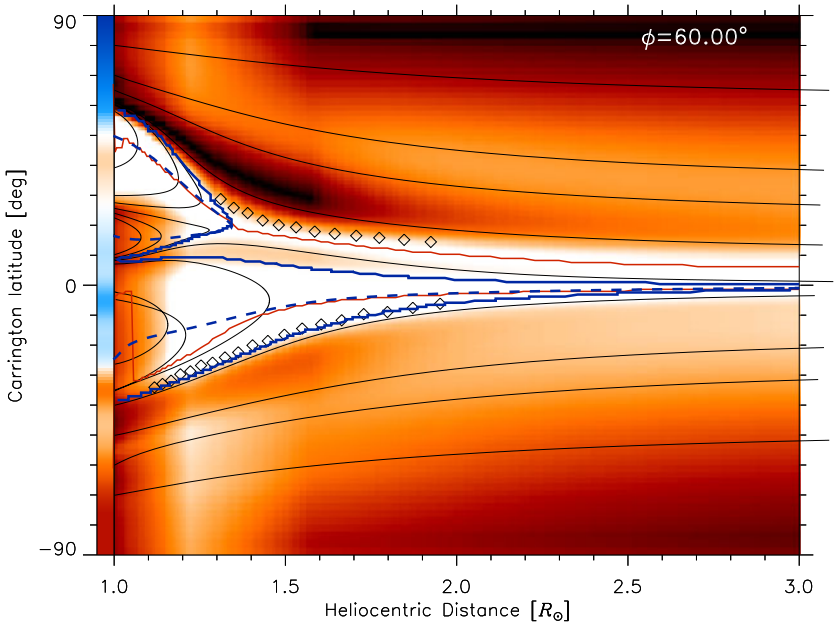

Figure 2 MHD simulation for CR 2066. Meridional cross-section of the radially filtered and re-scaled electron density at Carrington longitude 60°. Blue dashed lines mark the position of the magnetic neutral line. Solid blue lines show the boundary position between closed and open magnetic-field structures. Black diamonds mark the positions of the highest electron-density gradient. Black lines are magnetic-field lines. Red solid lines show the positions of the highest density. The color bar on the latitude axis shows the value of the radial component of the magnetic field [B_r] at the photospheric level, which was used as a lower boundary condition in the simulations.

For the streamer region, the highest densities represent either the position of the magnetic neutral line (and the current sheet) or magnetic-field lines originating from regions with higher electron density following the loop structures. For the pseudo-streamer region in the closed-field region, the behavior of the highest-density positions is similar to those for the streamer region. For the pseudo-streamer region in the open-field region, the highest-density position follows the behavior of the magnetic-field line. Black diamonds in Figure 2 mark the positions of the highest-density gradient at fixed heliocentric distances. These positions follow the behavior of the magnetic-field lines, and for the streamer region they coincide with the boundary position between the closed and open magnetic-field structure. From this we can deduce a general qualitative picture of the coronal magnetic-field structures directly from the reconstructed 3D electron density structure.

3.2. Retrieving Coronal Magnetic Field Structures from the EUVI 195 Å Emissivity

In this subsection we examine the relationship between the location of closed magnetic-field regions and the 3D structure of the EUVI 195 Å emissivity.

As mentioned in Section 3.1, the polytropic MHD model for CR 2066 predicts a much lower range of density values at a fixed heliocentric distance than is observed in reality. This is principally due to the overly simplified polytropic energy equation. This is a recognized shortcoming of the polytropic MHD model that has been addressed in recent improvements

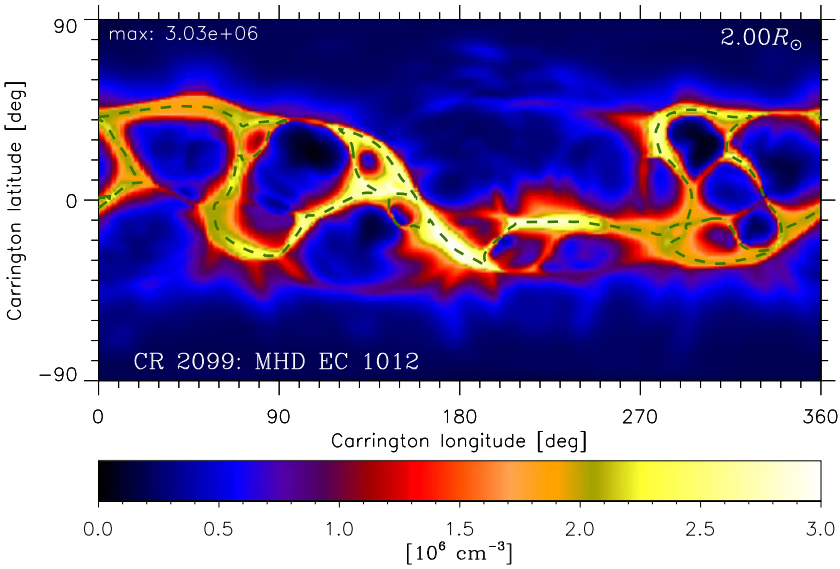

Figure 3 The electron density at heliocentric distance of 2 $R_\odot$ from a MHD simulation for the solar eclipse of 11 July 2010. Dashed lines denote the magnetic neutral line.

to the model. The newer thermodynamic MHD model uses an improved equation for energy transport in the corona that includes parallel thermal conduction along the magnetic-field lines, radiative losses, and parameterized coronal heating (Lionello, Linker, and Mikić, 2009). This thermodynamic MHD model produces more accurate estimates of plasma density and temperature in the corona. A detailed description is given by Mikić *et al.* (2007) and Lionello, Linker, and Mikić (2009). Its application to the total solar eclipse of 1 August 2008 was described by Rušin *et al.* (2010).

The thermodynamic simulation used SOHO/MDI magnetic-field data measured from 10 June – 4 July 2010 (a combination of CR 2097 and 2098), and an extension of the coronal-heating model described by Lionello, Linker, and Mikić (2009). The results of this simulation were used to predict the structure of the corona for the solar eclipse of 11 July 2010 www.predsci.com/corona/jul10eclipse/jul10eclipse.html. This model was also used to produce the artificial data for testing the tomography method for uncertainties, as described in Section 4. Figure 3 shows a spherical cross-section of the electron density at a heliocentric distance of 2 $R_\odot$.

Figure 4 shows meridional cross-sections of the EUVI 195 Å emissivity at the longitudes of 60 and 290° for the MHD result of the solar eclipse of 11 July 2010. Green dashed lines mark the magnetic neutral line. Solid green lines show the boundary positions between closed and open magnetic-field structures. Crosses mark the highest emissivity gradients in latitudinal direction. In most cases, the highest emissivity gradients coincide with the boundaries between closed and open magnetic-field regions. But sometimes these positions are shifted toward regions with higher emissivity, which is indicative of closed magnetic-field regions. If we assume that the boundary between open- and closed-field structures is related to the highest density gradient, as shown in Section 3.1, Figures 2 and 5, then this shift can be explained as a result of the dependence of the emissivity on the square of the electron density, *i.e.* ε varies as $G(T, N_e)N_e^2$, where N_e is electron density, T is the electron

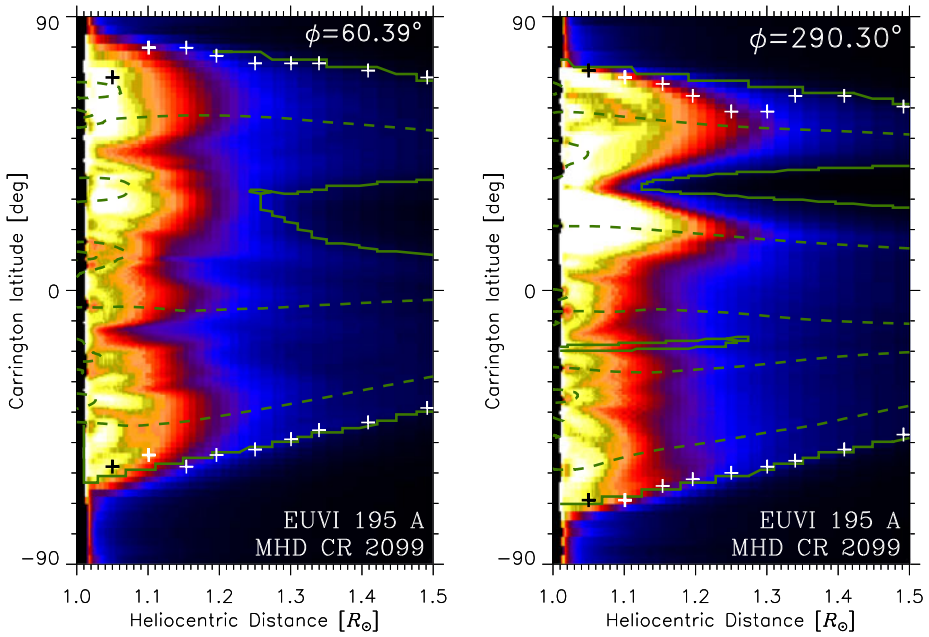

Figure 4 MHD simulation for the solar eclipse of 11 July 2010. Meridional cross-section of the EUVI 195 Å emissivity at Carrington longitudes 60° (left) and 290° (right). Green dashed lines plot the magnetic neutral line. Solid green lines show the boundary positions between closed and open magnetic-field structures. Crosses mark the highest-emissivity gradient in the latitudinal direction in the thermodynamic MHD model. The color bar on the latitude axis shows the radial component of the magnetic field [B_r] at the photospheric level that was used as lower boundary condition in the simulations.

temperature, and $G(T, N_e)$ is the line contribution function. Thus, this dependence might cause a shift of the highest gradient toward a region with higher density values.

4. Estimation of Uncertainties in the Tomography

As described in Section 2, the 3D coronal density was obtained by the regularized tomographic inversion, where we used the smoothing operation as a regularization. This method can introduce a small systematic error in the reconstructed density values which, in turn, generates the errors in the highest density gradients. Therefore, to estimate this systematic error, we used the 3D MHD model to create artificial pB-data for the tomographic inversion with the same temporal (or angular) and spatial sampling as in real data (28 images during half of a solar rotation, where each 340 × 340 image covers the FOV with radius of 4 $R_\odot$).

We used the thermodynamic MHD model described in Section 3.2 to produce the artificial pB-data and test the tomography method for errors. Figure 5 shows meridional cross-sections of the electron density at longitudes of 60 and 290° for the MHD result of the 2010 solar eclipse. Green dashed lines mark the magnetic neutral line. Solid green lines show the boundaries between closed and open magnetic-field structures. White crosses and diamonds highlight the highest density gradients at fixed heliocentric distances for the MHD model and tomography results, respectively. The error in determining the highest density gradient does not exceed 10° and the reconstructed positions tend to be less curved at heliocentric

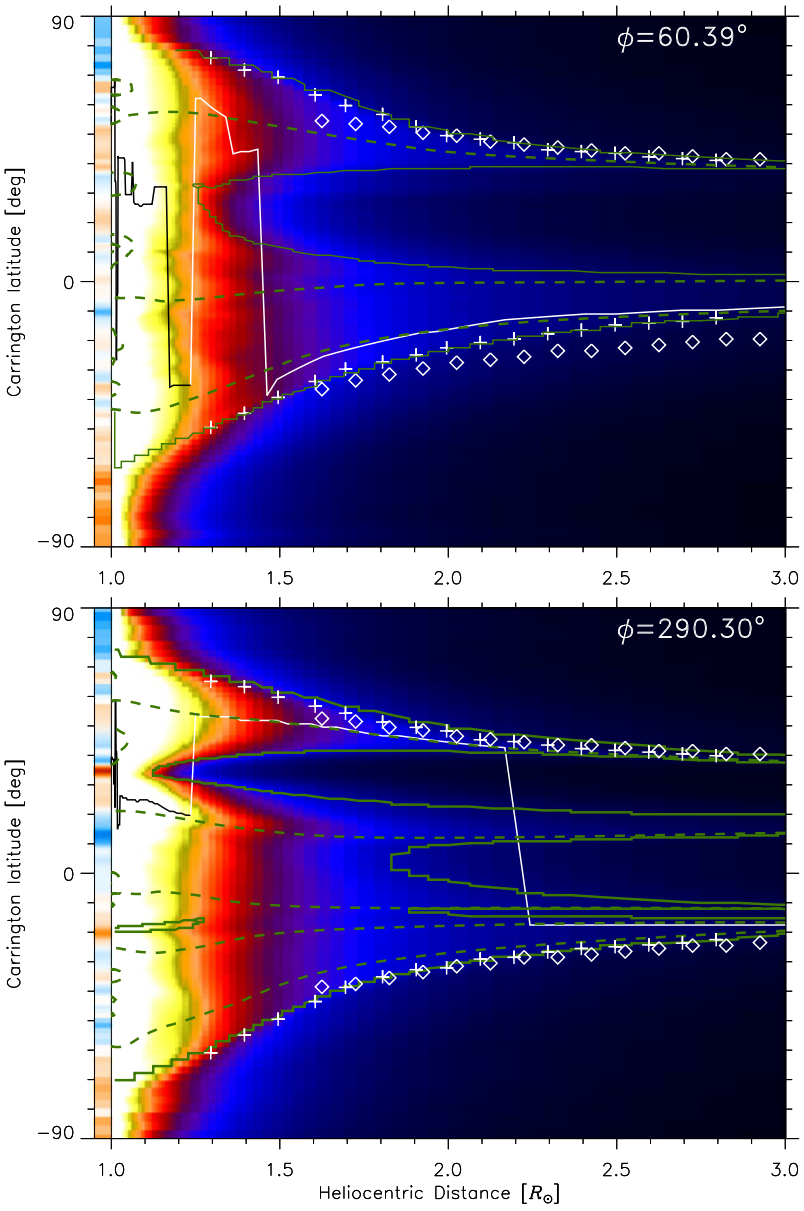

Figure 5 MHD simulation for the 11 July 2010 solar eclipse. Meridional cross-section of the electron density at Carrington longitudes 60° (top panel) and 290° (bottom panel). Green dashed lines denote the magnetic neutral line. Solid green lines show the boundaries between closed and open magnetic-field structures. Crosses and diamonds highlight the highest electron-density gradient for the results of the thermodynamic MHD model and the test tomographic reconstruction based on simulated COR-1 data, respectively.

distances near the lower limit of the reconstruction domain (1.5 $R_\odot$). This demonstrates that the highest density gradient obtained by the tomography can be used to determine the boundaries between closed and open magnetic-field structures.

5. 3D Coronal Structure During CR 2066

CR 2066 represents the deep minimum of the solar-activity cycle. Therefore, the 3D corona during CR 2066 is ideally suited for studying with the tomography method because the reconstruction errors are minimized owing to low coronal activity. We performed two types of tomographic reconstructions: a 3D reconstruction for the electron density based on STEREO/COR1 data, and a 3D reconstruction for the EUVI 195 Å emissivity [photons s^{-1} sr^{-1} cm^{-3}] based on STEREO/EUVI data. To demonstrate the general structure of the coronal streamer belt for CR 2066, Figure 6 shows a spherical cross-section of the electron density at a heliocentric distance of 2 $R_\odot$, and Figure 7 shows the spherical cross-section of the EUVI 195 Å emissivity at a heliocentric distance of 1.1 $R_\odot$.

Figure 8 shows several meridional cross-sections of the electron density (range from 1.5 to 4 $R_\odot$) and EUVI 195 emissivity (range from 1.05 to 1.29 $R_\odot$). A figure with a set of all cross-sections is available in the electronic supplemental material. The superimposed black–white lines plotted on the cross-sections show the highest density. Therefore, the lines represent either the magnetic neutral line (and the current sheet), or magnetic-field lines originating from regions with higher electron density (see Section 4 for justification). In most of the cross-sections, the superimposed lines become asymptotically radial at about 3 $R_\odot$.

Black crosses in Figure 8 show the highest density gradient at several heliocentric distances. Sometimes they are scattered over a wide range in latitude because of the reconstruction errors, which are most probably caused by coronal dynamics and/or noises in input data, but in most cases (for example at longitudes of 10, 50, 60, 90, 100, 160, 190, 350°), they smoothly follow and specify either the magnetic-field lines or the boundary between closed and open magnetic-field structures. At a heliocentric distance of 1.1 $R_\odot$, the black crosses mark the highest EUVI 195 emissivity gradient. The highest density gradients for tomographic reconstruction based on COR1 data are consistent with the highest emissivity gradient for tomographic reconstruction of EUVI 195 Å emissivity. Therefore, the locations of the black crosses suggest that the coronal magnetic field near the streamer belt becomes radial at about 2.5 $R_\odot$ and higher.

The green dashed contour lines in Figure 8 show the boundaries between open and closed magnetic-field structures in the polytropic MHD model. Although the boundaries between open and closed magnetic-field structures in the polytropic MHD model do not fully coincide with those derived by the tomography, the magnetic-field lines in the MHD model near the current-sheet positions become asymptotically radial at $\approx$2.5 $R_\odot$. Moreover, the MHD model provides guidance about how to distinguish which coronal structures in the tomographic 3D reconstructions are correlated to streamers, as opposed to pseudo-streamers: the "legs" of the boundary lines are rooted at the photospheric level in magnetic fields of opposite polarity in the case of streamers, and in fields of the same polarity in the case of pseudo-streamers. Since the latest thermodynamic MHD model produces more accurate estimates of the coronal plasma density and temperature, a more detailed comparison between coronal densities estimated from MHD models and observations will be performed in future work.

The black contour lines in Figure 8 show boundaries between open and closed magnetic-field structures in three PFSS models with source surface heliocentric distances [R_{SS}] at 1.5,

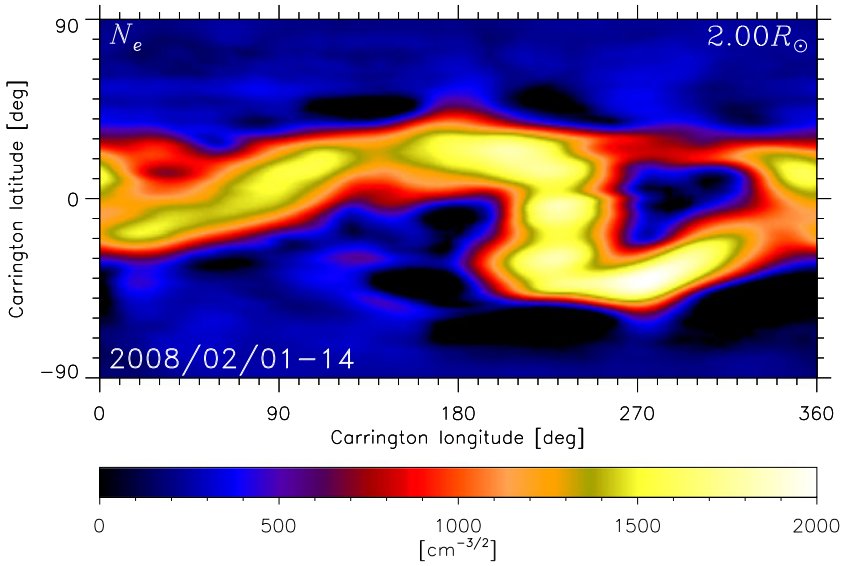

Figure 6 Spherical cross-section of the reconstructed electron density on square-root scale at a heliocentric distance of 2 $R_\odot$. The reconstruction is obtained by tomography based on COR-1 data obtained during 1–14 February 2008 (CR 2066).

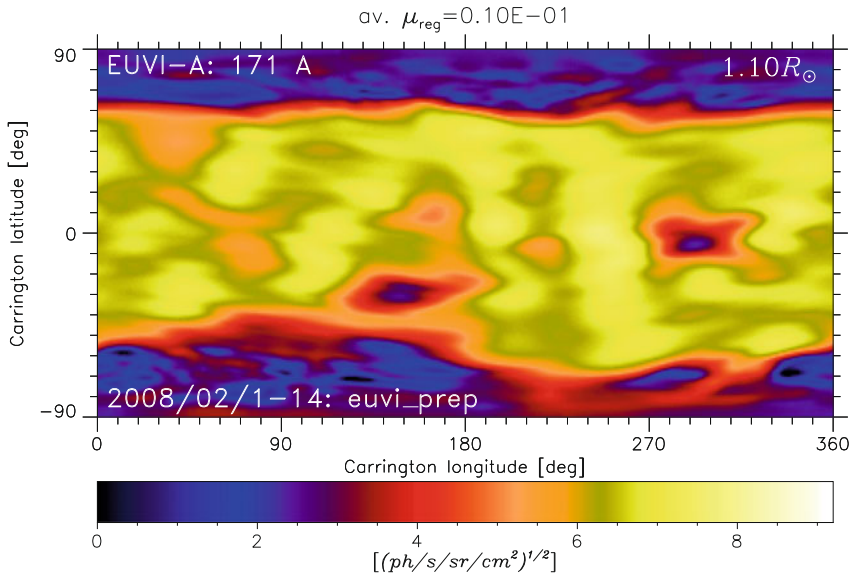

Figure 7 Spherical cross-section of the reconstructed 3D EUVI 195 Å emissivity on square-root scale at a heliocentric distance of 1.1 $R_\odot$. The reconstruction is obtained by tomography based on EUVI data obtained during 1 – 14 February 2008 (CR 2066).

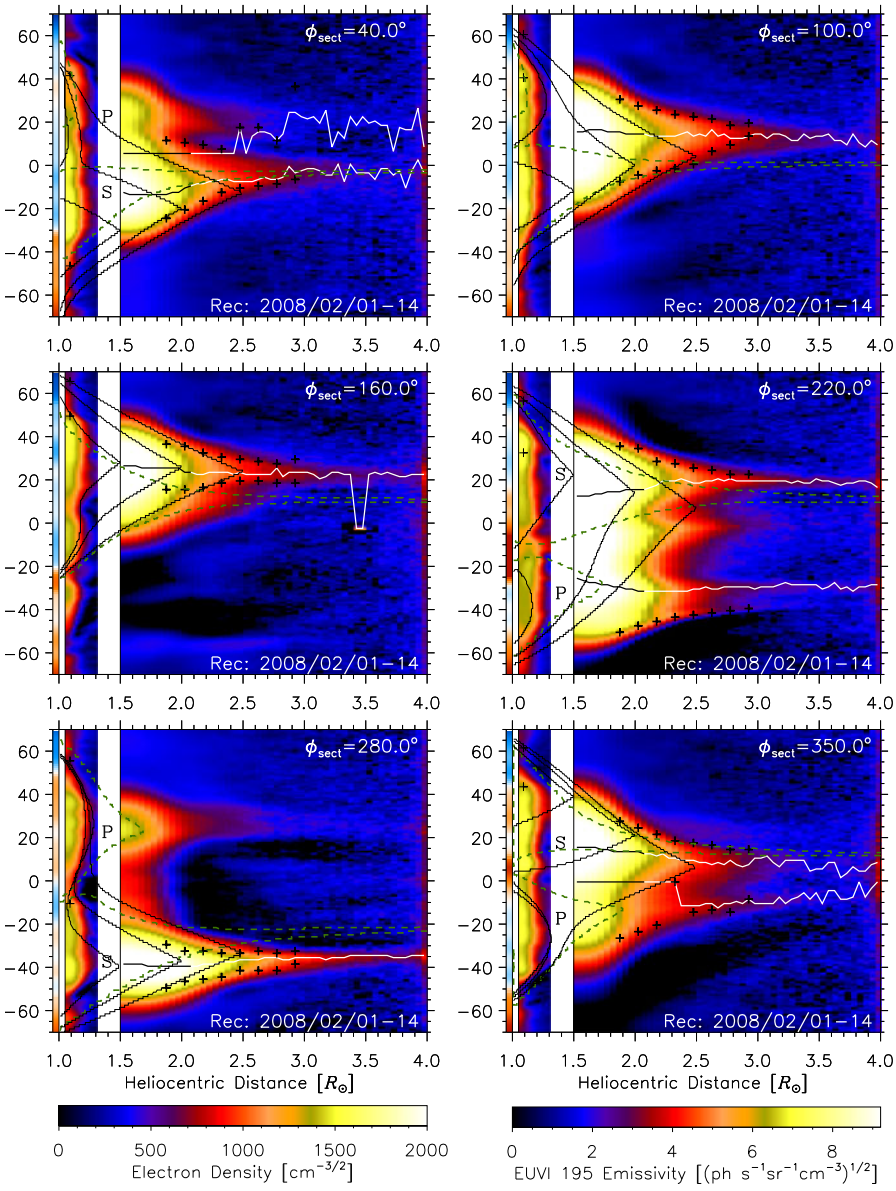

Figure 8 Reconstructions for CR 2066 based on COR1 data (electron density in the range from 1.5 to 4 $R_\odot$) and EUVI 195 Å data (emissivity in the range from 1.05 to 1.29 $R_\odot$). Cross-sections for Carrington longitudes of 40, 100, 160, 220, 280, and 350° are shown from left to right and upper to lower panels, respectively. The figure with a set of all cross-sections is available in the electronic supplementary material. Black and white lines mark the highest density. The contour black lines show the boundaries between open and closed magnetic-field structures for the PFSS models with the source surface located at 1.5, 2.0, and 2.5 $R_\odot$. The dashed green lines show the boundaries between open and closed magnetic-field structures for the polytropic MHD model. Crosses mark the highest density gradient at several heliocentric distances. The color bar on the left side of the latitude axis is the corresponding meridional cross-section for the radial component of the photospheric magnetic field used as a boundary condition for the MHD simulation. S and P mark streamers and pseudo-streamers, respectively.

2.0, and 2.5 $R_\odot$. The PFSS model with $R_{SS} = 2.5\ R_\odot$ does not coincide with the derived positions of the streamer and pseudo-streamer, nor with the coronal-hole positions indicated by the STEREO/EUVI 195 Å emissivity 3D reconstruction. The PFSS model with $R_{SS} = 1.5\ R_\odot$ appears to fit the latter two structures better, but does not satisfy the requirement for the field to become radial at about 2.5 $R_\odot$. Thus, the assumption of the potential nature of the coronal magnetic field is not satisfied even during the deep solar minimum.

6. Conclusion and Outlook

We applied STEREO-B/COR1 data for CR 2066 to derive the 3D coronal electron density during the deep solar minimum in February 2008 using the tomography method. We then complemented the density reconstruction with the results of 3D MHD simulations and 3D EUVI 195 Å emissivity to determine the relationship between the density, emissivity, and magnetic-field structures. Specifically, we found that

- the locations of density maximum in the 3D reconstructions can serve as an indicator for current-sheet and pseudo-streamer positions;
- the locations the highest density gradient in the 3D reconstructions can serve as an indicator for boundaries between closed and open magnetic-field structures.

Thus, we showed that 3D coronal electron-density reconstruction, especially when used in conjunction with 3D EUVI 195 Å emissivity reconstruction, and with the guidance provided by state-of-the-art 3D MHD simulations, can be instrumental in retrieving the geometry of the global solar coronal magnetic field. Specifically, this method can derive the locations of boundaries between open and closed magnetic-field structures, and distances where the magnetic-field lines become radially directed. The nearly realistic 3D coronal electron density and 3D EUVI 195 Å emissivity are both obtained by the tomography method. To estimate the error in determining these positions by the tomography, we tested the tomographic method with simulated pB-data produced by LOS-integrating the result of the thermodynamic MHD model. As a result of this test, we found that tomography can reliably determine these positions.

We then reconstructed the 3D coronal electron density and EUVI 195 Å emissivity based on real STEREO/COR1 and STEREO/EUVI observations, respectively, for CR 2066, which corresponds to deep solar minimum. The reconstructed radial dependence of the latitude positions of the highest density and emissivity and its gradient suggests that the magnetic-field lines become radial at about 2.5 $R_\odot$ and higher for most of the longitudinal positions. Moreover, we determined the boundaries between regions with open and closed magnetic-field structures. Because the 3D reconstructions are entirely based on *coronal* observations, the results can serve as a test and/or as an additional constraint for coronal models. As an initial step toward this goal, we analyzed the consistency of the PFSS model for different source surface distances with the reconstructed 3D electron density and EUVI 195 emissivity structures. We conclude that the assumption of the potential nature of the coronal global magnetic field is not satisfied even during the deep solar minimum. Would a linear force-free or NLFFF approximation offer a better description of the solar coronal magnetic field? How complex do the coronal structures appear during a solar maximum? These are topics of a study to be performed in the near future.

Acknowledgements The work of MK has been supported by the NASA Cooperative Agreement NNG11PL10A 670.008 to the Catholic University of America and NSF National Space Weather Program grant AGS0819971. VA acknowledges support from NASA grant SCEX22013D. The authors thank the anonymous referee for the insightful review of the manuscript.

References

Airapetian, V., Ofman, L., Sittler, E.C., Kramar, M.: 2011, Probing the thermodynamics and kinematics of solar coronal streamers. *Astrophys. J.* **728**, 67. DOI. ADS.

Altschuler, M.D., Newkirk, G.: 1969, Magnetic fields and the structure of the solar corona. I: Methods of calculating coronal fields. *Solar Phys.* **9**, 131. DOI. ADS.

Billings, D.E.: 1966, *A Guide to the Solar Corona*, Academic Press, San Diego, 323. ADS.

Blackwell, D.E., Petford, A.D.: 1966a, Observations of the 1963 July 20 solar eclipse. I. Spectroscopic separation of the F K components of the solar corona at large distances from the Sun. *Mon. Not. Roy. Astron. Soc.* **131**, 383. ADS.

Blackwell, D.E., Petford, A.D.: 1966b, Observations of the 1963 July 20 solar eclipse. II. The electron density in the solar corona in the region $5 < R/R < 16$ obtained from measurements of Fraunhofer line depth and the polarization of the F corona. *Mon. Not. Roy. Astron. Soc.* **131**, 399. ADS.

Boffin, H.M.J., Steeghs, D., Cuypers, J. (eds.): 2001, *Astrotomography*, *Lecture Notes in Physics* **573**, Springer, Berlin, 434. ADS.

Casini, R., Judge, P.G.: 1999, Spectral lines for polarization measurements of the coronal magnetic field. II. Consistent treatment of the Stokes vector for magnetic-dipole transitions. *Astrophys. J.* **522**, 524. DOI. ADS.

Charvin, P.: 1965, Étude de la polarisation des raies interdites de la couronne solaire. Application au cas de la raie verte λ 5303. *Ann. Astrophys.* **28**, 877. ADS.

Cormack, A.M.: 1963, Representation of a function by its line integrals, with some radiological applications. *J. Appl. Phys.* **34**, 2722. DOI. ADS.

Cormack, A.M.: 1964, Representation of a function by its line integrals, with some radiological applications. II. *J. Appl. Phys.* **35**, 2908. DOI. ADS.

Davila, J.M.: 1994, Solar tomography. *Astrophys. J.* **423**, 871. DOI. ADS.

Demoulin, P., Cuperman, S., Semel, M.: 1992, Determination of force-free magnetic fields above the photosphere using three-component boundary conditions. II – Analysis and minimization of scale-related growing modes and of computational induced singularities. *Astron. Astrophys.* **263**, 351. ADS.

Frazin, R.A., Janzen, P.: 2002, Tomography of the solar corona. II. Robust, regularized, positive estimation of the three-dimensional electron density distribution from LASCO-C2 polarized white-light images. *Astrophys. J.* **570**, 408. DOI. ADS.

Frazin, R.A., Kamalabadi, F.: 2005, Rotational tomography for 3D reconstruction of the white-light and EUV corona in the post-SOHO era. *Solar Phys.* **228**, 219. DOI. ADS.

Frazin, R.A., Vásquez, A.M., Kamalabadi, F., Park, H.: 2007, Three-dimensional tomographic analysis of a high-cadence LASCO-C2 polarized brightness sequence. *Astrophys. J. Lett.* **671**, L201. DOI. ADS.

Gary, G.A.: 2001, Plasma beta above a solar active region: rethinking the paradigm. *Solar Phys.* **203**, 71. DOI. ADS.

Hounsfield, G.N.: 1972, A method of and apparatus for examination of a body by radiation such as X-ray or gamma radiation. Patent. BP 1283915.

House, L.L.: 1977, Coronal emission-line polarization from the statistical equilibrium of magnetic sublevels. I – Fe XIII. *Astrophys. J.* **214**, 632. DOI. ADS.

Howard, R.A., Moses, J.D., Vourlidas, A., Newmark, J.S., Socker, D.G., Plunkett, S.P., Korendyke, C.M., Cook, J.W., Hurley, A., Davila, J.M., Thompson, W.T., St. Cyr, O.C., Mentzell, E., Mehalick, K., Lemen, J.R., Wuelser, J.P., Duncan, D.W., Tarbell, T.D., Wolfson, C.J., Moore, A., Harrison, R.A., Waltham, N.R., Lang, J., Davis, C.J., Eyles, C.J., Mapson-Menard, H., Simnett, G.M., Halain, J.P., Defise, J.M., Mazy, E., Rochus, P., Mercier, R., Ravet, M.F., Delmotte, F., Auchère, F., Delaboudinière, J.P., Bothmer, V., Deutsch, W., Wang, D., Rich, N., Cooper, S., Stephens, V., Maahs, G., Baugh, R., McMullin, D., Carter, T.: 2008, Sun Earth Connection Coronal and Heliospheric Investigation (SECCHI). *Space Sci. Rev.* **136**, 67. DOI. ADS.

Jiao, L., McClymont, A.N., Mikic, Z.: 1997, Reconstruction of the three-dimensional coronal magnetic field. *Solar Phys.* **174**, 311. DOI. ADS.

Judge, P.G.: 2010, The chromosphere: gateway to the corona? ...Or the purgatory of solar physics? *Mem. Soc. Astron. Ital.* **81**, 543. ADS.

Kramar, M., Inhester, B., Solanki, S.K.: 2006, Vector tomography for the coronal magnetic field. I. Longitudinal Zeeman effect measurements. *Astron. Astrophys.* **456**, 665. DOI. ADS.

Kramar, M., Jones, S., Davila, J., Inhester, B., Mierla, M.: 2009, On the tomographic reconstruction of the 3D electron density for the solar corona from STEREO COR1 data. *Solar Phys.* **259**, 109. DOI. ADS.

Kramar, M., Davila, J., Xie, H., Antiochos, S.: 2011, On the influence of CMEs on the global 3-D coronal electron density. *Ann. Geophys.* **29**, 1019. DOI. ADS.

Kramar, M., Inhester, B., Lin, H., Davila, J.: 2013, Vector tomography for the coronal magnetic field. II. Hanle effect measurements. *Astrophys. J.* **775**, 25. DOI. ADS.

Lee, C.O., Luhmann, J.G., Hoeksema, J.T., Sun, X., Arge, C.N., de Pater, I.: 2011, Coronal field opens at lower height during the solar cycles 22 and 23 minimum periods: IMF comparison suggests the source surface should be lowered. *Solar Phys.* **269**, 367. DOI. ADS.

Lin, H., Casini, R.: 2000, A classical theory of coronal emission line polarization. *Astrophys. J.* **542**, 528. DOI. ADS.

Lionello, R., Linker, J.A., Mikić, Z.: 2009, Multispectral emission of the Sun during the first Whole Sun Month: magnetohydrodynamic simulations. *Astrophys. J.* **690**, 902. DOI. ADS.

Luhmann, J.G., Li, Y., Arge, C.N., Gazis, P.R., Ulrich, R.: 2002, Solar cycle changes in coronal holes and space weather cycles. *J. Geophys. Res.* **107**, 1154. DOI. ADS.

Mikić, Z., Linker, J.A., Schnack, D.D., Lionello, R., Tarditi, A.: 1999, Magnetohydrodynamic modeling of the global solar corona. *Phys. Plasmas* **6**, 2217. DOI. ADS.

Mikić, Z., Linker, J.A., Lionello, R., Riley, P., Titov, V.: 2007, Predicting the structure of the solar corona for the total solar eclipse of March 29, 2006. In: Demircan, O., Selam, S.O., Albayrak, B. (eds.) *Solar and Stellar Physics Through Eclipses* **CS-370**, Astron. Soc. Pac., San Francisco, 299. ADS.

Moran, T.G., Davila, J.M., Morrill, J.S., Wang, D., Howard, R.: 2006, Solar and Heliospheric Observatory/Large Angle Spectrometric Coronagraph Polarimetric calibration. *Solar Phys.* **237**, 211. DOI. ADS.

Parker, E.N.: 1963, *Interplanetary Dynamical Processes*, Interscience, New York, 272. ADS.

Quémerais, E., Lamy, P.: 2002, Two-dimensional electron density in the solar corona from inversion of white light images – application to SOHO/LASCO-C2 observations. *Astron. Astrophys.* **393**, 295. DOI. ADS.

Radon, J.: 1917, Über die Bestimmung von Funktionen durch ihre Integralwerte längs gewisser Mannigfaltigkeiten. *Ber. Verh. Sächs. Akad. Wiss. Leipz., Math.-Phys. Kl.* **69**, 262.

Riley, P., Linker, J.A., Mikić, Z.: 2001, An empirically-driven global MHD model of the solar corona and inner heliosphere. *J. Geophys. Res.* **106**, 15889. DOI. ADS.

Rušin, V., Druckmüller, M., Aniol, P., Minarovjech, M., Saniga, M., Mikić, Z., Linker, J.A., Lionello, R., Riley, P., Titov, V.S.: 2010, Comparing eclipse observations of the 2008 August 1 solar corona with an MHD model prediction. *Astron. Astrophys.* **513**, A45. DOI. ADS.

Sahal-Brechot, S.: 1977, Calculation of the polarization degree of the infrared lines of Fe XIII of the solar corona. *Astrophys. J.* **213**, 887. DOI. ADS.

Sakurai, T.: 1989, Computational modeling of magnetic fields in solar active regions. *Space Sci. Rev.* **51**, 11. DOI. ADS.

Schatten, K.H., Wilcox, J.M., Ness, N.F.: 1969, A model of interplanetary and coronal magnetic fields. *Solar Phys.* **6**, 442. DOI. ADS.

Schrijver, C.J., DeRosa, M.L.: 2003, Photospheric and heliospheric magnetic fields. *Solar Phys.* **212**, 165. DOI. ADS.

Tadesse, T., Wiegelmann, T., Gosain, S., MacNeice, P., Pevtsov, A.A.: 2014, First use of synoptic vector magnetograms for global nonlinear, force-free coronal magnetic field models. *Astron. Astrophys.* **562**, A105. DOI. ADS.

Thompson, W.T., Reginald, N.L.: 2008, The radiometric and pointing calibration of SECCHI COR1 on STEREO. *Solar Phys.* **250**, 443. DOI. ADS.

Tikhonov, A.N.: 1963, Solution of incorrectly formulated problems and the regularization method. *Sov. Math. Dokl.* **4**, 1035.

Tomczyk, S., McIntosh, S.W.: 2009, Time–distance seismology of the solar corona with CoMP. *Astrophys. J.* **697**, 1384. DOI. ADS.

Tomczyk, S., McIntosh, S.W., Keil, S.L., Judge, P.G., Schad, T., Seeley, D.H., Edmondson, J.: 2007, Alfvén waves in the solar corona. *Science* **317**. DOI. ADS.

Tóth, G., van der Holst, B., Sokolov, I.V., De Zeeuw, D.L., Gombosi, T.I., Fang, F., Manchester, W.B., Meng, X., Najib, D., Powell, K.G., Stout, Q.F., Glocer, A., Ma, Y.-J., Opher, M.: 2012, Adaptive numerical algorithms in space weather modeling. *J. Comput. Phys.* **231**, 870. DOI. ADS.

van de Hulst, H.C.: 1950, The electron density of the solar corona. *Bull. Astron. Inst. Neth.* **11**, 135. ADS.

van der Holst, B., Sokolov, I.V., Meng, X., Jin, M., Manchester, W.B. IV, Tóth, G., Gombosi, T.I.: 2014, Alfvén Wave Solar Model (AWSoM): coronal heating. *Astrophys. J.* **782**, 81. DOI. ADS.

Wang, Y.-M., Sheeley, N.R. Jr.: 1992, On potential field models of the solar corona. *Astrophys. J.* **392**, 310. DOI. ADS.

Wiegelmann, T.: 2008, Nonlinear force-free modeling of the solar coronal magnetic field. *J. Geophys. Res.* **113**, 3. DOI. ADS.

Wiegelmann, T., Lagg, A., Solanki, S.K., Inhester, B., Woch, J.: 2005, Comparing magnetic field extrapolations with measurements of magnetic loops. *Astron. Astrophys.* **433**, 701. DOI. ADS.

Wilson, D.C.: 1976, The three dimensional solar corona. A coronal streamer, PhD thesis, National Center for Atmospheric Research, Boulder, CO. ADS.

Wuelser, J.-P., Lemen, J.R., Tarbell, T.D., Wolfson, C.J., Cannon, J.C., Carpenter, B.A., Duncan, D.W., Gradwohl, G.S., Meyer, S.B., Moore, A.S., Navarro, R.L., Pearson, J.D., Rossi, G.R., Springer, L.A., Howard, R.A., Moses, J.D., Newmark, J.S., Delaboudiniere, J.-P., Artzner, G.E., Auchere, F., Bougnet, M., Bouyries, P., Bridou, F., Clotaire, J.-Y., Colas, G., Delmotte, F., Jerome, A., Lamare, M., Mercier, R., Mullot, M., Ravet, M.-F., Song, X., Bothmer, V., Deutsch, W.: 2004, EUVI: the STEREO-SECCHI extreme ultraviolet imager. In: Fineschi, S., Gummin, M.A. (eds.) *Telescopes and Instrumentation for Solar Astrophysics*, *Proc. SPIE* **5171**, 111. DOI. ADS.

Zidowitz, S.: 1999, Coronal structure of the Whole Sun Month: a tomographic reconstruction. *J. Geophys. Res.* **104**, 9727. DOI. ADS.